# Evolutionary Group Dynamics in Stephan's Quintet

## Optical spectroscopy & radio observations with the LBT & IRAM 30m

Inaugural Dissertation

zur
Erlangung des Doktorgrades
der Mathematisch-Naturwissenschaftlichen Fakultät
der Universität zu Köln

vorgelegt von

**Lenita Mari Madeleine Yttergren**
aus Krylbo, Schweden

Köln, 2020

# Abstract

One of the most fundamental questions in astronomy is that of the evolution of galaxies. Ever since the quantum fluctuations present at the era of recombination, structures have evolved in the Universe. Dark matter halos facilitate congregation of baryonic matter and the gravitational attraction creates groups and clusters of galaxies.

Galaxies evolve through both external and internal processes. Internal processes are driven by instabilities in the galactic disk, spiral arms, bars and oval distortions, while external processes are driven by outside forces, such as galaxy mergers and harassment. External processes can have an immense impact on the galaxies involved, by altering the galaxies' morphology and content by moving large amounts of gas and inciting starbursts and active galactic nuclei (AGN).

Due to the abundance of gas and the proximity of the galaxies in the early Universe, it is accepted that galaxy mergers/interactions occurred often and were vital in driving galaxy evolution. The environment in which a galaxy resides plays an important role in its formation and evolution, and more than half of the galaxies in the Universe reside in galaxy groups. Compact galaxy groups are perfect laboratories for studying galaxy evolution through extreme galaxy interactions due to their galaxy density and activity. These groups can also reveal key information regarding the connections between galaxies and their environment, as well as details regarding galaxy evolution at high redshift. Low-redshift compact galaxy groups allow us to study the impact of galaxy interactions and mergers on galaxy evolution at high-resolution, thereby providing an insight into the conditions of the galaxies in the early Universe when such interactions were more common.

Stephan's Quintet is a nearby compact galaxy group of 5 galaxies with a rich and intriguing history of interactions. The past interactions can be traced via the tidal tails coursing through the group, while the current interaction is causing a galaxy-wide ridge of shock-driven star formation. This shocked star-forming ridge is enabled by the large amount of intergalactic gas present in the group, deposited in the intergalactic medium (IGM) during the previous galaxy interactions. Stephan's Quintet is one of the most well-studied groups in our Universe and every time the group has been observed in a new wavelength window or with higher resolution and sensitivity, new fascinating features have been revealed and our understanding of the processes and structures increased.

Multi-wavelength analyses of galaxies are essential, since it is only through comparison and combination of the tracers of galaxy dynamics (i.e., stars, atomic gas and molecular gas) that we can truly study the evolution of galaxies. To fill in blanks in the wavelength ranges covering Stephan's Quintet and contribute to increased understanding of our Universe, I have carried out optical spectroscopy and radio observations.

The optical wavelength regime provides information regarding the stellar population as well as the atomic gas, while spectroscopy enables spatial and spectral information to be gathered simultaneously. This facilitates studies of the abundances and kinematics as well as the excitation mechanisms across the group.

Covering a part of Stephan's Quintet in multiple slits with the Multi-Object Double

# Abstract

Spectrograph at the Large Binocular Telescope in Tucson, Arizona, USA, I am able to achieve a pseudo-Integral Field Spectroscopy observation of the main part of, and the most intense, interactions and activity in group. Focusing on the nucleus of the galaxies and the large-scale dynamics, I detail the kinematics of the IGM and the galaxies. I present an extensive analysis of the mapped area, including fluxes, velocity dispersions, line-of-sight velocities and excitation mechanisms in NGC7319, NGC7318A and B, NGC7317, the bridge, the west ridge and the star-forming ridge.

NGC7319 shows a disturbed galaxy, where the gaseous disk is decoupled from the stellar disk. I find a broad line region component in the nucleus, revealing for the first time the Seyfert 1 nature of this galaxy, and I confirm the presence of a blue outflow to the south-west of the nucleus at an average of $476 \pm 13.8$ km/s. The stellar and gaseous disks are approximately perpendicular to each other and the gas is excited by AGN radiation, indicating that the gas is present in a large-scale nuclear wind. The data further reveal extensive gas emission in the shocked star-forming ridge as well as in the west ridge (south-west of the NGC7318 pair) and the bridge connecting the NGC7318 pair and NGC7319. I confirm dual velocity components (as suggested by Duarte Puertas et al. (2019)) in several parts of the IGM and note that the shock increases the ionisation to LINER-like emission-line ratios in several regions along the star-forming ridge and the west ridge. Furthermore, the multiple velocity components present in many parts of the IGM and galaxies, spanning $5600 - 7000$ km/s, coincide with that of other galaxies, revealing the potential origin.

Cold molecular gas, best traced by CO emission detected in radio wavelengths, is a key ingredient in star formation and one of the main ingredients in galaxies. Analysing the behaviour of molecular gas is vital in determining the morphology and understanding the evolution of galaxies. I have, therefore, observed Stephan's Quintet using the IRAM 30m telescope in Sierra Nevada, Spain. Adopting an on-the-fly mapping technique I observed the $^{12}CO(1 \rightarrow 0)$, $(2 \rightarrow 1)$ and the $^{13}CO(1 \rightarrow 0)$ emission in a $5.67$ $arcmin^2$ area covering the group. I present maps and spectra of the emission, including abundances and velocities of the respective three CO lines, as well as molecular hydrogen gas masses. I further discuss the line ratios together with the excitation temperatures and the optical depth.

I find that the brunt of the CO emission is in/near NGC7319, extending towards and into the bridge and the star-forming ridge. $52 - 56\%$ of the molecular hydrogen gas mass in Stephan's Quintet is in/near NGC7319, while $38 - 40\%$ is in the star-forming ridge, the final $4 - 10\%$ is spread out across the NGC7318 pair and their surroundings. The distribution of $^{12}CO(2 \rightarrow 1)$, however, favours NGC7317, the NGC7318 pair, SQ-A and the star-forming ridge, which retain approximately half of the $^{12}CO(2 \rightarrow 1)$ emission, while NGC7319 contains less than $20\%$. This highlights the increased temperatures present in the shocked star-forming ridge. The data confirms the presence of multiple velocity components in the group, spanning $5600 - 7200$ km/s. Up to 4 clearly distinguishable velocity components can be found, with NGC7319 and the star-forming ridge showing the highest number of components. Again the velocity components often coincide with that of the other galaxies, tracing the complex history of the group. Furthermore, the CO line ratios indicate optically thick gas at low temperature in NGC7319 and the bridge. While in the star-forming ridge and SQ-A, the gas is found to be dense, optically thick and warm, as expected

considering the current interaction of the IGM and NGC7318B. The gas surrounding NGC7318B at a line-of-sight velocity of $\sim 5800$ km/s shows an inclination towards being warm, dense and optically thin.

This work favours a group evolution scenario of Stephan's Quintet that includes previous interactions of both NGC7319-NGC7317 and NGC7319-NGC7320C, and a scenario in which NGC7318B has passed through and is currently located in front of the group, supported by the multi-component IGM and the tidal streams that connect NGC7318B to the IGM and the galaxies. In addition, NGC7318B increases the group's energy and adds to the IGM gas content which stalls the gas depletion required for aging the group further. The enhancements of the passages of NGC7320C and NGC7318B are expected to be vital in hindering the group's imminent merger into a final fossil state. NGC7318B shows us the impact of diffuse IGM, while NGC7319 reveals a fascinating case of AGN feeding and feedback in a decoupled stellar/gas disk. NGC7319 shows lack of ongoing star formation while still appearing to contain molecular gas, although likely off-nuclear, with an outflow impacting the surrounding gas and structures - raising questions regarding the feeding mechanisms and lifetime of this AGN.

Stephan's Quintet differs from other groups due to the prominent extended tidal features and the currently occurring collision with NGC7318B. It is possible that these structures are short-lived and that all compact groups exhibit this kind of variety of galaxy interaction indicators, stellar and gaseous tidal features and galaxy-wide shock structures at some point during their evolution. Understanding these processes in Stephan's Quintet sheds light on the evolution of galaxies at a time in the history of the Universe when gas was abundant and interactions were common.

# Erklärung zur Dissertation

gemäß der Promotionsordnung vom 12. März 2020

Hiermit versichere ich an Eides statt, dass ich die vorliegende Dissertation selbstständig und ohne die Benutzung anderer als der angegebenen Hilfsmittel und Literatur angefertigt habe. Alle Stellen, die wörtlich oder sinngemäß aus veröffentlichten und nicht veröffentlichten Werken dem Wortlaut oder dem Sinn nach entnommen wurden, sind als solche kenntlich gemacht. Ich versichere an Eides statt, dass diese Dissertation noch keiner anderen Fakultät oder Universität zur Prüfung vorgelegen hat; dass sie - abgesehen von unten angegebenen Teilpublikationen und eingebundenen Artikeln und Manuskripten - noch nicht veröffentlicht worden ist sowie, dass ich eine Veröffentlichung der Dissertation vor Abschluss der Promotion nicht ohne Genehmigung des Promotionsausschusses vornehmen werde. Die Bestimmungen dieser Ordnung sind mir bekannt. Darüber hinaus erkläre ich hiermit, dass ich die Ordnung zur Sicherung guter wissenschaftlicher Praxis und zum Umgang mit wissenschaftlichem Fehlverhalten der Universität zu Köln gelesen und sie bei der Durchführung der Dissertation zugrundeliegenden Arbeiten und der schriftlich verfassten Dissertation beachtet habe und verpflichte mich hiermit, die dort genannten Vorgaben bei allen wissenschaftlichen Tätigkeiten zu beachten und umzusetzen. Ich versichere, dass die eingereichte elektronische Fassung der eingereichten Druckfassung vollständig entspricht.

Köln, 08.07.2020

(Lenita Mari Madeleine Yttergren)

# Weitere Publikationen des Autors

*'Interactions among intermediate redshift galaxies. The case of SDSSJ134420.86+663717.8'*
P. Misquitta, M. Bowles, A. Eckart, **M. Yttergren**, G. Busch, M. Valencia-S., N. Fazeli. Published in Astronomy & Astrophysics, Volume 639, id.A30, 14 pp., July 2020.

*'Near-infrared observations of the gas structure and kinematics in the circumnuclear region of NGC 1672'*
N. Fazeli, A. Eckart, G. Busch, **M. Yttergren**, F. Combes, P. Misquitta, C. Straubmeier. Published in Astronomy & Astrophysics, Volume 638, id.A36, 13 pp, June 2020.

*'GLINT. Gravitational-wave Laser INterferometry Triangle'*
S. Aria, R. Azevedo, R. Burow, F. Cahill, L. Ducheckova, A. Holroyd, V. Huarcaya, E. Järvelä, M. Koßagk, C. Moeckel, A. Rodriguez, F. Royer, R. Sypniewski, E. Vittori, **M. Yttergren**. Published in Experimental Astronomy, Volume 44, Issue 2, pp.181-208, November 2017.

*'A blueprint for a simultaneous test of quantum mechanics and general relativity in a space-based quantum optics experiment'*
S. Pallister, S. Coop, V. Formichella, N. Gampierakis, V. Notaro, P. Knott, R. Azevedo, N. Buchheim, S. de Carvalho, E. Järvelä, M. Laporte, J. Kaikkonen, N. Meshksar, T. Nikkanen and **M. Yttergren**. Published in EPJ Quantum Technology 2017 4:2, 7 February 2017.

*'Glass transition and relaxation dynamics of propylene glycol - water solutions confined in clay'*
K. Elamin, J. Björklund, F. Nyhlén, **M. Yttergren**, L. Maartensson, J. Swenson. Published in The Journal of Chemical Physics, 17 July 2014.

x

# Contents

# List of Figures

# List of Tables

List of Tables

# Abbreviations & Acronyms

**AGN** Active Galactic Nucleus
**ALMA** Atacama Large Millimeter/submillimeter Array
**AO** Adaptive Optics
**BLR** Broad-Line Region
**CCD** Charge-Coupled Device
**CFHT** Canada-France-Hawaii Telescope
**CLASS** The GILDAS based Continuum and Line Analysis Single-dish Software
**CMB** Cosmic Microwave Background
**CO** carbon monoxide
**DMH** Dark Matter Halo
**dx** Horizontal shifts
**EHT** Event Horizon Telescope
**ELT** Extremely Large Telescope
**EMIR** Eight MIxer Receiver
**FoV** Field of View
**FWHM** Full Width at Half Maximum
**GALEX** Galaxy Evolution Explorer
**GreG** Grenoble Graphic software
**HCG** Hickson Compact Group
**HRD** Hertzsrpung-Russel Diagram
**HST** Hubble Space Telescope
**IFS** Integral Field Spectroscopy
**IGM** Intergalactic Medium
**IMF** Initial Mass Function
**IR** Infrared
**IRAF** Image Reduction and Analysis Facility
**IRAM** Institut de Radioastronomie Millimétrique
**ISM** Interstellar Medium
**LBT** Large Binocular Telescope
**$\Lambda$CDM** Lambda Cold Dark Matter
**LIGO** Laser Interferometer Gravitational-Wave Observatory
**LINER** Low-Ionization Nuclear Emission-line Region
**LIRG** Luminous Infrared Galaxy
**LUCI** LBT Utility Camera in the Infrared
**MIR** Mid-Infrared
**MODS** Multi-Object Double Spectrograph
**NED** NASA/IPAC Extragalactic Database
**NIR** Near-Infrared
**NLR** Narrow-Line Region
**OTF** On-the-fly (an observation technique)
**PA** Position Angle
**PAH** Polycyclic Aromatic Hydrocarbon
**pPXF** Penalized Pixel-Fitting
**QSO** Quasi-Stellar Object

**rms** Root Mean Square
**SDSS** Sloan Digital Sky Survey
**SF** Star-Forming
**SFR** Star-Formation Rate
**SMBH** Super-Massive Black Hole
**SNR** Signal-to-noise ratio
**SQ** Stephan's Quintet
**TDG** Tidal Dwarf Galaxy
**ULIRG** Ultra-Luminous Infrared Galaxy
**UV** Ultraviolet
**VLTI** Very Large Telescope Interferometer
**WISE** Wide-field Infrared Survey Explorer

# 1

# Introduction

To be the Universe observing itself is the purpose of human existence. And we have fulfilled this purpose for as long as we can remember. Observing the night sky, searching for a description of our place within the cosmos, and understanding the continued evolution of the infinite Universe in which we reside, entices some of the most profound human thoughts and questions. How did the Universe come to exist? How will it end? Will it end? What are the building blocks of our Universe? What was and is the importance of dark matter and dark energy? How were structures such as stars, galaxies, galaxy groups and clusters formed? How do they evolve? These and many more are the questions, the mysteries, that astronomy aims to solve.

With the 17th century came the invention of the telescope, a truly revolutionary construction for the research field with unprecedented resolution and sensitivity. Telescopes have thenceforth allowed many astronomical objects to be classified and analysed, and have enabled the development of models to describe many astronomical phenomena. Today improving and developing new telescopes and methods to observe astronomical objects in all wavelength regimes, is an important and very active field, creating such fascinating structures as the Laser Interferometer Gravitational-Wave Observatory (LIGO), and the Event Horizon Telescope (EHT). And although, observations and simulations have enabled immense progress and many questions to be answered, many more questions remain and new questions arise continuously.

As the cosmic microwave background (CMB) reveals the state of the Universe prior to the formation of structures such as stars and galaxies, it shows us a Universe that at first glance appears isotropic (Planck Collaboration et al., 2018). Fortunately, the CMB contains quantum fluctuations, anisotropies, that allowed the gathering of matter and the formation of structure. We still do not know how these small anisotropies grew into the structures we see today, but it is generally agreed upon that dark matter halos and their galaxies gathered, forming larger structures, galaxy groups and clusters (Springel et al., 2005). The significance of the environment on the evolution of a galaxy is being debated within the construct of the "nature vs nurture" scenario, where the importance of the formation environment is placed against past experiences as the main influence on a galaxy's evolutionary path. As of today, the environment appears to have an important impact on a galaxy's evolution, as elliptical galaxies are more common in dense regions than star-forming spiral galaxies for example (Dressler, 1980).

It is believed that in the young Universe extreme galaxy interactions, such as galaxy mergers, were common and vital in driving galaxy evolution (Rodríguez-Baras et al., 2014). As many interacting/merging galaxies have been observed,

the process can be deemed common, and simulations show that the impact on the morphologies of the interacting galaxies often is substantial (Renaud et al., 2010; Hwang et al., 2012; Misquitta et al., 2020). Furthermore, it has been suggested that these kinds of interactions can trigger black hole activity and starbursts (Ellison, 2019). And stars are a particularly important player in the evolution of the Universe, as they are the origin of heavier chemical elements, such as iron and oxygen. A key aspect to our understanding of the formation and evolution of galaxies therefore lies in the kinematics of the stars and the gas (Cappellari, 2017).

More than half of the galaxies in the Universe are found in groups (Hickson, 1997). Galaxy groups are beautiful structures in the night sky, and due to the close proximity of the galaxies the rate of interactions and the amount of gas present in the intergalactic medium is high. This enables the creation of stunning structures and facilitates discovery of new and fascinating details of the processes affecting the medium and the group's galaxies. Galaxy groups are truly useful for studying galaxy properties and evolution as a function of the environment, and can reveal important details regarding the interconnected nature of galaxy evolution and group environment (Nishiura et al., 2000; Mihos, 2004; Kauffmann et al., 2004). Whether galaxy groups are gravitationally bound systems or not is currently a hot topic, and the observational definition of groups is still not well defined. Furthermore, nearby galaxy groups can provide us with a high resolution view on the extreme galaxy interactions that are believed to be particularly common in the early Universe (Rodríguez-Baras et al., 2014; Natale et al., 2010), revealing vital insights into galaxy evolution at higher redshifts and throughout cosmic time.

The bright nearby compact galaxy group Stephan's Quintet is an optimal candidate for studying a history of multiple galaxy interactions, shock induced star formation and galaxy evolution through extreme galaxy interactions. As this compact group has been extensively studied in multiple wavelength regimes, filling in the gaps proves enlightening and goes along the path of shedding light on the process of galaxy evolution. Exactly how this thesis is placed within the framework of the previous work on Stephan's Quintet and compact galaxy groups, is detailed in Chapter 3, after the proper background knowledge has been provided.

This thesis begins with a scientific background, in Chapter 2, regarding the known picture of structure formation and evolution, the necessary definitions and the importance of observations in different wavelength regimes. In Chapter 3, a background of the compact galaxy group Stephan's Quintet is presented, including a summary of the previous data published on this source. Thereafter, this work is split into two main parts, according to the observations and analysis carried out: optical spectroscopy with the Large Binocular Telescope (LBT) and radio observations with the IRAM 30m telescope. *Part I. Atomic Gas & Stellar Kinematics in Stephan's Quintet*, Chapter 4-7, contains a background to optical astronomy and the LBT, details on the data acquisition, reduction and analysis of the LBT optical spectroscopy data of the galaxy group, the results thereof and the summary and conclusions of these results. *Part II. Molecular Gas Kinematics in Stephan's Quintet*, Chapter 8-11, has a similar layout as Part I. Beginning with an introduction to radio astronomy and the IRAM 30m telescope, then detailing the acquisition, reduction procedure and analysis of the IRAM 30m radio data, as well as the results and the summary

and conclusions thereof. The *Summary & Conclusions* after each 'Part' refers only to the details obtained in *Part I* and *II* respectively. A further discussion, placing the work carried out here in relation to other works, including its impact on the history of Stephan's Quintet, compact groups, extreme galaxy interactions and galaxy evolution throughout cosmic time, is presented in the final chapter, Chapter *12. Concluding Discussion & Remarks.*

# 2

# Astronomical Background

The connections between the different processes and events in our Universe are many, complex and thoroughly entwined. This chapter provides a summary of the background knowledge necessary for understanding the results of this thesis, in as few words as possible.

The chapter begins with the distribution of matter in the Universe and the formation of structures, such as the congregation of matter into galaxies, and continues with the concept of galaxy evolution, via internal and external processes. Thereafter, star formation and active galaxies, including the classification and unification of active galactic nuclei as well as the feeding and feedback processes of super-massive black holes, are discussed. The next section includes galaxy groups, particularly compact galaxy groups and their specific aspects and importance in galaxy evolution. The chapter concludes with a summary of the advantages of observations in different wavelength regimes focused on tracers of galaxy evolution.

There is truly a magnificent amount of books and review articles on the topics discussed in this chapter, which forces a selection to be made. Unless stated otherwise the information detailed here relies on Sparke & Gallagher (2007); Netzer (2013); Schneider (2015).

## 2.1 Matter Distribution & Structure Formation

Let us begin by assuming a Lambda cold dark matter ($\Lambda$CDM) Universe, where the baryonic matter in the Universe makes up 4.89%, the dark matter 26.22% and the dark energy 68.89% (Planck Collaboration et al., 2018). The cosmic microwave background (CMB) shows the electromagnetic radiation from the recombination epoch, when the photons decoupled from matter, at a redshift of $z \sim 1100$, approximately 380000 years after the Big Bang. The CMB shows the state of the Universe before the formation of structures such as galaxies and stars. The CMB exhibits anisotropies, as can be seen in Fig.2.1, which shows an image of the CMB obtained with the Planck satellite. The anisotropies begun as quantum fluctuations in the primordial Universe, and grew under the inflation epoch and later under the influence of gravitational instabilities as the Universe expanded.
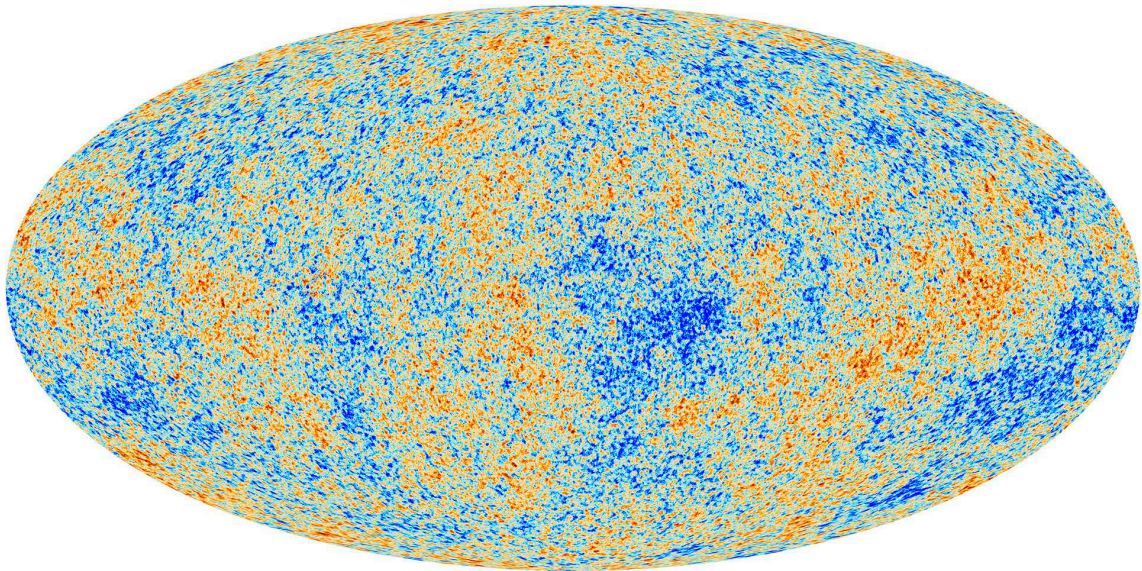


**Figure 2.1:** The cosmic microwave background as obtained with Planck. The temperature fluctuations are shown as colour differences. Credit: ESA and the Planck Collaboration.

The anisotropies are mirrored in primordial density fluctuations. As the dark matter density fluctuations reach critical mass they collapse forming pressure-supported virialised objects called dark matter halos (DMHs). Baryonic matter falls into the DMHs, cooling and forming structures such as galaxies, galaxy groups ($< 50$ galaxies, typically $\sim 1 - 2$ Mpc across), galaxy clusters ($50 - 1000$ galaxies, $\sim 10$ Mpc across) and superclusters ($\sim 100$ Mpc across). Approximately half of the galaxies in the Universe are contained in groups and clusters. The clusters no longer expand with the accelerated expansion of the Universe, due to their mutual gravitation attraction.

The filamentary structure of the Universe and the correlation of dark to baryonic matter can be seen in Fig.2.2, which displays the distribution of matter as obtained by the Millennium Simulation. The Millennium Simulation is a 3D N-body simulation of the matter distribution of the Universe (Springel et al., 2005). Fig.2.2

displays two snapshots from the Millennium Simulation, showing the distribution of light, to the left, compared to the distribution of dark matter, to the right. A supercluster is present near the center of the image, its size, 125 Mpc/h, is marked in the image to the right.

Observationally, the distribution of dark matter can be obtained from observing the gravitational effect of dark matter on light, i.e., lensing. Fig.2.3 displays the Sloan Digital Sky Survey (SDSS) map of the large scale structure of the Universe, where each dot is an observed galaxy coloured according to the g-r colour of that galaxy.

Galaxy clusters themselves, can be observed in X-ray, since their intergalactic medium (IGM) is filled with hot gas (T$\sim 10^7$ K) that emits in X-ray. Furthermore, galaxy clusters are typically split into regular and irregular, where the regular clusters are in a relaxed state and dominated by elliptical galaxies, and irregular clusters contain a fraction of spirals close to as large as the fraction in the general distribution of field galaxies.
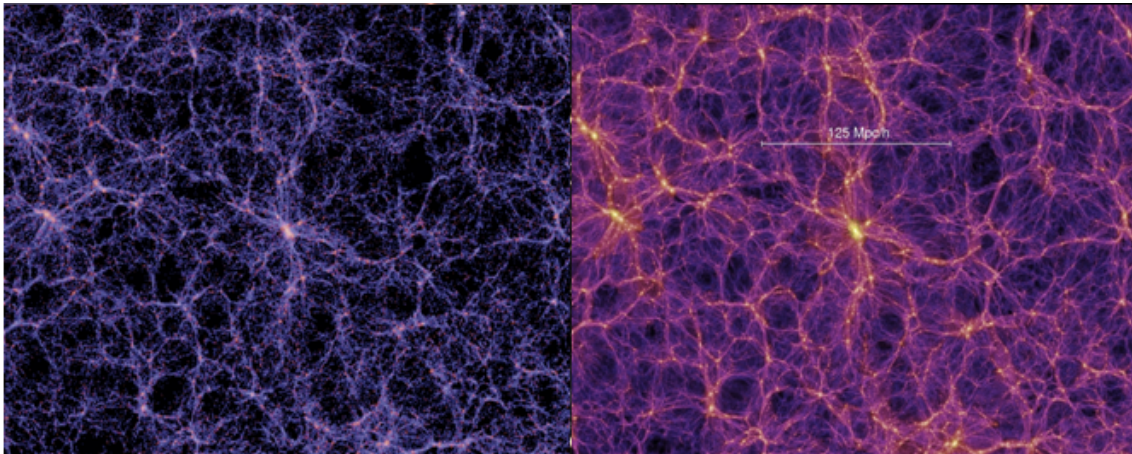


**Figure 2.2:** 3D N-body simulation of the cosmic web as described the ΛCDM model. *Left:* The distribution of light. *Right:* The distribution of dark matter. Credit: the Millennium Simulation
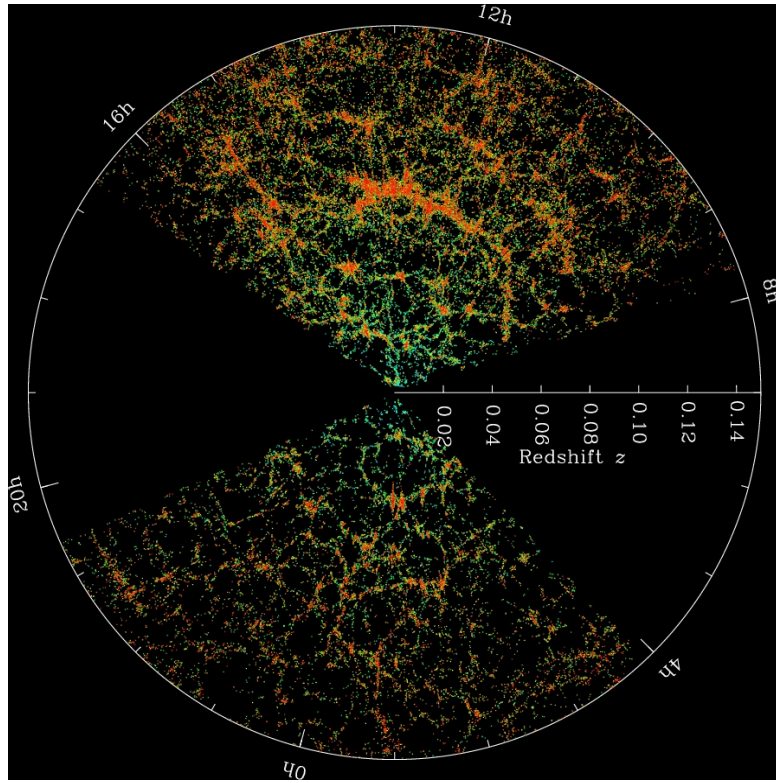
**Figure 2.3:** The large scale structure of the Universe as observed by the SDSS. Each dot represents a galaxy, coloured according to its g-r colour. Credit: M. Blanton and SDSS.

## 2.2 Galaxy Evolution[1]

First, note that this thesis adopts the classical Hubble classification, illustrated in Fig.2.4, as elaborated by de Vaucoleur (de Vaucouleurs, 1959). As an example of the classification, the notation of the spiral galaxies, NGC7319 and NGC7320C, can be described as:

- NGC7319 SB(s)bc pec: a barred (B) rather loosely wound (bc) spiral galaxy, with a weak inner spiral (s) and peculiar/disturbed morphology (pec).
- NGC7320C (R)SAB(s): a spiral galaxy with a weak bar (AB), a weak inner spiral (s) and an outer ring (R).

Note that inner rings in general occur at the bar ends, i.e., at the inner Lindblad resonance. While the outer rings typically have a radius of approximately a factor of 1.2 times the radius of the bar. Additionally, it is common that the inner and outer rings contain HI, as well as star formation due to the accumulation of gas at these locations. For elliptical galaxies, the numbering system is in regards to the galaxy's ellipticity, where a E0 galaxy appears round on the sky and an E5 galaxy's semi minor axis is half of the semi major axis. Therefore, the naming convention of an elliptical galaxy depends on the viewing angle, contrary to spiral galaxy naming. Furthermore, the later the Hubble type, the bluer the spectrum is and the stronger the emission lines are, indicating that the later Hubble type the younger galaxy.

---

[1]Apart from the aforementioned books, this chapter relies heavily on Kormendy (2013) and the references therein.
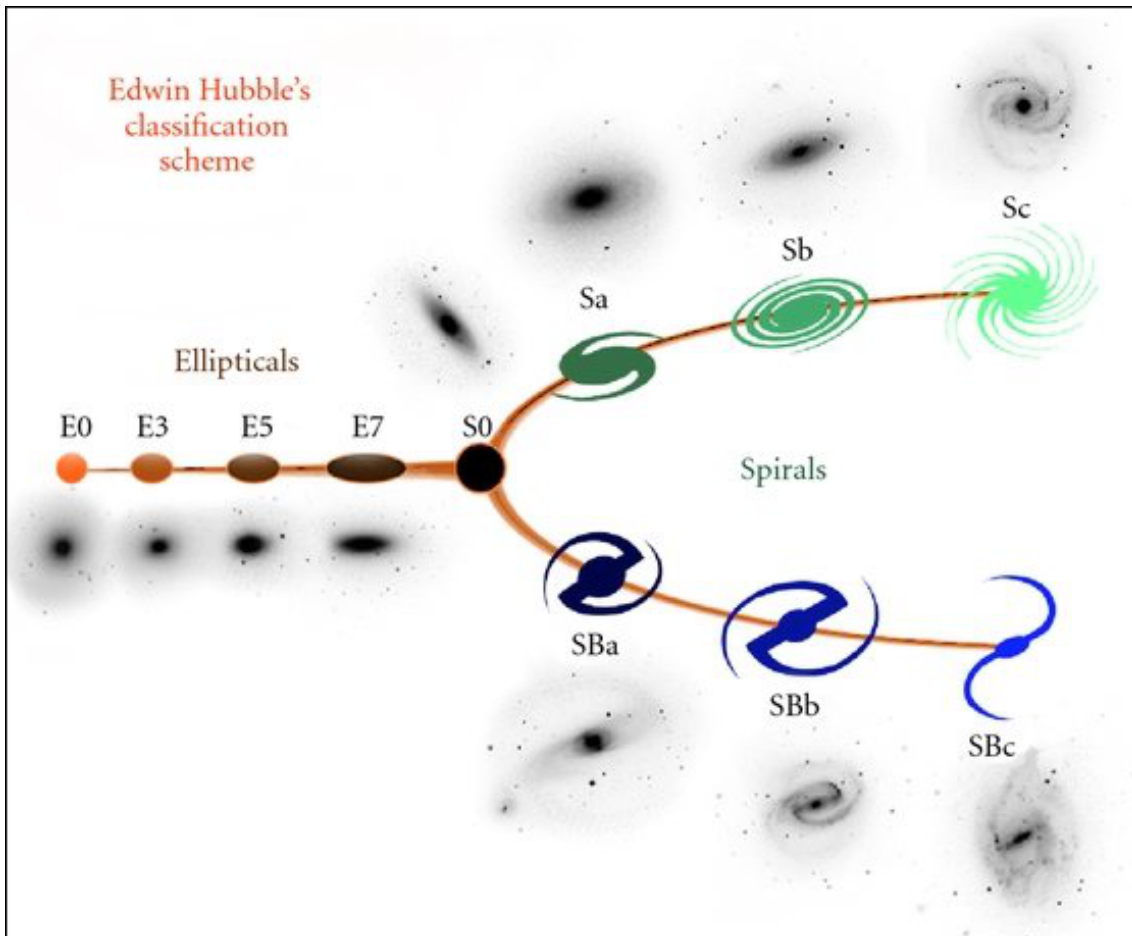
**Figure 2.4:** The Hubble classification scheme. Credit: NASA and ESA.

In the early Universe, galaxy evolution was driven by fast processes, such as hierarchical clustering and galaxy mergers. "Fast" is defined as happening on a free-fall timescale, a timescale that is proportional to the gravitational constant, $G$, and the density of the structure formed, $\rho$, as: $t \propto (G\rho)^{-1/2}$. But as the Universe continues to expand the slow processes will eventually succeed to dominate the evolution of galaxies. Slow processes, i.e., secular, occur over the time span of many galaxy rotations and internal secular evolution is driven by non-axisymmetric structures, such as spiral patterns and bars. External processes driving secular evolution can be, for example, minor mergers or galaxy harassment. Fig.2.5 displays the galaxy evolution process split into four aspects; slow, fast, internal and external. In general, galaxies are expected to evolve from ordered rotational systems, i.e., spiral disk galaxies, into systems governed by random motion, i.e., elliptical galaxies.

## 2.2.1 Secular Evolution in Spiral Galaxies

The second law of thermodynamics states that all closed systems aim to maximise entropy, i.e., disorder. An ordered system, such as a spiral galaxy, is continuously at odds with this law, entailing that an increase of order in one region simultaneously increase the disorder in another region. The spiral pattern, i.e., the density waves,
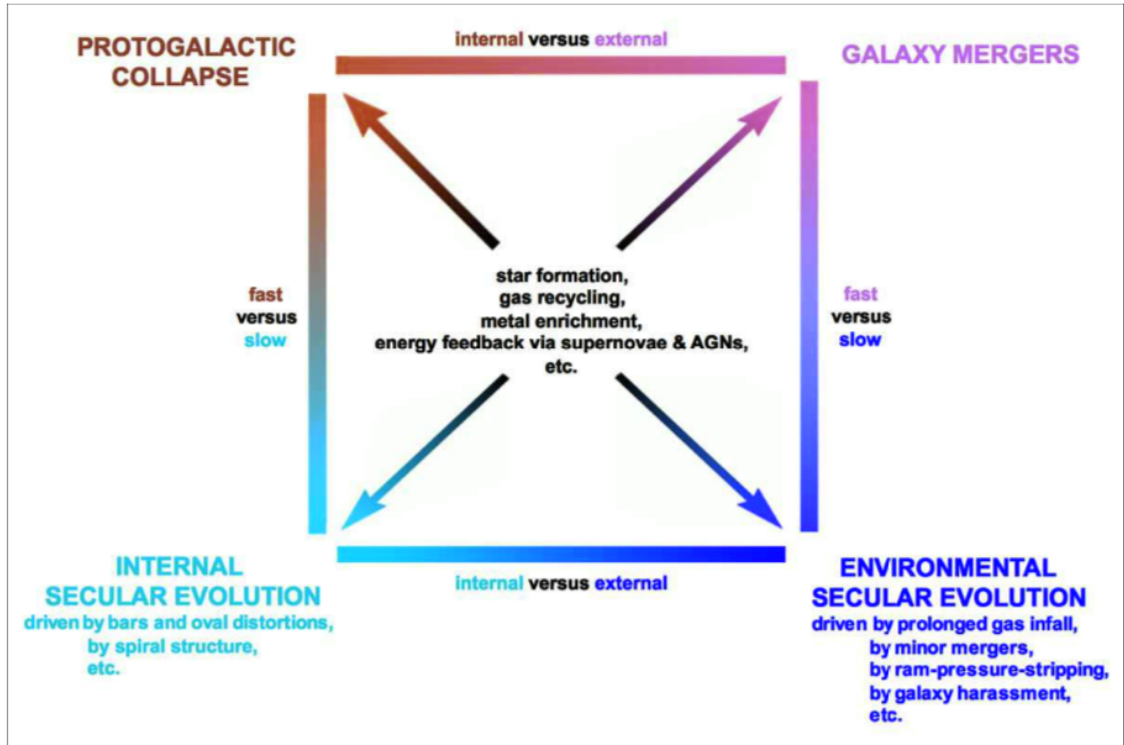
**Figure 2.5:** The process of galaxy evolution illustrated as fast vs slow and internal vs external. Image based on Kormendy (2013).

are particularly useful in this process, as they transport energy/angular momentum outwards, making inner regions denser and outer regions more diffuse.

In a spiral galaxy almost all of the energy of motion is due to the ordered rotation. At radius $r$ the energy of such a system, $E(r)$, and the corresponding angular momentum, $L(r)$, can be described as:

$$E(r) = \frac{r}{2}\frac{d\phi}{dr} + \phi, \qquad L(r) = \left(r^3\frac{d\phi}{dr}\right)^{1/2}, \qquad (2.1)$$

where $\phi$ is the potential energy (Tremaine, 1989). The angular speed of rotation, $\omega(r) = dE/dL$, can then be related to the potential energy as: $\omega = \sqrt{(r^{-1}d\phi/dr)}$. As the disk spreads, a particle of unit mass at radius $r_2$ moves outward and gains angular momentum, $dL$, relative to a particle of unit mass at radius $r_1$, where $r_1 < r_2$. The change in energy that occurs is:

$$dE = dE_1 + dE_2 = \left[-\left(\frac{dE}{dL}\right)_1 + \left(\frac{dE}{dL}\right)_2\right]dL = [-\omega(r_1) + \omega(r_2)]dL. \qquad (2.2)$$

Since $\omega(r)$ typically decreases outwards, the energy change is negative, leading to the conclusion that the spreading of a disk results in a lower energy state.

Measuring the speed, $V(r)$, of a circular orbit at radius $r$, the radial-force equation enables an estimation of the mass within that radius:

$$\frac{V^2(r)}{r} = \frac{GM(<r)}{r^2}, \qquad (2.3)$$

where $G$ is the gravitational constant. The speed, $V(r)$, makes up the rotation curve of a galaxy and can be obtained from the the line-of-sight velocity, $V_{los}$:

$$V_{los}(r, i) = V_s + V(r) \sin i \cos \phi. \tag{2.4}$$

The line-of-sight velocity is also called the radial velocity, and it is the velocity that is commonly observed. $V_s$ is the systemic velocity, which is the line-of-sight velocity of the centre of the galaxy. $i$ is the angle of which the disk is tilted, measured from face on at $i = 0$, and $\phi$ is the azimuth angle in the disk. Common peak values of the rotation speed of spiral galaxies are $V_{max} = 150 - 300$ km/s, but values up to 500 km/s have been observed. Brighter and more massive spiral galaxies rotate faster and their luminosity is related to their peak rotation speed according to the Tully-Fisher relation:

$$\frac{L_I}{4 \times 10^{10} L_{I,\odot}} \approx \left( \frac{V_{max}}{200 km/s} \right)^4 \tag{2.5}$$

where the luminosity is measured in the I band at $0.8 \mu m$. An interesting tidbit, is that the Tully-Fisher relation indicates a clear correlation between the amount of dark matter, which governs the rotation curve, and the luminous baryonic matter.

Spiral galaxies often show warping or flaring (disk spreading) in the outer edges of the disks. It is also common, especially in barred galaxies, that $V(r) \neq 0$ along the apparent minor axis, showing radial motions, which is often comprised of gas moving towards the center of the galaxy. Furthermore, stellar bars exert gravitational torques on gas, creating shocks that can be traced by dust lanes and flows to the central region.

As gas moves into the centre of a galaxy, it adds to the dense inner regions of bulges, bars and black hole accretion disks. The feeding processes of black holes remain shrouded in mystery, but will be discussed briefly in Chapter 2.4. When all the angular momentum has been transferred outside of the corotation radius, or when the system has been disturbed through interactions/collisions, so a rotational disk can no longer be maintained, and the gas of the galaxy has been pulled out of the galaxy, fed into the central black hole or formed into stars - the galaxy is expected to reach a state very similar to an elliptical galaxy.

### 2.2.2 Kinematics of Elliptical Galaxies

While the luminosity of a spiral galaxy is connected to its rotational velocity, the luminosity of an elliptical galaxy is linked to its velocity dispersion, and a higher velocity dispersion means a higher luminosity. This chapter will detail how elliptical galaxies contain information about their origin, and that their slow rotation indicate that they have yet to relax into a final state.

Elliptical galaxies are gas poor, and a kinematic analysis relies on the stellar absorption features. The velocity dispersion of elliptical galaxies is commonly $\sim 200$ km/s, but range from $\sim 50$ km/s in the least luminous ellipticals up to 500 km/s in the centres of the brightest objects. The luminosity in the V band can be connected to the velocity dispersion, $\sigma$, of the galaxy, via the Faber-Jackson relation:

$$\frac{L_V}{2 \times 10^{10} L_{\odot}} \approx \left( \frac{\sigma}{200 km/s} \right)^4 \tag{2.6}$$

The Faber-Jackson relation can also be used to estimate distances, although it is better to use the $D-\sigma$ relation, or the fundamental plane relation. The $D-\sigma$ relation relates the galaxy's central brightness to the luminosity, often setting $D$ as the radius where the average surface brightness in the B-band is $20-21$ $mag\ arcsec^{-2}$. The fundamental plane relation connects the effective radius, $R_e$, and the central velocity dispersion, $\sigma_c$, to the surface brightness, $I_e = I(R_e)$, as:

$$R_e \propto \sigma_c^{1.2} I_e^{-0.8}. \tag{2.7}$$

The rotation of elliptical galaxies are expected to follow the virial theorem. The virial theorem relates the long-term averages of the kinetic, $KE$, and potential, $PE$, energies of a bound system to each other as:

$$2\langle KE_{zz}\rangle + \langle PE_{zz}\rangle = 0. \tag{2.8}$$

A virialised system evolves by heat transfer, where if the centre is hotter than the outer regions, the heat flows outward, which in turn makes the centre contract and heat up. This cycle repeats until the central region collapses. The process requires different amounts of time depending on the structure in question, for globular clusters it is short and their collapse is imminent, but for elliptical galaxies this process is longer than the age of the Universe. The fact that elliptical galaxies have not yet reached a relaxed state can be deduced from the difference in the expected and observed rotation velocities.

Let us begin with deriving the velocity we expect in an elliptical galaxy. The kinetic and potential energies of a star, $\alpha$, at position $\boldsymbol{x}_\alpha$, gravitationally influenced by the other stars in the galaxy, of masses $m_\beta$ at positions $\boldsymbol{x}_\beta$, can be described as:

$$KE_{zz} = \frac{1}{2}\sum_\alpha m_\alpha v_{z\alpha}^2, \tag{2.9}$$

$$PE_{zz} = -\sum_{\substack{\alpha,\beta \\ \alpha\neq\beta}} \frac{1}{2}\frac{Gm_\alpha m_\beta}{|\boldsymbol{x}_\alpha - \boldsymbol{x}_\beta|^3}(z_\alpha - z_\beta)^2, \tag{2.10}$$

where $v_{z\alpha}$ is the $z$-component of the velocity of star $\alpha$ and $v_{z\beta}$ the $z$-velocity for star $\beta$. Assuming that the galaxy is axisymmetric and rotates around the z-axis, and that the rotation speed, $V$, and the velocity dispersions, $\sigma_x$ and $\sigma_z$, are near constant along their axes, the potential and kinetic energies in the two directions can be related as:

$$\frac{\langle PE_{zz}\rangle}{\langle PE_{xx}\rangle} = \frac{\langle KE_{zz}\rangle}{\langle KE_{xx}\rangle} \approx \frac{\sigma_z^2}{\frac{1}{2}V^2 + \sigma_x^2} \approx \left(\frac{B}{A}\right)^{0.9} = (1-\epsilon)^{0.9}, \tag{2.11}$$

where $B/A$ is the galaxy's axis ratio and $\epsilon \equiv 1 - B/A$ is the ellipticity. The measured/observed speed, $V_m$, is a fraction of the true rotation speed, $V$, i.e., $V_m \approx \pi V/4$. Combining this knowledge with the assumption of isotropic motions, i.e., $\sigma_x = \sigma_z = \sigma$, an equation describing the observed velocity as a function of ellipticity emerges:

$$\left(\frac{V_m}{\sigma}\right) \equiv \frac{\pi}{4}\sqrt{2[(1-\epsilon)^{-0.9} - 1]} \approx \sqrt{\frac{\epsilon}{(1-\epsilon)}}. \tag{2.12}$$

Unfortunately, the values provided from Eq.2.12 do not match observations, Eq.2.12 results in too high values, indicating an anisotropic velocity dispersion. The slow observed rotation must be compensated by random motions and indicate that the relaxation is not complete. Actually, it is common to find kinematically decoupled cores in elliptical galaxies, where the inner part of the galaxy maintain a rotation separate from the outer parts of the galaxy - a clear indication of a system that retains information about how it was assembled and that it has yet to develop rotational axisymmetry.

### 2.2.3   Galaxy Mergers & Interactions

Galaxy encounters and mergers have immense impact on the galaxies involved, altering their shape and structure by moving large amounts of gas and inciting starbursts and potentially active galactic nucleus (AGN). If mergers trigger AGNs at all redshifts or not is still up for debate, but there are clear indications of a connection between mergers and AGN at z∼0 (Ellison (2019) and references therein). AGNs will be further discussed in Chapter 2.4.

An interaction between two galaxies, introduce a non-axisymmetric perturbation that breaks the conservation of angular momentum in the individual circular orbits, allowing gas to be funneled to within kpc distances from the nuclei. As most AGNs subsist in gas-rich spiral galaxies, it is reasonable to assume that they are fed with interstellar medium (ISM). Instabilities must be present in the system to enable transfer of the gas inwards, and at the very inner pc's the viscosity is expected to take over the gas transfer. Mergers are particularly efficient in inducing instabilities and changes in galactic systems, which may be optimal for inciting such gas transfer. Adding to the conviction of the AGN feeding and starbursts abilities of mergers, is that the atomic and molecular gas fractions have been found to be enhanced in those systems. $H_2$ gas fractions in mergers have been found to be enhanced by a factor of 2-3 (Violino et al., 2018), while HI gas fractions by a factor of 3 (Ellison et al., 2018).

The impact of the merger/interaction event depends on the masses of the galaxies involved. Low-mass galaxies, i.e., dwarf satellites, orbit larger disk galaxies, and merge with the larger galaxy with negligible major impact on the spiral structure of the large galaxy. These kinds of mergers aid in triggering strong inflows of gas and bursts of star formation, and are believed to be a common occurrence, keeping galaxies star forming over long periods of time.

However, when two galaxies of approximately equal mass interact, the impact is distinct. Fig.2.6 displays 10 currently interacting galaxies, imaged by the SDSS. Particularly interesting is that several of these mergers consist of one confirmed AGN and one starburst galaxy, where the radio emission originates from the starburst galaxy (currently being researched by my colleague Persis Misquitta). A typical example of a merger between two spiral galaxies of similar mass, a major merger, is displayed in Fig.2.7, simulated by V.Springel & S.D.M.White at MPA Garching in 1999. The first close encounter at 1 Gyr after the beginning of the simulation, results in two open bisymmetric spirals, while stars and gas in the outskirts of the encounter are ejected into what later forms tidal tails. The bridge that is created between the

**Figure 2.6:** A sample of 10 mergers imaged by the SDSS, illustrating the extreme interactions present in such merging objects.

galaxies at ~1 Gyr, is destroyed after the second close encounter, but the large tidal tails remain as an indication of the violent history. The final state of the simulation is a spheroidal system, similar to an elliptical galaxy. Although, observations show disturbed, interacting and peculiar galaxies with rings or bars, with colours that do not agree with those of elliptical galaxies. Combining simulations with observations is the best path towards understanding the process of such galaxy interactions and mergers (Toomre & Toomre, 1972; Barnes & Hernquist, 1992, 1996; Hopkins et al., 2008; Misquitta et al., 2020).

Observing the star formation rate (SFR) of the Universe reveals an increase at $z = 1 - 3$ (Lilly et al., 1996; Madau et al., 1996; Sobral et al., 2013). Most stars in the Universe formed during this period which also coincides with a peak in black hole activity (Stott et al., 2013). Star formation in this period does not follow the main sequence star formation present in today's Universe (more details on star formation is given in Chapter 2.3). Suggestions of an increase in the gas accretion rate has been put forward (Dekel et al., 2009), but observations suggest that it was an increase in galaxy merger rate that drove the increase in SFR at $z \sim 2$ (Somerville et al., 2001; Hopkins et al., 2006). However, Stott et al. (2013) find no increase in number density of star-forming galaxies, nor increase in merger rate at z~ $1 - 2$, and Pearson et al. (2019) deduced that in general merger have negligible effect on the SFR of galaxies. So although, large impact on SFR by galaxy merger, is observed, it is less common. Galaxy mergers may not have a significant and consistent effect on SFR, but astronomers agree that the process does induce starbursts.

In addition, the tidal debris of interacting galaxies can form self-gravitating entities called tidal dwarf galaxies (TDGs) (Zackrisson & Riehm, 2010; Duc, 2012; Lisenfeld et al., 2016). TDGs are similar to common irregular dwarf galaxies or blue compact dwarfs, however, they exhibit a higher metallicity and lack of dark matter.
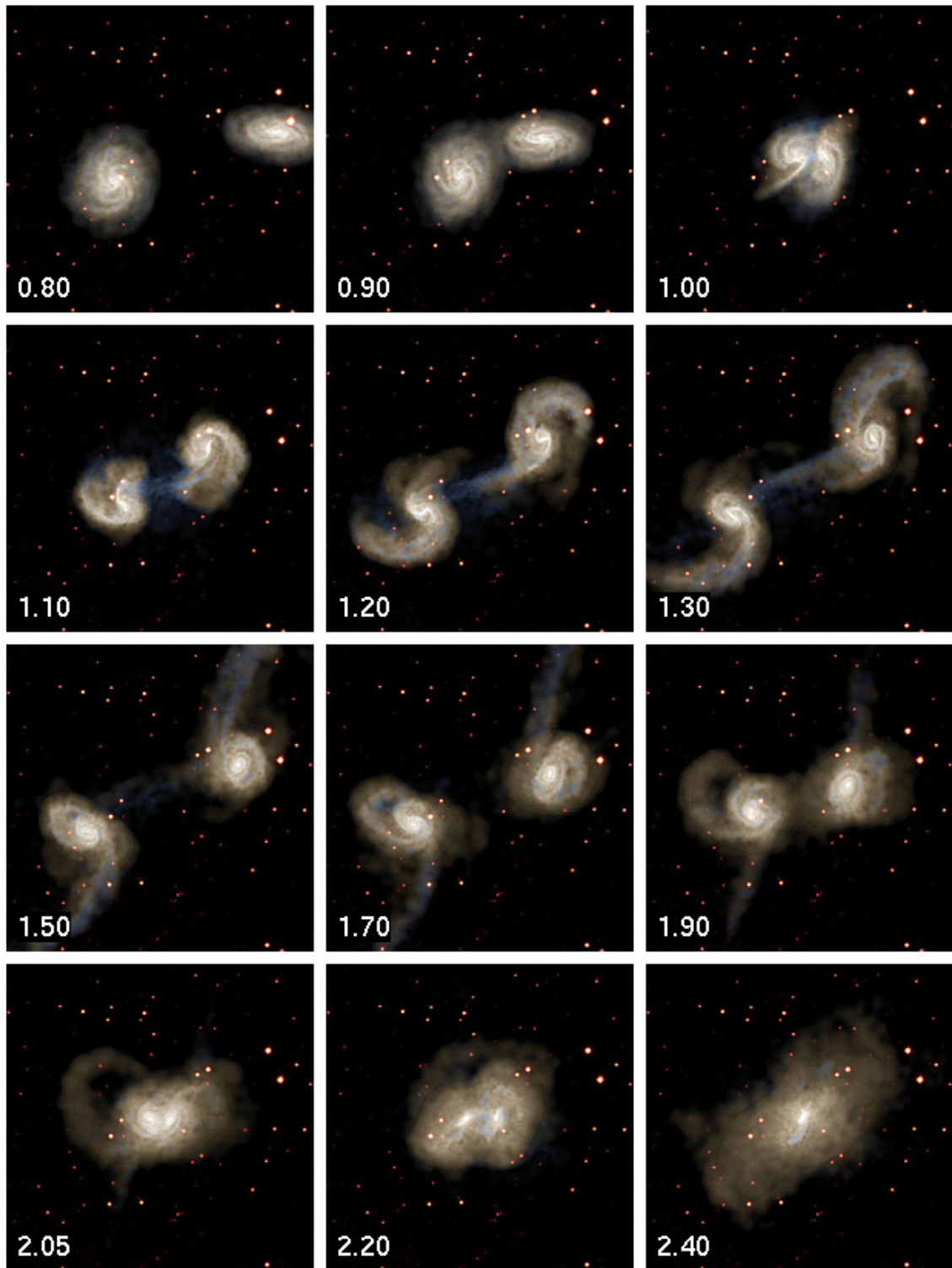
**Figure 2.7:** An example simulation of a merger scenario between two galaxies of similar size. The numbers is the time in Gyr from the start of the simulation. Credit: Max-Planck Institute of Astrophysics, simulated by V.Springel & S.D.M.White at MPA Garching in 1999.

### 2.2.4 Shocks

Astronomical shocks can be induced by a number of powerful phenomena, such as supernovae, density waves at the corotation radius, compression of gas at the bar ends and galaxy interactions, whenever one collection of matter moves into another faster than the local sound speed. Due to the low densities in the Universe, the shocks are often collisionless. Inside galaxy clusters shocks are induced by mergers, turbulent flow motions and infall of warm-hot intergalactic medium along filaments (Ryu et al., 2003; Ha et al., 2018). On galaxy scales, extended shock excitation caused by major gas flow due to merger processes has been observed in several nearby galaxies, commonly in ultra-luminous and luminous infrared galaxies (ULIRGs, LIRGs) (Monreal-Ibero et al., 2010; Rich et al., 2011, 2015). It is common for late-stage mergers to exhibit significant ongoing shock excitation (Rich et al., 2015).

In the collision interface, the medium is heated by the kinetic energy and as it cools, the formation of molecular hydrogen combined with the compression of the ISM/IGM facilitate star formation. The infalling gas can fuel both star formation and AGN activity. And in turn, AGNs drive massive galactic outflows and additional shocks into the ISM and IGM.

In galaxy groups it is common that the galaxies are gas poor, after having lost their gas to the IGM in previous interactions with the other group members (more details of galaxy groups are provided in Chapter 2.5). As new galaxies rush to join the group their relative velocity with regards to the hot IGM gas is faster than the galaxy's own speed of sound, creating a shock at the intersection of the galaxy's gas and the hot IGM.

Common shocks in the Universe include radiation mediated shocks from supernovae explosions, relativistic shocks by AGN jets, accretion shocks at the edge of galaxy clusters and bow shocks caused by stellar winds. Radiation mediated shocks are not collisionless, and have obtained their name from the manner in which the shock dissipates, i.e., the shock dissipation mechanism is radiative. Relativistic shocks are induced in processes involving strong magnetic fields and particles accelerated up to ultra-relativistic energies. They are commonly invoked in gamma-ray bursts, pulsar wind nebulae and AGN jets. Accretion shocks occur at the surface of a compact object and are caused by the compact object accreting matter from its environment at supersonic speed. Bow shocks occur when flowing ambient plasma, such as stellar wind, interacts with the magnetosphere of an object, such as a planet.

## 2.3 Star Formation

Star formation is playing a vital part in the evolution of the Universe and galaxies throughout cosmic time, driving creation of elements heavier than hydrogen and helium, and infusing the IGM through stellar winds and supernovae. The light from stars dominate the emission observed from galaxies, unless there is a luminous Quasi-Stellar Object (QSO) present in which the non-continuum emission from the nucleus overpower the continuum emission from the stellar population.

When self-gravitating molecular gas clouds cool they lose their radiative pressure support, contracting under gravity and forming dense cold gas clouds suitable for star formation. The Jeans criterion estimates the mass and radius of a cloud in which gravity overcomes the radiative pressure:

$$M_J = \left(\frac{5k_bT}{Gm}\right)^{3/2}\left(\frac{3}{4\pi\rho}\right)^{1/2}, \qquad R_J = \sqrt{\frac{15k_bT}{4\pi Gm_pm\rho}}, \tag{2.13}$$

where $T$ is the temperature within the cloud, $k_b$ is the Boltzmann constant, $G$ is the gravitational constant, $m$ is the particle mass, $m_p$ the proton mass and $\rho$ the density of the cloud. The typical temperatures present at cloud collapse, $\sim 10$ K, require effective radiative cooling. Molecular hydrogen cooling is insufficient, a more efficient coolant is carbon monoxide (CO), since CO molecules can reach collisionally excited states and reduce the cloud temperature as they radiate. Stars form via direct collapse of a gas cloud or via fragmentation. It is common that clouds, during collapse, remain radiatively transparent, i.e., sustain a constant temperature, while increasing its density. This transparency leads to a decrease of the Jeans mass and thereby fragmentation and structure formation of various masses simultaneously, i.e., formation of stellar clusters.

The initial mass of a star is used to determine its type, luminosity and life. The initial mass function (IMF) represent the number of stars that form of a given mass:

$$\int_{m_L}^{m_U} m\phi(m)\,dm = 1M_\odot, \tag{2.14}$$

where $\phi(m)\,dm$ is the fraction of stars within a mass interval of $dm$ around mass $m$. The limits $m_L$ and $m_U$, are usually set to $\sim 0.1M_\odot$ and $\sim 100M_\odot$ respectively, based on the fact that stars with a mass of $\lesssim 0.08M_\odot$ cannot ignite hydrogen and stars with a mass of $\gtrsim 100M_\odot$ have not been observed. To estimate $\phi(m)$ the Salpeter-IMF is often used: $\phi(m) \propto m^{-2.35}$. The Salpeter-IMF is derived from observations of stellar mass spectra of young star clusters and a good fit for stars more massive than our sun. The IMF is subjected to uncertainties and there are many questions remaining regarding the IMF, the IMF research field is a very active field.

Individual stars are classified by their spectral type, i.e., their atomic and molecular spectral lines. The lettered classification: O, B, A, F, G, K, M, ranges from the hottest O-type stars to the coldest M-type stars. In addition, each letter is further decomposed by a combination with a number sequence, 0-9, where 0 is the hottest and 9 the coolest for that type. There are further extensions of the classification, such as roman numerals noting different types of giants and dwarfs, as well as main

sequence stars. The stellar classification is commonly displayed in a Hertzsprung-Russel diagram (HRD), where the absolute magnitude of the star is shown as a function of the spectral type. Fig.2.8 displays the HRD of the observations of stellar populations by Gaia. Most of the stars lie within the main sequence (marked in Fig.2.8), and depending on their initial mass they follow different evolutionary tracks through the diagram.
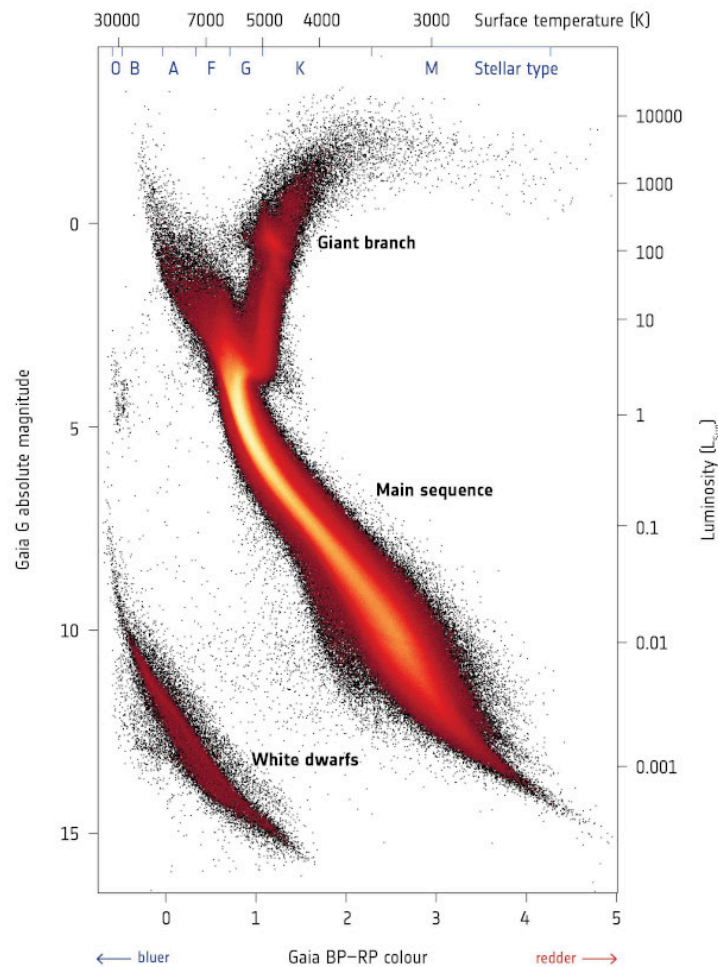


**Figure 2.8:** The Hertzsprung-Russell diagram as observed by Gaia. Credit: ESA/Gaia/DPAC, CC BY-SA 3.0 IGO.

The colour of the stellar population is particularly useful for studying the star formation history in a galaxy, as individual stars cannot be distinguished in distant systems, and the age of a star is related to its colour. It is expected that SFR, star formation per unit time, decreases over time, since the gas content is depleted, and the spectral distribution can be related to the ratio of the SFR of today and the

SFR of the past. SFR per unit area, $\Sigma_{SFR}$, can be related to the surface gas mass density, $\Sigma_{gas}$, according to the Schmidt-Kennicutt law:

$$\frac{\Sigma_{SFR}}{M_\odot \ yr^{-1} \ kpc^{-2}} = (2.5 \pm 0.7) \times 10^{-4} \left(\frac{\Sigma_{gas}}{M_\odot \ pc^{-2}}\right)^{1.4 \pm 0.15}. \qquad (2.15)$$

One would imagine that the atomic gas is less relevant than the molecular gas regarding star formation, and $\Sigma_{SFR}$ is essentially proportional to $\Sigma_{H_2}$, as expected since stars form in molecular clouds. But the connection to atomic gas is not insignificant, molecules form from atoms, and the Schmidt-Kennicutt law can be understood as a combination of $\Sigma_{SFR} \propto \Sigma_{H_2}$ and the increase of the molecular fraction in gas clouds due to increase in gas density. Furthermore, SFR indicators can be observed in several wavelength ranges, the methods are detailed per wavelength regime in chapter 2.6.

As the SFR is the gas mass that is being converted into stars per unit time, it can be written as:

$$SFR = \psi(t) = -\frac{dM_{gas}}{dt}, \qquad (2.16)$$

and the total spectral luminosity of a galaxy is then given as:

$$F_\lambda(t) = \int_0^t \psi(t - t') S_{\lambda, Z(t-t')}(t') \ dt', \qquad (2.17)$$

where $S_{\lambda, Z(t-t')}(t')$ is the spectral energy distribution of the stellar population, i.e., the emitted energy per wavelength of a group of stars of initial metallicity $Z$ and age $t'$. Models of stellar evolution and stellar atmospheres are required to compute $S_{\lambda, Z(t-t')}(t')$. $S_{\lambda, Z(t-t')}(t')$ actually accounts for the different evolutionary tracks in the HRD, such as that of the sun in Fig.2.9.

Young stellar populations are dominated by massive stars with strong ultraviolet (UV) emission. After $10^7 - 10^8$ years a shift is observed, where the UV emission diminishes and the near-infrared (NIR) emission increases as the massive stars evolve into red supergiants. After a few $10^7$ yr, a spectral break at $\sim 4000$ Å often appears. This feature, generally dubbed the "4000 Å-break", is induced by strong transitions of singly ionised calcium and the hydrogen Balmer lines (the Balmer lines are listed in Fig.2.15). This break can be used to estimate redshifts of early-type galaxies. Observations show a SFR peak at $z \sim 2$ which has been attempted to be explained with an increase in gas accretion or an increase in galaxy merger rate, however, neither of these options have been unambiguously proven to be correct. However, galaxy interactions and mergers have shown to cause starbursts.

Only very nearby stars can be individually resolved, and the stars of other galaxies are observed as one spectrum consisting of a superposition of a multitude of stars. Libraries consisting of a collection of observed stellar spectra can then be used to determine stellar population ages and kinematics. There are several such libraries available online, advantageously used together with Python tools such as Penalized Pixel-Fitting (pPXF) (Cappellari & Emsellem, 2004; Cappellari, 2017).
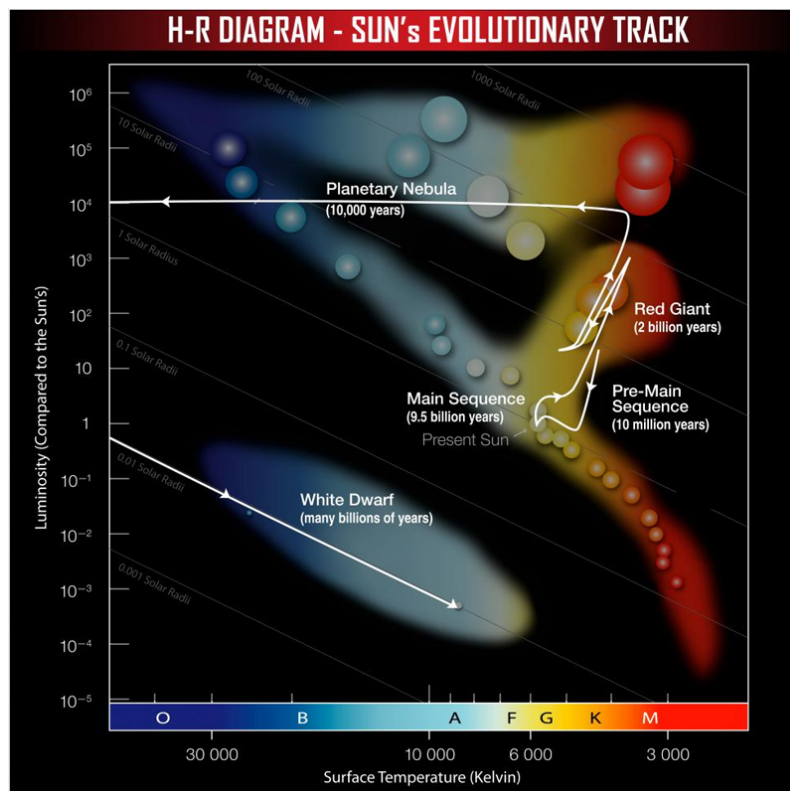
**Figure 2.9:** A Hertzsprung-Russell diagram including the evolutionary track of the sun. Credit: NASA/CXC/SAO.

## 2.4 Black Holes

There are three main groups of black holes; those created at the end state of the evolution of massive stars, stellar-mass black holes ($M_{BH} \sim 5-10s\ M_{\odot}$); those in the centres of globular clusters, intermediate-mass black holes ($M_{BH} \sim 100s - 10^5 M_{\odot}$); and those in the centre of galaxies, super-massive black holes (SMBHs) ($M_{BH} \geq 10^5 M_{\odot}$). Although the existence of SMBHs have been theorised for more than a century, the first direct evidence of a SMBH was obtained in 2019. Using an array of radio telescopes dubbed the Event Horizon Telescope, the shadow of the SMBH, in the elliptical galaxy M87, was captured, as displayed in Fig.2.10 (Event Horizon Telescope Collaboration et al., 2019).

There is a vast selection of research and information available on black holes, their feeding and feedback. This chapter is brief, for further information the reader is referred to other material already published, such as the book by Netzer (2013). This chapter begins with a brief recount of the classification and unification of AGN, after which a discussion of the feeding and feedback processes in black holes is presented.



**Figure 2.10:** The first direct evidence of a black hole, showing the shadow of the black hole in the elliptical galaxy M87. Credit: The Event Horizon Collaboration.

### 2.4.1 AGN Classification & Unification

Active SMBHs, i.e., AGNs, cause some of the most spectacular and energetic physical events in the Universe. For the centre of a galaxy to be classified as an AGN, one or more of the following requirements must be fulfilled:

- It contains a compact nuclear region, that displays significant emission beyond what can be expected in this type of galaxy through common stellar processes.

- The center displays a distinct signature of non-stellar continuum emission, including non-thermal radio and/or X-ray emission.
- Its spectrum exhibits strong emission lines, whose line ratios indicate excitation typical of a non-stellar radiation field.
- It shows variations in line and/or continuum emission.

The detailed study of AGN started when Schmidt (1963) discovered QSOs. While Seyfert galaxies, with their high central surface brightness and broad nuclear emission lines, were discovered earlier (Seyfert, 1943), it was not until Khachikian & Weedman (1974) that they were suspected of being AGN. QSOs are highly luminous objects, whereas Seyfert galaxies show low luminosity and often also low redshift. Another high luminosity subclass of AGN are blazars, which exhibit relativistic jets directed towards Earth, showing rapid variability and compact features. Low-ionisation nuclear emission-line regions (LINERs), are low-luminosity objects with strong [NII], [SII] and Balmer line emission, and are mostly found in disk galaxies.

AGNs have been classified and identified using their emission line spectra. In broadest terms AGNs are split into Seyfert Type 1 (two velocity dispersion components: 100-1000 km/s and 1000-20000 km/s) and Seyfert Type 2 (velocity dispersion of 300-1000), stating the presence and absence of broad optical emission lines respectively[2]. The Seyfert classification may also be extended further, into decimal points, based on the relative intensity of the broad and narrow component of the Balmer lines, and thereby, enabling distinguishing between, for example, type 1.5 and 1.8. The type 2 Seyferts can be further divided into radio-loud and radio-quiet using the 5 GHz radio emission relative to the optical B-band monochromatic luminosity.

Unified AGN models unite two or more types of AGN by stating that the different observed aspects are different viewing angles of the same object (for e.g., Antonucci (1993)). A sketch of a simple version of the geometric unification model is illustrated in Fig.2.11. The SMBH in the centre is fed via the optically thick, geometrically thin accretion disk surrounding it, and as the accretion disk loses angular momentum it radiates in UV to optical wavelengths. The hot corona, surrounding the accretion disk, Compton upscatters the photons into emitting in the X-ray wavelength regime. Typically $0.1 - 1$ pc from the nucleus, high-density ($\sim 10^{10} cm^{-3}$) gas clouds are moving in roughly Keplerian orbits (typically $1000 - 3000$ km/s) - this is the origin of the broad-line region (BLR). Conversely, the narrow-line region (NLR) consist of low-density clouds ($\sim 10^{4} cm^{-3}$) at lower velocities (typically $300 - 1000$ km/s), and can reach distances from the SMBH of hundreds and even thousands of parsecs, as is the case for extended-NLR galaxies when the low-density clouds extends far as an ionisation cone. The NLR is the origin of the intense narrow forbidden lines emitted by AGN. The dusty torus surrounding the central region, is a dusty toroidal structure and its dust grains radiate in infrared. The torus typically extends $0.1 - 10$ pc and is one of the most important structures for describing the differences between the different types of AGN. The presence of the torus has been confirmed in several nearby Seyfert galaxies using the Atacama Large Millimeter/submillimeter

---

[2]Seyfert Type 1/2 are also often called Seyfert 1/2 or simply Type 1/2. Historically "Seyfert (Type)" refer to the optical AGN, while "Type" refer to AGN across the electromagnetic spectrum. In this thesis these three notations are used interchangeably meaning the AGN classification across the electromagnetic spectrum.

Array (ALMA) and the Very Large Telescope Interferometer (VLTI) (Hönig (2016); Combes et al. (2019) amongst others). When the viewing angle is such that the central region is obscured by a torus, the AGN can be identified via X-ray or radio observations.
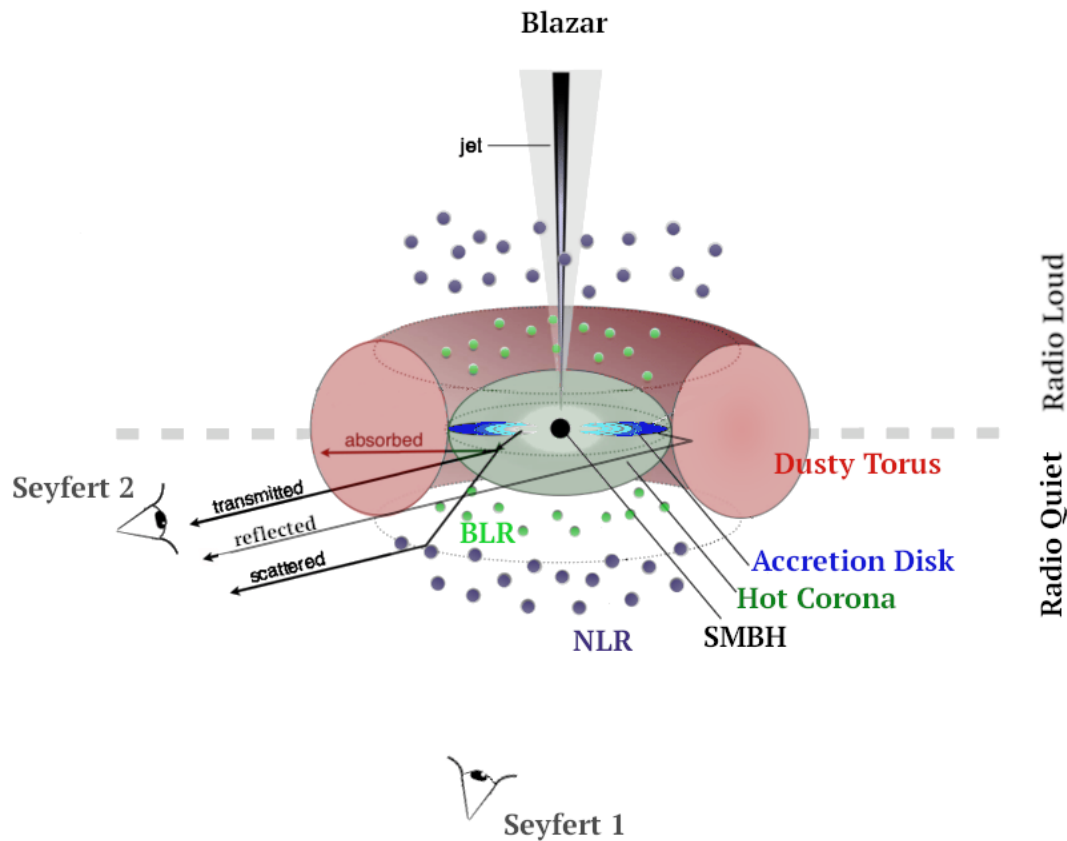


**Figure 2.11:** A sketch of the geometric unification model of AGN. The SMBH at the center is surrounded by an accretion disk and high density clouds (BLR origin). The dusty torus obscures the AGN, whereas low density clouds further from the SMBH constitutes the NLR. The type/classification of the AGN is then simply a result of the different viewing angles. Image design inspired by Beckmann & Shrader (2012).

Unfortunately, the geometric unification model of AGN cannot explain the observations in the extreme cases, such as for line-less AGNs, the really low-luminous LINERs, the high-luminosity high-redshift AGNs, the "True Seyfert 2"s and the changing-look AGNs (those who are observed to change their Seyfert type over time, for example Fazeli et al. (2019)). In addition, Dultzin-Hacyan et al. (1999); Koulouridis et al. (2006); Jiang et al. (2016) found more type 2 galaxies than type 1 galaxies in close galaxy pairs. Suggesting that galaxy interactions might be the cause of transforming a galaxy from star forming into type 2, and thereafter, it may evolve into a type 1. Another option is that galaxy interactions drive more dust towards the nucleus, enabling the obscuration seen in type 2 Seyferts. But it is possible that the geometric unification model simply breaks down in the intense gravitational interactions that occur in galaxy collisions/mergers.

## 2.4.2 Feeding & Feedback

The black hole in the centre of our galaxy, Sgr A$^*$ is quiescent, i.e., does not have a permanent accretion disk. While Sgr A$^*$ mainly emits in the sub-millimetre wavelengths, there are flaring events of NIR and X-ray radiation, suggesting that occasional feeding of the SMBH is occurring.

Most AGNs are found in gas-rich galaxies, indicating that ISM is the fuel. Inwards transfer of gas and accretion onto a central SMBH, requires loss of angular momentum of the infalling gas. The maximum energy that can be released by a black hole accretion disk is limited by the Eddington luminosity, $L_{Edd}$, which also sets the limit of the maximum gas mass accretion rate, called the Eddington accretion rate, $\dot{m}_{Edd}$. The Eddington luminosity and the Eddington accretion rate are:

$$L_{Edd} = \frac{4\pi cGN\mu m_p}{\sigma_T} \approx 1.26 \times 10^{38} \frac{M_{BH}}{M_\odot} \ erg \ s^{-1}, \tag{2.18}$$

$$\dot{m} = \frac{L}{ec^2} \approx 0.18\frac{1}{e}\left(\frac{L}{10^{46}erg/s}\right) M_\odot \ yr^{-1}, \tag{2.19}$$

$$\dot{m}_{Edd} \equiv \frac{L_{Edd}}{L}\dot{m} \approx \frac{1}{e}2 \times 10^{-9} \ M_{BH} \ yr^{-1}, \tag{2.20}$$

where $\mu$ is the mean molecular weight and $\sigma_T$ is the Thomson cross section. $e$ denotes the efficiency of the conversion of infalling mass into energy, and is usually of the order of $\sim 0.1$. $M_{BH}$ is the SMBH mass, which can be estimated using observational data in a number of ways, such as via the $M_{BH} - \sigma_*$-relation or reverberation mapping.

Galaxy interactions and mergers increase the probability for triggering AGN activity, but the extent to which mergers are the cause of the AGN population, is still unclear. Some authors find that mergers play a minor role in triggering luminous AGN (Villforth et al., 2017; Hewlett et al., 2017; Steinborn et al., 2018), while others find that the dominant triggering mechanism of AGN are, in fact, mergers (Urrutia et al., 2008; Glikman et al., 2015; Fan et al., 2016). In addition, some studies reveal a tendency for barred galaxies to host AGN (Knapen et al., 2000; Laurikainen et al., 2004), while others disagree (Ho et al., 1997; Mulchaey & Regan, 1997).

The process of AGN feedback, i.e., energy transfer from the AGN to the gas, is key in solving the "overcooling" problem. The "overcooling" problem is the contradiction observed in the lack of massive luminous galaxies, that are expected considering the high rate of gas cooling within them. The quenching of star formation via AGN feedback may be the explanation and may also be the bridge/transition between the "blue cloud" of star-forming galaxies and "red and dead" massive elliptical galaxies. AGNs have not only been observed to quench star formation, although it is more common, but the outflows of AGNs have been observed to trigger star formation as well (Silk & Norman, 2009).

AGN feedback can be split into two main modes: radiative mode and kinetic mode. While there are galaxies where both modes are present, generally one mode dominates. Radiative mode occurs in AGN where the accretion is close to the Eddington limit, i.e., radiatively efficient, where photons couple to the gas and transfer the momentum. Radiative feedback usually occurs in QSOs and is therefore more common

at redshifts of z∼ 1 − 2, where QSO activity peak. The result of the radiative mode is radiation pressure, powerful winds at speeds of more than 500 km/s, and outflows. Thereby, the radiative mode quenches further accretion onto the SMBH, by blowing away the gas. Kinetic feedback, on the other hand, is powered by mechanical jets. Jets occur in AGN with lower accretion rate and thereby lower luminosity. A jet heats up the circumgalactic and halo gas while emptying its surroundings of gas, and thereby quench star formation. For the reader's satisfaction, Fig.2.12 shows 6 examples of galaxies with jets, the extension of the radio jets are illustrated using contours from the radio FIRST survey overlaid on an SDSS image. However, the exact method of jet release and its origin is yet to be revealed.
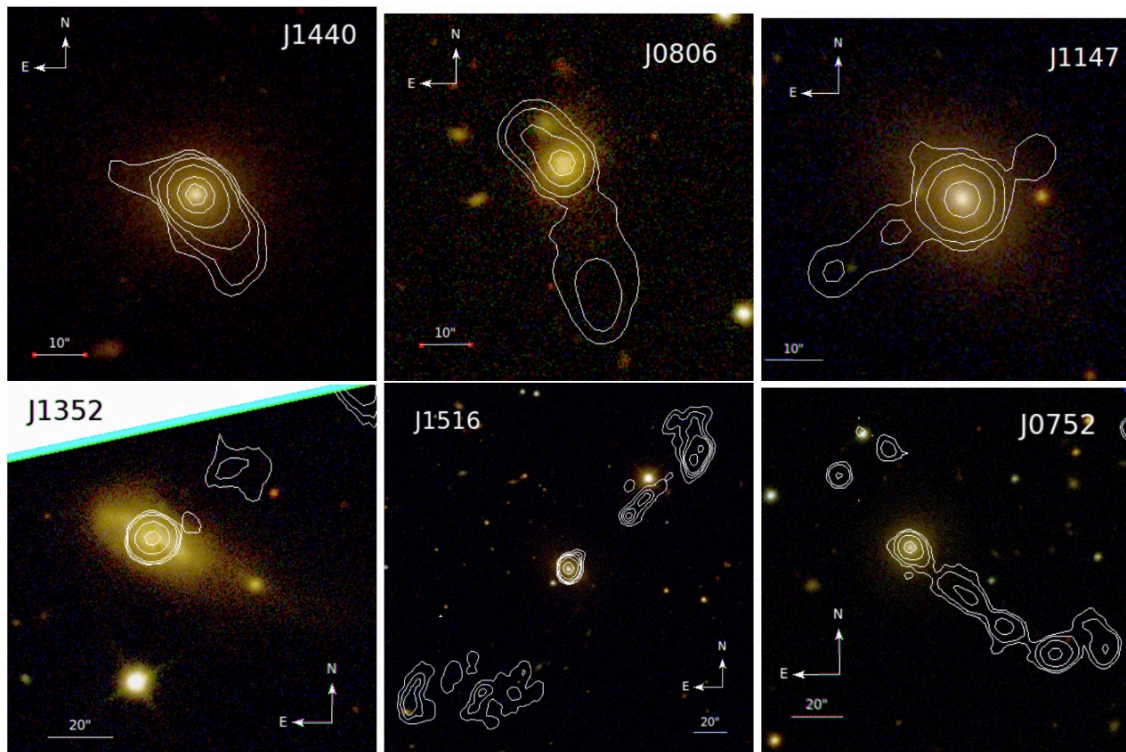


**Figure 2.12:** Examples of the shape of jets in active galaxies. Optical SDSS images have been overlaid with radio FIRST contours with arbitrary scales to facilitate the depiction of the radio structures.

## 2.5   Galaxy Groups[3]

Galaxy groups, associated with intermediate-mass dark matter halos (Natale et al., 2010), are systems bound together by their dark matter and mutual gravitational attraction. Galaxy groups typically contain less than 50 galaxies, and due to the shallow gravitational potential, complex baryon physics have a significant impact, by, for example, cooling and AGN feedback. Furthermore, galaxy groups are the densest environments in the Universe, within which $50 - 70\%$ of the galaxies reside.

At early epochs gas fueling of galaxies is thought to proceed via cold gas accretion in low-mass dark matter halos, but in the high-mass DMHs hosting galaxy groups, the higher virial temperatures of the intergalactic medium inhibits this process (Dekel & Birnboim, 2006; Natale et al., 2010). Because of the high densities, the interactions between galaxies and between galaxy and IGM should effectively remove interstellar gas from the group, which leads to quenching of star formation in the group's galaxies. However, simultaneously, these same interactions cause chemical enrichment of the IGM when it is mixed with the stripped galaxy ISM, which may cool the IGM and thereby facilitate accretion onto existing galaxies and new star-forming systems. The interplay of these processes, and their overall effect on galaxy evolution and star formation activity is still under investigation.

In this chapter a summary of the different types of galaxy groups and their connections is presented. Following is a section discussing some of the important properties of galaxy groups as well as the peculiarities of compact group galaxies.

### 2.5.1   Types of Groups

Galaxy groups are classified as: loose, compact, poor or fossil. Loose groups are the most common type of groups, consisting of around 50 galaxies, they are commonly classified as an intermediate state between compact groups and rich clusters. Einasto et al. (2003) find that a nearby large cluster can enhance the evolution of a neighbouring loose group, complicating the attempts to find common values for all loose groups. Furthermore, Mamon (1986); Diaferio et al. (1994) suggested that loose groups are the birth places of compact groups, that compact groups may be transient unbound cores of loose groups.

Compact groups are close congregations of a small number of galaxies. The Hickson Compact Groups (HCGs) is a well-known catalogue of 100 compact groups, with groups are located at a median redshift of approximately 0.03. The HCGs typically have $4 - 5$ galaxies per group, with galaxy separations close to the size of the galaxies themselves. The HCGs have been found to be dynamically dominated by dark matter, to contain large amounts of diffuse gas, and, while they trace the large-scale structure, they tend to prefer low-density environments. Compared to a random distribution of galaxies, a compact group tend to consist of a similar type of galaxies. However, the environment of the compact group may affect its properties (Díaz-Giménez & Zandivarez, 2015). In addition, the intense galaxy interactions

---

[3]There is extensive research and publications available on galaxy groups. Apart from the aforementioned books, this chapter relies on the information provided in Hickson (1997) and the references therein, unless otherwise stated.

in compact groups are expected to be particularly inducive to mergers, indicating that the lifetimes of compact groups should be quite short and that they may be sustained via dynamical evolution with loose groups. The end state of compact groups is a point of discussion, it has been suggested that they evolve into ULIRGs and then elliptical galaxies, or that they form fossil groups (Wiens et al., 2019). To illustrate how compact galaxy groups look, see Fig.2.13 which shows two HCGs: HCG79, commonly called the Seyfert's Sextett, and HCG40.

**(a)** **(b)**
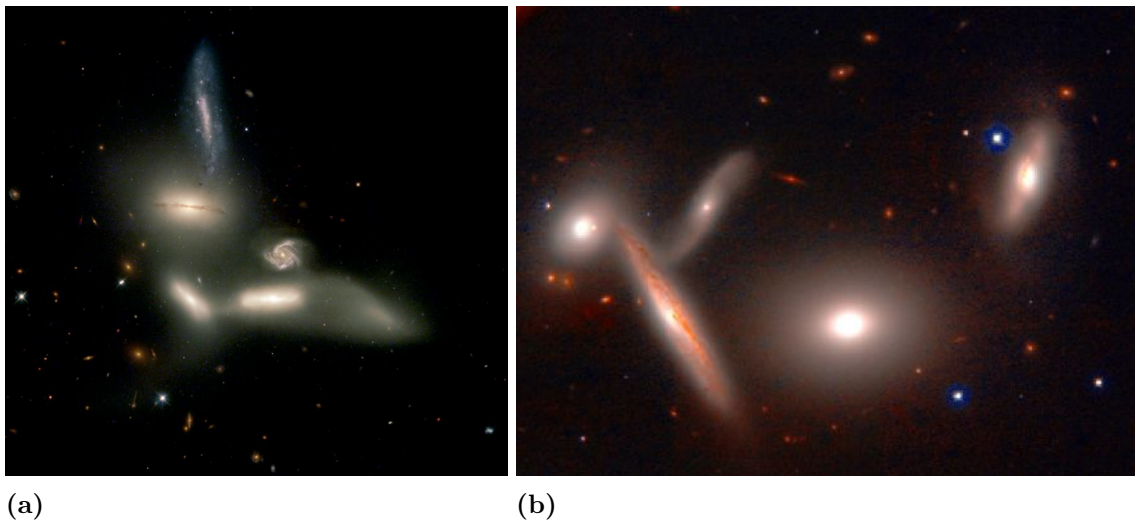
**Figure 2.13:** Images of two Hickson Compact Groups.
(a) HCG79, Seyfert's Sextet. Credit: NASA, J. English (U. Manitoba), S. Hunsberger, S. Zonak, J. Charlton, S. Gallagher (PSU), and L. Frattare (STScI);
(b) HCG40. Credit: CISCO, Subaru 8.3-m Telescope, NAOJ.

Poor groups contain less than 5 bright galaxies. Most galaxies in the local Universe, belong to poor groups, including our local group. High-redshift surveys bring poor groups closer to the definition of loose groups but observing the types of galaxies in the poor groups show large fractions of early-type galaxies, in disagreement with the loose groups. The high galaxy density and low velocity dispersions may provide favourable conditions for galaxy mergers, which might explain the relatively large number of ellipticals.

Lastly, fossil groups. Fossil groups are spatially extended X-ray sources (Jones et al., 2003), luminous due to diffuse hot gas, resembling a large elliptical galaxy. The system is often dominated by a E or cD galaxy and there are several suggestions for explanations to the origin of fossil groups: (i) fossil groups may be old systems that have avoided falling into galaxy clusters, while continuing to merge with other galaxies, (ii) they may have formed as a result of galaxy merging within a compact group or (iii) they were originally poor groups which evolved, with the help of compact groups, into their current state. So far, fewer fossil groups than expected have been detected.

## 2.5.2  Properties & Peculiarities of Compact Groups

43% of all HCG galaxies show interaction/merger signatures (Mendes de Oliveira & Hickson, 1994), which indicates that the compact groups are not chance alignments of galaxies at different redshifts or filaments seen edge on. A high fraction of the HCGs also show diffuse X-ray emission, indicating that the systems are physically dense, not transient structures and, again, that groups are not simply chance alignments. Furthermore, the X-ray observations show that, in most compact groups, gas and dark matter are more extended than the optical galaxies and decoupled from the galaxies. Contrary to loose groups, where the dark matter is concentrated around the individual galaxies. Another difference between compact and loose groups is the amount of neutral hydrogen. Compact groups are typically deficient in neutral hydrogen by a factor of 2 compared to loose groups, indicating that the interactions in compact groups have removed much of the gas from the galaxies.

Assuming that groups are bound dynamical systems puts requirements on the evolution of them. An ongoing process of forming or replacing compact groups must be present, and the relics of merged groups have to make up a significant population. Unambiguous explanations to these aspects are still being researched. Plauchu-Frayn et al. (2012) states that compact groups probably formed during the last $\sim 3$ Gyr from the primordial small-mass density fluctuations, and that the HCGs are in a non-equilibrium state, currently merging under dissipationless conditions, i.e., without gas. Dissipationless merging could also explain the long lifetimes of compact groups.

While the individual galaxies in compact groups first appear normal, detailed studies often show peculiar spectra and/or morphology. Several differences between compact group galaxies and isolated galaxies have been found, such as:

- There is a significantly smaller fraction of late-type, spiral, galaxies in compact groups than in other environments.
- The types of galaxies in the same group are often similar.
- The velocity dispersion of ellipticals in compact groups are lower than that of isolated ellipticals.
- The radio emission from the nuclei of group spirals is enhanced compared to that from isolated spirals.
- Galaxies in compact groups typically have mass-to-light ratios of $30 - 50\%$ lower than that of isolated galaxies.

In addition there seem to be further correlations between different aspects of compact groups, such as: (i) only the highest-mass galaxy is inclined to develop a radio source, (ii) a higher radio-to-optical luminosity is found in galaxies with an excess of nearby neighbours, the nearer the higher and (iii) a higher velocity dispersion is related to a lack of late-type galaxies in the group.

There is a multitude of additional interesting questions that arise from the study of compact galaxy groups, such as:

- What are the end products of the evolution of these groups?
- Does the end products have properties consistent with any known population of objects?
- Where do compact groups fit into the overall clustering hierarchy?
- What is the connection of compact groups to morphological segregation?

- What is the connection between compact group environment and AGN triggering/activity?
- What is the role of compact groups in the evolution of galaxies throughout cosmic time?

Mergers are expected to be particularly common in compact galaxy groups and the physical processes occurring in the group environment play a fundamental role in determining the star formation history of the Universe (Natale et al., 2010). Compact galaxy groups show an excess of extreme galaxy interactions, such interactions that are suspected to be a vital factor in driving galaxy evolution at high redshift (Rodríguez-Baras et al., 2014), and may be particularly efficient at triggering AGN activity (De Rosa et al., 2017). Compact galaxy groups are truly perfect laboratories for studying the dynamics of galaxies and the IGM, the triggering of star formation, feedback mechanisms and AGN fueling, i.e., in more direct and brief terms: galaxy evolution.

## 2.6 Observations to Trace Physical Properties

The atmosphere imposes restrictions on observations with ground-based telescopes, via turbulence and opacity. Astronomical seeing, i.e., turbulence in the atmosphere causing variations of the optical refractive index, can be avoided using space-based telescopes or compensated for by using a method called adaptive optics (AO), where the mirror shape is adjusted in real-time based on the atmospheric reflective index. Other important limitations of ground-based telescopes are the atmospheric transmission, telluric absorption and emission lines, and the infrared emission from the Earth. That the atmosphere absorbs certain wavelengths and emits in others, must be accounted for when planning observations. But more importantly, the atmosphere is only transparent in certain wavelength windows, shown in Fig.2.14.
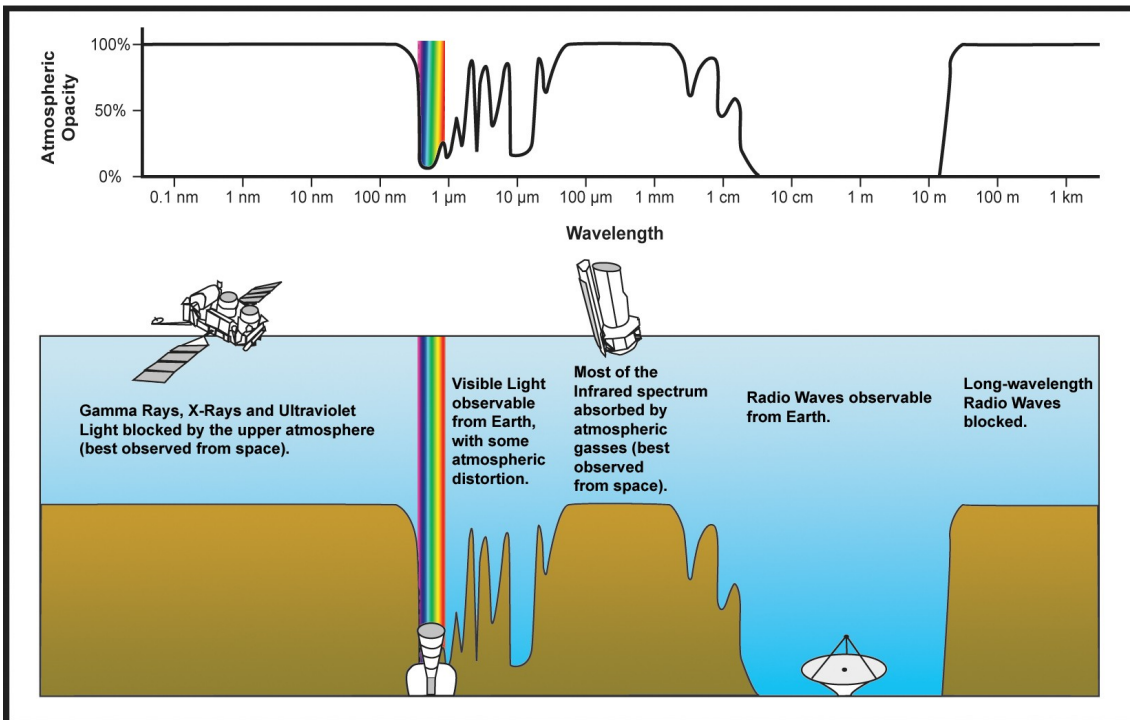


**Figure 2.14:** Atmospheric opacity as a function of wavelength. Credit: NASA.

Furthermore, we ought to take note of the different conventions optical and radio astronomers use to calculate line-of-sight velocities and sky frequencies. The radio convention is

$$v_{radio} = c\frac{\lambda - \lambda_0}{\lambda} \neq cz \qquad f_{sky} = f_0\left(1 - \frac{v_{radio}}{c}\right), \qquad (2.21)$$

whereas the optical convention is

$$v_{opt} = c\frac{\lambda - \lambda_0}{\lambda_0} = cz \qquad f_{sky} = f_0\frac{1}{1 + v_{opt}/c}, \qquad (2.22)$$

where $\lambda_0$ is the wavelength at the origin, and $\lambda$ is the observed wavelength. This thesis adheres to the optical convention.

Stars are birthplaces for heavier chemical elements, such as iron and oxygen. At the end of a star's lifetime, these elements may be ejected into the surrounding area, chemically enriching the ISM. Gas is a prerequisite for star formation, as stars form in molecular gas clouds, while molecular gas generally form from atomic gas. Molecular gas is the main ingredient in star formation and growth of super-massive black holes, and it is directly connected to feedback mechanisms of star formation and AGN. Stars can be observed directly in ultraviolet (UV), optical and near-infrared (NIR) continuum, and as stellar light is absorbed by dust it can be re-emitted in mid/far-IR wavelengths. Dust also plays an important role in heating and cooling the ISM, and aid in facilitating molecule formation and thereby star formation. Massive stars, supernovae and X-ray binaries can all emit X-ray radiation, while the synchrotron radiation created by supernovae also emit in radio. Star formation rate indicators exist in several wavelength regimes, and are sensitive to slightly different ranges of stellar population ages.

In this chapter I will briefly go through the most important detectable physical properties in each wavelength regime, while putting the focus on the optical and radio regimes and the methods used for the work carried out in this thesis. Note that, depending on the redshift of the observed objects, the emission/absorption lines may shift so far as to change wavelength regime. In general terms, the wavelength regimes here are split as follows:

- Radio: $\lambda \approx 1$ mm $-100$ km
- Infrared: $\lambda \approx 750$ nm $-1$ mm
    - Far-IR: $\lambda \approx 40\mu$m $-1$mm
    - Mid-IR: $\lambda \approx 5\mu$m $-40\mu$m
    - Near-IR: $\lambda \approx 900 - 5000$ nm
- Optical: $\lambda \approx 320 - 900$ nm
- Ultraviolet: $\lambda \approx 10 - 320$ nm
- X-ray: $\lambda \approx 0.1 - 10$ nm

## 2.6.1 Radio

Radio continuum emission traces non-thermal processes, such as AGNs and shocks, while line emission in the radio wavelength regime include important elements such as the molecular gas tracer CO at 1-3 mm and the neutral HI gas at 21 cm. The hyper-fine transition of neutral hydrogen at 21 cm is a great tracer for the cold neutral atomic gas content of galaxies.

Cold molecular gas, the most important ingredient in star formation, is best traced by carbon monoxide (CO) emission lines. CO is the second most common interstellar molecule (with $H_2$ being the first), and using the observed CO gas mass, the $H_2$ gas mass can be estimated as:

$$M(H_2) = 4.8 \ L_{CO} \ M_\odot \ K^{-1} \ km^{-1} \ s \ pc^{-2} \qquad (2.23)$$

CO is easier then $H_2$ to observe, due to its permanent dipole moment and its strong emission in radio frequencies. However, there are some aspects that must be taken into account when estimating gas mass from CO. Uncertainties in CO measurements increase in low metallicity clouds and at low total column densities CO can become

thermalised and optically thick, leading to an underestimation of the mass of the cloud. Weaker isotopes of CO, such as $^{13}$CO, penetrate deeper into the cloud and provide the extinction of the cloud, which solves this issue. A conversion factor, $\alpha \equiv M_{gas}/L'_{CO}$ can then be obtained, which for example for the Milky Way is $\alpha = 4.6 M_{\odot}$. Then the molecular gas mass can be properly estimated from $M_{gas} = \alpha L'_{CO}$ using:

$$L'_{CO} = 3.25 \times 10^7 \left( \frac{S_{CO}\Delta v}{Jy \ km \ s^{-1}} \right) \left( \frac{\nu_{obs}^{-2}}{GHz} \right) \left( \frac{D}{Mpc} \right)^2 (1+z)^{-3}, \qquad (2.24)$$

where $S_{CO}\Delta v$ is the integrated flux of the CO emission line, $D$ is the luminosity distance, and $\nu_{obs}$ is the observed frequency (Solomon & Vanden Bout, 2005).

In addition, radio emission is a particularly useful tracer of AGN jets. But it is in quiescent galaxies, where synchrotron radio emission originates from relativistic electrons accelerated in supernovae remnants, that an estimate of the SFR can be obtained in the radio regime:

$$\frac{SFR_{1.4GHz}}{M_{\odot}yr^{-1}} \sim \frac{L_{1.4GHz}}{8.4 \times 10^{27} erg \ s^{-1} \ Hz^{-1}} \qquad (2.25)$$

## 2.6.2 Infrared

The infrared wavelength regime is particularly useful for tracing star formation activity. The mid-infrared (MIR) wavelengths trace warm dust close to star-forming regions, but can be produced by both thermal (star formation) and non-thermal (AGN) photons (Sulentic et al., 2001).

Hydrogen recombination lines are the most widely used lines in SFR estimations, as they trace HII regions around massive stars. Hydrogen recombination lines are emitted by hydrogen atoms as they cascade towards the ground state via radiative transitions, after having captured free electrons into their excited states. The Paschen and Bracket recombination series can be observed in the NIR, their wavelengths are listed in Fig.2.15. Dust attenuation decreases with wavelength, which improves the SFR estimations in the IR, therefore, the Paschen-$\alpha$ line is particularly useful. Furthermore, fine-structure cooling lines, such as [NeII] and [CII] can be correlated to the hydrogen recombination lines, and therefore also used for SFR estimations, although with increased scatter.

In the case of obscured stellar regions, the UV and optical stellar emission gets absorbed and re-emitted as thermal emission by dust in the IR wavelength regime. This emission can then be used to study obscured star-forming regions. Telescopes that pursue this method of observing stars are, for example, the Wide-Field Infrared Survey Explorer (WISE), and the Spitzer and Herschel Space Telescopes. The thermal emission of young stellar populations peak at $\sim 60\mu$m. While the old or low-mass stellar populations can cause dust emission in $100 - 150\mu$m. However, since dust absorbs only a small portion of the stellar emission, estimating the SFR using dust emission causes an underestimation of the SFR, and the contribution of the old stellar population is subjected to uncertainties.

Dust in itself can reveal information regarding the conditions of the ISM and Polycyclic aromatic hydrocarbon (PAH) is observed in dust. PAHs are organic

molecules in honeycomb structures which dominate the emission in wavelengths of $5 - 20\mu$m.

Warm molecular gas consist mainly of $H_2$. $H_2$ is small and has no permanent dipole moment, it requires temperatures over 1000 K for the rotational and vibrational transitions of this molecule to be visible in the NIR. As these transitions originate on the surface of molecular clouds, they are expected to trace approximately 30% of the molecular gas mass. Furthermore, there are several empirical relations available connecting warm and cold molecular gas masses.
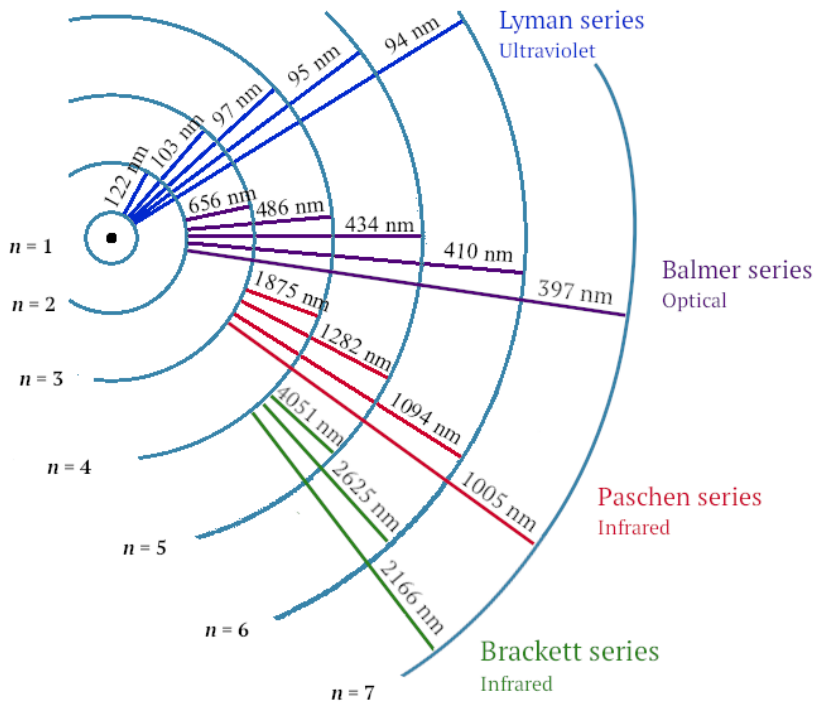


**Figure 2.15:** A selection of hydrogen recombination lines from the Lyman, Balmer, Paschen and Brackett series.

### 2.6.3  Optical

As stated in the previous section, hydrogen recombination lines are the most widely used lines for SFR estimates, and the Balmer series, listed in Fig.2.15, are often present in the optical spectra of galaxies. As the H$\alpha$ emission originates in the HII regions around young hot stars with $M \gtrsim 10M_\odot$, the SFR can be empirically estimated as:

$$\frac{SFR_{H\alpha}}{M_\odot yr^{-1}} = \frac{L_{H\alpha}}{1.3 \times 10^{41} \ erg \ s^{-1}} \tag{2.26}$$

Furthermore, the forbidden [NII] $\lambda6583$ line, usually present in the optical spectrum, is more sensitive to shocks and non-thermal processes. Other forbidden metal lines, such as [OII], can also be used to estimate SFR, but with large uncertainties due

to a complex dependence on the conditions of the ISM. Also note that the optical emission lines are subjected to extinction by dust and atmosphere.

Emission lines in optical galaxy spectrum are caused by AGN activity, as well as active star formation. In the case of active star formation the emission originates from the ionised HII regions around newly-formed hot stars, while AGN presence can be directly confirmed if broad emission lines are observed, or the nuclear activity confirmed in another wavelength regime, such as strong non-thermal radio emission. However, distinguishing between the source of the emission is often non-trivial. To deduce the mechanism behind the gas excitation, the emission line ratios introduced by Baldwin et al. (1981) and expanded upon by Veilleux & Osterbrock (1987), called the BPT diagrams, are extremely useful. The optical emission lines required for the BPT diagrams are: [OIII]$\lambda$5008.2Å, H$\beta$, [NII]$\lambda$6585.3Å, H$\alpha$, [OI]$\lambda$6302.0Å, [SII]$\lambda$6718.3Å and [SII]$\lambda$6732.7Å. The separation of AGN from star-forming galaxies are then provided by the following equations (star-forming below and AGN above):

$$\log\left(\frac{[\text{OIII}]}{H\beta}\right) = \frac{0.72}{\log([\text{SII}]/H\alpha) - 0.32} + 1.30, \tag{2.27}$$

$$\log\left(\frac{[\text{OIII}]}{H\beta}\right) = \frac{0.73}{\log([\text{OI}]/H\alpha) + 0.59} + 1.33, \tag{2.28}$$

$$\log\left(\frac{[\text{OIII}]}{H\beta}\right) = \frac{0.61}{\log([\text{NII}]/H\alpha) - 0.47} + 1.19, \tag{2.29}$$

$$\log\left(\frac{[\text{OIII}]}{H\beta}\right) = \frac{0.61}{\log([\text{NII}]/H\alpha) - 0.05} + 1.30. \tag{2.30}$$

Eq.2.30, proposed by Kauffmann et al. (2003), is based on observational data and called the pure star-forming line. Eq.2.29 is the maximum starburst line and is based on theoretical modelling by Kewley et al. (2001). An object that falls in between these two lines, is considered composite or transitional. Furthermore, two lines have been added to the BPT diagrams to separate the AGNs into Seyferts and LINERs (Seyfert above, LINER below):

$$\log\left(\frac{[\text{OIII}]}{H\beta}\right) = 1.89\log\left(\frac{[\text{SII}]}{H\alpha}\right) + 0.76, \tag{2.31}$$

$$\log\left(\frac{[\text{OIII}]}{H\beta}\right) = 1.18\log\left(\frac{[\text{OI}]}{H\alpha}\right) + 1.30. \tag{2.32}$$

### 2.6.4 Ultraviolet

The UV spectrum is dominated by young stellar populations, such as O and B stars formed over the last $10 - 300$ Myr. This implies that the SFR scales linearly with UV luminosity, and the UV flux over a certain wavelength interval can be converted to SFR via the use of stellar synthesis models. UV observations of nearby galaxies require space-based telescopes, such as the Galaxy Evolution Explorer (GALEX) or the Hubble Space Telescope (HST). However, UV emission is very sensitive to interstellar dust obscuration, so the dust attenuation must be corrected for before a reliable measure of the SFR can be obtained. Typically the escape fraction of UV photons from a Lyman-break galaxy is $\sim 0.2$, which means that to obtain the SFR the observed UV flux have to be corrected with a factor of $\sim 5$.

### 2.6.5 X-ray

The X-ray emission of quiescent galaxies originates in high-mass X-ray binaries, members of young stellar populations, and bremsstrahlung from hot ISM. These origins are expected to scale with the SFR, indicating that the X-ray luminosity can be used as a good indicator for SFR when the AGN contribution can be excluded. In the presence of an AGN, Compton upscattering of photons in the hot corona contributes to the X-ray emission.

In compact galaxy groups hot virialised gas in the intragalactic medium emits in X-ray. Thereby X-ray emission in compact groups provides information about the hot IGM as well as being an independent measure of high-energy processes. Detailed X-ray studies of compact groups can provide important insights into IGM chemical enrichment and whether galaxy interactions or galactic winds are the primary source of entropy increase and enrichment of the IGM.

# 3

# The Story of Stephan's Quintet & this Thesis
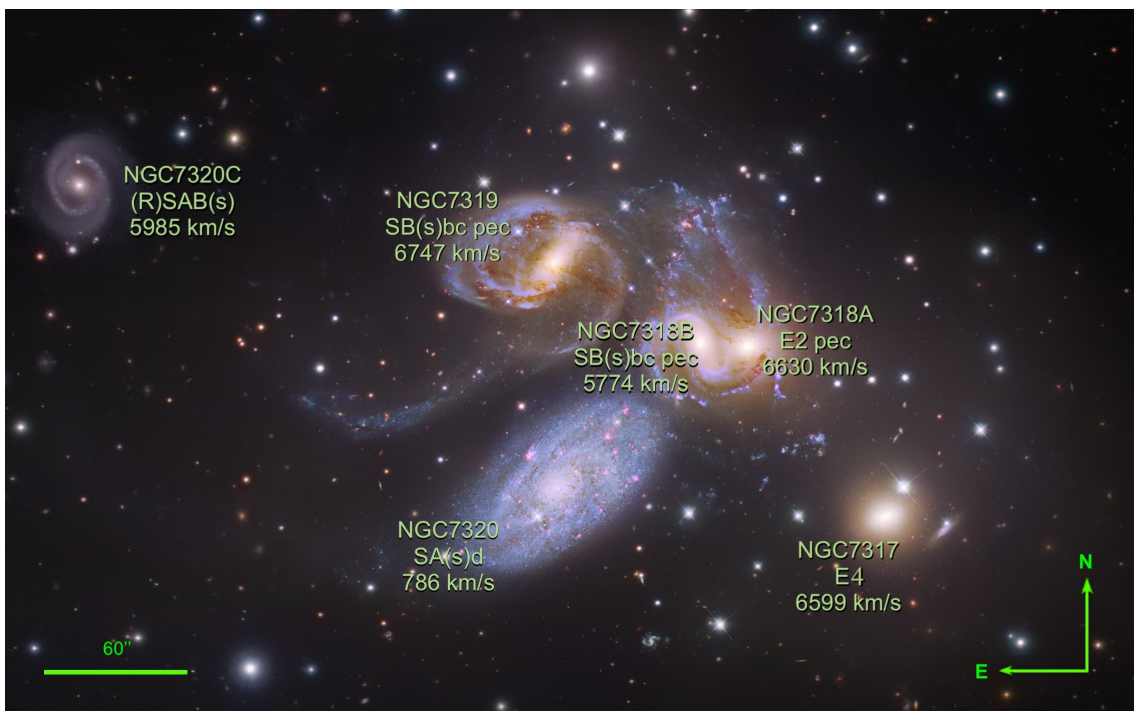


**Figure 3.1:** A Subaru telescope and Hubble Space Telescope WFC3 composite colour image of Stephan's Quintet (based on the image processed by Robert Gendler and Judy Schmidt). Velocities and morphologies as provided by the NASA/IPAC Extragalactic Database (NED). Adopting an average distance to Stephan's Quintet of 88.6 Mpc (as Duarte Puertas et al. (2019)), where 1" corresponds to ∼435 pc.

Discovered by Édouard Stephan in the 19th century (Stephan, 1877), Stephan's Quintet (SQ, HCG92) is now one of the most well-known and well-studied compact galaxy groups. Located at RA 22h35m59s, Dec +33d57.5m, at a redshift of 0.0215, the group reveals multiple interactions, both previous and ongoing (e.g., Allen & Hartsuiker (1972); Allen & Sullivan (1980); Shostak et al. (1984); Moles et al. (1997, 1998); Fedotov et al. (2011)), and every time SQ is observed in new observational windows, with new instruments, new information and fascinating details emerge.

In Fig.3.1 the galaxies of SQ: NGC7317, NGC7318A, NGC7318B NGC7319 and NGC7320C, are shown on a Subaru telescope and Hubble Space Telescope WFC3

composite image. NGC7320, first believed to be part of SQ, was revealed to be a foreground galaxy, at a much lower redshift (z=0.00262) (Burbidge & Burbidge, 1961). The core group of SQ, composed of NGC7317, NGC7318A and NGC7319, has been and still is subjected to the brunt of the dynamical harassment. NGC7317 is a gas-poor elliptical galaxy, its gas might have been stripped during a previous passage through the group's centre (e.g., Sulentic et al. (2001); Rodríguez-Baras et al. (2014); Duc et al. (2018)). The second elliptical galaxy of the group is NGC7318A. NGC7318A may have interacted with NGC7318B already, forming arm-like structures (such as the SW tail marked in Fig.3.2).

NGC7318B is a gas-rich spiral, dubbed "the new intruder" or simply "the intruder", and is currently entering the group from behind at a line-of-sight velocity relative to the rest of the group of ∼900 km/s (Xu et al., 2003). NGC7318B is interacting with the inter-galactic gas deposited in the IGM during the previous passages of NGC7317 and NGC7320C. The NGC7318B-IGM interaction is particularly stunning, due to the high relative velocity of the intruder galaxy the interaction is a high speed collision that is creating a galaxy-wide shock. The shocked region displays widespread star formation, a wide range of velocities and high velocity dispersion (e.g., Gao & Xu (2000); Sulentic et al. (2001); Xu et al. (2003, 2005); O'Sullivan et al. (2009); Iglesias-Páramo et al. (2012); Konstantopoulos et al. (2014)). The shocked star-forming ridge is, together with the tidal tails, the most studied structures of SQ. For the two large tidal tails to the south-east of NGC7319, there are two suggested formation scenarios; that they formed consecutively, through one interaction between NGC7319 and NGC7320C and one between NGC7319 and NGC7318A; or that they formed simultaneously in one interaction between NGC7319 and NGC7320C (Renaud et al., 2010; Hwang et al., 2012). See Fig.3.2 for a map of the naming convention and structure of the different tidal and interaction features of SQ.

NGC7320C is located approximately 3′ to the east of NGC7319. NGC7320C's path through the group can be traced via the tidal tail(s), and it was during the previous interaction with NGC7319 that the ISM of NGC7320C was stripped and deposited in the IGM between NGC7319 and the NGC7318 pair (Moles et al., 1997; Lisenfeld et al., 2004). Last but not least, NGC7319, a galaxy that has been involved in all previous interactions. NGC7319 is Seyfert 2 spiral galaxy, exhibiting a large outflow (Aoki et al., 1996), and is the only confirmed active galaxy of the group.

Furthermore, there are suggestions of tidal dwarf galaxies being present in SQ (e.g., Mendes de Oliveira et al. (2001); Amram et al. (2002), amongst others). Another interesting aspect of SQ is the peculiar distribution of cool gas. The HI emission seem to be located outside the optical emission (Allen & Sullivan, 1980; Shostak et al., 1984; Williams et al., 1999, 2002), and the cool molecular gas is displaced from the galaxies, appearing only in isolated clumps in the IGM and near NGC7319 (Gao & Xu, 2000; Appleton et al., 2017).

This means, that in Stephan's Quintet we have, apart from the peculiar distribution of cool gas, (i) multiple previous interactions that can be traced, (ii) large amount of gas in the intergalactic medium, (iii) currently closely interacting galaxies (potentially a precursor to a merger), (iv) a galaxy-wide shock, as well as (v) widespread star formation, predominantly outside of the galaxies themselves. As is clear, SQ is a fascinating galaxy group, and considering its dynamical state and the

multiple studies carried out covering all wavelength regimes, it is an ideal candidate for an in depth analysis of the dynamics and evolution of compact galaxy groups and the galaxies therein. SQ is optimal for studying galaxy-galaxy interactions, galaxy-IGM interactions and galaxy evolution through galaxy interactions/harassment. It is also expected that a thorough understanding of the kinematics of compact galaxy groups can reveal important details regarding galaxy evolution at higher redshifts, as the conditions present in compact groups are expected to be similar to the environment of early galaxies.

This brief description of the dynamical history of Stephan's Quintet is supported by multiple studies, both numerical and observational, spanning all wavelength regimes. This chapter therefore continues with a summary of the simulations of SQ and then the observational studies carried out in radio, infrared, optical, UV and X-ray. This chapter is by no means fully comprehensive, as that would result in a complete book by itself, but this chapter provides a summary of a large selection of studies made of Stephan's Quintet to reach a sufficient understanding. Throughout the chapter, a DSS2 R-band image will be used as a base, showing the optical positions of the galaxies in reference to the emission in other wavelengths. The chapter finishes with placing the work presented in *Part I* and *Part II* of this thesis, into the context of SQ and astronomy.
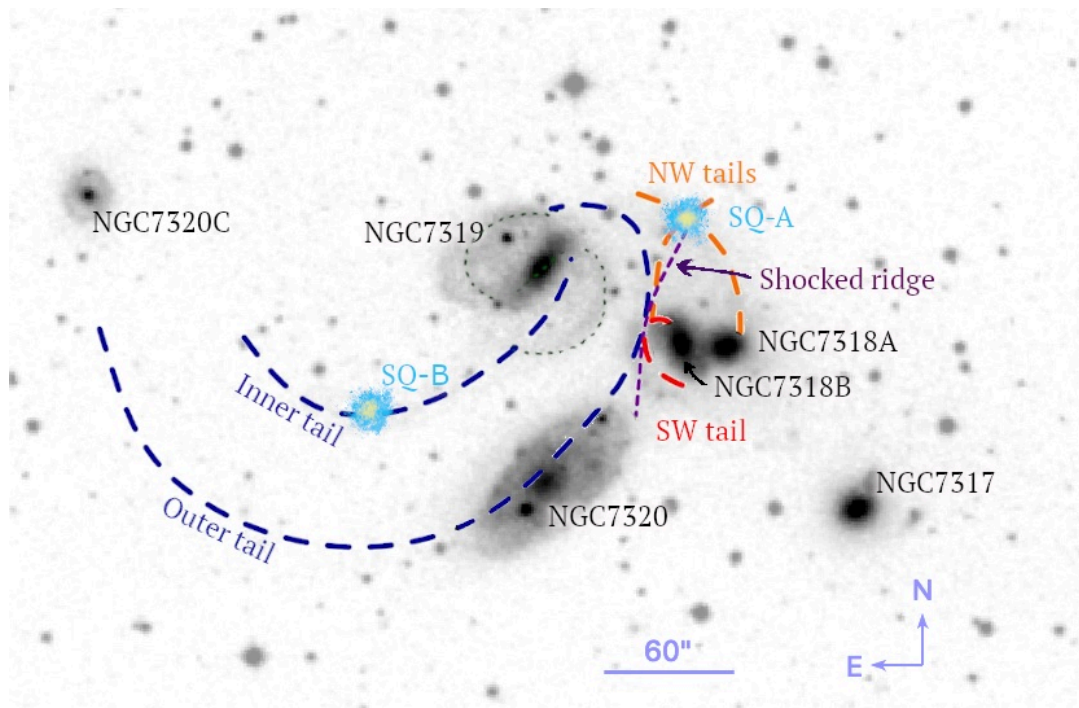


**Figure 3.2:** An adjusted R-band image of Stephan's Quintet, overlaid with markings stating the naming convention of the different important tidal and interaction structures in the group. Figure design inspired by Renaud et al. (2010).

## 3.1  Simulations

N-body simulations carried out by Renaud et al. (2010) and Hwang et al. (2012) shed light on the interaction history of Stephan's Quintet. Renaud et al. (2010) describe a possible formation story of SQ using collisionless N-body simulations and considering separate interactions as a series of connected events. The important structures in the group are shown in Fig.3.2; the inner and outer tail, SQ-A, SQ-B, the shocked ridge, the SW tail, the NW tails and the galaxies themselves, the bar and spiral arms of NGC7319 are also marked with dotted lines. Renaud et al. (2010) suggest that the outer tail formed in the interaction between NGC7320C and NGC7319, while the inner tail formed at a later event, during the interaction between NGC7318A and NGC7319. This is in agreement with the ages of the stellar populations in the tidal tails obtained via observational studies.

However, Hwang et al. (2012), when adopting hydrodynamics into the simulations, obtain models that suggest that the two long tidal tails have been formed during the same encounter, i.e., the encounter between NGC7319 and NGC7320C, and that other member have not passed close to the tidal tails after their formation. Hwang et al. (2012) states that it is possible to create the inner tidal tail through an encounter between NGC7318A and NGC7319, but it is very difficult to do so and preserve the outer tail in the process. Therefore, they favour that both tidal tails were created in the interaction between NGC7319 and NGC7320C, and note that the fact that the tidal tails have different star formation history does not mean that they may not have formed in the same event. There are also indications that NGC7318B have interacted with NGC7318A in the past, Hwang et al. (2012) state that the proof lies in the SW-arm that shows a tail-like feature and NGC7318B that shows a stripped gas disk. The models Hwang et al. (2012) present also support the galaxy-wide shock and star-forming ridge, as well as it being triggered by the emergence of NGC7318B. Which creates a timeline such as this:

1. NGC7319 and NGC7320C interact and produce the inner and outer tail simultaneously.
2. NGC7318A and NGC7318B interact and induce spiral waves that collide with the IGM and create multiple arm-like tidal structures.
3. NGC7318B collides with the IGM and produces the large-scale shock.

The interactions appear to take place one after another, as separate encounters between two main members at each time. Fig.3.3 illustrates the timeline as provided by O'Sullivan et al. (2009); Renaud et al. (2010); Hwang et al. (2012). There are parts of the timeline that are highly difficult to predict and these are marked with question marks, it may have been during an encounter in the very beginning of the groups existence that NGC7317 lost most of its gaseous content (Duc et al., 2018).

Note that Renaud et al. (2010); Hwang et al. (2012) have not taken into account the gas removal from each disk nor the disturbed structures in the NGC7318 pair. Hwang et al. (2012) explain the shortcomings of their model on the lack of resolution and the approximations placed upon the heating and cooling. They have also neglected dynamical friction and cannot reproduce the location of SQ-A nor the shape of the SW tail properly. Furthermore, the simulations must expand to include molecular gas and be able to reproduce the results of the observations of

CO and H$_2$ as well.
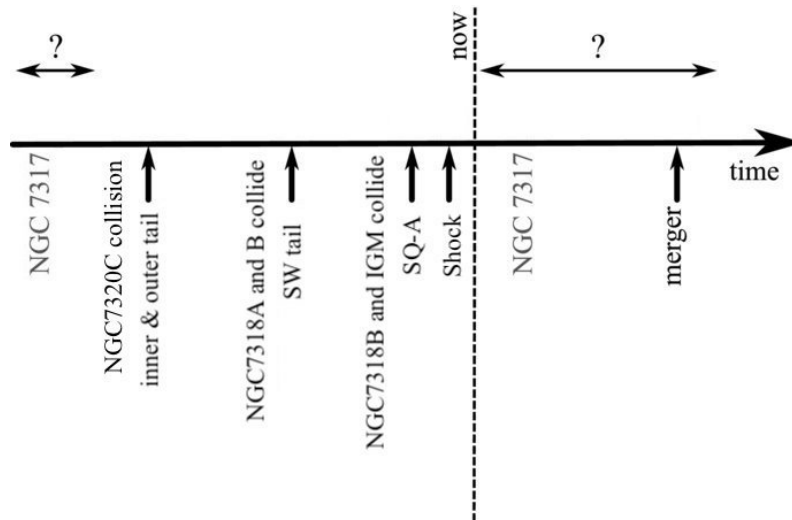


**Figure 3.3:** Timeline of the interactions and creation of tails and shocks in Stephan's Quintet as described by O'Sullivan et al. (2009); Renaud et al. (2010); Hwang et al. (2012). Highly difficult time periods to predict, i.e., very early times and future, are marked with question marks and are subjected to arbitrary assumptions. Figure design inspired by the image by Renaud et al. (2010).

## 3.2 Radio

Radio continuum emission from objects as distant as SQ, trace non-thermal processes, such as AGNs and shocks (Sulentic et al., 2001). The galaxy-wide shocked ridge was first detected in 21 cm radio continuum observations by Allen & Hartsuiker (1972) and later confirmed by VLA observations by several astronomers, e.g., van der Hulst & Rots (1981); Williams et al. (2002); Xanthopoulos et al. (2004); Xu et al. (2003); Nikiel-Wroczyński et al. (2013). The green contours in Fig.3.4 represents the 4.86 GHz (6.17 cm) VLA radio continuum maps by Xu et al. (2003) overlaid on a R-band image of SQ, note how they trace the shocked ridge.

The red contours in Fig.3.4 show the total HI column density distribution as a function of position as deduced from the VLA observations presented by Williams et al. (2002). As the distribution of HI shows, most of the neutral hydrogen has been stripped from the galaxies during the previous interactions (Verdes-Montenegro et al., 2001; Shostak et al., 1984). But surprisingly, SQ is lacking HI content compared to predictions, by as much as a factor of 3 (Verdes-Montenegro et al., 2001). The HI emission traces the two tidal tails as well as the NW tails. The HI emission in the tidal tails, has a mean line-of-sight velocity of 6610 km/s, according to Williams et al. (2002), and through careful study of the morphology, velocity dispersion and kinematics it is suggested that this HI tail consists of two separate structures. The HI data also indicates that the outer tidal tail previously filled the IGM between NGC7319 and the NGC7318 pair, and makes up the gas that is now being ionized by the interaction with NGC7318B.
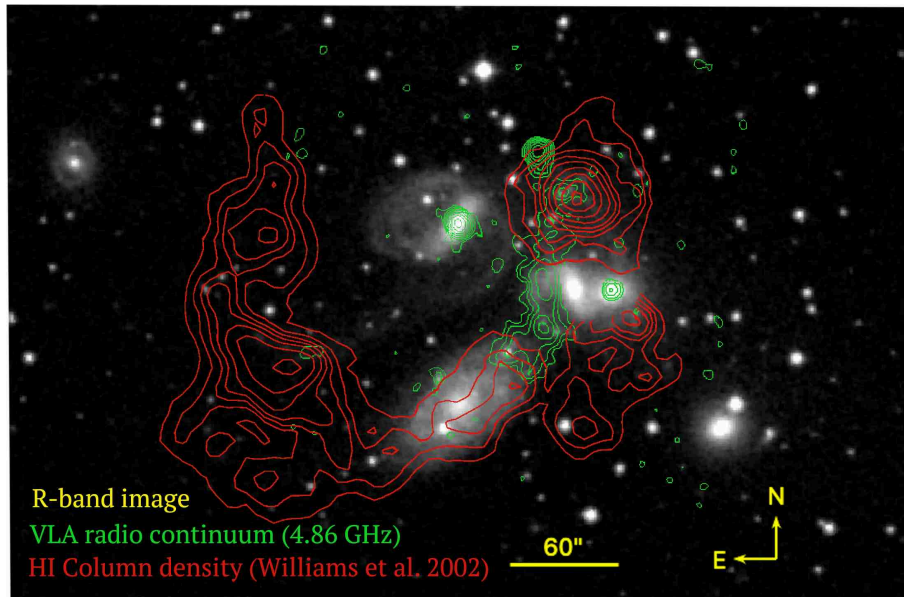
**Figure 3.4:** The green contours show the 4.86 GHz (6.17 cm) VLA radio continuum as presented by Xu et al. (2003), while the red contours trace the total column density of HI obtained with the VLA as presented in Williams et al. (2002), overlaid on a R-band image of Stephan's Quintet.

Molecular gas, strongly correlated with star formation rate, is concentrated in dust clouds in/in front of NGC7319 and in the leftovers from the previous interactions, i.e., the star-forming ridge, SQ-A and the tidal tails (Yun et al., 1997; Gao & Xu, 2000; Smith & Struck, 2001; Braine et al., 2001; Sulentic et al., 2001). The main focus of the CO observations of SQ, has been on the star-forming ridge (e.g. Guillard et al. (2012)) and the tidal tails (e.g. Lisenfeld et al. (2002, 2004); Petitpas & Taylor (2005); Gao & Xu (2000)), providing estimates of velocities and molecular gas mass at these chosen locations. NGC 7319 has been studied using IRAM 30m in 1995 (Leon et al., 1998), but only at one beam position, and the $22''$ beam did not cover the entire galaxy. Therefore, these observations failed to detect the CO deposit in the north of NGC7319 revealed by BIMA observations (Gao & Xu, 2000). In addition, there is CARMA data available of SQ (observed in 2010 by Guillard et al.), this data shows $CO(1 \rightarrow 0)$ emission in the north CO deposit detected by BIMA, in the star-forming ridge, but also in the bridge and SQ-A. Fig.3.5 displays the CARMA $^{12}CO(1 \rightarrow 0)$ contours in green and the BIMA $^{12}CO(1 \rightarrow 0)$ integrated intensity contours (as presented in Gao & Xu (2000)) in red, overlaid on an R-band image. As can be seen in the figure, the CO is predominantly located around NGC7319, to the north, and in the bridge, but there are also several CO congregations in the ridge and SQ-A.

Lisenfeld et al. (2002) use IRAM 30m to study the $^{12}CO(1 \rightarrow 0)$ and $(2 \rightarrow 1)$ in SQ-A and SQ-B. They find that SQ-A shows two main line-of-sight velocities, 6030 and 6700 km/s, where the lower velocity component is located south of the starburst region and coincides with X-ray and radio continuum emission. The weaker CO emission at 6700 km/s, is more spatially concentrated and therefore Lisenfeld et al. (2002) conclude that the shock only affects the gas at 6700 km/s and that the
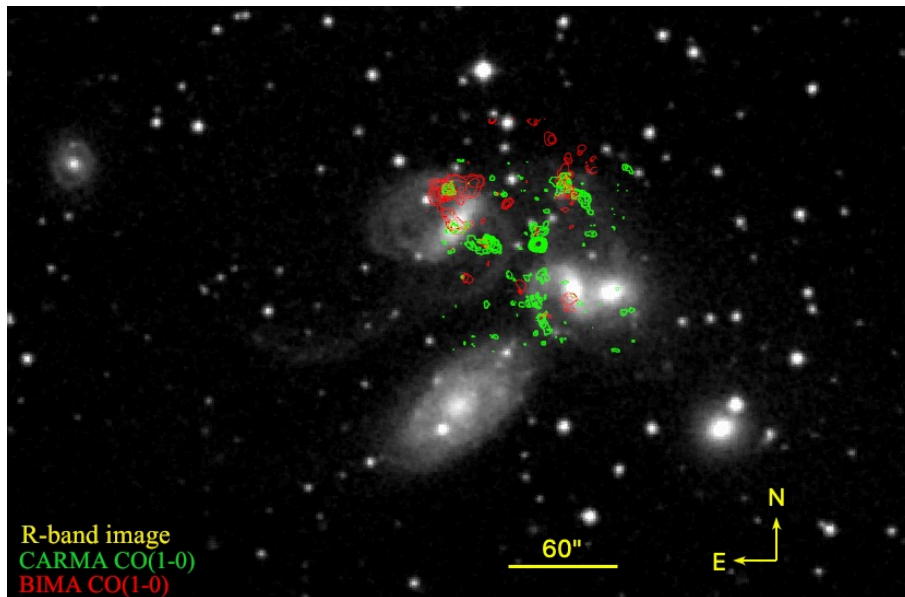
**Figure 3.5:** The green contours show the CARMA CO(1 → 0), while the red contours trace the BIMA CO(1 → 0) integrated intensity (as presented in Gao & Xu (2000)), overlaid on a R-band image of Stephan's Quintet.

cohabitation of the two velocity components is simply a projection. In SQ-B they find a line-of-sight velocity of 6625 km/s and due to the spatial extensions of the HI and CO emission, Lisenfeld et al. (2002) state that the molecular gas in SQ-B is formed in place and, out of the objects in SQ, this is the one that most resembles a tidal dwarf galaxy.

Furthermore, Smith & Struck (2001) obtained $^{12}$CO(1 → 0) data of SQ using the 3 mm SIS receiver on the National Radio Astronomy Observatory. They observed NGC7319, NGC7318A, NGC7318B and SQ-A, and found barely detectable emission in NGC7318B, significant emission in NGC7319 at a line-of-sight velocity of 6764 km/s and a dual velocity component in SQ-A at 5774 and 6630 km/s. Guillard et al. (2012) report IRAM 30m and APEX observations of the $^{12}$CO(1 → 0), (2 → 1) and (3 → 2) lines in the shocked ridge and SQ-A. They find multiple velocity components in all observed areas. While SQ-A show a PAH-to-CO surface luminosity ratio compatible with the classical Schmidt-Kennicutt law, the ridge shows a PAH-to-CO ratio lower than normal, which may be caused by high turbulence within the molecular gas.

## 3.3 Infrared

SQ-A was discovered in infrared by Xu et al. (1999) and is associated with the collision between NGC7318B and the IGM. The location of this starburst is quite unusual, 20 kpc away from the centres of neighbouring galaxies, and it is the first observation of an ongoing starburst triggered by such high speed collisions (Xu et al., 2003; Appleton et al., 2017).

From observations with IRAS (Verdes-Montenegro et al., 1998; Allam et al., 1996),
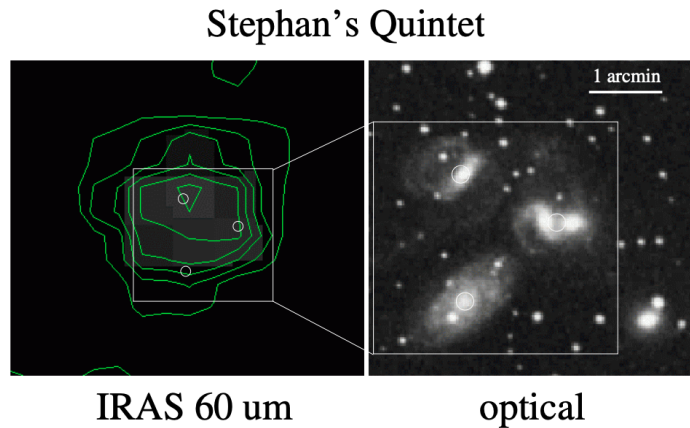
**Figure 3.6:** IRAS 60 $\mu$m continuum map, showing extended emission throughout the galaxy group. NGC7319 is the brightest object, showing emission of a factor of 2 brighter than the other galaxies in the group.

ISOCAM (Xu et al., 1999; Sulentic et al., 2001) and ISOPHOT (Xu et al., 2003), it is clear that the brunt of the IR emission originates from the foreground galaxy NGC7320, near the nuclei of NGC7319 and from two separate compact starburst regions, SQ-A and SQ-B. NGC7319 and NGC7320 have been detected in 60 $\mu$m and 100 $\mu$m, while only NGC7319 was detected in 12 $\mu$m, 25 $\mu$m and 100 $\mu$m (Sulentic et al., 2001). As can be seen in the IRAS 60 $\mu$m continuum map in Fig.3.6, the galaxies of SQ as well as the intergalactic medium are covered in molecular gas. The luminosity of NGC7319 is approximately a factor 2 brighter than the others.

Mid-IR spectroscopy, using Spitzer Infrared Spectrograph (IRS), of the star-forming ridge (Appleton et al., 2006; Cluver et al., 2010; Appleton et al., 2017), showed a FWHM of approximately 800 km/s for the $H_2$ gas in this region, centred at a velocity in between that of the core group and that of the intruder, NGC7318B. The highest shock velocity is found between SQ-A and the NGC7318 pair. Futhermore, the $H_2$ gas extends towards NGC7319, forming a bridge to the centre of the active galaxy. The green contours in Fig.3.7a shows the extension of the $H_2$ emission in SQ as obtained by the Spitzer spectrograph and presented in Appleton et al. (2017).

Far-IR observations using Herschel (Appleton et al., 2013, 2017) show that [CII] emission can be enhanced in turbulent areas in collisional environments. Fig.3.7b shows Herschel [CII] contours in green as presented in Appleton et al. (2013) overlaid on a R-band image, the white jagged edges show the boundary of the mapped area. The [CII] emission shows an extension towards NGC7319, i.e., the bridge, but due to the limited area mapped, the outflow in NGC7319 can neither be confirmed nor denied. Guillard et al. (2010) find faint dust and PAH emission in the star-forming ridge, indicating that PAHs and dust grains survive in extreme environments such as galaxy-IGM collisions. Natale et al. (2010) confirms this by detecting PAH 8 $\mu$m emission.

Furthermore, Natale et al. (2010) analyse a selection of multi-wavelength data, focusing on MIR and FIR. They conclude that star formation regions are located
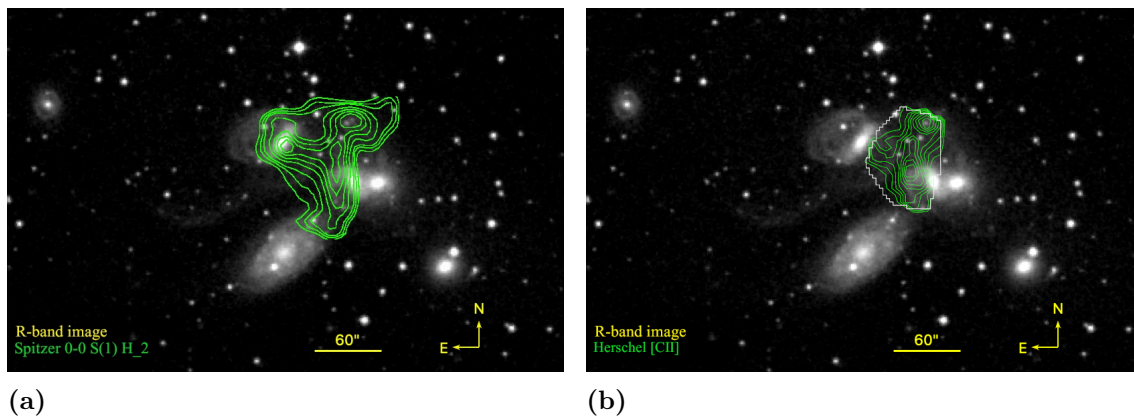
**Figure 3.7:** (a) Contours of the Spitzer warm $H_2$ line emission of the 0-0 S(1) $H_2$transition (as presented in Appleton et al. (2017)) overlaid on a R-band image; (b) Herschel integrated [CII] contours (Appleton et al., 2013, 2017) overlaid on an R-band image. The white jagged outline shows the edge of the mapped area.

in the edges of the galaxies, on the tidal structures and in the IGM. SQ-A, SQ-B and the star-forming ridge show star formation efficiencies similar to spiral galaxies. They also find that in NGC7319 the FIR dust emission does not correspond to the cold gas distribution, indicating that the FIR emission is not related to the star formation in this galaxy.

## 3.4 Optical

After being discovered in the optical by Stephan (1877) at the Marseille Observatory, many optical studies have followed, some of the more recent ones are presented by Moles et al. (1998); Iglesias-Páramo & Vílchez (2001); Sulentic et al. (2001); Gallagher et al. (2001); Fedotov et al. (2011); Iglesias-Páramo et al. (2012); Trancho et al. (2012); Konstantopoulos et al. (2014); Rodríguez-Baras et al. (2014); Duc et al. (2018); Duarte Puertas et al. (2019). Optical imagery reveals the morphology and interactions of the group, displaying the galaxies themselves, as well as the tidal tails and the extended diffuse light produced by previous interactions and galaxy gas stripping (Sulentic et al., 2001). Fig.3.8a shows a DSS2 B-band ($\lambda$ =4400 Å) image overlaid with contours highlighting the diffuse extended emission. While Fig.3.8b displays a DSS2 R-band ($\lambda$ =7000 Å) image overlaid with green markings showing the presence of H$\alpha$ emission obtained with SITELLE as presented by (Duarte Puertas et al., 2019).

By applying photometry to Hubble Space Telescope images Fedotov et al. (2011) state that the stellar clusters in the inner tail formed 150-200 Myr ago, the outer tail ∼400 Myr ago, and practically all of the stellar clusters in NGC7317 and NGC7318A/B were formed over 2 Gyr ago. They also find that the NGC7318 pair and SQ-A show ongoing star formation, as seen by the number of stellar clusters younger than 10 Myr. In addition, there is a gap in the star cluster distribution for the NGC7318 pair at 400 Myr to 2 Gyr, indicating that the interaction-induced

star formation begun approximately 400 Myr ago. NGC7319 shows continuous star formation, with a decrease in recent years due to gas stripping and an increase at the formation of the inner tail, ∼200 Myr ago, and potentially at the formation of the outer tail, 500 Myr−1 Gyr ago. Previous studies show similar ages, and Moles et al. (1997); Gallagher et al. (2001) suggested that the inner tail was formed ∼200 Myr ago, and the outer tail 500 − 700 Myr ago. These ages are in agreement with those adopted for the simulations by Renaud et al. (2010); Hwang et al. (2012), however, remember that Hwang et al. (2012) imply that the inner and outer tail must have formed in the same interaction event to maintain their shape.

Moles et al. (1998) state that NGC7317 and NGC7318A show properties of elliptical galaxies, and NGC7319 shows a barred spiral disk, while NGC7318B maintains a relatively undisturbed spiral structure despite the current collision, indicating that the interaction recently commenced. They continue to note that the presence of the two tidal tails is a clear sign of previous interaction, and both point to NGC7320C. The shocked ridge is another distinct sign of an interaction, marking the ongoing collision between NGC7318B and the IGM of the core group. Moles et al. (1998) further note that the diffuse optical light detected in the SQ area, is a clear indication of a long dynamical history of the group. Duc et al. (2018) support this, by presenting deep optical images of SQ, obtained with the Canada-France-Hawaii Telescope (CFHT). Focusing on low surface brightness structures, they present an extended diffuse halo of old stars extending towards NGC7317, indicating that the group was formed earlier than previously thought and that a previous interaction between NGC7317 and the other members of the group is likely to have occurred.



(a)                                                    (b)
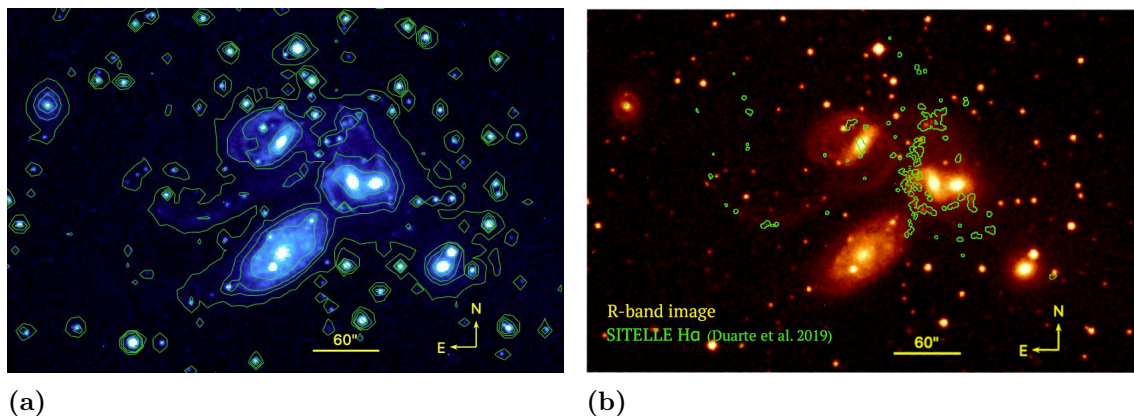
**Figure 3.8:** Optical images of Stephan's Quintet based on the data provided by the ESO Online Digitized Sky Survey. (a) B-band image with contours to highlight the extension of the diffuse emission; (b) R-band image overlaid with green borders showing the Hα emission regions (based on the data presented in Duarte Puertas et al. (2019)).

When it comes to optical spectroscopic studies of SQ, very few high resolution and high S/N observations exist (Sulentic et al., 2001), but several studies have been carried out, such as those by Di Mille et al. (2008); Iglesias-Páramo et al. (2012); Trancho et al. (2012); Rodríguez-Baras et al. (2014); Duarte Puertas et al. (2019). A large outflow from the NGC7319 nucleus was observed by Aoki et al. (1996) using optical long slit spectroscopy at the Cassegrain spectrograph attached

to the 1.88 m telescope at Okayama Astrophysical Observatory. Aoki et al. (1996) report an outflow that extends $10''$ to the south-southwest with velocities of an average of 300km/s blue-shifted from the systematic velocity, and a max velocity of 500km/s. Rodríguez-Baras et al. (2014) study the excitation mechanisms of the gas in the NGC7318 pair, NGC7319 and NGC7317 using the 3.5 m telescope of the Centro Astronómico Hispano Alemán at Calar Alto. They analyse the spectra of the individual galaxies and conclude that the gas in the galaxies of SQ is excited by a mixture of photoionisation caused by AGN and shock precursors.

The multiple of velocity components in the shocked ridge, that was found in the CO emission (Guillard et al., 2012), are mirrored in the optical spectroscopy observations (Iglesias-Páramo et al., 2012; Konstantopoulos et al., 2014; Rodríguez-Baras et al., 2014; Duarte Puertas et al., 2019), which implies a complex interplay between the pre- and post-shocked gas already in the group, and the gas of the intruder. Duarte Puertas et al. (2019) carefully fit dual-velocity components to the H$\alpha$ - [NII] emission in several of the emitting blobs in the star-forming ridge. Through this process they find five different velocity systems in SQ:

1. Associated with the intruder NGC7318B, at $5600 - 5900$ km/s
2. Associated with SQ-A, at $5900 - 6100$ km/s
3. Associated with the shocked star-forming ridge, at $6100 - 6600$ km/s
4. Associated with the inner tidal tail, SQ-A and the north part of NGC7319, at $6600 - 6800$ km/s
5. Associated with the connecting filaments between the star-forming ridge and SQ-A, at $6800 - 7000$ km/s

In addition, Duarte Puertas et al. (2019) confirm the presence of a gaseous bridge between the star-forming ridge and the nuclei of NGC7319.

## 3.5 Ultraviolet

Xu et al. (2005) present the first UV images of Stephan's Quintet obtained with the Galaxy Evolution Explorer (GALEX) satellite, Fig.3.9 shows the contours of the far-UV emission presented by Xu et al. (2005) overlaid on an R-band image. There is widespread UV emission throughout the group, and Xu et al. (2005) note that most of the UV emission is related to the SQ-A, the inner tail and the spiral galaxies, NGC7318B and NGC7319. In addition, Xu et al. (2005) state that the inner tail is extended in UV and has a loop-like structure, while the outer tail consists of stars of one stellar population of an age of approximately 10 Gyr. de Mello et al. (2012) present Gemini spectra of several UV emitting regions in the two tails and speculate that tidal dwarf galaxies or massive star-forming regions are more likely to form in HI tails in compact galaxy groups than in more simple galaxy interactions.
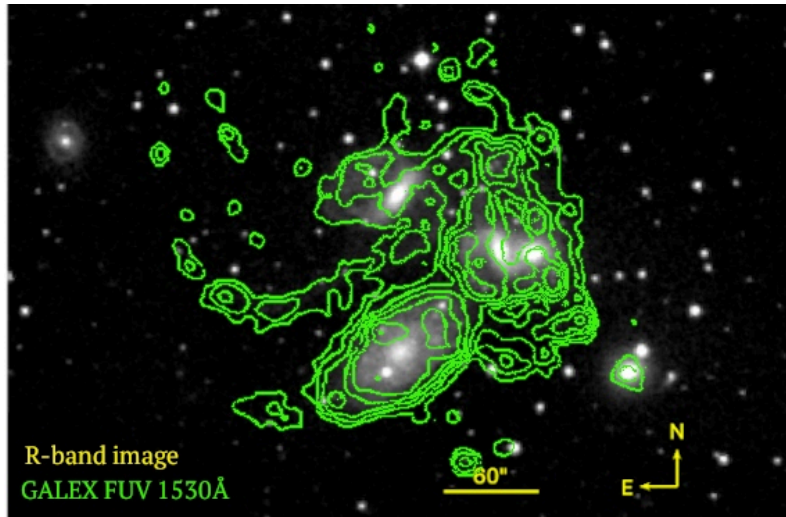
**Figure 3.9:** Contours of the GALEX FUV emission as presented in Xu et al. (2005) overlaid on an R-band image.

## 3.6 X-ray

X-ray data on compact galaxy groups provide another independent measure on high-energy processes and information about the hot IGM. In Stephan's Quintet X-ray emission may be created by star formation, including stellar winds and supernovae; accretion and shock heating of primordial gas; and/or shock heating of cold gas by the intruder NGC7318B (O'Sullivan et al., 2009). It is the last option, the shock heating caused by the IGM-NGC7318B collision, that has received the most support in literature.

Sulentic et al. (1995); Pietsch et al. (1997) showed via ROSAT HRI observations that most of the X-ray emission in SQ comes from the AGN in NGC7319 and the star-forming ridge. Trinchieri et al. (2003); O'Sullivan et al. (2009) support this with higher resolution and higher signal-to-noise Chandra observations of the group, and they detail an oblique shock that is propagating into the IGM HI cloud and heating the gas. Fig.3.10a illustrate the extension of the Chandra X-ray emission, overlaid on a R-band image. O'Sullivan et al. (2009) maintain that the star formation in the ridge is driven by radiative cooling, but dust may play a role in cooling directly after the passage of the shock. In addition, Trinchieri et al. (2003); O'Sullivan et al. (2009) find diffuse hot gas emission in the group, that most likely have been heated during the previous interactions.

XMM-Newton observations, presented by Trinchieri et al. (2005), detail that the ISM stripping in SQ is manifested in the growth of the diffuse emission from the IGM and the secular evolution of the morphology of the group's galaxies. The XMM-Newton data, illustrated using contours in Fig.3.10b, reveal a halo with a complex structure, implying a galaxy group far from dynamical relaxation.

The presence of the star-forming ridge in high resolution X-ray maps (Pietsch et al., 1997; Sulentic et al., 2001; Trinchieri et al., 2003), coinciding with the radio emission (Allen & Hartsuiker, 1972; van der Hulst & Rots, 1981), is a significant confirmation that the ridge is created by a shock front. It is expected that such a
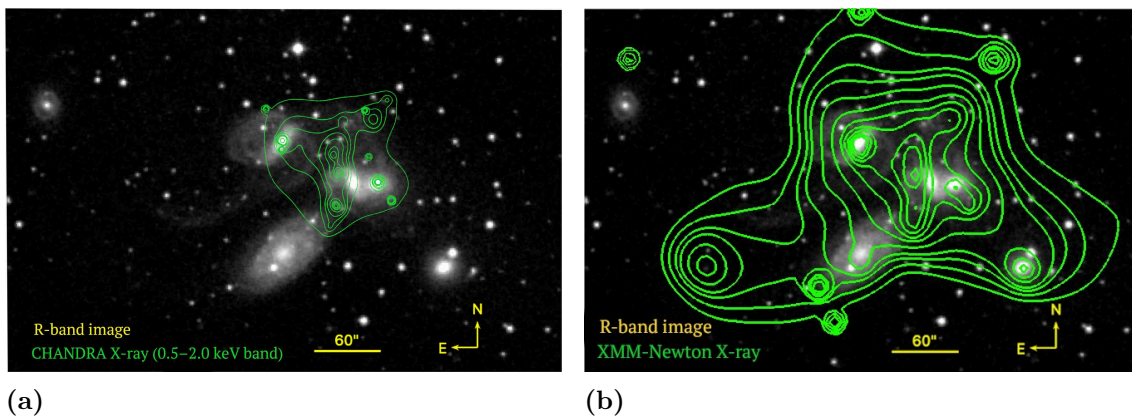
**Figure 3.10:** A R-band image of Stephan's Quintet overlaid with (a) Chandra X-ray contours (as observed by Trinchieri et al. (2003)); (b) XMM-Newton contours (as observed by Trinchieri et al. (2005)).

shock would be created when the cold gas of the IGM collides with the cold gas of an intruder galaxy at high velocity. In the case of SQ, the presence of widespread cold HI in the IGM (Shostak et al., 1984; Williams et al., 2002; Xu et al., 2003), together with the high relative velocity of the intruder, ∼900 km/s (Xu et al., 2003), supports the hypothesis that the ridge is a shock front created by the collision between NGC7318B and the IGM of the group (Sulentic et al., 2001). Furthermore, O'Sullivan et al. (2009) note that the deficit of HI gas in SQ (Verdes-Montenegro et al., 2001), can be compensated for by the amount of X-ray gas present, i.e., the lost HI has been heated in the previous interactions and is now emitting in X-ray, it is possible that all the hot gas originates from this shock heated HI.

## 3.7 The Aims of this Thesis

Despite the extensive and numerous previous studies of this enchanting compact galaxy group, many questions remain unanswered. In particular, very few high-resolution and high signal-to-noise spectroscopic studies have been carried out. The spectroscopic studies that have been carried out have been focused on particular regions of SQ (Lisenfeld et al., 2004; Cluver et al., 2010; Trancho et al., 2012) or on certain emission lines such as only Hα (Duarte Puertas et al., 2019). Rodríguez-Baras et al. (2014) present optical spectra of the galaxies in SQ, but at too low spatial and spectral resolution to enable an analysis of the kinematics, even if they would have included the IGM and the tidal features.

Analysing the stellar and gas kinematics, of not only the individual galaxies, but also of the tidal structures that connect them, are vital in understanding the formation and evolution of the group (Cappellari, 2017). In a compact galaxy group such as Stephan's Quintet, understanding the processes and interactions at play, enable an understanding of galaxy evolution and star formation through extreme interactions, conditions believed to be prominent in earlier epochs of the Universe's history.

This brings us to *Part I* of this thesis, *Atomic Gas & Stellar Kinematics in Stephan's Quintet*, where I present and analyse my optical spectroscopy data covering SQ, obtained with the Large Binocular Telescope (LBT).

Remembering that the three main ingredients in a galaxy are stars, atomic gas and molecular gas, the conclusion is that, apart from the stellar and atomic gas information obtained from the optical spectroscopy, information regarding the molecular gas must also be included in a kinematic analysis. It is important that the system is studied as a whole and in high resolution, to reach a better proper understanding of the complex processes occurring in this interactive galaxy group.

The literature on the molecular gas content and kinematics in SQ, show that the focus of previous observations has been on particular features, such as the star-forming ridge (e.g. Guillard et al. (2012)) and the tidal tails (e.g. Gao & Xu (2000); Lisenfeld et al. (2002); Petitpas & Taylor (2005)). A suspicious aspect of the published literature is the discrepancies. Observations, claimed to be in the same location, provide ambiguous results and incite questions regarding calibration and analysis procedures (see for example Smith & Struck (2001); Lisenfeld et al. (2002); Guillard et al. (2012)). The amount of molecular gas left in the galaxies is still unclear, and so are the details of the interactions between the intergalactic medium and the galaxies.

In *Part II* of this thesis, *Molecular Gas Kinematics in Stephan's Quintet*, I present and analyse my IRAM 30m CO observations of SQ. To negate potential issues with varying calibration of different pointings, suspected to be present in the previous literature, and to obtain a full view of the group, I map the whole area using a continuously moving beam, a method called on-the-fly mapping.

The conditions in compact galaxy groups, the high galaxy density and the large amount of gas in the IGM, are expected to be common for galaxies in the young Universe. And extreme galaxy interactions, such as those occurring in compact groups, are suspected to be a vital factor in driving galaxy evolution at high redshift (Rodríguez-Baras et al., 2014). Thereby, the physical processes occurring in the environment of galaxy groups play a fundamental role in determining the star formation history of the Universe (Natale et al., 2010). In addition, Stephan's Quintet, with its low redshift and high brightness, is ideal to use as a template for compact galaxy groups, a template that can be used when analysing galaxy groups and interactions at higher redshifts, and the work presented here brings us one step closer to such a template.

In conclusion, the purpose of this work is to carry out a thorough kinematic analysis of the compact galaxy group, Stephan's Quintet, using the kinematics of the three main galaxy ingredients, i.e., atomic gas and stars (obtained with the LBT, presented in *Part I*) and molecular gas (obtained with IRAM 30m, presented in *Part II*). By combining the information contained in these three different tracers of galaxy dynamics, additional light is shed on compact galaxy groups, galaxy interaction/harassment and galaxy evolution throughout cosmic time.

# Part I

# Atomic Gas & Stellar Kinematics in Stephan's Quintet

# 4

# Optical Astronomy

In the beginning we observed the Universe in optical light using our own eyes, but in the 17th century optical astronomy in Europe made great advances. Advances that were enabled by the invention and development of optical telescopes by Galileo Galilei, Johannes Kepler and Sir Isaac Newton. In this chapter an introduction to optical telescopes is provided, as well as further detail of the Large Binocular Telescope, the telescope that was used to obtain the data presented in Chapter 6.

## 4.1 Optical Telescopes

The basic setup of an optical telescope is as follows: a primary lens or mirror focuses the light from the astronomical object on to its focal point, where the light is subjected to a secondary lens/mirror and then recorded or observed through an eyepiece. Today there are three main categories of optical telescopes:
- Refracting telescopes, which utilise lenses as primary and secondary. The larger the primary lens is the more power the telescope can provide, which increases the brightness and clarity of the image. The secondary smaller convex lens is responsible for magnification.
- Reflecting telescopes, have the same setup as refracting telescopes but uses mirrors instead of lenses as primary and secondary. The primary, a curved mirror, is often called a reflector.
- Compound/catadioptric telescopes, combine the refracting and reflecting telescope technologies. These telescopes use curved mirrors and lenses to pass the light through a small hole at the centre of the primary mirror, where the light can be observed via an eyepiece or registered using, for example, a camera or a Charge-Coupled Device (CCD) detector.

The Rayleigh criterion states that a telescope's resolution is directly related to the diameter of the telescope and described as follows:

$$\Theta = 1.22 \frac{\lambda}{D} \tag{4.1}$$

where $\Theta$ is the angular resolution, $\lambda$ is the wavelength of the incoming light and $D$ is the diameter of the lens/mirror. A straight forward method, as described by the Rayleigh criterion in Eq.4.1, to increase the resolution of the observations is to use larger lenses/mirrors, but the larger a lens is, the more pronounced the imperfections are, which blurs the image, and a larger lens also has a longer focal length. The reflecting telescopes were revolutionary as they enabled the manufacturing of significantly shorter telescopes, higher resolution and lower production costs.

Apart from the size of the lens/mirror used for obtaining the astronomical data, there are other factors that limit the resolution and resultant image quality. Observers must take into account the astronomical seeing and the imperfections of the telescope. Astronomical seeing is the effect of turbulence in the atmosphere, causing variations in the refractive index and limiting the angular resolution that can be achieved. To counteract the issue with astronomical seeing, telescopes are placed in space, high-flying airplanes or on high mountains. For continuously correcting for the changes in the refractive index, the adaptive optics technology (AO) is particularly useful for ground-based telescopes as the issue is mitigated by the mirror shape being adjusted in real-time based on the atmospheric reflective index. Another approach to increase the resolution is to combine the effort of several telescopes across the world, this is called interferometry, and increases the resolution by synthetically increasing the "diameter" of the telescope. Interferometry combines the signals from two or more telescopes, and by using a large number of telescopes an observation can be produced that has a resolution of a single telescope with a diameter equivalent to the maximum physical separation of the telescopes (commonly called the baseline), i.e. we can replace the lens/mirror diameter $D$ in Eq.4.1 with the baseline to obtain an approximation of the angular resolution achieved with an interferometric array.

Physicists have been studying the spectrum of the light ever since Isaac Newton in the late 17th century. Albeit studying the spectra of nearby celestial objects and particularly bright stars using prisms has been done for several centuries, it was not until the early 20th century, and the invention of high-quality reflection gratings, that spectroscopy became widely adopted in optical astronomy. The resolution of a prism is defined by its size, and as the case is with lenses, a larger prism has more pronounced imperfections. Reflection gratings instead use diffraction and mirrors, thereby allowing an easier and less costly construction as well as a high precision even in the instance of low incoming emission.

Long-slit spectroscopy is particularly useful in astronomical studies, as this method can provide both spatial and spectral information simultaneously. The basic idea is that a very narrow long slit is placed over the area of interest, only a small amount of light is allowed through, the light is thereafter passed through a dispersive device, such as a prism or a diffraction grating which splits the light into a wavelength spread. The observer, therefore, obtains spatial information from the position of the emission along the slit, and spectral information through the diffraction of the light perpendicular to the slit. Long-slit spectroscopy provides us with line-of-sight velocities, abundances of elements and velocity dispersions. From this data observers can obtain information about the rotation of galaxies, the expansion of nebula, excitation mechanisms of gaseous clouds, and much more. Integral Field Spectroscopy (IFS) can be seen as an extension of long-slit spectroscopy. In IFS different techniques are used to cut the image into slices, and then, in each pixel of a slice, the spectrum is extracted. This enables the observer to obtain the spectrum in each pixel in the Field-of-View (FoV) simultaneously. Resulting in a data cube, wherein each pixel has a spectrum associated with it, thereby providing in depth information about the sources in the full FoV.

## 4.2 The Large Binocular Telescope

In this chapter an introduction to the Large Binocular Telescope (LBT) and the LBT instrument the Multi-Object Double Spectrograph (MODS) is presented. Unless stated otherwise, the information provided here is supported by Wagner et al. (2014); Rothberg et al. (2016).

In southeastern Arizona, near Tucson, we find the LBT on Mount Graham at an altitude of 3221 m. The LBT is, as the name entails, a binocular telescope, in Fig.4.1 a front view of the telescope is depicted, showing the two mirrors with the shutters open. The mirrors are identical, 8.41 m in diameter, and mounted on a common altitude-azimuth mounting for a combined collecting area of an 11.8 m single dish telescope. The distance between the centres of the mirrors are 14.4 m, enabling interferometric observations with the spatial resolution of a 22.8 m edge-to-edge baseline. The common altitude-azimuth mounting and constant baseline ensures a non-changing angular resolution of the interferometer as it tracks astronomical objects across the sky. The LBT is the first of the Extremely Large Telescopes (ELTs) and adheres to two main missions; to be the first ELT, investigating new technologies to be used for future ELT generations; and to be a leading 8-m class telescope.



**Figure 4.1:** The Large Binocular Telescope. Credit: LBTO

Combining the binocular design with adaptive optics using adaptive Gregorian secondary mirrors, the LBT offers an exceptional combination of wide FoV, high angular resolution and high sensitivity (due to the large mirrors and therefore large light collection area). The LBT is the first telescope where the adaptive optics is integrated into the telescope itself, via the deformable secondary mirror. Combining the secondary mirror and the deformable adaptive optics mirror in this manner, ensures that no thermal background noise is introduced with the addition of the adaptive optics system.
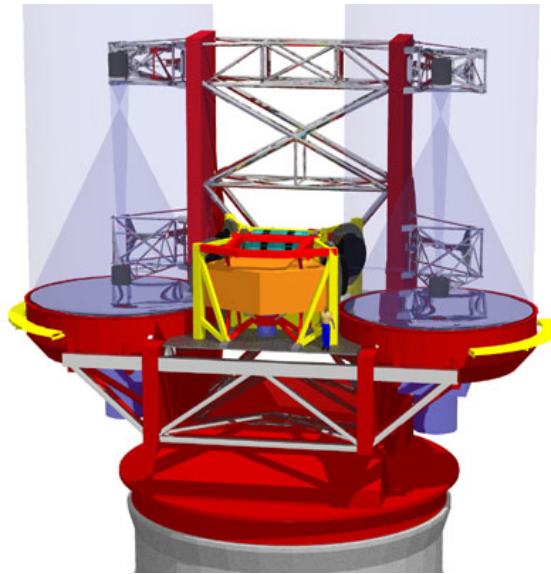
**Figure 4.2:** The Large Binocular Telescope schematic. The optical path illustrated in transparent blue. Credit: Press release from MPG PRI SP 2/2001, figure rendering: Dr. Tom Herbst, MPIA.

The LBT operates in the optical and the near-infrared wavelength regimes, utilising several different instruments. All instruments are mounted on the telescope at once, and can be accessed by moving swing arms with the required optics in and out of the main beam. Fig.4.2 illustrates the layout of the LBT, and the two optical paths are sketched in blue. Currently the active instruments at the LBT are:

- The Large Binocular Cameras (LBC)
  - Two wide-field cameras mounted on the prime focus swing arms of the LBT.
  - LBC Blue is optimised for observations in 3500-6500Å.
  - LBC Red is optimised for 5500-10000Å.
  - Average pixel scale is $0.2255''/pix$.
  - Science FoV is $23' \times 25'$.
- Multi-Object Double CCD Spectrographs/Imagers (MODS1 and MODS2)
  - Two identical seeing-limited spectrographs/imagers.
  - Wavelength range 3200-10000Å.
  - FoV of $6' \times 6'$.
  - Average pixel scale is $0.12''/pix$ (blue), $0.123''/pix$ (red)
  - Gratings provide a resolution of R∼2000, while double-pass prisms provide R=500-150.
  - Multi-object option available, using laser-machined focal-plane slit masks.
- LBT Utility Camera in the Infrared (LUCI1 and LUCI2)
  - Two infrared multi-mode instruments capable of long-slit and multi-slit spectroscopy as well as imaging.
  - Wavelength ranges zJHK bands from 0.89 (LUCI1) and 0.96 (LUCI2) to 2.44μ$m$.
  - FoV $4' \times 4'$ (seeing-limited) and $30'' \times 30''$ (AO mode)

- – Image scale is $0.12''/pix$ (for imaging), $0.25''/pix$ (for spectroscopy) and $0.015''/pix$ (for AO mode).
- – Resolution $\sim$2000 for H+K to 6500-8500 in single band z, J, H, K.

- LMIRcam on LBTI
  - – A camera and coronagraph[1].
  - – FoV is $11'' \times 11''$
  - – Pixel scale is 10.7 $mas/pix$.
  - – Optimised for 3-5µm, and can be used at shorter wavelengths.

- Potsdam Echelle Polarimetric and Spectroscopic Instrument (PEPSI)
  - – A polarimeter[2] and spectrograph.
  - – Wavelength range 3830-9070Å.
  - – Spectral resolution up to 250000.
  - – Sky diameter of spectrograph $\sim 0.7 - 2''$.

The LBT is an international collaboration of universities and institutions from Germany (LBTB: LBT Beteiligungsgesellschaft, who coordinates the participation of five German institutes), Italy (INAF: Istituto Nazionale di Astrofisica) and USA, the University of Arizona and the Ohio State University (who coordinates the participation of four additional US universities). While some partners focus their attention on using the LBT as a laboratory to develop new equipment, others turned to the LBT to obtain high quality data and robust scientific results. Fig.4.3 shows the typical view of the AllSky camera of the LBT, obtained by the author during the observations for this thesis.
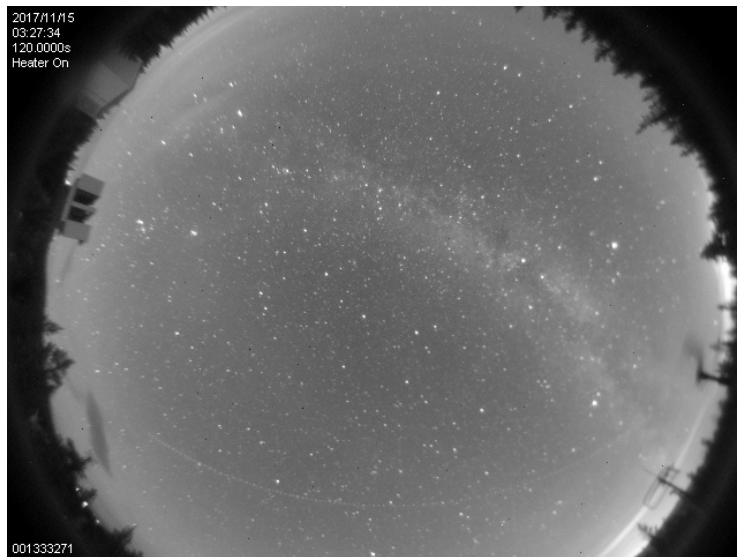


**Figure 4.3:** An example of a typical view from the AllSky camera of the LBT.

---

[1]A coronagraph is an instrument that is able to block out the light of a star to enable study of nearby objects, objects that would otherwise have been covered by the light of the star. The name, coronagraph, comes from the fact that these instruments are most often intended for observations of the corona of the nearby star.

[2]A polarimeter measures the polarisation of electromagnetic waves.
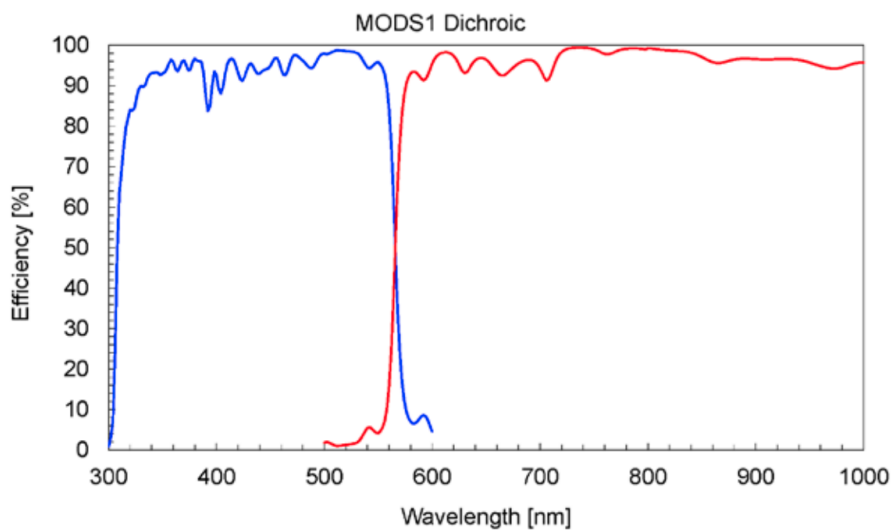
**Figure 4.4:** The transmission and reflection curves of MODS1 dichroic. Credit: MODS Instrument Manual, OSU-MODS-2011-003, R.W.Pogge.

## 4.2.1 The Multi-Object Double Spectrograph

The information detailed in this chapter relies on the paper by Pogge et al. (2010), as well as Wagner et al. (2014); Rothberg et al. (2016). The Multi-Object Double Spectrograph (MODS) can, as previously stated, be used for imaging, long-slit and multi-object spectropscopy. Covering the UV to near-IR wavelengths, 3200-10000Å, with a FoV of $6' \times 6'$, it offers the options of an empty mask for imaging, a custom multi-object slit mask or the choice of one of the standard slit masks: a 5' segmented long slit[3] with widths of 0.3", 0.6", 0.8", 1.0", 1.2" or 5". While the FoV of MODS is $6' \times 6'$, there is a reduced image quality outside of the inner $4' \times 4'$. The two MODS spectrographs are identical and mounted at the direct Gregorian foci.

After passing through the slit mask the light reaches a dichroic prism that splits the light at 5650Å into the red and blue channels (if dual mode is chosen). The dichroic passes the blue light and reflects the red, the transmission (blue) and reflection (red) curves are shown in Fig.4.4. Thereafter, as seen in Fig.4.5, both channels have a separate collimator, disperser, mirror, corrector and a field flattener (FF) including a CCD detector. It is also possible to direct the light into the red or blue channel only, thereby extending the wavelength coverage over the dichroic cross-over-region at the cost of the wavelength range in the non-chosen channel.

There are three different operating modes for MODS: imaging, grating spectroscopy and prism spectroscopy. The important difference between grating and prism spectroscopy lies in the resolution. Where grating spectroscopy provides a spectral resolution of 2000-1850, and prism spectroscopy 500-140.

---

[3]The segmented MODS long-slits consist of five 60″ long slits, separated by 3" struts. The struts are present to maintain the integrity of the slit mask.
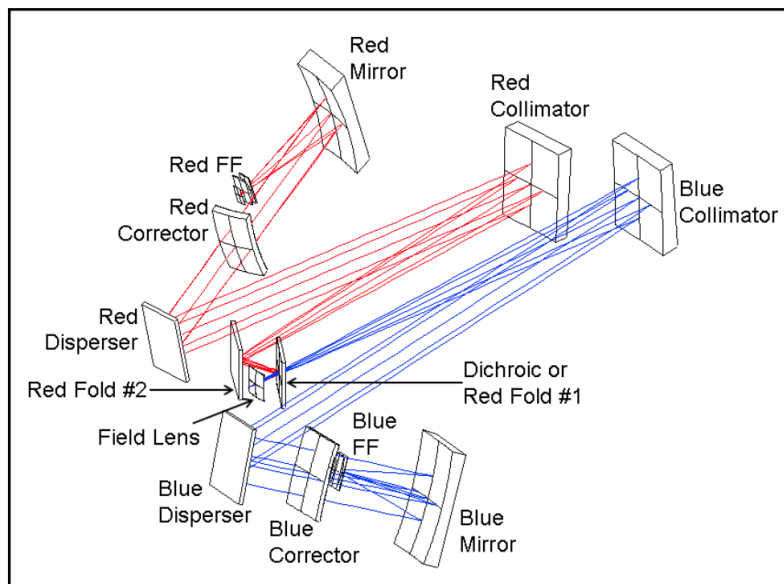
**Figure 4.5:** The optical schematic of the Multi-Object Double Spectrograph. Credit: MODS Instrument Manual, OSU-MODS-2011-003, R.W.Pogge.

# 5

# Observational Setup & Data Treatment[1]

The atomic gas and stellar kinematics study of this thesis relies on data obtained with MODS at the Large Binocular Telescope, Tucson, Arizona, US. The observations cover the main part of, and the most intense, interactions in this galaxy group, i.e., the interaction between the NGC7318 pair, the large deposit of IGM and galaxy wide shocked ridge between NGC7319 and the NGC7318 pair, as well as NGC7319, NGC7318A, NGC7318B and NGC7317 themselves. With a $1''$ spatial resolution and an average 15 km/s spectral resolution I study the physical characteristics of the complex processes occurring in the compact galaxy group Stephan's Quintet. This chapter details the setup of the observations, the data reduction and the initial spectral analysis.

## 5.1   Observational Setup & Exposure Times

Optical long-slit spectroscopy observations were carried out with MODS, on the 13th and 15th of November 2017. Observations were performed in single mode, i.e., with MODS1 only, since MODS2 was non-functional at this time. Spectra were obtained in the wavelength range 3200 - 10000Å, with the $1.0''$ slit. The DIMM seeing averaged at $0.8''$ throughout the observation period, thus the emission can be expected to have been contained within the slit.

The observations have been carried out in a pseudo-IFS manner, covering the vital regions of SQ through the use of several slit positions. The area is undersampled to increase the signal-to-noise ratio in the data obtained and to focus the study, detailed here, on the global properties of SQ. The slit positions have been carefully chosen to ensure proper coverage of the nucleus of each of the galaxies contained within the observed area. The first slit, the 0 position in Fig.5.1, was centred on the nuclei of NGC7318B and NGC7319 at a position angle (PA) of 242° of the telescope, thereafter the slit was shifted horizontally, dx, in steps of $3''$ each, covering the region as shown in Fig.5.1 in a total of 7 slit positions. In addition, a single slit was positioned covering NGC7317, also illustrated in Fig.5.1.

At each slit position 3 exposures of 300s each were executed, and then a second set of exposures after a $10''$ dither along the slit (to account for bad pixels and the struts in the slit mask), resulting in a total of $6 \times 300s$ per dx-position. However, due to the weather conditions $dx = 9''$ and NGC7317 were only executed $4 \times 300s$

---

[1]The reduced data is available in the open repository of my supervisor's research group.

as clearly stated in table 5.1. Note that positive dx-shifts are to the left of the 0-position, since a positive shift is a shift to the right of the telescope, so position $dx = 9''$ is the position covering the NGC7318A nuclei.

**Table 5.1:** The exposure times for the observations at each slit position:

| Shift | Exposure time |
|---|---|
| 9 | $4 \times 300s$ |
| 6 | $6 \times 300s$ |
| 3 | $6 \times 300s$ |
| 0 | $6 \times 300s$ |
| -3 | $6 \times 300s$ |
| -6 | $6 \times 300s$ |
| -9 | $6 \times 300s$ |
| NGC7317 | $4 \times 300s$ |
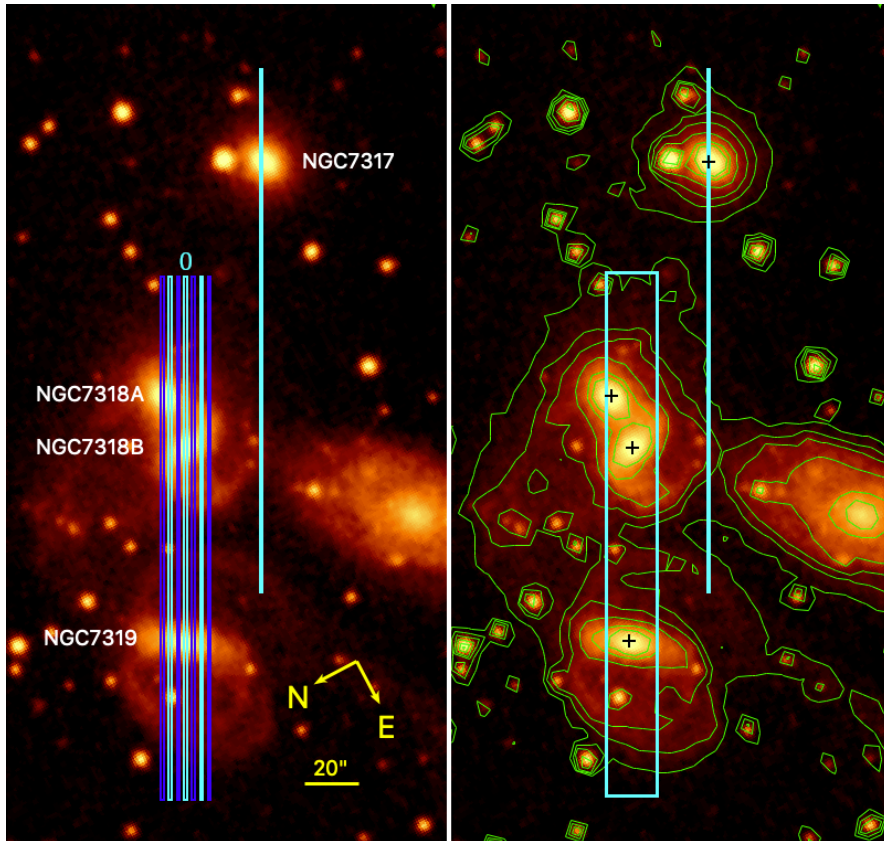


**Figure 5.1:** *Left:* DSS9 red image showing the positions of 8 slits used for the observations. The 7 slits covering NGC7319 and the NGC7318 pair are alternately coloured in light and dark blue to enable distinction between them. The 8th slit covers NGC7317. *Right:* Region covered by observations illustrated over the DSS9 red image overlaid with arbitrary contours to show extension of emission. 7 slits construct the rectangular area, while a single slit covers NGC7317. The crosses pinpoint the positions of the galaxies, from top to bottom: NGC7317, NGC7318A, NGC7318B and NGC7319.

For the imminent flux calibrations and telluric corrections, spectrophotometric standard stars G191-B2B (DA0 type) and BD+33 2642 (B2IV type) were observed with the 5″ slit during the same night as the observations. Furthermore, the required calibration frames of biases, flat fields and arc lamps (exposures done with lamps used for the subsequent wavelength calibration) were obtained during the observation period[2].
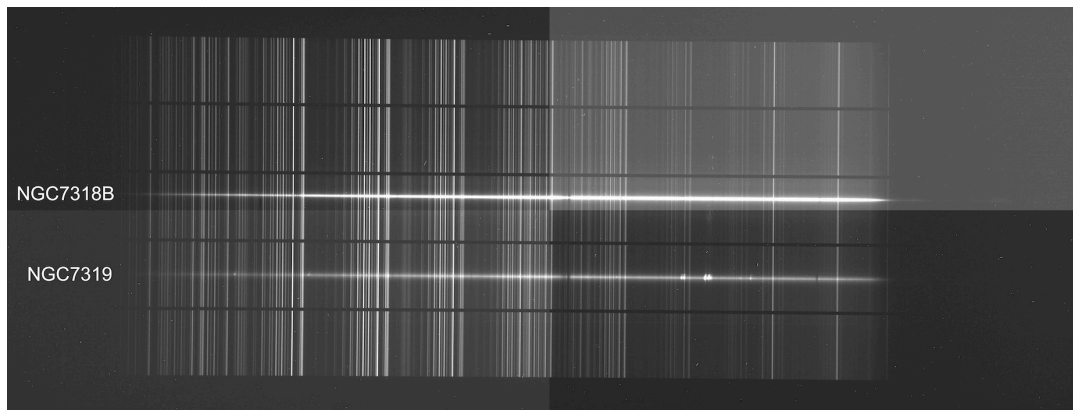


**Figure 5.2:** The raw image of one exposure of MODS1 Red at $dx = 0$. Along the x-axis is the wavelength direction, and the y-axis is the spatial direction along the slit. The dark spaces are the struts in the slit, ensuring the integrity of the slit mask.

## 5.2 Data Reduction

The calibration frames, together with the science observations frames, have been put through the MODS Basic CCD Reduction package, provided by the LBT observatory, and further reduced using the Image Reduction and Analysis Facility (IRAF). The MODS CCD Reduction Package is made available by the LBT observatory due to the particularities of this instrument. Each MODS CCD is divided into 4 quadrants that are read out simultaneously, these quadrants are clear in the raw images, as is the differences between the bias levels in the even and odd pixel readout channels, see Fig.5.2 (the wavelength axis of MODS Red is flipped in the raw images, with the highest wavelengths to the left and the lowest to the right, this is corrected for in the MODS CCD Reduction package). This readout scheme is unique to MODS and must be corrected for using the provided MODS CCD Reduction scripts. Common IRAF tasks are not sufficient. IRAF, developed by the National Optical Astronomy Observatories for the astronomical community, has been and still is a common tool for reducing astronomical data (Barnes, 1993), despite being unsupported[3].

---

[2]For more details on what to take into account when creating the observation scripts and how to carry out the observations, please see the highly useful MODS Instrument Manual available via the LBT web page, `lbto.org`.

[3]If you are starting down the path of reducing your data today, note that IRAF, albeit being a very useful tool, was developed in the 90's and is no longer supported (as is the case with the python versions on which IRAF can run). Therefore, I would advise against using IRAF and instead recommend exploring and choosing more recently developed tools for reducing your data, perhaps Python's Specutils package.
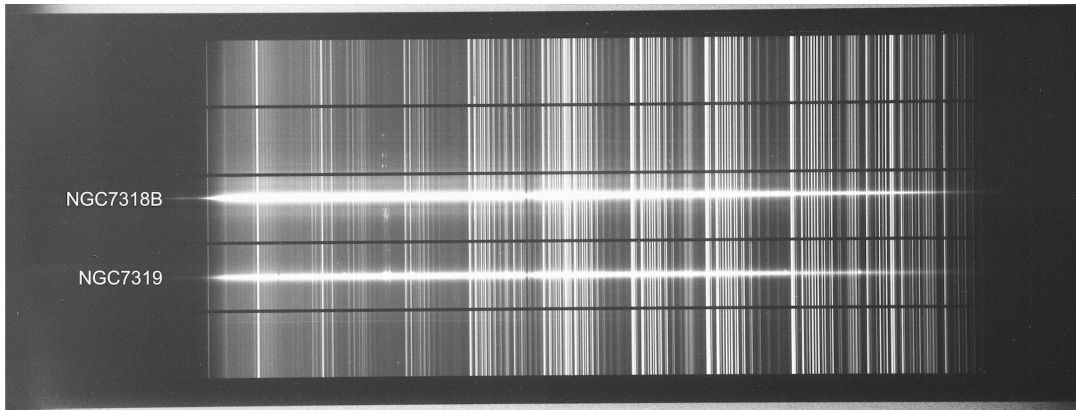
**Figure 5.3:** The same as the image in Fig.5.2 but after bias subtraction and flat fielding, showing the effect of the MODS CCD Reduction Package.

Carrying out the bias subtraction and flat fielding using the MODS CCD Reduction Package provide an image such as that in Fig.5.3. Thereafter following the standard procedure for reducing long-slit spectra with IRAF, I begun by trimming the images, removing cosmic rays and rectifying them in both directions, spectral and spatial. Depending on your data, rectification in the spatial direction might not be necessary, in most cases it is not. For SQ it was, however, paramount. When aiming to properly study the extended emission in this compact galaxy group, one cannot rely on the common and useful iraf.apall aperture extraction task. This task extracts a bright trace of an astronomical object by following the peak emission in each wavelength, but the extended emission in SQ does not show a bright trace across all wavelengths, and it is highly extended, it therefore defies the use of iraf.apall. Instead I carefully rectified the images in the spatial direction as well as the spectral direction, enabling cutting of the image into vertical stripes for further reduction and analysis.

Regarding the process of rectification, in the spectral direction it is done by identifying the emission lines in the arc lamp frames, and creating a transformation matrix that when applied to the science frames goes through the image and places the peak emission at the value stated by the user. For the spatial direction two science frames separated by a *dy*-shift are combined and by indicating the position of the traces of the galaxies the transformation matrix is created and can be applied to all science frames.

Thereafter, the background was subtracted and the science frames were corrected for atmospheric extinction. Additionally, the blue part of the spectra have an innate shift of a few Ångstrom, which was corrected using the auroral line [OI]$\lambda$5578.9Å. Finally the images for each slit position were combined, resulting in images such as those shown in Fig.5.4, where slit position $dx = 3''$ and $dx = 6''$ for MODS1 Red are shown in Fig.5.4a and Fig.5.4b respectively.

The combined image of each slit position was thereafter cut into horizontal stripes, using an appropriate spatial resolution considering what we could reach with the astronomical seeing present during the observations, i.e., $1''$. In each stripe the spectrum was averaged across the spatial direction and flux calibrated using the standard star, G191-B2B or BD+33 2642, depending on which night the data had

been obtained. The spectra were adjusted to the average redshift of the group ($z = 0.0215$), to facilitate the subsequent analysis of the data, and corrected for interstellar extinction. For MODS1 Red the spectra were additionally corrected for telluric lines.



**(a)**

**(b)**
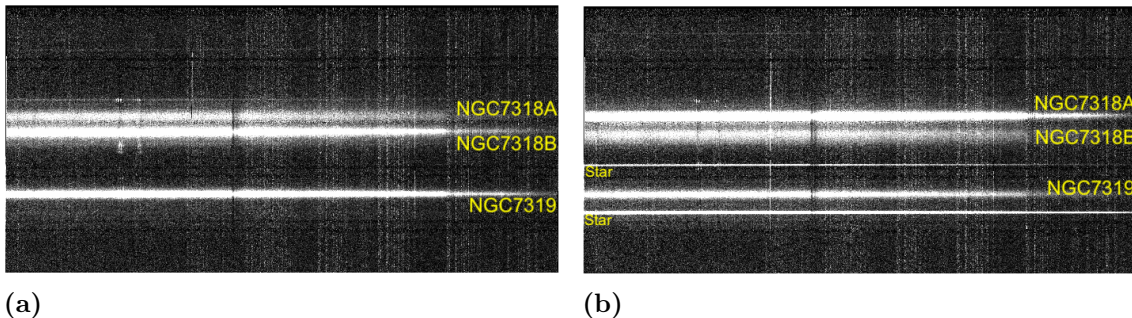
**Figure 5.4:** After going through the MODS CCD Reduction Package, trimming, rectification and background subtraction, we obtain images such as these. Displaying two examples for MODS1 Red. The layout of the corresponding MODS1 Blue, is similar. The traces are labelled for clarification. (a) The $dx = 3''$ shift; (b) The $dx = 6''$ shift.

## 5.2.1 Challenges

If the rectification in the spatial direction is not done properly, the cutting into vertical stripes will result in spectra showing the emission of different objects along the slit at different wavelengths in the same spectrum, disabling any abundance analysis that can be carried out, including investigation of the excitation mechanisms. This is, therefore, a step that must be approached with meticulousness.

The background subtraction was a particularly delicate procedure for SQ. Due to the large amounts of extended gas, the IRAF background task had difficulties finding a baseline for the background in the images. Different approaches, using different settings as well as creating a full background image from a part of the slit void of clear emission, were attempted, but in the end the IRAF background task gave the most satisfactory results after sufficient adjustments.

## 5.3   Initial Scientific Analysis

This chapter concerns the initial analysis of the optical spectroscopy data. The process of fitting the stellar continuum and the gaseous emission lines, as well as the accompanying challenges, are detailed below. But first, let us arrange the individual spectra into a map.

The spectrum in one slit position in one $1''$ bin is called a spaxel (a spectrum pixel). The spaxels are combined into a map covering the region observed, the NGC7317 slit position is not part of this map due to its large separation from the rest ($27''$ from the $dx = 0$ position). Between each slit position there are $2''$ without observations, due to the $3''$ slit shifts, and to enable proper ratios of the maps and a complete image, the spectra are linearly interpolated to cover these empty areas between slits. This interpolation also ensures that proper line intensities are retained and the full picture can be analysed. However, it must be remembered that the interpolated areas may hide smaller features. Also to be remembered, as stated in Chapter 5.1, is that the observational setup was designed with special attention to ensure that the nucleus of all galaxies in the area would be covered by a slit and therefore, only extended regions, galactic disks between slits and similar are subjected to interpolation.

To obtain information about the stellar and gaseous components in the spectra I turned to the Penalized Pixel-Fitting method for the continuum emission and Python's curvefit for the gas emission lines. Note, that to ensure proper fitting and avoiding regions dominated by low signal-to-noise a flux threshold on the gas emission line fit and stellar continuum fit of a signal-to-noise ratio (SNR) of 2 has been applied to all fits.

### 5.3.1   The Stellar Continuum

Penalized Pixel-Fitting (pPXF) (Cappellari & Emsellem, 2004; Cappellari, 2017) is a tool for extracting the stellar kinematics from a galaxy spectrum by fitting the full spectrum at once. pPXF can also be adopted for stellar population and gas emission line fitting. For the stellar kinematics the software uses a maximum penalized likelihood approach to fit the absorption line spectra using stellar templates. The stellar templates used in this thesis are from the MILES stellar template library (Sánchez-Blázquez et al., 2006; Vazdekis et al., 2010; Falcón-Barroso et al., 2011). This library contains 985 well-calibrated stars in the wavelength range 3525-7500Å at a spectral resolution of 2.51Å, R$\sim$2000. During the fitting process, pPXF optimises $\sim 10 - 20$ stellar templates that together fits the spectrum with the highest accuracy. Local extinction is accounted for in a pPXF built-in function as a reddening component in the spectral fit.

An illustrattion of the method of pPXF is shown in Fig.5.5. In this figure the reader can see the spectra of two of the galaxies contained within the SQ map, and the pPXF fit to these spectra. The grey vertical stripes are the regions blocked out from the continuum fit, since these are the wavelengths of possible gaseous emission lines. The red line is the continuum fit and the bottom green+blue line is the resultant continuum subtracted spectrum. By fitting the spectra in this manner in

the whole SQ mapped area, the stellar velocity dispersions and line-of-sight velocities of the stellar component are obtained as a function of position.
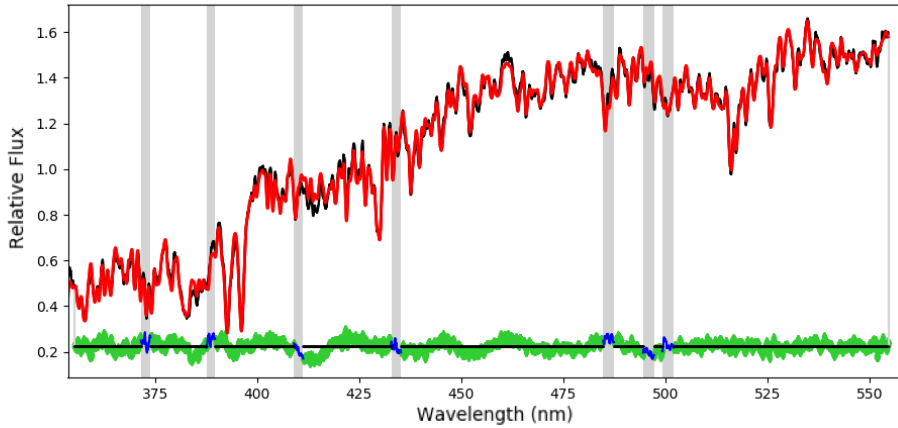


**(a)**
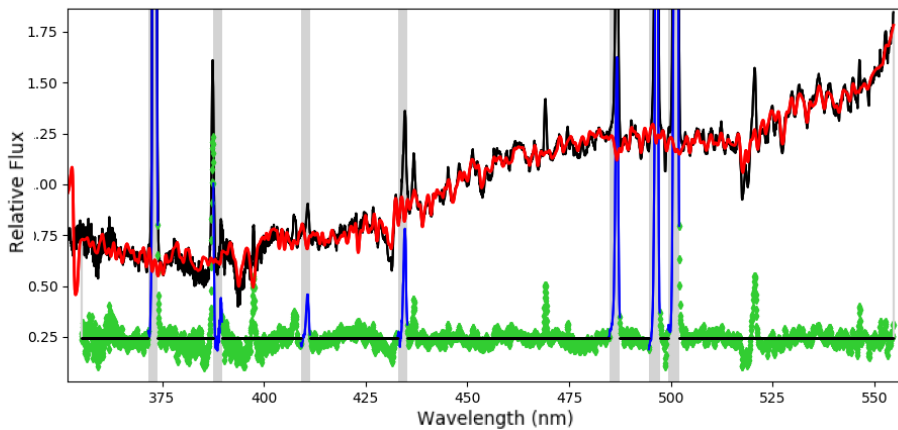


**(b)**

**Figure 5.5:** Two examples of the continuum fit with pPXF chosen from the observed SQ region. The grey vertical stripes block out gas emission lines from the continuum fit, the red line is the pPXF fit, the green+blue line is the resultant continuum subtracted spectrum. (a) The quiescent galaxy NGC7318B; (b) The active galaxy NGC7319.

## 5.3.2   The Gas Emission Lines

To be able to analyse the gas kinematics, information of the gaseous emission lines must be obtained, such as fluxes, velocity dispersions and line-of-sight velocities. The gas emission lines are fitted using manually defined multiple-Gaussian functions and Python's SciPy curvefit optimization module. Two examples of such a fitting are shown in Fig.5.6 for the NGC7319 nucleus. To the left, i.e., Fig.5.6a, the H$\beta\lambda4862.68$ and [OIII]$\lambda4932.603, 4960.295, 5008.240$ lines are shown, having been fitted with a five component Gaussian function, ensuring agreeing velocity dispersion and fixed

distances, $\Delta\lambda$, between the [OIII] lines. The fifth Gaussian is the BLR H$\beta$, however the H$\beta$ is quite weak in this spectrum so distinguishing the NLR and BLR of the H$\beta$ is not possible. Fig.5.6b shows the H$\alpha\lambda6564.61$ - [NII]$\lambda6549.86, 6585.27$ complex, fitted with a four component Gaussian function. As for the [OIII] lines, the velocity dispersions and line-of-sight velocities of the [NII] lines have been confined by the requirement that the velocity dispersions of both [NII] lines must agree and the $\Delta\lambda$ must remain constant, i.e. both lines must shift equally due to the Doppler effect.

The example, shown in Fig.5.6, covers the nucleus of the active galaxy NGC7319, therefore there is a broad H$\alpha$ component present, in the other parts of the observed area this is not the case since a BLR requires the presence of an AGN. There is broadening of lines in other regions of the observed area as well, however, this broadening is caused by a multiple of velocity components and in many cases dual velocity components can be fitted to the spectrum.



**(a)**                                                    **(b)**
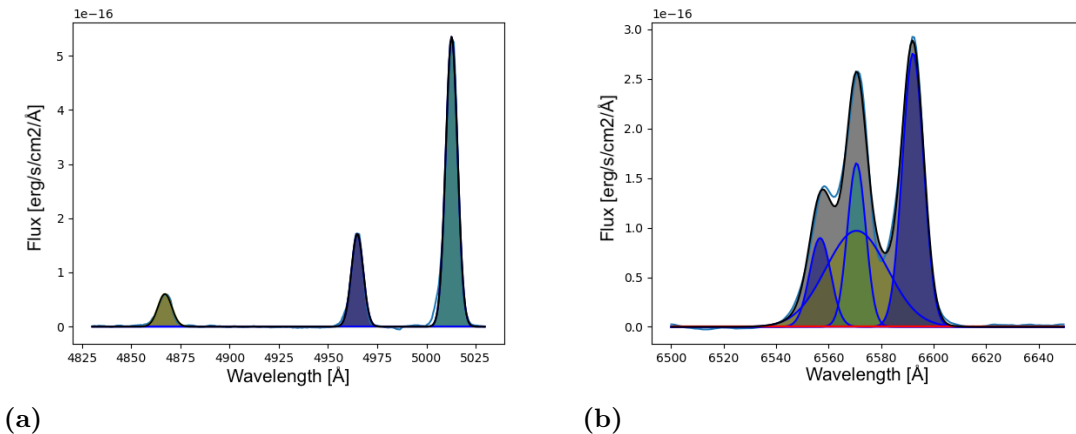
**Figure 5.6:** Examples of the gas emission line fits using Python's curvefit and manually defined multiple-Gaussian functions. (a) The fit of the H$\beta\lambda4862.68$ and [OIII]$\lambda4932.603, 4960.295, 5008.240$ lines; (b) The fit of the H$\alpha\lambda6564.61$ and [NII]$\lambda6549.86, 6585.27$ lines.

### 5.3.3   Particularly Challenging Aspects

Stephan's Quintet presented particular difficulties with the large amounts of extended emission and variations across the observed area. Due to the large variations, finding one algorithm that worked satisfactorily across the entire map was an immense challenge. Fitting each spectrum by hand was not feasible either, since the observed mapped area provided 200 spectra per slit for MODS Red and MODS Blue respectively, and for 7 slits this results in 2800 spectra. The additional slit position covering NGC7317, adds another 80, 40 MODS Red and 40 MODS Blue, which puts us at a total of 2880 spectra to fit.

The extended regions, in particular, often show weak or non-existent gas emission lines, or certain lines and not others - i.e., no general restrictions can be put on which lines are present and which are not. The large variations in line-of-sight velocity

cause an additional issue. The line-of-sight velocities in SQ spans 1000km/s, and this is of course reflected in the large shifts of the emission lines across the different regions of the mapped area. To be able to fit all regions properly strict region-specific restrictions on the fitting parameters must be adopted. The validity of the gas emission line and stellar continuum fits have been checked in a number of handpicked regions covering the end points and middle of the line-of-sight velocity range. The gas emission line fits have also been checked in regions covering high emission, low emission and lack of emission, while the stellar continuum fits have been checked in the case of high, low and absence of stellar continuum.

In addition, there are several regions with multiple velocity components. Several regions in the star-forming ridge show clear dual velocity components, while certain regions in NGC7319 also indicate the presence of dual velocities. To ensure proper fitting of the dual velocity components, additional limitations must be put on some of the fitting parameters. The lines that require additional restrictions are [NII] and [SII] due to their nested aspects. Osterbrock & Ferland (2006) provide expected ranges for the ratios between several atomic transitions, and in the case of the SQ regions with dual velocity components the average values of these ratios have been adopted as a pre-condition for the fit. The reason the average values can be chosen here lies in the fact that the main focus is on the kinematics and the velocities of these different components, and the slight increase in uncertainty this introduces does not decrease the effect and robustness of the subsequent kinematic analysis. The line ratios adopted are $[NII]\lambda 6585.27/6549.86 = 3$ and $[SII]\lambda 6732.67/3718.29 = 1.3$. Fig.5.7 shows a region in the star-forming ridge with clear dual velocity components and how they were fitted. More details of different regions with dual velocity components are presented and discussed in Chapter 6.



(a)                                    (b)
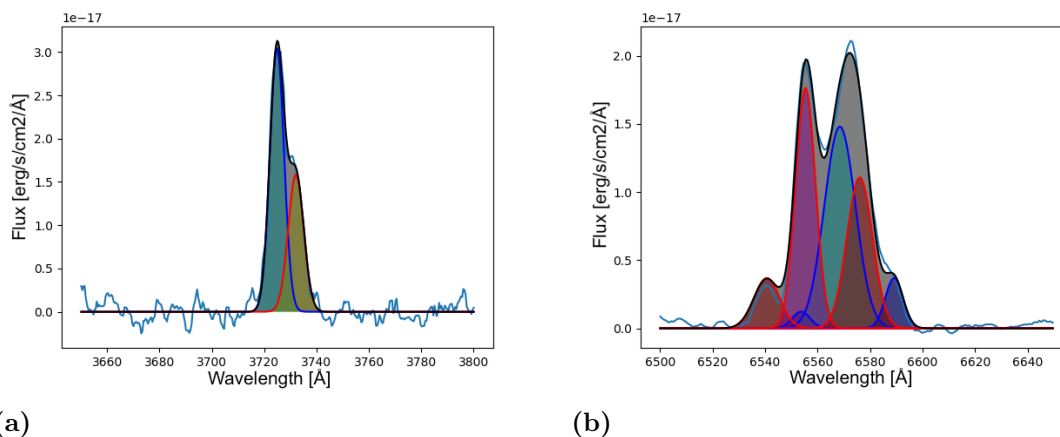
**Figure 5.7:** Example of the dual velocity components in the gas emission lines of region SF_2. The lines have been fitted using Python's curvefit and manually defined Gaussian functions with multiple emission lines. (a) The dual velocity components of the $[OII]\lambda 3727.092$ line; (b) The fit of the dual velocity components of the $H\alpha\lambda 6564.61$-$[NII]\lambda 6549.86, 6585.27$ complex, where the [NII] line ratio has been set to 3. The Gaussians shaded in red belong to one velocity component, while the ones shaded in blue belong to the other.

# 6

# Results & Discussion

This chapter details the results of the analysis of the optical spectroscopy data obtained with the Large Binocular Telescope, as explained in the previous chapter. The chapter is split into four main parts: the active galaxy NGC7319, the star-forming ridge, the NGC7318 pair and NGC7317. The "bridge", connecting NGC7319 and the NGC7318 pair, is discussed as a sub-chapter of NGC7319, and the "west ridge" is a sub-chapter of the star-forming ridge. The west ridge is the notation adopted for the emitting area to the southwest of the NGC7318 pair, which is at the top in Fig.6.1, the regions marked SF_12-15 are considered part of the area deemed the west ridge in this thesis. The regions marked in Fig.6.1 are $1.5''$ radii circles of summed spectra chosen for closer analysis. 32 such positions have been chosen as pinpointed in Fig.6.1.

Full maps of the fluxes, line-of-sight velocities and/or velocity dispersions of the galaxies are presented whenever suitable, considering noise and presence of emission. The orientation of presented maps are in agreement to the orientation of the observed area as showed in Fig.5.1 and 6.1, i.e., north in the maps is rotated 118° in mathematically positive direction from what is seen as "up" in the maps presented in this thesis. Furthermore, this chapter details the excitation mechanisms and the kinematics in each area, as well as a discussion of the multiple velocity components present.
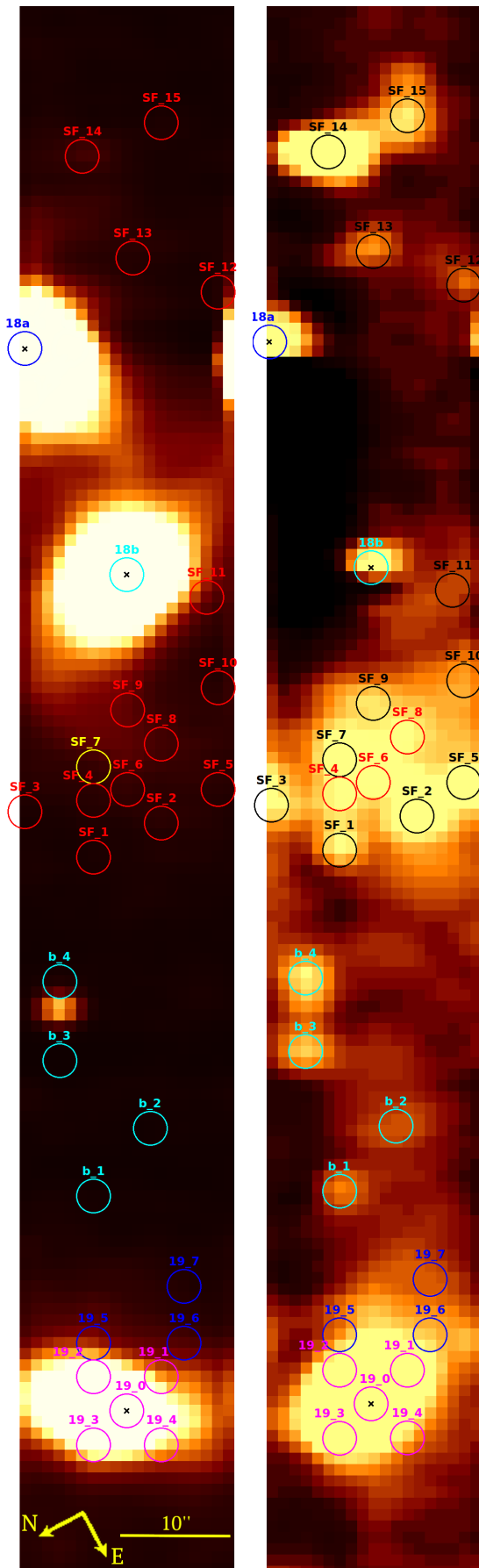
**Figure 6.1:**
*Left:* The regions picked for closer analysis shown on a stellar continuum image constructed from the LBT data;
*Middle:* The regions picked for closer analysis shown on an image of the emission of the $H\alpha - [NII]$ complex observed with the LBT, which provides the basis of the choice of regions;
*Below:* The area encompassed in the two images to the left is marked on a Subaru telescope and Hubble Space Telescope WFC3 composite colour image (based on the image processed by Robert Gendler and Judy Schmidt). 7 slits construct the rectangular area, included here is the single slit to the right which covers NGC7317.
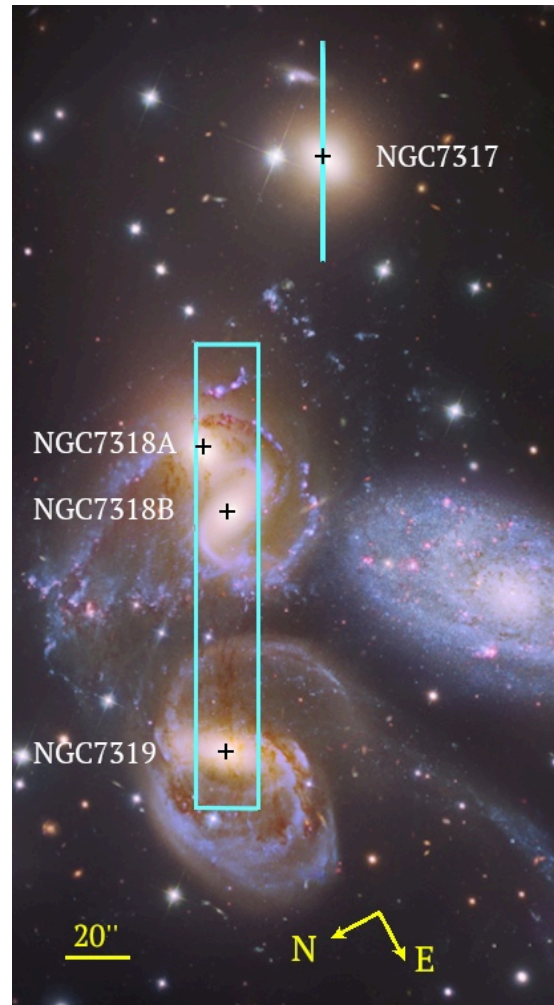
# 6.1 The Active Galaxy NGC7319

NGC7319 is the only confirmed active galaxy in SQ, displaying a large-scale bar and an outflow (Aoki et al., 1996; Rodríguez-Baras et al., 2014). This chapter begins by presenting the gas emission line fluxes, and the gas and stellar line-of-sight velocities and velocity dispersions as functions of position in NGC7319. Thereafter an analysis and discussion of the kinematics and the outflow follow, including details of the excitation mechanisms. The chapter finishes with an analysis of the kinematics and excitation mechanisms in the bridge.

## 6.1.1 Maps & Spectra

Let us begin by studying Fig.6.2-6.9. These figures show the stellar continuum as well as the continuum-subtracted line-emission maps of the gaseous atomic species: [OII]$\lambda$3727, H$\beta$, [OIII]$\lambda$5008, [OI]$\lambda$6302, H$\alpha$, [NII]$\lambda$6585 and [SII]$\lambda$6716,6732. The flux, line-of-sight velocities and velocity dispersions of the NGC7319 area are displayed as a function of position, with a cross marking the centre of NGC7319, i.e., the peak continuum emission of the galaxy. For the sake of the maps, no dual velocity components are allowed in the fit, a broader velocity dispersion might be the result. Contrary to H$\alpha$, only 1 velocity component has been fitted to H$\beta$ as the H$\beta$ is too weak to warrant BLR and NLR fitting simultaneously.

Dual velocity components are, however, adopted into the fitting of the individual regions, 19_0-7 as marked in Fig.6.1. The spectra of these regions are displayed in Fig.6.10-6.17. Vertical dotted lines mark different gas emission lines, at the group average redshift $z = 0.0215$, as the spectra are also corrected to this redshift. Note the strong emission lines and the weak continuum emission/absorption features. The values obtained in the fitting of the continuum and emission features of these spectra are presented in the table in Fig.6.19 and 6.20, the number of velocity components are chosen as the spectra requires.



**(a)**          **(b)**          **(c)**
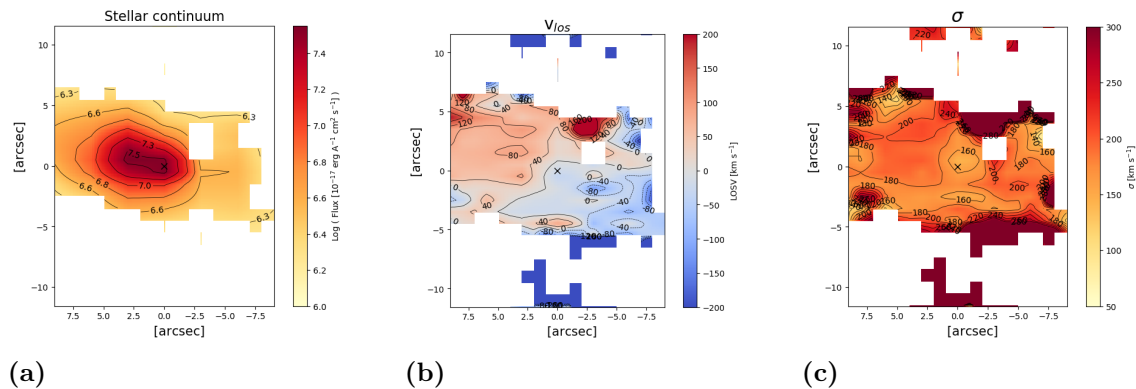
**Figure 6.2:** Stellar continuum in NGC7319. Map orientation as in Fig.6.1. (a) Integrated stellar continuum emission; (b) Line-of-sight velocity; (c) Velocity dispersion.

**(a)**　　　　　　　　　**(b)**　　　　　　　　　**(c)**
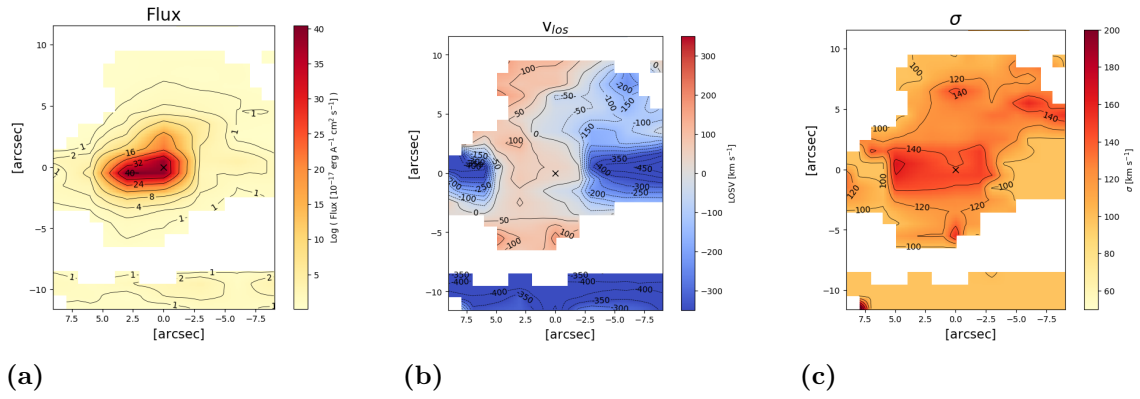
**Figure 6.3:** [OII]$\lambda$3727 emission in NGC7319. (a) Flux; (b) Line-of-sight velocity; (c) Velocity dispersion.
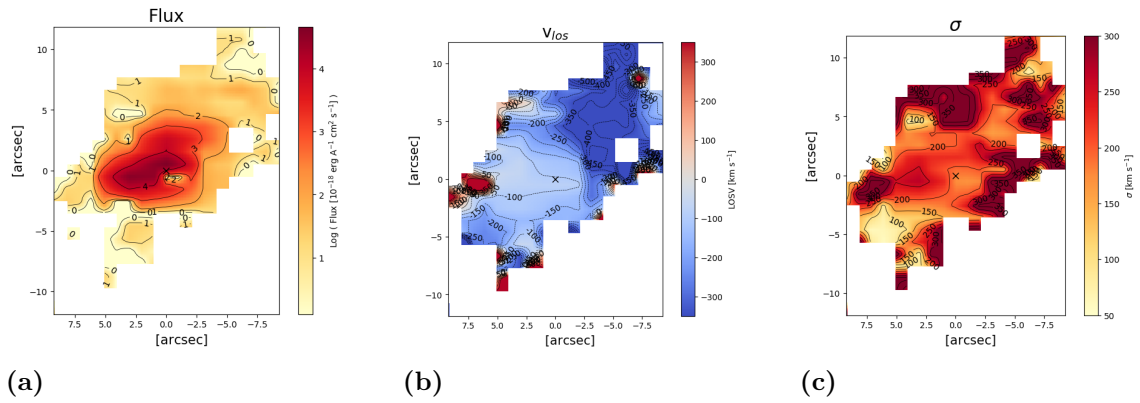


**(a)**　　　　　　　　　**(b)**　　　　　　　　　**(c)**

**Figure 6.4:** H$\beta$ NLR emisison in NGC7319. (a) Flux; (b) Line-of-sight velocity; (c) Velocity dispersion.



**(a)**　　　　　　　　　**(b)**　　　　　　　　　**(c)**
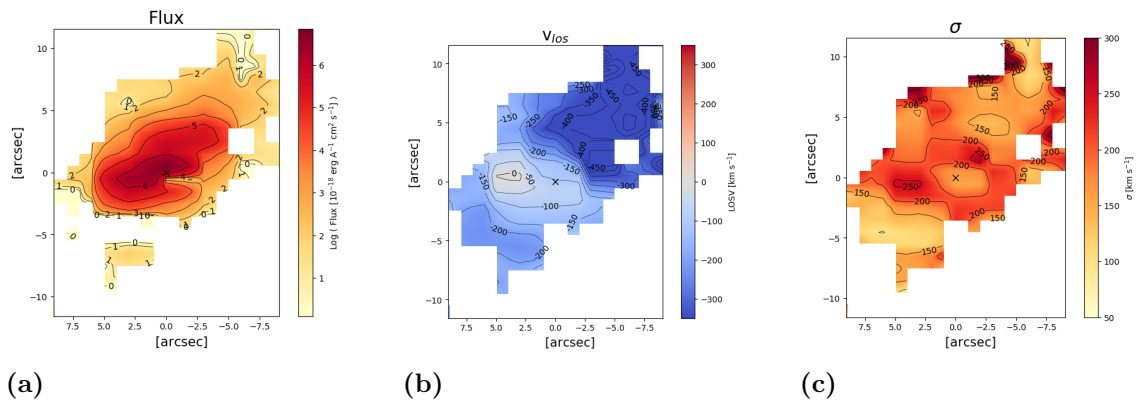
**Figure 6.5:** [OIII]$\lambda$5008 emission in NGC7319. (a) Flux; (b) Line-of-sight velocity; (c) Velocity dispersion.
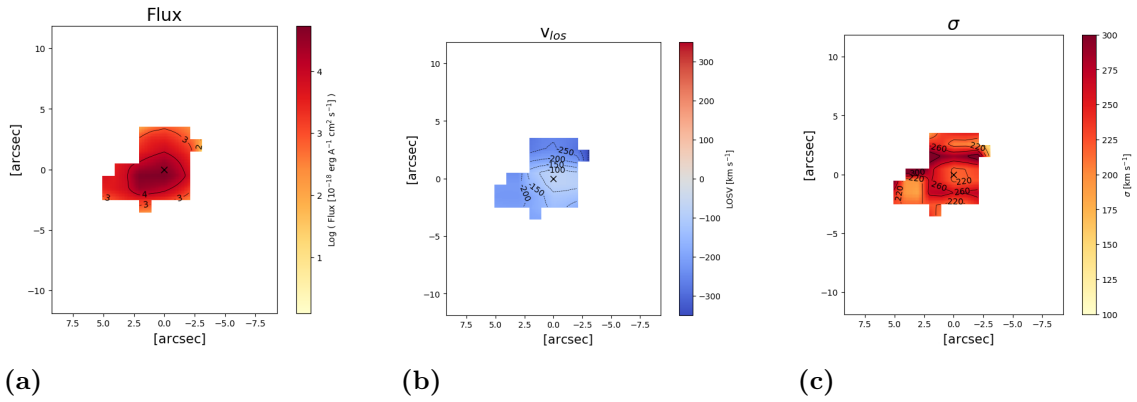
**Figure 6.6:** [OI]$\lambda$6302 emission in NGC7319. (a) Flux; (b) Line-of-sight velocity; (c) Velocity dispersion.
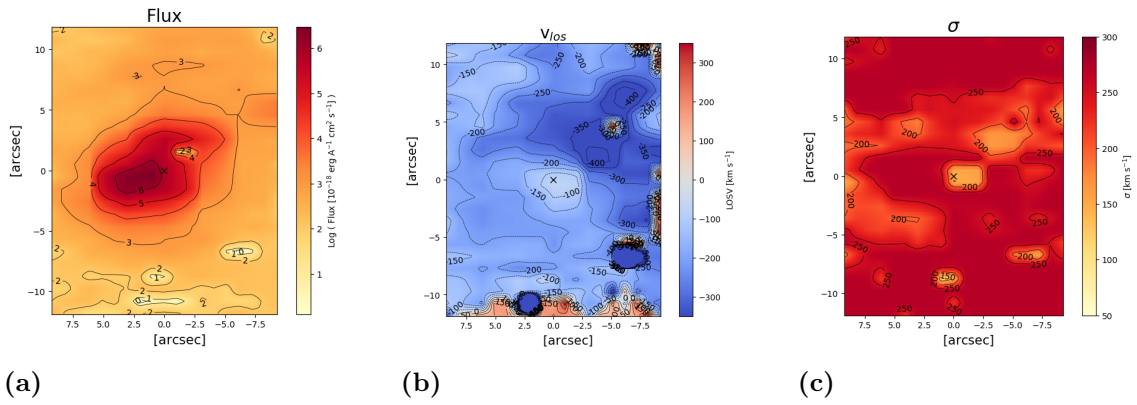


**Figure 6.7:** H$\alpha$ NLR emission in NGC7319. (a) Flux; (b) Line-of-sight velocity; (c) Velocity dispersion.
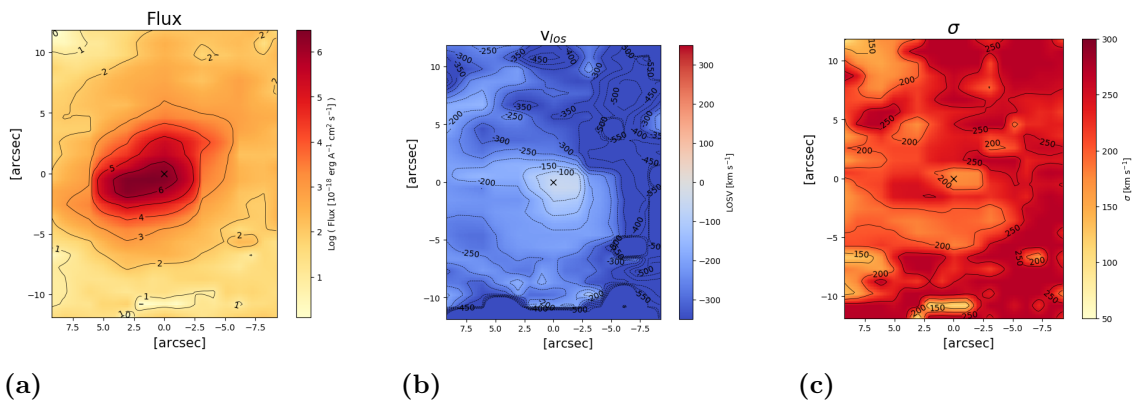


**Figure 6.8:** [NII]$\lambda$6585 emission in NGC7319. (a) Flux; (b) Line-of-sight velocity; (c) Velocity dispersion.

75
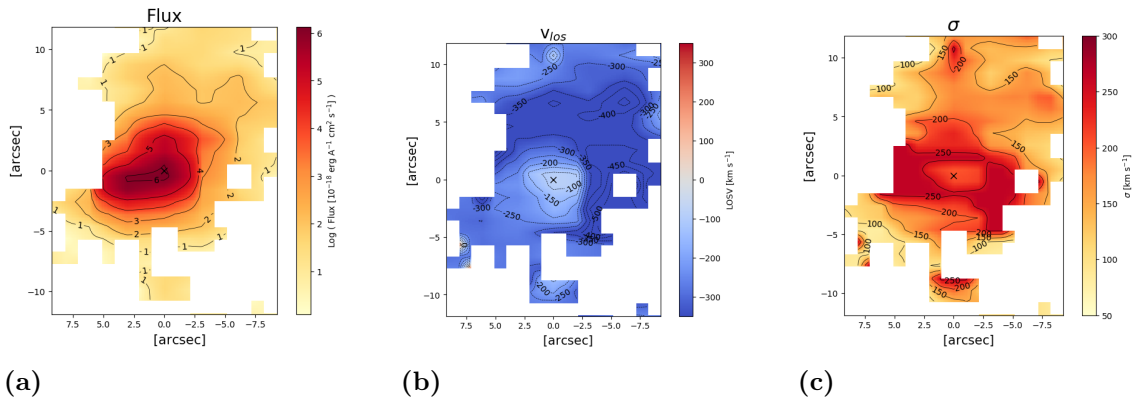
**Figure 6.9:** [SII]$\lambda$6718,6732 emission in NGC7319. (a) Flux; (b) Line-of-sight velocity; (c) Velocity dispersion.
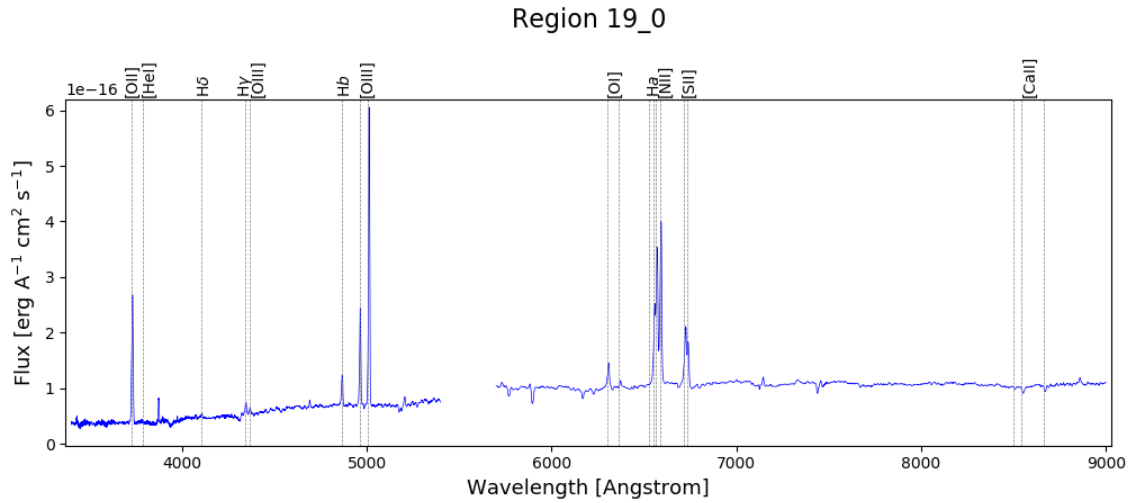


**Figure 6.10:** Spectrum of region 19_0. Vertical dotted lines mark the expected line centres of different gas emission lines at the group average redshift of 0.0215, the spectrum is also corrected to this average redshift.
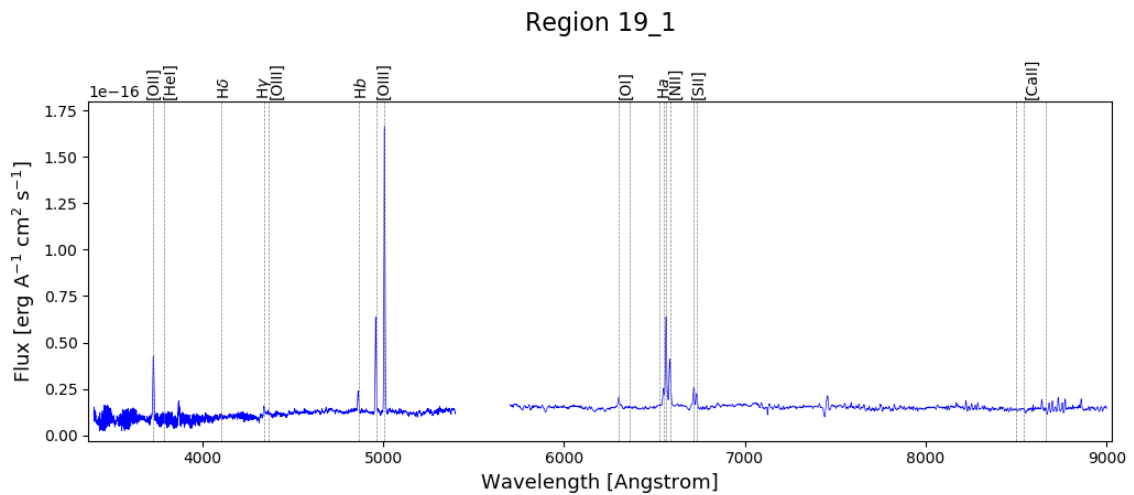


**Figure 6.11:** Same as Fig.6.10 but for region 19_1.
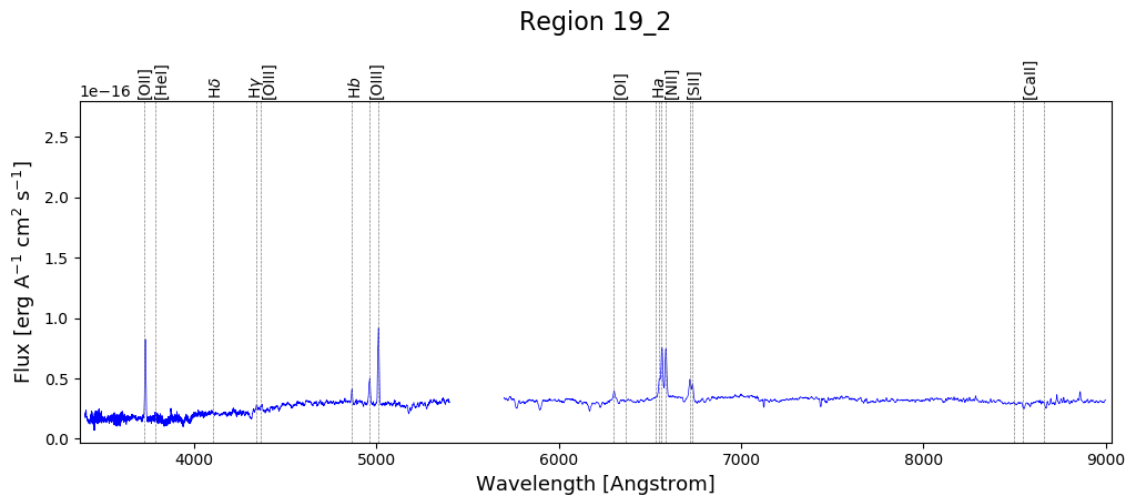
**Figure 6.12:** Same as Fig.6.10 but for region 19_2.
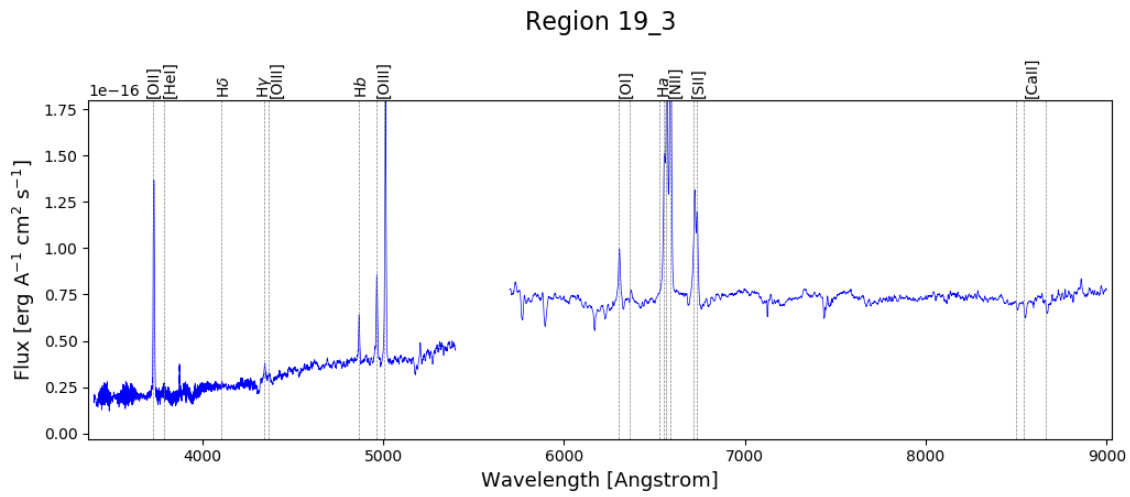


**Figure 6.13:** Same as Fig.6.10 but for region 19_3.
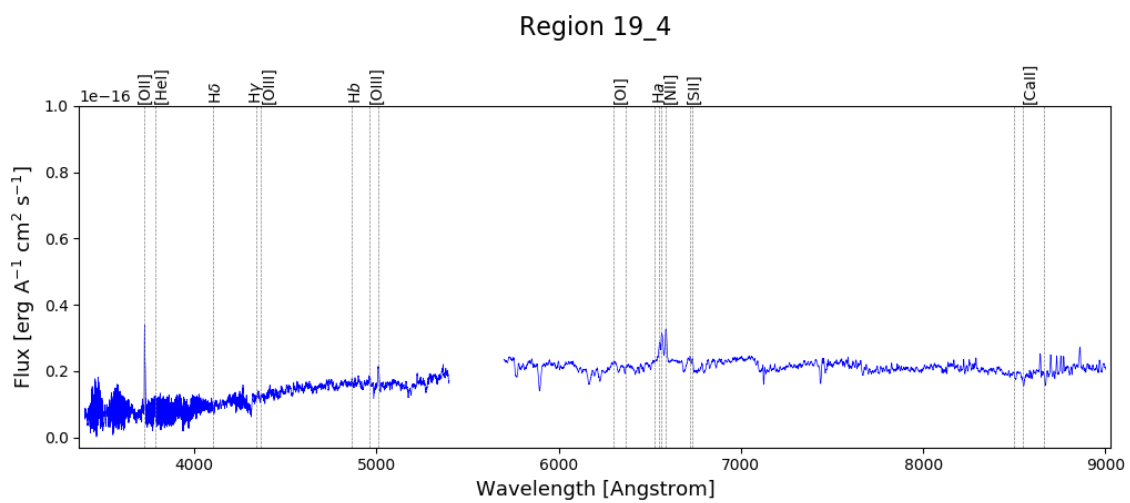


**Figure 6.14:** Same as Fig.6.10 but for region 19_4.
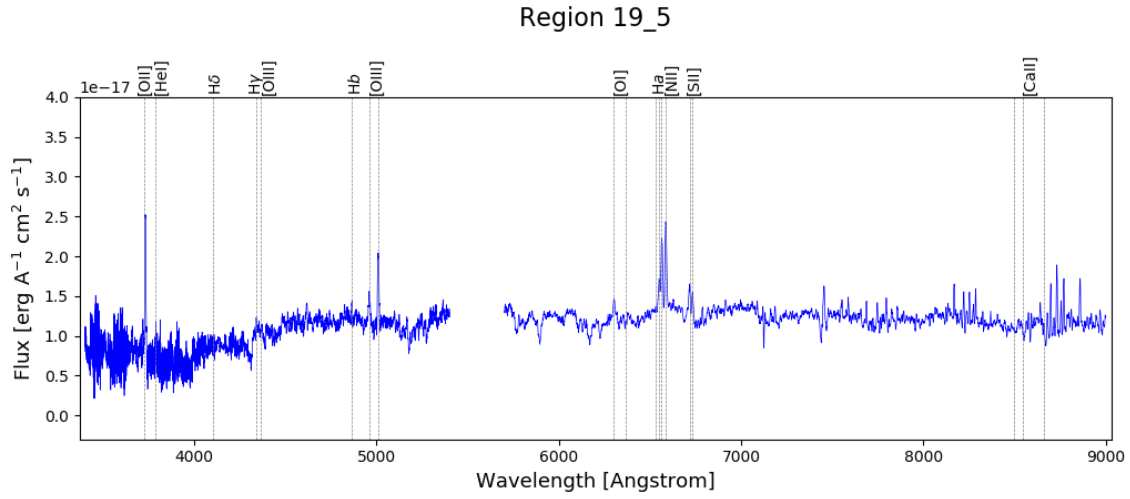
**Figure 6.15:** Same as Fig.6.10 but for region 19_5.
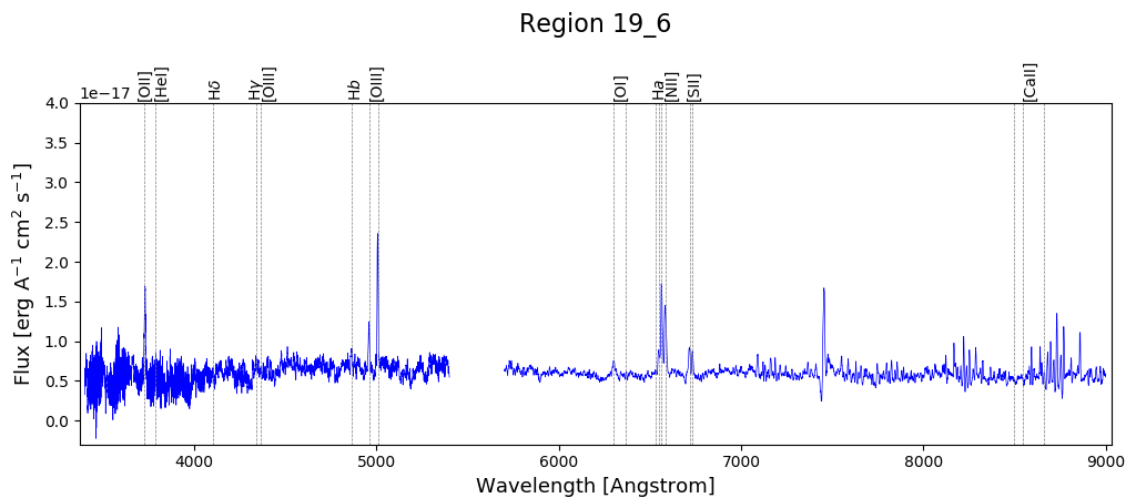


**Figure 6.16:** Same as Fig.6.10 but for region 19_6.
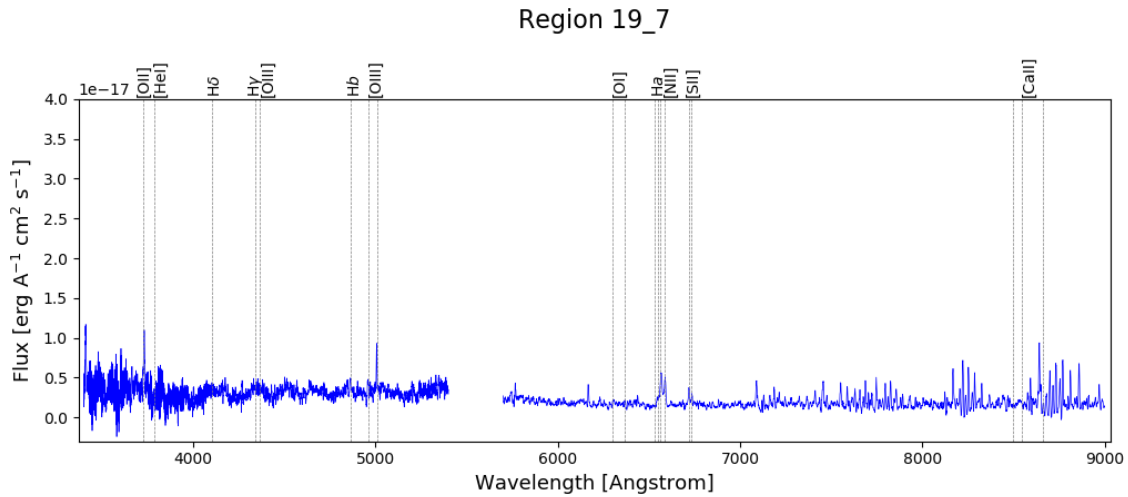
**Figure 6.17:** Same as Fig.6.10 but for region 19_7.

NGC7319 is classified as a Seyfert 2 galaxy, stating the absence of BLR emission. However a broad velocity component of Hα is required to achieve a good fit in the nuclear region, which Fig.6.18 illustrates with the fit of the Hα−[NII] complex at the galaxy's centre. Osterbrock & Ferland (2006) detail a subdivision of the Seyfert classification into Seyfert 1.5, 1.8 and 1.9, where a Seyfert 1.9 displays a weak broad component in the Hα line and not in higher-order Balmer lines, a Seyfert 1.8 shows weak broad components in both Hα as well as Hβ and in a Seyfert 1.5 the NLR and BLR emission lines are comparable. Indicating that the NGC7319 nucleus should be reclassified as a Seyfert 1.9, as a BLR cannot be distinguished in the Hβ line. However, the Hα BLR is not particularly weak and the Hβ suffers from extinction, deeper observations and a good correction for extinction is likely to reveal a different subclassification.
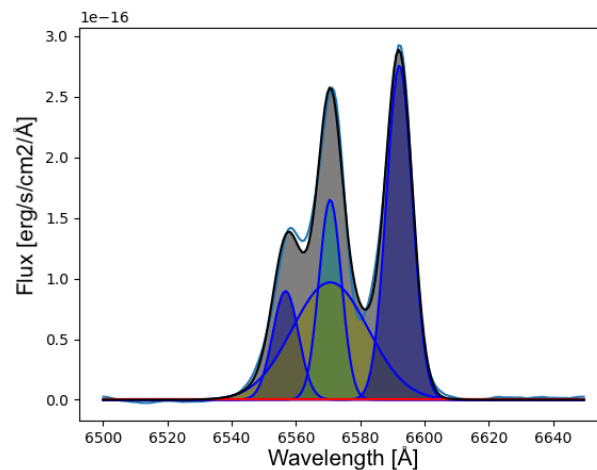


**Figure 6.18:** The fit of the Hα−[NII] emission from the central 1.5" of NGC7319 (region 19_0).

| | Vel comp | | Region 19_0 | 19_1 | 19_2 | 19_3 |
|---|---|---|---|---|---|---|
| Hß_NLR | high | Flux | 5.28E-16 ± 2.54E-17 | 8.98E-17 ± 7.99E-18 | 1.13E-16 ± 5.76E-18 | 2.19E-16 ± 8.56E-18 |
| | | Vlos | 6708.6 ± 8.7 | 6393.5 ± 14.7 | 6642.2 ± 8.6 | 6703.5 ± 6.6 |
| | | Vel.Disp | 211.1 ± 8.7 | 192.4 ± 14.7 | 195.8 ± 8.6 | 197.1 ± 6.6 |
| | low | Flux | - | - | - | - |
| | | Vlos | - | - | - | - |
| | | Vel.Disp | - | - | - | - |
| Hα_BLR | high | Flux | 2.86E-15 ± 1.24E-16 | - | - | - |
| | | Vlos | 6713.7 ± 2.2 | - | - | - |
| | | Vel.Disp | 537.2 ± 18.2 | - | - | - |
| Hα_NLR | high | Flux | 1.44E-15 ± 6.17E-17 | 4.80E-16 ± 5.51E-18 | 5.79E-16 ± 5.67E-18 | 2.01E-15 ± 2.36E-17 |
| | | Vlos | 6713.7 ± 2.2 | 6425.2 ± 1.6 | 6536.9 ± 1.8 | 6639.8 ± 2.3 |
| | | Vel.Disp | 159.0 ± 4.4 | 174.1 ± 1.7 | 233.0 ± 2.0 | 259.3 ± 2.6 |
| | low | Flux | - | - | - | - |
| | | Vlos | - | - | - | - |
| | | Vel.Disp | - | - | - | - |
| [NII] 6550 | high | Flux | 9.07E-16 ± 2.65E-17 | 1.01E-16 ± 3.06E-18 | 1.83E-16 ± 2.91E-18 | 9.02E-16 ± 1.21E-17 |
| | | Vlos | 6753.9 ± 1.7 | 6414.4 ± 38.5 | 6547.6 ± 36.1 | 6622.3 ± 39.1 |
| | | Vel.Disp | 184.8 ± 2.0 | 220.6 ± 3.5 | 227.2 ± 1.9 | 235.1 ± 1.8 |
| | low | Flux | - | - | - | - |
| | | Vlos | - | - | - | - |
| | | Vel.Disp | - | - | - | - |
| [NII] 6585 | high | Flux | 2.79E-15 ± 4.05E-17 | 3.14E-16 ± 5.81E-18 | 5.06E-16    4.93E-18 | 2.10E-15 ± 1.91E-17 |
| | | Vlos | 6752.2 ± 1.7 | 6414.6 ± 3.3 | 6547.0    1.8 | 6621.3 ± 1.7 |
| | | Vel.Disp | 183.8 ± 2.0 | 219.4 ± 3.5 | 226.0    1.9 | 233.8 ± 1.8 |
| | low | Flux | - | - | - | - |
| | | Vlos | - | - | - | - |
| | | Vel.Disp | - | - | - | - |
| [OI] 6302 | high | Flux | 5.98E-16 ± 1.52E-17 | 7.75E-17 ± 4.85E-18 | 1.36E-16 ± 6.78E-18 | 4.10E-16 ± 1.27E-17 |
| | | Vlos | 6728.9 ± 4.8 | 6496.8 ± 12.1 | 6566.0 ± 9.5 | 6640.9 ± 5.8 |
| | | Vel.Disp | 234.6 ± 5.1 | 234.6 ± 12.5 | 234.6 ± 10.1 | 234.6 ± 6.2 |
| | low | Flux | 1.13E-16 ± 1.53E-17 | 2.24E-17 ± 4.66E-18 | 4.98E-17 ± 6.49E-18 | 9.64E-17 ± 1.24E-17 |
| | | Vlos | 5837.6 ± 25.6 | 5720.3 ± 39.7 | 5685.8 ± 24.6 | 5811.1 ± 24.3 |
| | | Vel.Disp | 234.6 ± 27.3 | 234.6 ± 41.2 | 234.6 ± 26.1 | 234.6 ± 25.9 |
| [OII] 3727 | low | Flux | 2.11E-15 ± 2.33E-17 | 2.67E-16 ± 4.06E-18 | 4.80E-16 ± 3.45E-18 | 1.00E-15 ± 8.72E-18 |
| | | Vlos | 6843.5 ± 2.8 | 6660.1 ± 3.1 | 6842.1 ± 1.4 | 6846.8 ± 2.0 |
| | | Vel.Disp | 293.7 ± 2.8 | 241.0 ± 3.1 | 227.8 ± 1.4 | 266.8 ± 2.0 |
| [OIII] 5008 | high | Flux | 4.02E-15 ± 2.30E-17 | 1.05E-15 ± 7.42E-18 | 5.79E-16 ± 5.93E-18 | 1.23E-15 ± 8.54E-18 |
| | | Vlos | 6711.5 ± 0.8 | 6389.9 ± 1.0 | 6596.6 ± 1.8 | 6717.8 ± 1.2 |
| | | Vel.Disp | 174.1 ± 0.8 | 167.0 ± 1.0 | 211.7 ± 1.8 | 201.3 ± 1.2 |
| | low | Flux | - | - | - | - |
| | | Vlos | - | - | - | - |
| | | Vel.Disp | - | - | - | - |
| [SII] 6718 | high | Flux | 1.32E-15 ± 2.49E-17 | 1.01E-16 ± 2.55E-18 | 2.15E-16 ± 5.49E-18 | 7.85E-16 ± 1.68E-17 |
| | | Vlos | 6716.2 ± 4.8 | 6416.5 ± 4.1 | 6493.6 ± 6.4 | 6584.6 ± 6.2 |
| | | Vel.Disp | 226.0 ± 3.5 | 161.9 ± 3.3 | 220.0 ± 4.6 | 250.5 ± 4.5 |
| | low | Flux | - | - | - | - |
| | | Vlos | - | - | - | - |
| | | Vel.Disp | - | - | - | - |
| [SII] 6732 | high | Flux | 9.11E-16 ± 1.94E-17 | 7.49E-17 ± 2.11E-18 | 1.65E-16 ± 4.60E-18 | 6.07E-16 ± 1.41E-17 |
| | | Vlos | 6715.6 ± 4.8 | 6416.5 ± 4.0 | 6493.5 ± 6.4 | 6584.3 ± 6.2 |
| | | Vel.Disp | 225.5 ± 3.5 | 161.5 ± 3.3 | 219.6 ± 4.6 | 250.0 ± 4.5 |
| | low | Flux | - | - | - | - |
| | | Vlos | - | - | - | - |
| | | Vel.Disp | - | - | - | - |
| stellar | | Vlos | 6813.7 ± 12.2 | 6919.6 ± 54.3 | 6882.0 ± 18.1 | 6809.0 ± 15.9 |
| | | Vel.Disp | 159.4 ± 13.0 | 402.9 ± 56.5 | 205.7 ± 19.9 | 172.9 ± 15.6 |

**Figure 6.19:** Table containing the flux in $ergcm^2s^{-1}$, line-of-sight velocity and velocity dispersion in km/s, of each atomic species, as well as the stellar component, in region 19_0-3 marked in Fig.6.1.

| | Vel comp | | 19_4 | 19_5 | 19_6 | 19_7 |
|---|---|---|---|---|---|---|
| Hß_NLR | high | Flux | 2.22E-17 ± 5.42E-18 | 1.75E-17 ± 4.50E-18 | 1.11E-17 ± 3.17E-18 | - |
| | | Vlos | 7501.6 ± 58.7 | 7501.6 ± 61.8 | 7501.6 ± 43.4 | - |
| | | Vel.Disp | 305.1 ± 64.6 | 305.1 ± 68.1 | 178.6 ± 44.1 | - |
| | low | Flux | 2.64E-17 ± 4.29E-18 | 2.62E-17 ± 3.47E-18 | 3.99E-17 ± 3.97E-18 | 1.55E-17 ± 3.02E-18 |
| | | Vlos | 6595.7 ± 26.6 | 6622.0 ± 20.7 | 6450.0 ± 24.1 | 6443.6 ± 34.7 |
| | | Vel.Disp | 196.7 ± 27.2 | 187.4 ± 21.0 | 290.4 ± 24.8 | 207.0 ± 34.7 |
| Hα_BLR | high | Flux | - | - | - | - |
| | | Vlos | - | - | - | - |
| | | Vel.Disp | - | - | - | - |
| Hα_NLR | high | Flux | 1.91E-16 ± 3.81E-18 | 1.63E-16 ± 3.38E-18 | 1.86E-16 ± 3.41E-18 | 1.26E-16 ± 7.75E-18 |
| | | Vlos | 6611.3 ± 3.9 | 6533.6 ± 3.8 | 6457.5 ± 3.3 | 6642.3 ± 13.0 |
| | | Vel.Disp | 250.8 ± 4.3 | 234.2 ± 4.2 | 232.6 ± 3.7 | 271.4 ± 11.5 |
| | low | Flux | - | - | - | 2.11E-17 ± 4.91E-18 |
| | | Vlos | - | - | - | 6279.5 ± 18.7 |
| | | Vel.Disp | - | - | - | 192.0 ± 15.5 |
| [NII] 6550 | high | Flux | 6.83E-17 ± 2.11E-18 | 4.95E-17 ± 1.64E-18 | 3.62E-17 ± 1.48E-18 | 8.50E-18 ± 1.06E-18 |
| | | Vlos | 6602.2 ± 74.9 | 6508.0 ± 80.0 | 6360.2 ± 74.7 | 6642.8 ± 13.0 |
| | | Vel.Disp | 219.4 ± 4.3 | 221.6 ± 3.9 | 245.5 ± 4.9 | 131.1 ± 9.0 |
| | low | Flux | - | - | - | 1.54E-17 ± 1.58E-18 |
| | | Vlos | - | - | - | 6279.1 ± 18.8 |
| | | Vel.Disp | - | - | - | 194.6 ± 14.2 |
| [NII] 6585 | high | Flux | 1.28E-16 ± 2.95E-18 | 1.45E-16 ± 2.97E-18 | 1.43E-16 ± 3.33E-18 | 2.55E-17 ± 1.96E-18 |
| | | Vlos | 6601.3 ± 4.0 | 6507.6 ± 3.6 | 6360.6 ± 4.4 | 6641.7 ± 12.9 |
| | | Vel.Disp | 218.2 ± 4.3 | 220.4 ± 3.9 | 244.2 ± 4.9 | 130.4 ± 8.9 |
| | low | Flux | - | - | - | 4.63E-17 ± 3.55E-18 |
| | | Vlos | - | - | - | 6280.0 ± 18.7 |
| | | Vel.Disp | - | - | - | 193.6 ± 14.1 |
| [OI] 6302 | high | Flux | 5.52E-17 ± 5.77E-18 | 4.96E-17 ± 4.13E-18 | 1.52E-17 ± 3.72E-18 | 1.26E-17 ± 2.39E-18 |
| | | Vlos | 6617.5 ± 19.9 | 6535.0 ± 15.9 | 7037.2 ± 50.4 | 6701.7 ± 36.1 |
| | | Vel.Disp | 234.6 ± 21.2 | 234.6 ± 16.8 | 234.6 ± 47.5 | 234.6 ± 38.4 |
| | low | Flux | 4.16E-17 ± 5.48E-18 | 2.43E-17 ± 4.01E-18 | 3.88E-17 ± 3.71E-18 | 1.04E-17 ± 2.37E-18 |
| | | Vlos | 5731.4 ± 24.9 | 5639.6 ± 31.4 | 6338.8 ± 19.7 | 5874.0 ± 43.1 |
| | | Vel.Disp | 234.6 ± 26.4 | 234.6 ± 33.3 | 234.6 ± 18.6 | 234.6 ± 45.8 |
| [OII] 3727 | low | Flux | 1.31E-16    5.31E-18 | 1.16E-16    3.53E-18 | 8.49E-17    4.00E-18 | 4.13E-17 ± 3.27E-18 |
| | | Vlos | 6666.4    6.5 | 6845.9    5.7 | 6700.8    10.8 | 6795.5 ± 13.3 |
| | | Vel.Disp | 185.0    6.5 | 217.1    5.7 | 267.6    10.8 | 194.9 ± 13.3 |
| [OIII] 5008 | high | Flux | 2.02E-17 ± 7.58E-18 | 6.73E-17 ± 1.21E-17 | 9.29E-17 ± 1.22E-17 | - |
| | | Vlos | 6871.7 ± 50.1 | 6616.8 ± 37.5 | 6337.3 ± 6.4 | - |
| | | Vel.Disp | 126.0 ± 34.1 | 181.7 ± 23.7 | 147.5 ± 9.3 | - |
| | low | Flux | 3.04E-17 ± 7.38E-18 | 1.95E-17 ± 9.15E-18 | 4.12E-17 ± 1.25E-17 | 2.94E-17 ± 2.44E-18 |
| | | Vlos | 6565.5 ± 31.3 | 6357.9 ± 15.7 | 6451.6 ± 61.9 | 6356.8 ± 8.7 |
| | | Vel.Disp | 124.9 ± 21.2 | 86.6 ± 21.1 | 296.2 ± 46.9 | 121.1 ± 8.7 |
| [SII] 6718 | high | Flux | 1.97E-17 ± 5.20E-18 | - | - | 1.79E-17 ± 1.01E-18 |
| | | Vlos | 6535.3 ± 27.8 | - | - | 6542.8 ± 8.0 |
| | | Vel.Disp | 112.7 ± 21.7 | - | - | 149.7 ± 6.8 |
| | low | Flux | 2.84E-17 ± 6.97E-18 | 2.58E-17 ± 2.78E-17 | 2.96E-17 ± 1.17E-17 | - |
| | | Vlos | 6130.5 ± 40.9 | 6350.4 ± 203.5 | 6360.7 ± 68.5 | - |
| | | Vel.Disp | 185.3 ± 38.1 | 152.9 ± 93.9 | 145.8 ± 37.3 | - |
| [SII] 6732 | high | Flux | 1.51E-17 ± 4.00E-18 | - | - | 1.25E-17 ± 8.03E-19 |
| | | Vlos | 6535.1 ± 27.7 | - | - | 6542.5 ± 8.0 |
| | | Vel.Disp | 112.5 ± 21.6 | - | - | 149.4 ± 6.8 |
| | low | Flux | 2.18E-17 ± 5.36E-18 | 1.99E-17 ± 2.14E-17 | 2.27E-17 ± 8.98E-18 | - |
| | | Vlos | 6131.1 ± 40.9 | 6350.6 ± 203.1 | 6360.8 ± 68.4 | - |
| | | Vel.Disp | 184.9 ± 38.0 | 152.5 ± 93.7 | 145.4 ± 37.2 | - |
| stellar | | Vlos | 6766.6 ± 25.1 | 6792.0 ± 42.8 | 6600.0 ± 61.8 | - |
| | | Vel.Disp | 183.2 ± 26.1 | 273.7 ± 36.4 | 390.4 ± 62.3 | - |

**Figure 6.20:** Continuation of the table in Fig.6.19, showing the values for region 19_4-7.

### 6.1.2   Kinematics & Rotation

While the stellar contribution is weak on the edges of the galaxy, in the centre clear absorption can be found, and the mean stellar line-of-sight velocity and velocity dispersion in the central 1.5" is $6813.7 \pm 12.2$ km/s and $159.4 \pm 13.0$ km/s, respectively. The values of regions further from the nucleus are listed in the table in Fig.6.19.

From studying the maps of the gas emission, Fig.6.3-6.9, the velocity dispersion displays an inclination to a lower value coinciding with the centre, surrounded by a ring of higher velocity dispersion. See for example the [OIII]$\lambda$5008 velocity dispersion in Fig.6.5c, where the ring is clear and then the velocity dispersion returns to lower values again along the direction of the outflow (towards the upper right in the maps). The velocity dispersion of H$\alpha$, Fig.6.7c, shows a lovely arch-like structure of lower velocity dispersion, approximately following the shape of the stellar bar, with a particularly low spot along the suspected outflow. To some extent the increased velocity dispersions coincide with an increase in the change of the line-of-sight velocities, confirming that the velocity dispersion measured is a combination of the actual velocity dispersion and the change in the velocity field within that spaxel.

In the velocity dispersion map of [OII]$\lambda$3727, Fig.6.3c, the two areas of lower velocity dispersion to the left and right of the nucleus, coincide with its blue-shifted line-of-sight velocity regions shown in Fig.6.3b. The line-of-sight velocity of [OII] differ from the shape of the other gaseous species in NGC7319, as [OII] favours the bar and nuclear regions. Further note that [OI]$\lambda$6302, in Fig.6.6, is distinctly concentrated around the galaxy's centre, while higher ionised oxygen and other gaseous species are more extended.

The centre of the galaxy is marked as the peak emission of the continuum, and the main portion of the continuum emission then extends to the north-west, i.e., the upper left in the images, of the nucleus of NGC7319. Whereas, the gaseous emission extends to the south-west and north-east, i.e., the upper right and lower left, as can be seen in Fig.6.21a, where the stellar continuum is overlaid with the contours of the [OIII] flux. The centre of the [OIII] velocity field coincides with the peak of its velocity dispersion. Thereafter, following the angle of the outflow, there are two regions of lower velocity dispersion, on each side of the velocity field centre. The other position of large velocity dispersion coincides with the area in which the line-of-sight velocity is the same as that of the stellar velocity field centre.

Furthermore, the centre of the gaseous velocity field is offset from that of the stellar component to the right and slightly up, to approximately $-3\Delta$RA and $+1\Delta$Dec. This shift is illustrated in Fig.6.21b, where the velocity field contours of the [OIII] line is overlaid on the stellar velocity field. The RA-shift is subjected to the interpolation between the slits and may be ambiguous, but the Dec-shift is however along the slit and in the $1''$ resolution. This offset of the stellar and gas centres is either due to extinction of the stellar continuum or displacement of the gas caused by the previous interactions.

Also note that the position angle of the stellar and gas fields are approximately perpendicular. This is the case for all gaseous velocity fields apart from that of the [OII]$\lambda$3727 line where the position angle of the velocity field of [OII], Fig.6.3b, appear to be somewhere in between that of the stellar field and the other gaseous species' field. In addition, the [OII] velocity field shows two positions of particularly
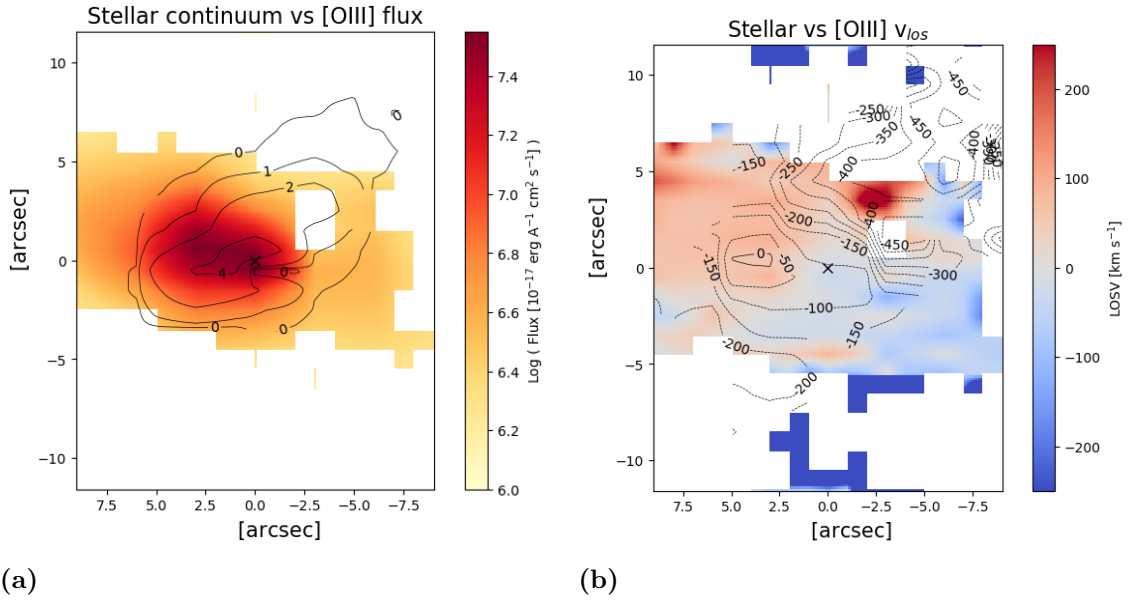
**Figure 6.21:** The discrepancy between the stellar and [OIII]$\lambda$5008 disks in NGC7319. (a) Integrated stellar continuum emission overlaid with integrated [OIII] emission line flux; (b) Stellar line-of-sight velocity in a blue-to-red colour map overlaid with [OIII] line-of-sight velocity contours.

blue-shifted line-of-sight velocity along the horizontal axis in the image. The H$\alpha$ and [NII] line-of-sight velocity maps in Fig.6.7b and 6.8b show a particularly beautiful bright upper path tracing an arm-like structure at a higher line-of-sight velocity than its surrounding, of $\gtrsim -200$ km/s.

The differences between the gaseous disk and the stellar disk may be interpreted as a highly disturbed galaxy where the gaseous disk has been pulled out of the stellar rotation plane by the previous interactions in the group and further follows the outflow. However, it is highly unlikely that such a large-scale disturbance would have left the stellar disk and bar intact, and without having significantly disturbed the galaxy morphology and stripped the galaxy from its gaseous content. The most likely interpretation is that what we are seeing here is ionised gas in the from of a nuclear or stellar wind.

A rotation field cannot be properly fitted to the stellar velocity field, Fig.6.2b, due to the peculiarities, in particular the high velocity blob at approximately $-3\Delta$RA and $+3\Delta$Dec.

### 6.1.3 The Outflow

An outflow in the south-west region of the nucleus was first reported by Aoki et al. (1996), and later followed by an IFS study presented in Boschetti et al. (2003); Di Mille et al. (2008). Whereas, 22GHz observations by Baek et al. (2019) reveled the absence of powerful nuclear radio jets. Aoki et al. (1996) reported outflow velocities of an average of 300km/s blue-shifted from the systematic velocity, and a max of 500km/s. We find a mean of $476.6 \pm 13.8$ km/s in the [OIII]$\lambda$5008 line blue-shifted from the systemic stellar line-of-sight velocity of the galaxy, in this region. How the [OIII] line-of-sight velocity relates to the stellar and the H$\alpha$ velocity fields is illustrated in Fig.6.22, where in (a) the stellar velocity field have been subtracted from the [OIII] velocity field, and in (b) it is the H$\alpha$ velocity field that has been subtracted from the [OIII] velocity field. As can be seen, the blue-shifted line-of-sight velocity in the area of the outflow is clear, while the [OIII]$-$H$\alpha$ map also shows a red-shifted line-of-sight velocity of the [OIII] line to the left (north-west) of the nucleus.



(a)          (b)
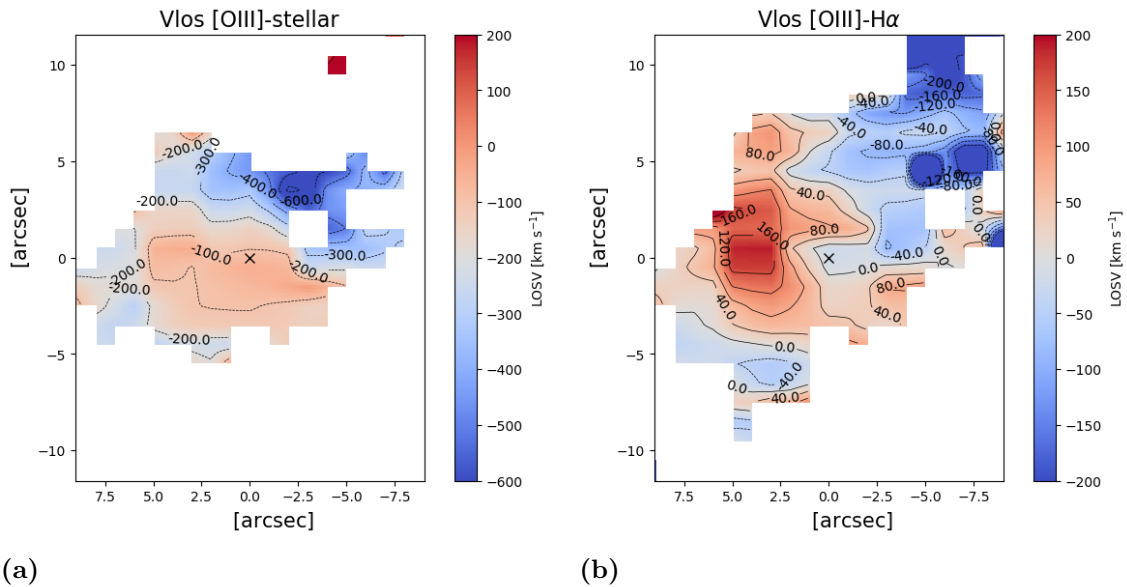
**Figure 6.22:** Illustrating how the [OIII]$\lambda$5008 velocity field relates to that of the stellar component as well as H$\alpha$. (a) The [OIII] velocity field subtracted by the stellar line-of-sight velocity field; (b) The [OIII] velocity field subtracted by the H$\alpha$ line-of-sight velocity field.

Rodríguez-Baras et al. (2014) have in their Fig.6 followed the outflow and plotted how the H$\alpha$$-$[NII] complex changes as we move further away from the nucleus. The data presented here, using the higher resolution of the LBT, confirms the H$\alpha$$-$[NII] ratio variations along the outflow. Of the 8 positions chosen near and in NGC7319 (as shown in Fig.6.1), it is clear that in position 19_1 (Fig.6.11) and 19_6 (Fig.6.16) the H$\alpha$ flux is distinctly higher than the [NII]$\lambda$6585 flux, which is contrary to the case at position 19_0 (Fig.6.10) and 19_5 (Fig.6.15). Exactly where the H$\alpha$ flux exceeds that of the NII$\lambda$6585 is illustrated in Fig.6.24a, where the logarithmic flux value of 0 denotes where the fluxes of [NII] and H$\alpha$ are equal, and positive red values

show where the [NII] flux exceeds that of Hα flux and negative blue values where Hα exceeds that of [NII].

Furthermore, the LBT data reveals dual velocity components in NGC7319. Fig.6.23 shows the most prominent positions of broadened/dual velocity components, and the shape of the [OIII]λ5008 line in these positions (positions have been chosen only on the slits, to ensure that the shape is not affected by the interpolation). While for the maps the line was fitted using a single but broadened component, it is clear that there are most likely multiple velocity components present, perhaps one tracing the outflow and one the disk or gas deposits from previous interactions.



(a)　　　　　　　　　　(b)　　　　　　　　　　(c)
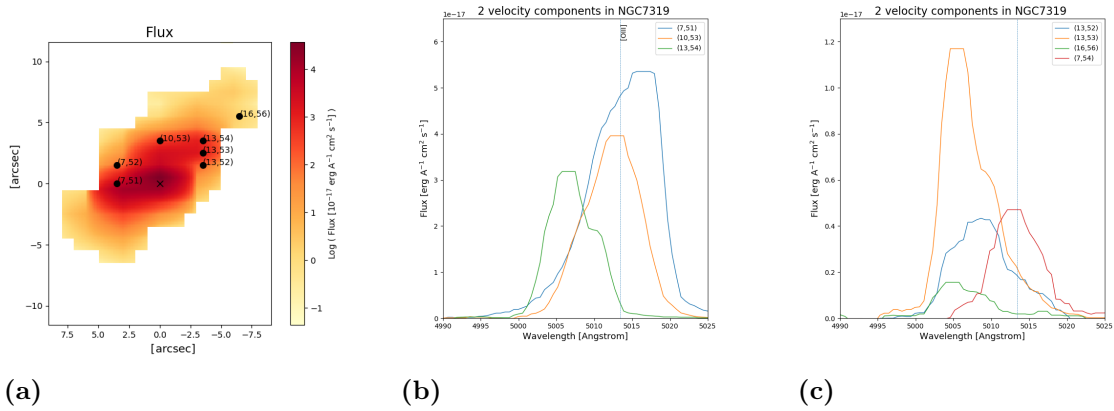
**Figure 6.23:** Showing the presence of multiple velocity components in NGC7319, via the shape of the [OIII]λ5008 line in several positions. (a) A selection of positions in which the spectrum shows clear broadening/multiple components in the [OIII] line; (b) and (c) The [OIII] line shape for the positions shown in (a), separated into two graphs due to amplitude differences.

As in Aoki et al. (1996), a red counterpart of the outflow is not detected, unless the whole gaseous disk is a bipolar outflow. It is possible that we are looking at off-nuclear star-forming regions or that we are looking down an outflow funnel, as traced by the strong emission of [OIII] in the direction of the outflow. It is unlikely that the increased line-of-sight velocity is a tidal effect, since the bar of NGC7319 remains undisturbed. The fact that the stellar and gaseous disks are near perpendicular to each other (Fig.6.21), indicates that the gas is the outflow/wind. Although a significant contribution from star formation cannot be excluded, it is possible that all of the gas constitutes a bipolar outflow, but the dual velocity components displayed in Fig.6.23 indicate that the gas is in more than one congregation.

### 6.1.4 Excitation Mechanisms using the BPT Diagnostic Diagrams

To deduce the mechanism behind the gas excitation we can utilise the emission line ratios introduced by Baldwin, Philips & Terlevich in 1981 and expanded upon by Veilleux & Osterbrock (1987), commonly called the BPT diagrams, as presented in Chapter 2.6.3, Eq.2.27-2.32. The [NII]/H$\alpha$, [SII]/H$\alpha$, [OI]/H$\alpha$ and [OIII]$\lambda$5008/H$\beta$ ratios are displayed in Fig.6.24 and 6.25. Temperature sensitive ratios such as the [OIII]$\lambda$5008/H$\beta$ ratio are particularly good indicators of shocked regions, as shocked gas can retain the high temperatures. As can be seen in Fig.6.25b, the higher ratio values trace the outflow/wind. In addition, a small area with an increase in the ratio values of [NII]/H$\alpha$, [SII]/H$\alpha$ as well as [OI]/H$\alpha$, is present along the outflow, approximately at a distance of 3" from the nucleus, coinciding with the centre of the gas velocity fields.

Region 19_0-6, marked in Fig.6.1, are placed the BPT diagnostic diagrams in Fig.6.26-6.28 (region 19_7 does not show sufficient emission for the BPT diagrams). Included is the BPT position for b_4, which is the only position in the bridge with sufficient emission to enable placing in the BPT diagrams, the bridge is discussed in the subsequent chapter. As can be seen the regions in NGC7319 are ionised by AGN/Seyfert radiation. 19_4 is the only region in NGC7319 that is deviating from this, this is most likely caused by the low emission in this region, being positioned out of the area of the outflow as well as being on the opposite side of the area of the disk attached to the tidal arms.
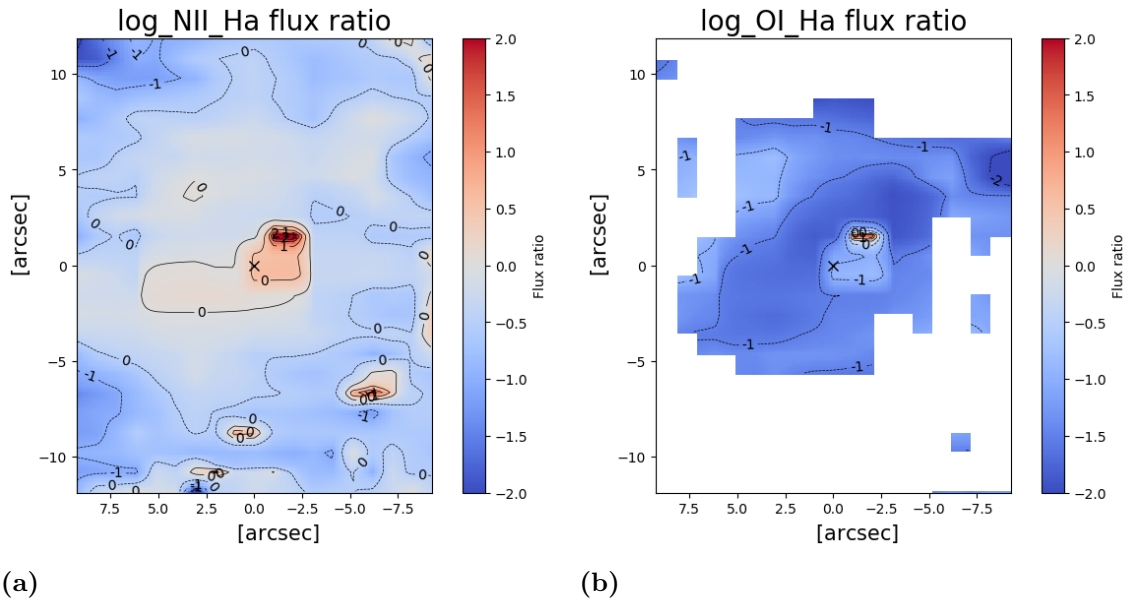


**Figure 6.24:** Line ratios in NGC7319. (a) log([NII]/H$\alpha$); (b) log([OI]/H$\alpha$).
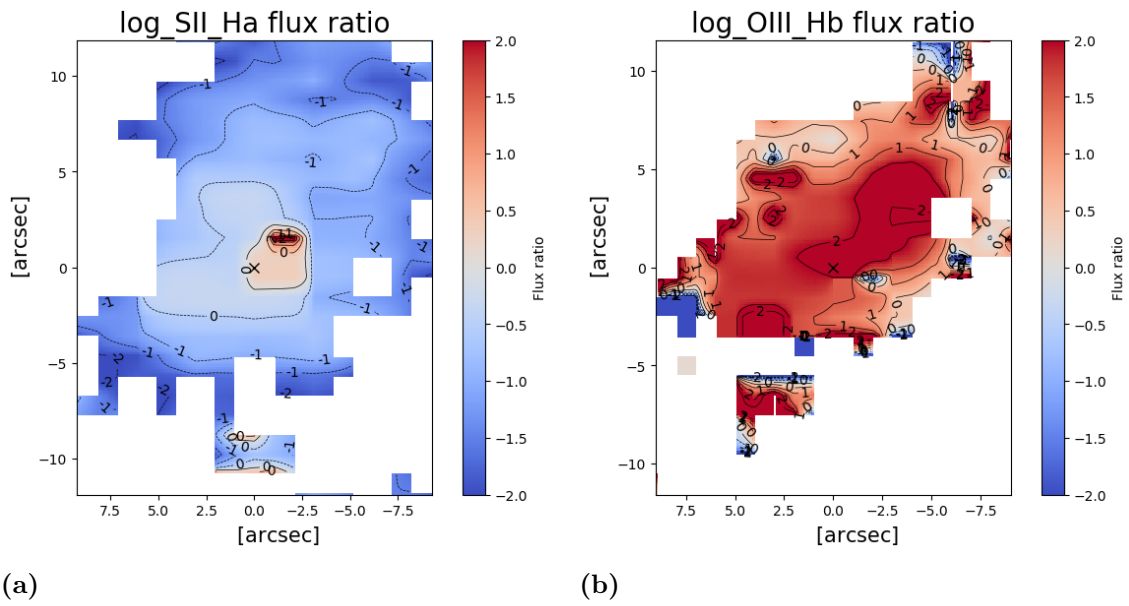
**Figure 6.25:** Line ratios in NGC7319. (a) log([SII]/Hα); (b) log([OIII]/Hβ).
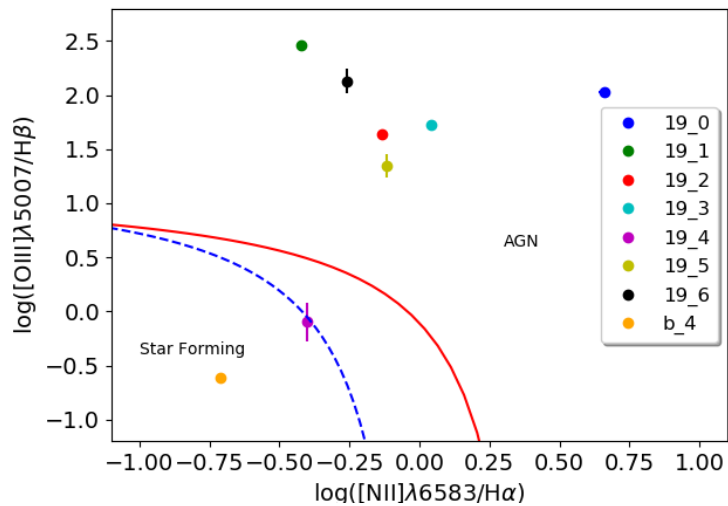


**Figure 6.26:** BPT diagnostic diagram, log([NII]λ6585/Hα) vs log([OIII]λ5008/Hβ), for region 19_0-6 and b_4.
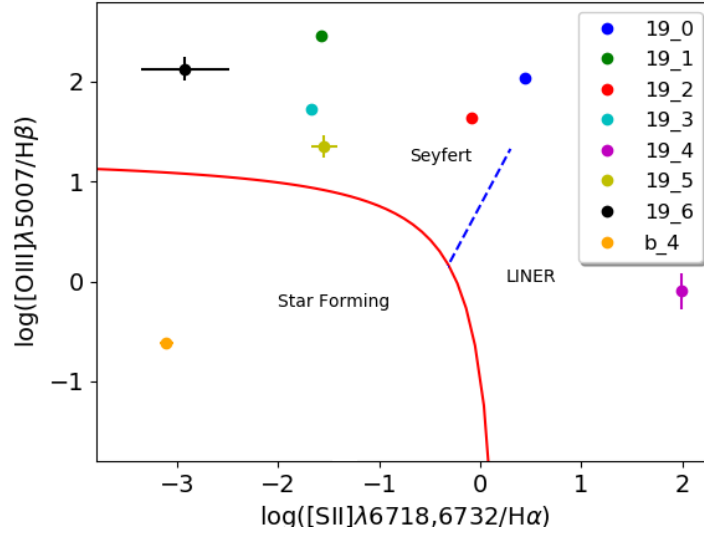
**Figure 6.27:** BPT diagnostic diagram, $\log([\text{SII}]\lambda6718,6732/\text{H}\alpha)$ vs $\log([\text{OIII}]\lambda5008/\text{H}\beta)$, for region 19_0-6 and b_4.
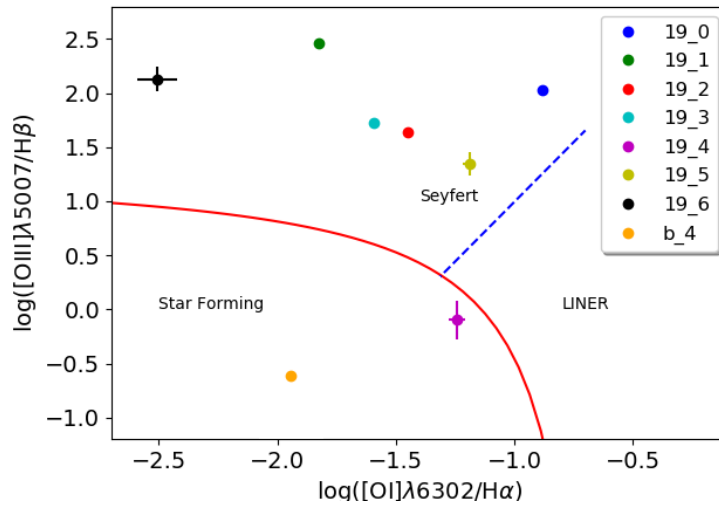


**Figure 6.28:** BPT diagnostic diagram, $\log([\text{OI}]\lambda6302/\text{H}\alpha)$ vs $\log([\text{OIII}]\lambda5008/\text{H}\beta)$, for region 19_0-6 and b_4.

### 6.1.5 The Bridge

As can be seen in the $H\alpha - [NII]$ emission displayed in Fig.6.1, there is a large amount of gas present in the bridge, coinciding with the molecular gas in the area (e.g., Appleton et al. (2017)). Fig.6.29-6.32 show the spectrum of the regions b_1-4 respectively. As can be seen the stellar continuum is negligible, while there is significant gaseous emission. [OII]$\lambda$3727, $H\alpha$, [NII]$\lambda$6550,6583, [SII]$\lambda$6718,6732 are the most prominent emission lines in these regions, while [OIII]$\lambda$5008 and [OI]$\lambda$6302 also make an appearance in b_3 and b_4 (closer to the star-forming ridge). The values yielded by fitting the emission lines are presented in the table in Fig.6.33.
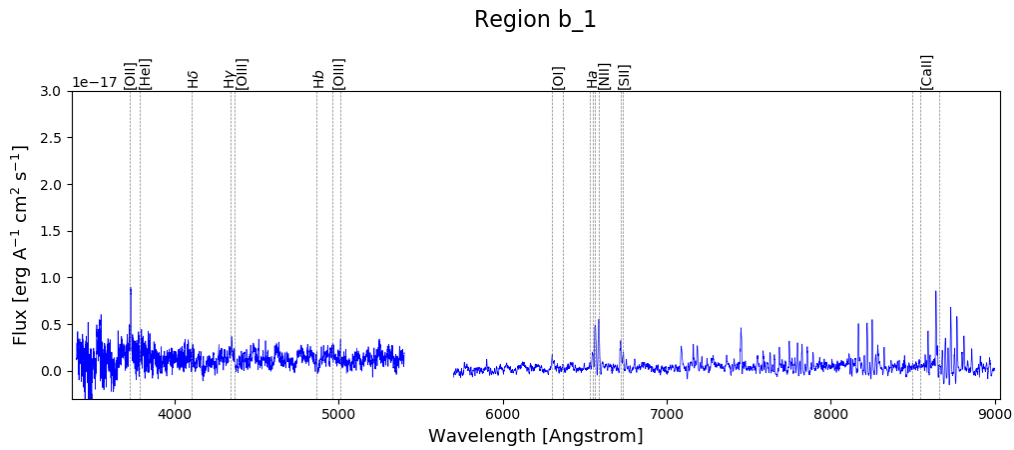


**Figure 6.29:** Spectrum of region b_1.
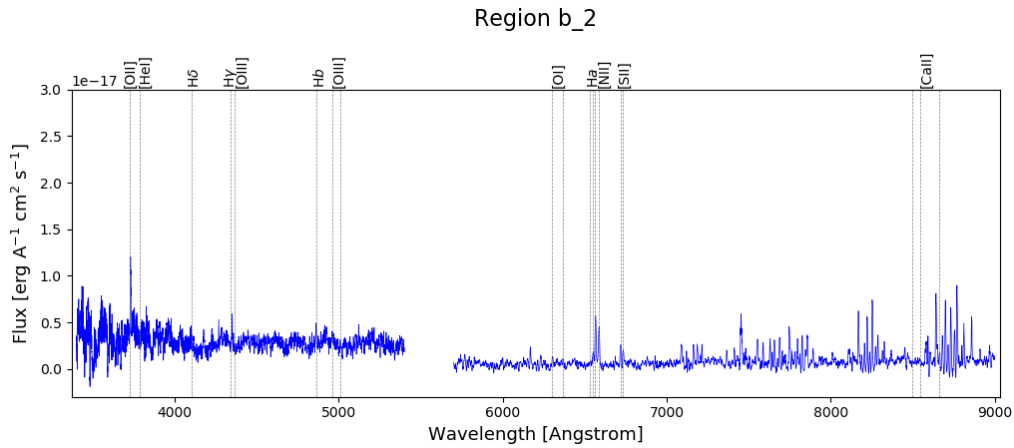


**Figure 6.30:** Spectrum of region b_2.
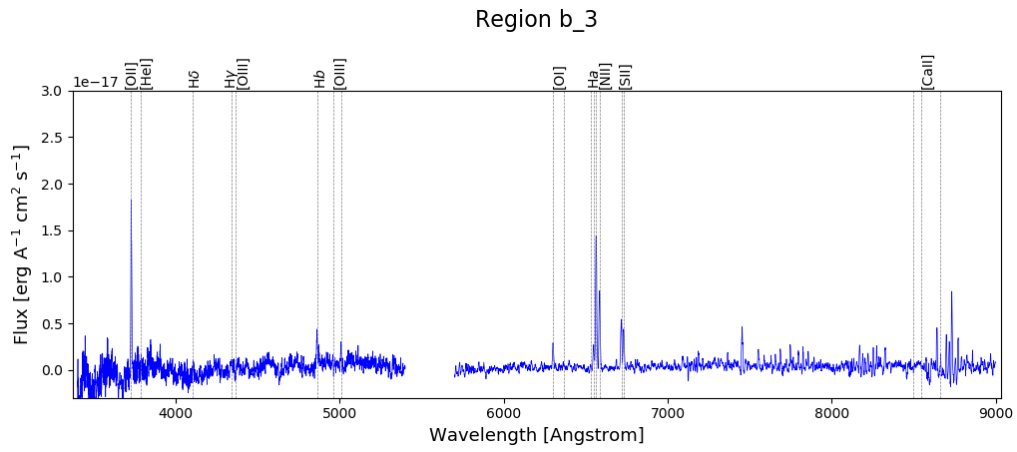
**Figure 6.31:** Spectrum of region b_3.
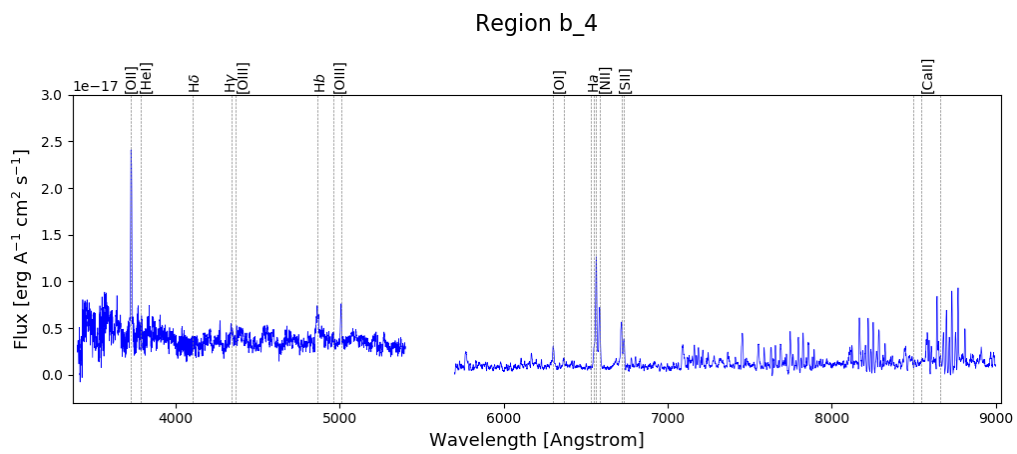


**Figure 6.32:** Spectrum of region b_4.

| | Vel comp | | Region b_1 | b_2 | b_3 | b_4 |
|---|---|---|---|---|---|---|
| Hß_NLR | high | Flux | - | 5.95E-18 ± 1.71E-18 | 3.18E-17 ± 3.03E-18 | 4.77E-17 ± 3.49E-18 |
| | | Vlos | - | 6438.8 ± 19.8 | 6397.9 ± 20.0 | 6467.4 ± 22.9 |
| | | Vel.Disp | - | 78.1 ± 19.8 | 245.6 ± 20.0 | 367.3 ± 22.9 |
| | low | Flux | - | - | - | - |
| | | Vlos | - | - | - | - |
| | | Vel.Disp | - | - | - | - |
| Hα_NLR | high | Flux | 1.32E-16 ± 4.99E-18 | 1.39E-16 ± 1.43E-17 | 2.07E-16 ± 2.84E-18 | 2.23E-16 ± 3.83E-18 |
| | | Vlos | 6611.8 ± 10.8 | 6553.0 ± 19.2 | 6419.1 ± 2.3 | 6438.4 ± 3.4 |
| | | Vel.Disp | 271.4 ± 7.6 | 271.4 ± 18.9 | 207.4 ± 2.5 | 261.3 ± 3.9 |
| | low | Flux | 2.43E-17 ± 3.66E-18 | 6.10E-18 ± 3.86E-18 | - | - |
| | | Vlos | 6350.4 ± 8.8 | 6228.9 ± 31.9 | - | - |
| | | Vel.Disp | 119.4 ± 10.9 | 225.3 ± 87.8 | - | - |
| [NII] 6550 | high | Flux | 9.87E-18 ± 9.93E-19 | 1.20E-17 ± 1.95E-18 | 2.44E-17 ± 1.23E-18 | 2.31E-17 ± 1.45E-18 |
| | | Vlos | 6612.2 ± 10.8 | 6553.3 ± 19.3 | 6341.4 ± 49.8 | 6346.2 ± 68.1 |
| | | Vel.Disp | 133.6 ± 9.1 | 126.4 ± 11.4 | 213.1 ± 4.1 | 233.9 ± 6.1 |
| | low | Flux | 2.31E-17 ± 1.30E-18 | 1.15E-17 ± 2.92E-18 | - | - |
| | | Vlos | 6350.2 ± 8.8 | 6228.4 ± 31.9 | - | - |
| | | Vel.Disp | 170.1 ± 7.7 | 161.2 ± 28.3 | - | - |
| [NII] 6585 | high | Flux | 2.96E-17 ± 2.16E-18 | 3.61E-17 ± 3.64E-18 | 1.25E-16 ± 2.79E-18 | 1.10E-16 ± 3.36E-18 |
| | | Vlos | 6611.3 ± 10.7 | 6552.7 ± 19.2 | 6341.9 ± 3.8 | 6346.7 ± 5.6 |
| | | Vel.Disp | 132.9 ± 9.1 | 125.8 ± 11.4 | 212.0 ± 4.1 | 232.7 ± 6.1 |
| | low | Flux | 6.94E-17 ± 3.25E-18 | 3.44E-17 ± 6.39E-18 | - | - |
| | | Vlos | 6350.7 ± 8.8 | 6229.6 ± 31.8 | - | - |
| | | Vel.Disp | 169.2 ± 7.7 | 160.3 ± 28.1 | - | - |
| [OI] 6302 | high | Flux | 1.39E-17 ± 3.00E-18 | - | 3.18E-17 ± 1.86E-18 | 3.20E-17 ± 1.85E-18 |
| | | Vlos | 7005.6 ± 45.8 | - | 6398.7 ± 9.8 | 6454.4 ± 11.7 |
| | | Vel.Disp | 234.6 ± 41.3 | - | 204.7 ± 10.2 | 234.6 ± 11.3 |
| | low | Flux | 2.53E-17 ± 3.00E-18 | 1.36E-17 ± 2.30E-18 | 9.14E-18 ± 1.99E-18 | 1.18E-17 ± 1.87E-18 |
| | | Vlos | 6329.3 ± 25.1 | 6449.3 ± 31.9 | 5648.2 ± 40.6 | 5740.6 ± 32.2 |
| | | Vel.Disp | 234.6 ± 22.6 | 234.6 ± 34.1 | 232.6 ± 43.6 | 234.6 ± 31.1 |
| [OII] 3727 | low | Flux | 3.16E-17 ± 2.80E-18 | 4.40E-17 ± 3.40E-18 | 1.07E-16 ± 3.47E-18 | 1.65E-16 ± 3.27E-18 |
| | | Vlos | 6843.0 ± 12.4 | 6784.3 ± 11.3 | 6623.3 ± 5.4 | 6578.5 ± 4.4 |
| | | Vel.Disp | 161.6 ± 12.4 | 169.2 ± 11.3 | 191.8 ± 5.4 | 255.7 ± 4.4 |
| [OIII] 5008 | high | Flux | 7.83E-18 ± 1.47E-18 | - | 8.22E-18 ± 2.15E-18 | 2.59E-17 ± 2.49E-18 |
| | | Vlos | 6561.5 ± 16.8 | - | 6412.2 ± 22.0 | 6437.4 ± 13.9 |
| | | Vel.Disp | 105.3 ± 16.7 | - | 96.7 ± 22.0 | 167.7 ± 13.9 |
| | low | Flux | - | - | - | - |
| | | Vlos | - | - | - | - |
| | | Vel.Disp | - | - | - | - |
| [SII] 6718 | high | Flux | 2.54E-17 ± 1.19E-18 | 1.59E-17 ± 1.00E-18 | 4.26E-17 ± 1.11E-18 | 5.24E-17 ± 1.50E-18 |
| | | Vlos | 6511.1 ± 7.0 | 6520.2 ± 6.7 | 6389.9 ± 3.5 | 6427.4 ± 5.5 |
| | | Vel.Disp | 154.7 ± 5.9 | 123.9 ± 6.3 | 146.5 ± 3.0 | 182.2 ± 4.3 |
| | low | Flux | - | - | - | - |
| | | Vlos | - | - | - | - |
| | | Vel.Disp | - | - | - | - |
| [SII] 6732 | high | Flux | 1.71E-17 ± 9.24E-19 | 1.29E-17 ± 8.67E-19 | 3.68E-17 ± 1.01E-18 | 3.26E-17 ± 1.12E-18 |
| | | Vlos | 6511.0 ± 7.0 | 6520.1 ± 6.7 | 6390.0 ± 3.5 | 6427.4 ± 5.5 |
| | | Vel.Disp | 154.4 ± 5.8 | 123.6 ± 6.3 | 146.1 ± 3.0 | 181.9 ± 4.2 |
| | low | Flux | - | - | - | - |
| | | Vlos | - | - | - | - |
| | | Vel.Disp | - | - | - | - |
| stellar | | Vlos | - | - | - | - |
| | | Vel.Disp | - | - | - | - |

**Figure 6.33:** Table containing the flux in $ergA^{-1}cm^2s^{-1}$, line-of-sight velocity and velocity dispersion in km/s, of each atomic species, as well as the stellar component, in each of the region b_1-4 marked in Fig.6.1.

91

#### 6.1.5.1 Gas Kinematics & Excitation Mechanisms

There are dual velocity components present in region b_1 and b_2, as can be seen in the fit of the H$\alpha-$[NII] emission in these regions, presented together with the fit of region b_3 in Fig.6.34. These velocity components range $\sim 5650 - 7000$ km/s, as is clear from the table in Fig.6.33. While the velocity dispersion in the bridge, shows values of $\sim 80-370$ km/s, with the highest velocity dispersions closest to the star-forming ridge.

Only one of the regions in the bridge have sufficient emission to enable an analysis of the excitation mechanisms using the BPT diagrams (detailed in chapter 2.6.3), and this is region b_4. As is clear from Fig.6.24a-6.24b, the ionisation of region b_4 is due to star-formation, as expected due to its proximity to the star-forming ridge.

**(a)**

**(b)**

**(c)**
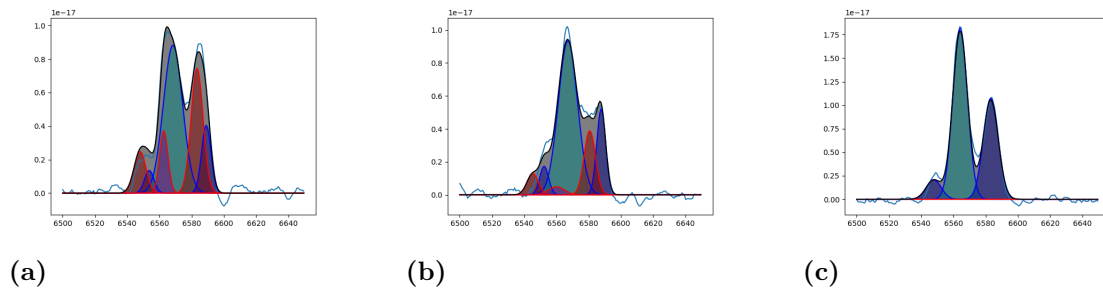
**Figure 6.34:** The fit of the H$\alpha-$[NII] emission in the bridge. The blue lines denote one velocity component and the red ones the other. The black lines is the resultant best fit. (a) Region b_1; (b) Region b_2; (c) Region b_3.

## 6.2 The Star-Forming Ridge

Gas that has been stripped from the galaxies during previous interactions and deposited in the IGM is colliding with NGC7318B at high velocity, creating a galaxy-wide shocked star-forming ridge. The H$\alpha-$[NII] emission displayed in Fig.6.1, clearly shows the large amount of gas accumulated in the shocked SF ridge. There is also a significant amount of gas in a region south-west (above in Fig.6.1) of NGC7318A, in what here, for the purpose of discussion, is called the west ridge. In this chapter the spectra and fits of these regions are presented, including a discussion of the dual velocity components present at certain locations and the excitation mechanisms wherever possible. As will be seen the stellar continuum is negligible in this area and this chapter therefore relies on the gaseous components.

### 6.2.1 Spectra

The spectra of the region SF_1-15, pinpointed in Fig.6.1, are presented in Fig.6.35-6.49. Note the bright emission of H$\alpha$, [OII], [OIII], [NII] and [SII]. While the SF ridge shows bright emission in H$\alpha$, [NII], [SII] and [OII], the west ridge also shows significant emission in H$\beta$ and [OIII] but negligible emission in [OII].

As can be seen from the spectra in Fig.6.35-6.49, the stellar continuum is too weak to garner a proper fit. The values obtained from the fits of the gas emission lines are presented in the tables in Fig.6.50-6.53.
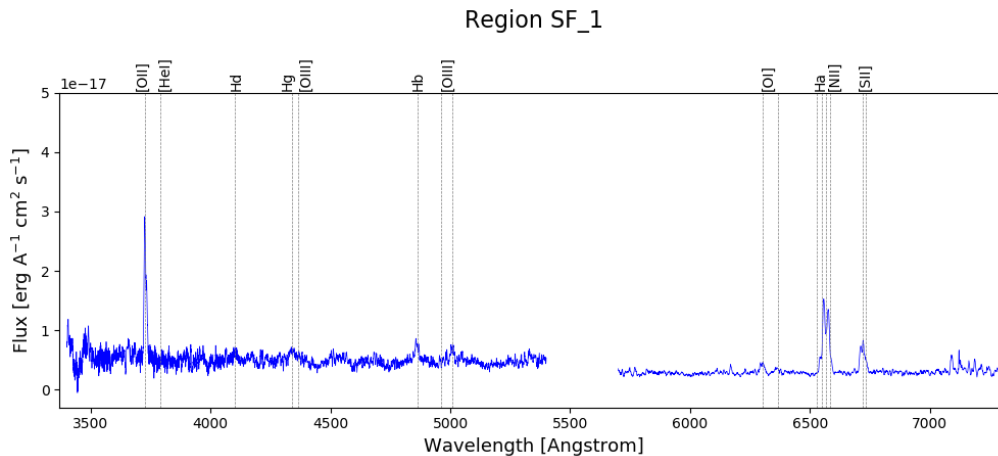


**Figure 6.35:** Spectrum of region SF_1. Vertical dotted lines mark the expected line centres of different gas emission lines at the group average redshift of 0.0215, the spectrum is also corrected to this average redshift.
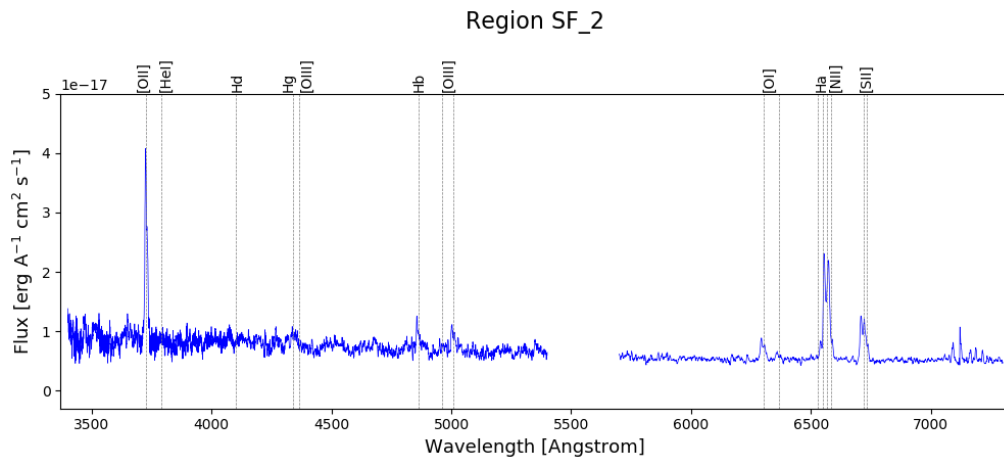
**Figure 6.36:** Same as Fig.6.35 but for region SF_2.
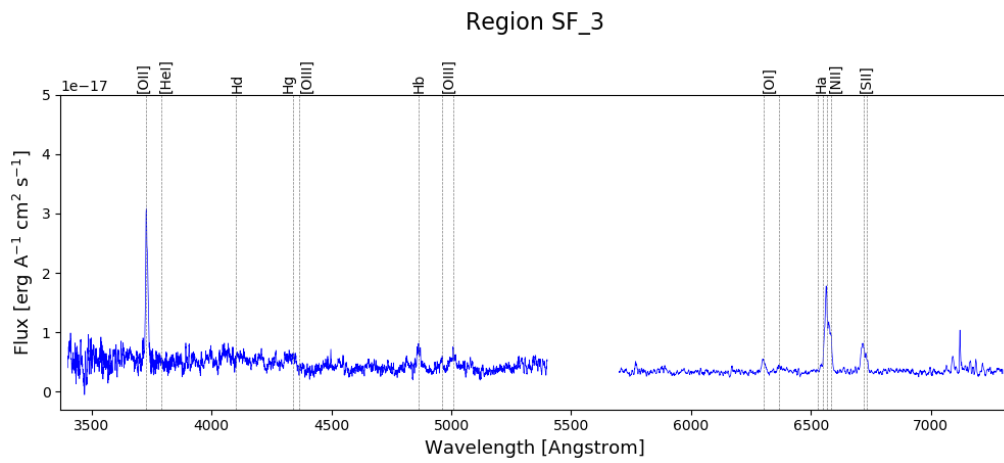


**Figure 6.37:** Same as Fig.6.35 but for region SF_3.
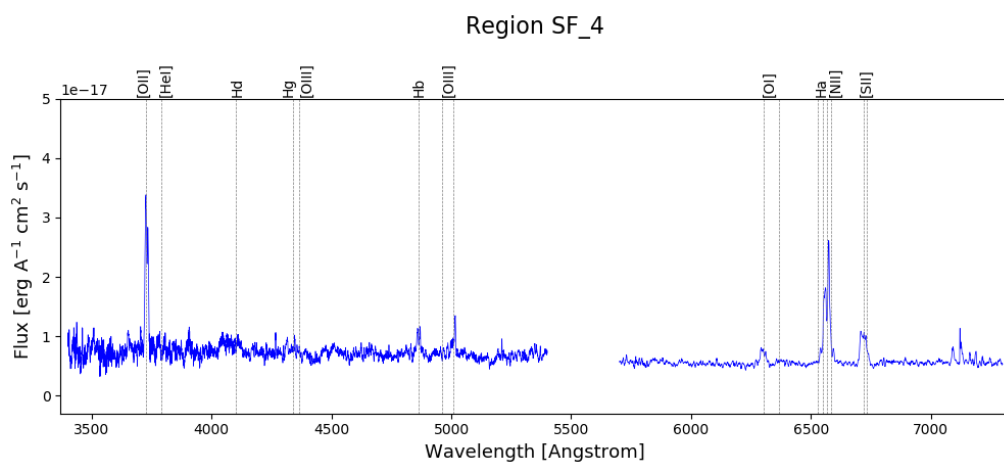


**Figure 6.38:** Same as Fig.6.35 but for region SF_4.
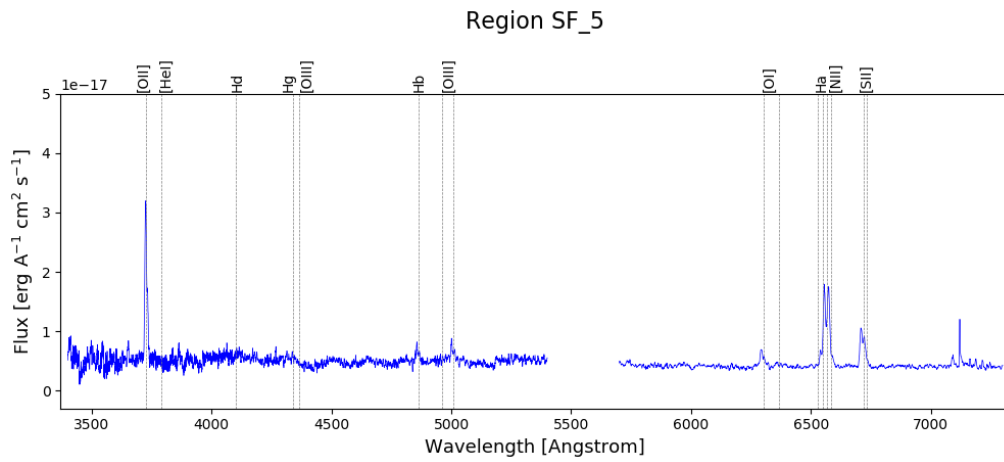
**Figure 6.39:** Same as Fig.6.35 but for region SF_5.
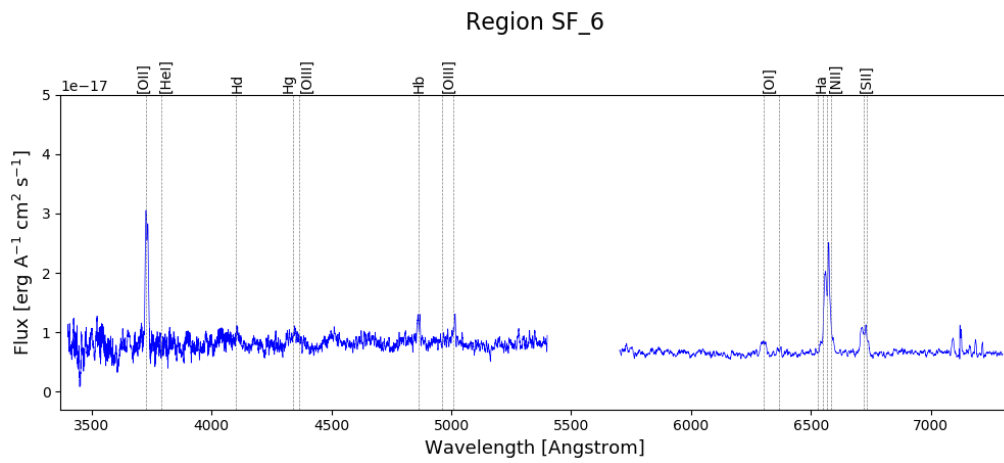


**Figure 6.40:** Same as Fig.6.35 but for region SF_6.
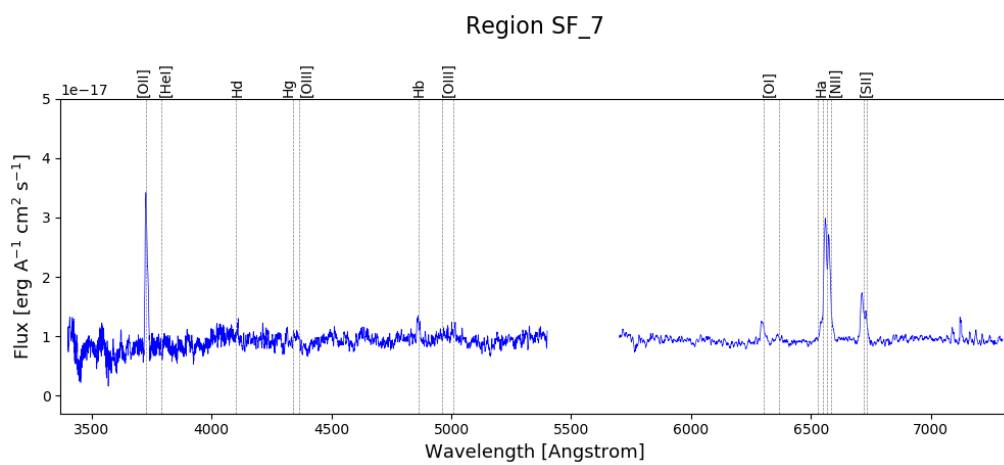


**Figure 6.41:** Same as Fig.6.35 but for region SF_7.
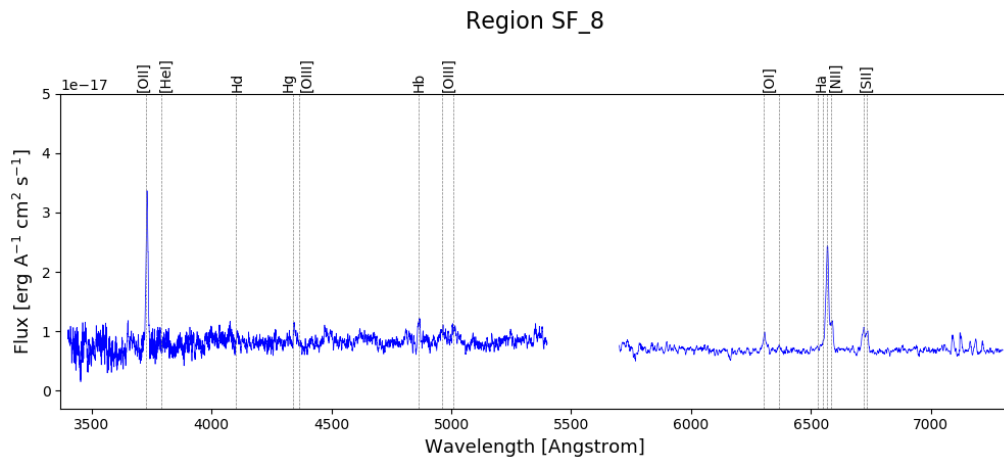
**Figure 6.42:** Same as Fig.6.35 but for region SF_8.
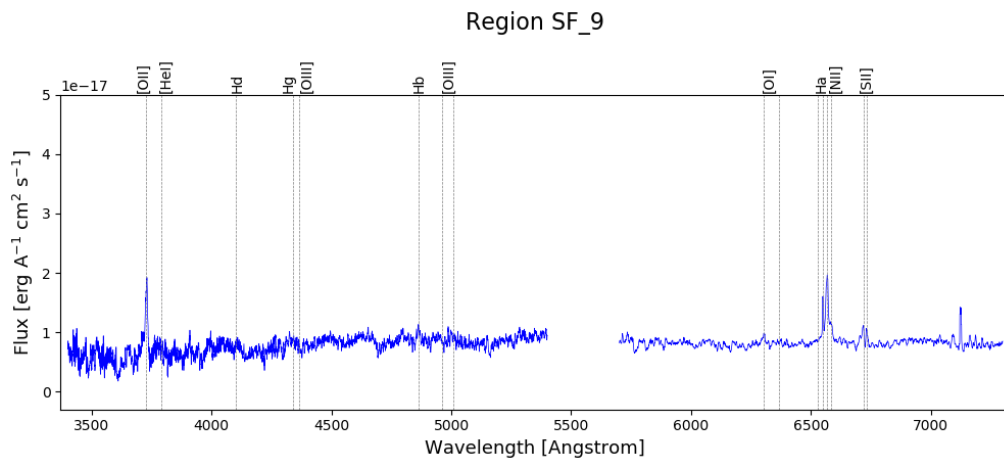


**Figure 6.43:** Same as Fig.6.35 but for region SF_9.
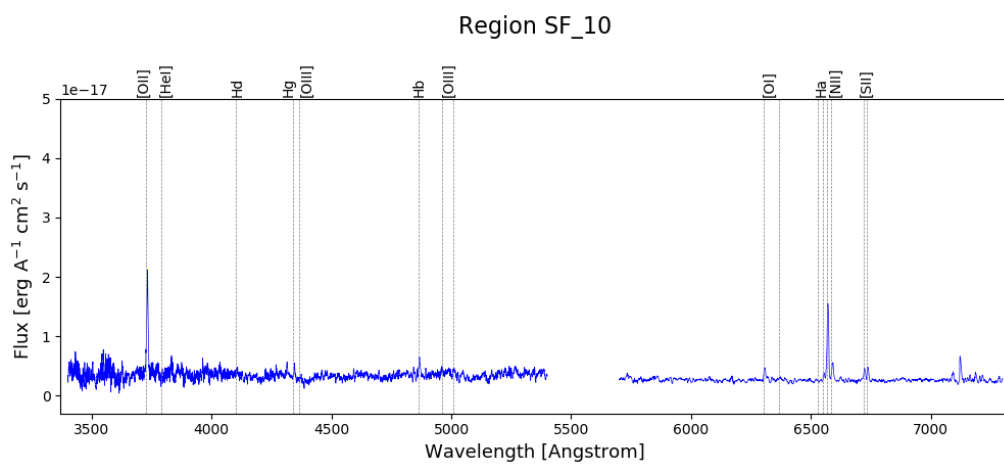


**Figure 6.44:** Same as Fig.6.35 but for region SF_10.
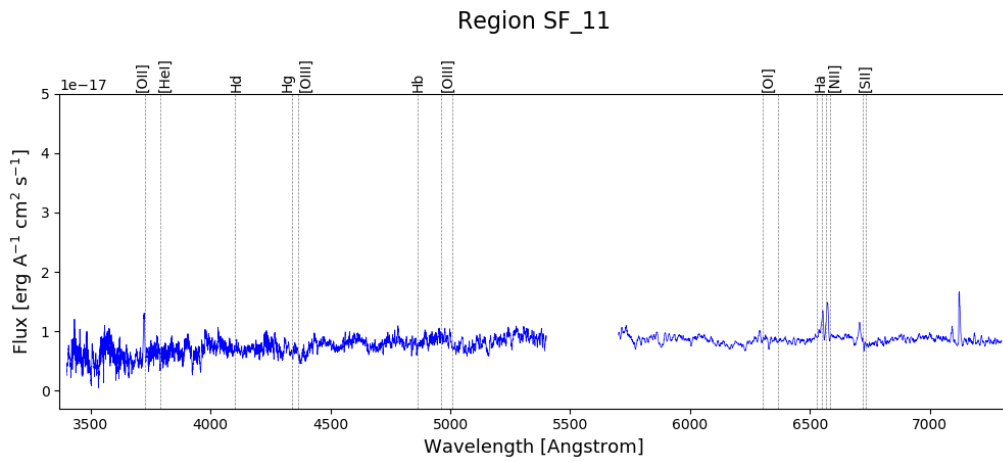
**Figure 6.45:** Same as Fig.6.35 but for region SF_11.
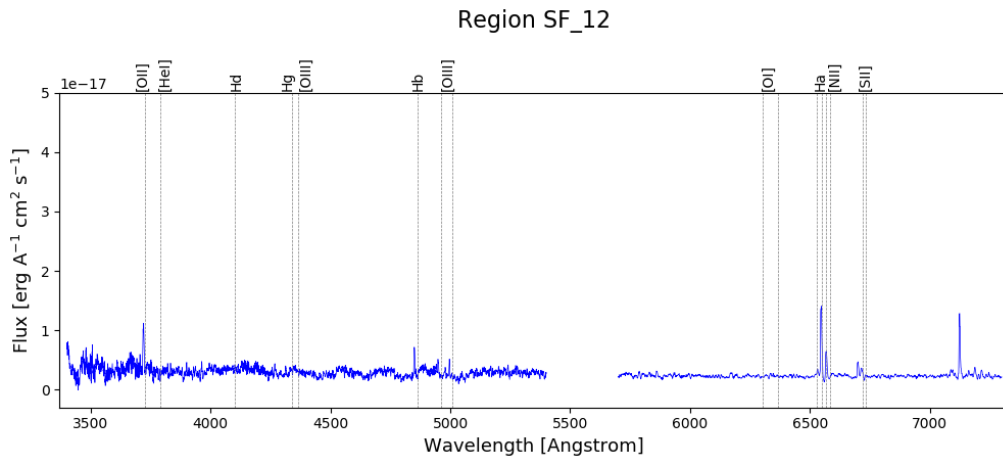


**Figure 6.46:** Same as Fig.6.35 but for region SF_12.
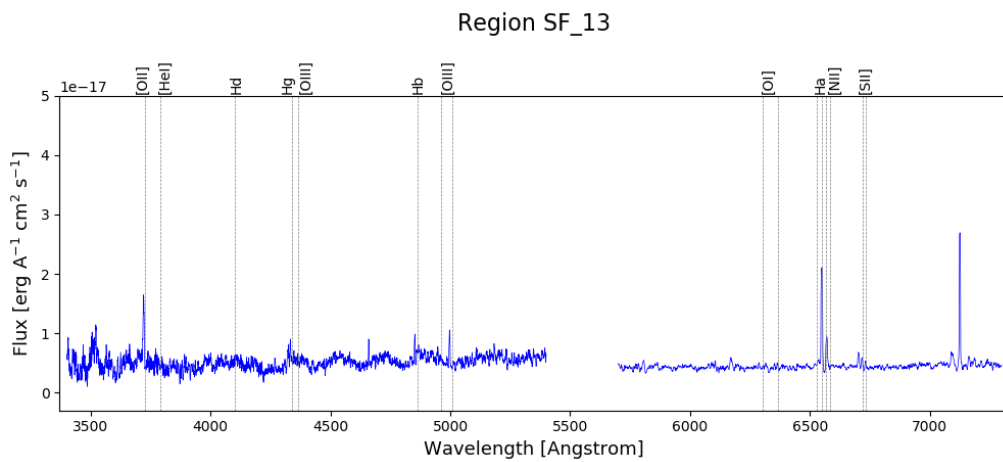


**Figure 6.47:** Same as Fig.6.35 but for region SF_13.
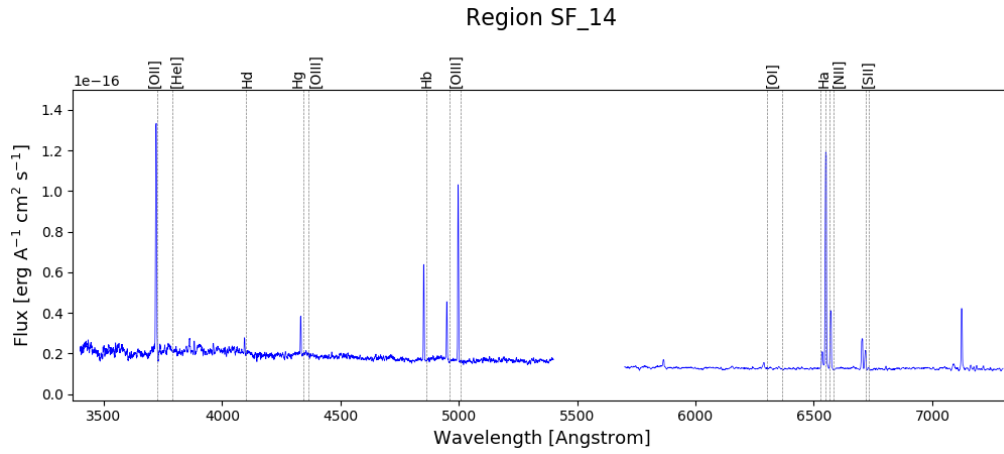
**Figure 6.48:** Same as Fig.6.35 but for region SF_14.
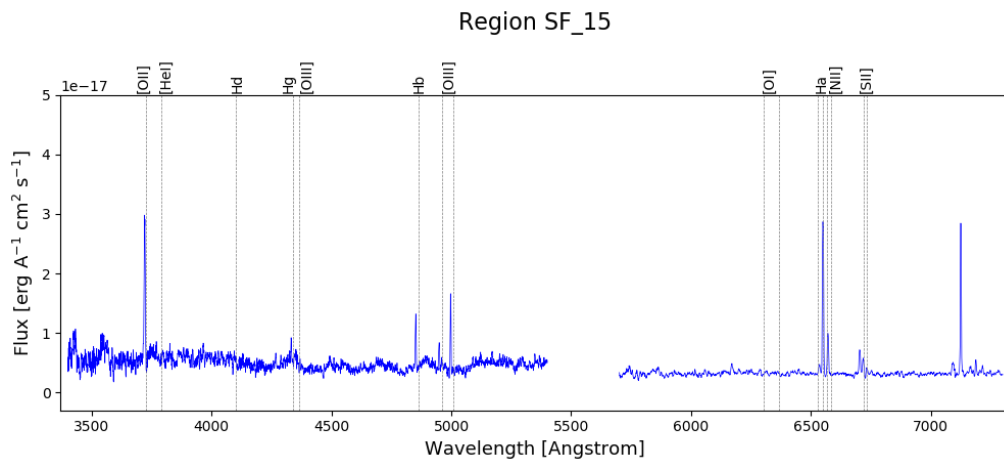


**Figure 6.49:** Same as Fig.6.35 but for region SF_15.

| | Vel comp | | Region SF_1 | SF_2 | SF_3 | SF_4 |
|---|---|---|---|---|---|---|
| Hß_NLR | high | Flux | 9.44E-18 ± 2.76E-18 | 3.77E-17 ± 9.68E-18 | - | 2.24E-17 ± 3.04E-18 |
| | | Vlos | 6801.5 ± 26.4 | 6525.6 ± 73.9 | - | 6838.0 ± 13.5 |
| | | Vel.Disp | 113.6 ± 27.2 | 305.1 ± 64.3 | - | 120.2 ± 13.6 |
| | low | Flux | 3.82E-17 ± 4.47E-18 | 2.64E-17 ± 6.25E-18 | - | 4.59E-17 ± 4.47E-18 |
| | | Vlos | 6122.0 ± 27.8 | 6040.1 ± 14.3 | - | 6198.1 ± 19.8 |
| | | Vel.Disp | 305.1 ± 31.1 | 120.3 ± 18.5 | - | 260.7 ± 22.1 |
| Hα_NLR | high | Flux | 1.73E-16 ± 1.15E-17 | 2.21E-16 ± 1.08E-17 | 2.63E-16 ± 1.89E-17 | 2.01E-16 ± 7.06E-18 |
| | | Vlos | 6778.5 ± 14.2 | 6615.1 ± 9.0 | 6420.1 ± 13.0 | 6815.6 ± 5.7 |
| | | Vel.Disp | 271.4 ± 15.3 | 271.4 ± 11.3 | 271.4 ± 15.6 | 178.4 ± 5.4 |
| | low | Flux | 1.96E-16 ± 6.38E-18 | 1.68E-16 ± 5.09E-18 | 1.43E-17 ± 9.45E-18 | 2.09E-16 ± 6.20E-18 |
| | | Vlos | 6143.4 ± 8.1 | 6016.4 ± 4.8 | 6047.7 ± 12.4 | 6170.8 ± 5.5 |
| | | Vel.Disp | 225.3 ± 4.8 | 173.8 ± 3.7 | 110.3 ± 4.8 | 225.3 ± 5.7 |
| [NII] 6550 | high | Flux | 2.04E-18 ± 8.69E-19 | 1.04E-17 ± 1.12E-18 | 1.95E-17 ± 2.04E-18 | 7.39E-18 ± 1.74E-18 |
| | | Vlos | 6779.3 ± 14.2 | 6615.5 ± 9.0 | 6420.0 ± 13.0 | 6816.4 ± 5.7 |
| | | Vel.Disp | 153.8 ± 54.9 | 154.9 ± 13.6 | 160.1 ± 12.5 | 225.8 ± 43.7 |
| | low | Flux | 3.82E-17 ± 1.59E-18 | 4.55E-17 ± 1.91E-18 | 2.98E-17 ± 2.59E-18 | 3.47E-17 ± 2.59E-18 |
| | | Vlos | 6142.7 ± 8.1 | 6015.5 ± 4.8 | 6046.8 ± 12.4 | 6170.2 ± 5.5 |
| | | Vel.Disp | 225.8 ± 6.2 | 224.7 ± 7.7 | 164.6 ± 9.3 | 225.8 ± 14.5 |
| [NII] 6585 | high | Flux | 6.11E-18 ± 2.23E-18 | 3.13E-17 ± 2.83E-18 | 5.85E-17 ± 4.77E-18 | 2.22E-17 ± 4.40E-18 |
| | | Vlos | 6777.5 ± 14.1 | 6614.5 ± 9.0 | 6420.1 ± 12.9 | 6814.4 ± 5.7 |
| | | Vel.Disp | 152.9 ± 54.6 | 154.0 ± 13.5 | 159.2 ± 12.5 | 224.6 ± 43.4 |
| | low | Flux | 1.15E-16 ± 3.38E-18 | 1.36E-16 ± 4.83E-18 | 8.93E-17 ± 5.40E-18 | 1.04E-16 ± 6.82E-18 |
| | | Vlos | 6144.3 ± 8.1 | 6017.8 ± 4.7 | 6048.9 ± 12.3 | 6171.7 ± 5.5 |
| | | Vel.Disp | 224.6 ± 6.2 | 223.5 ± 7.7 | 163.8 ± 9.2 | 224.6 ± 14.5 |
| [OI] 6302 | high | Flux | 2.50E-17 ± 4.02E-18 | 3.32E-17 ± 3.09E-18 | 1.55E-17 ± 3.55E-18 | 2.99E-17 ± 3.41E-18 |
| | | Vlos | 6662.4 ± 36.5 | 6686.6 ± 19.8 | 6828.9 ± 54.8 | 6797.4 ± 22.9 |
| | | Vel.Disp | 234.6 ± 29.2 | 234.6 ± 17.7 | 234.6 ± 38.3 | 234.6 ± 22.4 |
| | low | Flux | 3.15E-17 ± 3.91E-18 | 4.93E-17 ± 2.99E-18 | 3.30E-17 ± 3.59E-18 | 4.84E-17 ± 3.40E-18 |
| | | Vlos | 6050.0 ± 27.7 | 6023.3 ± 12.6 | 6249.4 ± 26.4 | 6075.5 ± 14.1 |
| | | Vel.Disp | 234.6 ± 22.1 | 231.7 ± 11.2 | 234.6 ± 18.5 | 234.6 ± 13.8 |
| [OII] 3727 | high | Flux | 7.90E-17 ± 7.69E-18 | 1.19E-16 ± 9.50E-18 | 1.98E-16 ± 7.99E-18 | 1.12E-16 ± 4.82E-18 |
| | | Vlos | 6925.0 ± 21.8 | 6842.8 ± 18.7 | 6738.4 ± 18.2 | 7047.2 ± 7.1 |
| | | Vel.Disp | 233.0 ± 18.1 | 233.5 ± 14.5 | 363.0 ± 9.2 | 190.0 ± 6.8 |
| | low | Flux | 1.48E-16 ± 7.04E-18 | 2.07E-16 ± 8.79E-18 | 5.04E-17 ± 7.14E-18 | 1.99E-16 ± 5.69E-18 |
| | | Vlos | 6324.1 ± 9.5 | 6259.4 ± 8.9 | 6439.5 ± 8.8 | 6349.5 ± 6.0 |
| | | Vel.Disp | 205.9 ± 7.5 | 210.4 ± 6.6 | 132.9 ± 12.3 | 251.6 ± 6.2 |
| [OIII] 5008 | high | Flux | 1.96E-17 ± 7.60E-18 | 3.55E-17 ± 8.31E-18 | 1.59E-17 ± 5.70E-18 | 3.80E-17 ± 3.13E-18 |
| | | Vlos | 6711.1 ± 83.2 | 6703.8 ± 61.4 | 6950.1 ± 65.1 | 6887.4 ± 9.1 |
| | | Vel.Disp | 214.0 ± 58.5 | 296.2 ± 57.9 | 205.3 ± 52.6 | 133.2 ± 9.2 |
| | low | Flux | 2.18E-17 ± 8.34E-18 | 3.11E-17 ± 6.14E-18 | 3.23E-17 ± 7.17E-18 | 3.72E-17 ± 4.70E-18 |
| | | Vlos | 6136.8 ± 94.5 | 6050.5 ± 31.2 | 6302.9 ± 60.2 | 6149.7 ± 29.2 |
| | | Vel.Disp | 241.6 ± 70.1 | 185.8 ± 26.7 | 296.2 ± 53.2 | 296.2 ± 32.5 |
| [SII] 6718 | high | Flux | 2.75E-17 ± 4.59E-18 | 3.34E-17 ± 5.08E-18 | 4.52E-17 ± 3.56E-17 | 2.44E-17 ± 2.10E-18 |
| | | Vlos | 6518.0 ± 29.6 | 6546.7 ± 33.3 | 6340.9 ± 176.0 | 6905.7 ± 22.9 |
| | | Vel.Disp | 167.2 ± 19.8 | 220.1 ± 26.9 | 220.1 ± 56.7 | 220.1 ± 16.4 |
| | low | Flux | 4.21E-17 ± 4.70E-18 | 7.16E-17 ± 4.57E-18 | - | 7.28E-17 ± 2.10E-18 |
| | | Vlos | 6092.6 ± 20.7 | 6008.9 ± 11.8 | - | 6026.5 ± 7.7 |
| | | Vel.Disp | 173.8 ± 14.1 | 193.1 ± 9.3 | - | 220.1 ± 5.5 |
| [SII] 6732 | high | Flux | 2.12E-17 ± 3.53E-18 | 2.57E-17 ± 3.91E-18 | 3.48E-17 ± 2.74E-17 | 1.88E-17 ± 1.62E-18 |
| | | Vlos | 6517.9 ± 29.5 | 6546.4 ± 33.3 | 6341.1 ± 175.6 | 6904.7 ± 22.8 |
| | | Vel.Disp | 166.8 ± 19.7 | 219.6 ± 26.8 | 219.6 ± 56.6 | 219.6 ± 16.4 |
| | low | Flux | 3.24E-17 ± 3.62E-18 | 5.51E-17 ± 3.52E-18 | - | 5.60E-17 ± 1.61E-18 |
| | | Vlos | 6093.4 ± 20.7 | 6009.8 ± 11.8 | - | 6027.4 ± 7.6 |
| | | Vel.Disp | 173.4 ± 14.0 | 192.7 ± 9.3 | - | 219.6 ± 5.5 |

**Figure 6.50:** Table containing the flux in $ergcm^2s^{-1}$, line-of-sight velocity and velocity dispersion in km/s, of each atomic species, in region SF_1-4 marked in Fig.6.1.

| | Vel comp | | SF_5 | SF_6 | SF_7 | SF_8 |
|---|---|---|---|---|---|---|
| Hß_NLR | high | Flux | 8.48E-18 ± 2.31E-18 | 1.49E-17 ± 3.16E-18 | 1.05E-17 ± 3.28E-18 | 2.82E-17 ± 5.79E-18 |
| | | Vlos | 6699.7 ± 30.1 | 6809.9 ± 13.0 | 6827.1 ± 26.0 | 6679.1 ± 33.4 |
| | | Vel.Disp | 131.8 ± 30.0 | 84.0 ± 14.3 | 108.2 ± 26.9 | 170.5 ± 28.4 |
| | low | Flux | 2.93E-17 ± 3.25E-18 | 5.01E-17 ± 5.36E-18 | 5.14E-17 ± 5.21E-18 | 1.53E-17 ± 4.76E-18 |
| | | Vlos | 6043.5 ± 22.2 | 6269.8 ± 23.2 | 6243.9 ± 22.0 | 6276.8 ± 37.6 |
| | | Vel.Disp | 255.4 ± 24.7 | 275.9 ± 25.7 | 275.0 ± 24.2 | 127.1 ± 29.0 |
| Hα_NLR | high | Flux | 1.66E-16 ± 5.21E-18 | 1.94E-16 ± 5.83E-18 | 2.29E-16 ± 1.24E-17 | 2.33E-16 ± 5.31E-18 |
| | | Vlos | 6673.8 ± 7.3 | 6813.0 ± 5.1 | 6776.7 ± 11.8 | 6654.9 ± 5.9 |
| | | Vel.Disp | 271.4 ± 7.1 | 184.9 ± 4.8 | 249.0 ± 11.4 | 201.9 ± 3.0 |
| | low | Flux | 1.45E-16 ± 2.72E-18 | 2.18E-16 ± 5.88E-18 | 2.88E-16 ± 8.30E-18 | 8.56E-17 ± 5.43E-18 |
| | | Vlos | 6023.5 ± 3.5 | 6228.8 ± 5.4 | 6181.3 ± 7.0 | 6275.6 ± 12.1 |
| | | Vel.Disp | 191.3 ± 2.7 | 225.3 ± 5.0 | 225.3 ± 4.4 | 199.9 ± 7.5 |
| [NII] 6550 | high | Flux | 6.60E-18 ± 6.52E-19 | 7.10E-18 ± 1.30E-18 | 5.58E-18 ± 1.25E-18 | 9.88E-18 ± 9.88E-19 |
| | | Vlos | 6674.4 ± 7.3 | 6813.9 ± 5.1 | 6777.5 ± 11.8 | 6655.3 ± 6.0 |
| | | Vel.Disp | 193.5 ± 15.8 | 219.8 ± 32.9 | 204.0 ± 36.8 | 144.4 ± 8.9 |
| | low | Flux | 3.16E-17 ± 9.96E-19 | 3.44E-17 ± 1.87E-18 | 4.37E-17 ± 1.90E-18 | 2.54E-17 ± 1.58E-18 |
| | | Vlos | 6022.5 ± 3.6 | 6228.3 ± 5.4 | 6180.7 ± 7.1 | 6275.2 ± 12.1 |
| | | Vel.Disp | 225.8 ± 5.4 | 225.8 ± 10.4 | 225.8 ± 7.8 | 213.5 ± 10.7 |
| [NII] 6585 | high | Flux | 1.98E-17 ± 1.66E-18 | 2.13E-17 ± 3.27E-18 | 1.67E-17 ± 3.11E-18 | 2.96E-17 ± 1.99E-18 |
| | | Vlos | 6673.1 ± 7.2 | 6811.9 ± 5.1 | 6775.6 ± 11.7 | 6654.2 ± 5.9 |
| | | Vel.Disp | 192.5 ± 15.7 | 218.6 ± 32.7 | 202.9 ± 36.6 | 143.6 ± 8.9 |
| | low | Flux | 9.47E-17 ± 2.35E-18 | 1.03E-16 ± 4.86E-18 | 1.31E-16 ± 4.65E-18 | 7.63E-17 ± 3.93E-18 |
| | | Vlos | 6024.8 ± 3.5 | 6229.5 ± -5.4 | 6182.1 ± 7.0 | 6276.1 ± 12.0 |
| | | Vel.Disp | 224.6 ± 5.3 | 224.6 ± 10.3 | 224.6 ± 7.7 | 212.3 ± 10.6 |
| [OI] 6302 | high | Flux | 1.99E-17 ± 2.75E-18 | 3.36E-17 ± 4.72E-18 | 2.70E-17 ± 5.17E-18 | 4.13E-17 ± 6.91E-18 |
| | | Vlos | 6659.5 ± 29.9 | 6781.1 ± 30.5 | 6771.7 ± 41.9 | 6691.6 ± 40.7 |
| | | Vel.Disp | 234.6 ± 26.0 | 234.6 ± 26.4 | 234.6 ± 35.9 | 234.6 ± 28.2 |
| | low | Flux | 4.37E-17 ± 2.72E-18 | 4.01E-17 ± 4.68E-18 | 6.08E-17 ± 5.08E-18 | 1.97E-17 ± 6.88E-18 |
| | | Vlos | 5999.6 ± 13.4 | 6121.7 ± 25.2 | 6120.7 ± 18.1 | 6113.0 ± 84.6 |
| | | Vel.Disp | 234.6 ± 11.7 | 234.6 ± 21.9 | 234.6 ± 15.5 | 234.6 ± 58.5 |
| [OII] 3727 | high | Flux | 5.35E-17 ± 3.72E-18 | 1.39E-16 ± 1.03E-17 | 1.10E-16 ± 1.44E-17 | 2.25E-16 ± 7.78E-18 |
| | | Vlos | 6935.9 ± 11.0 | 6979.4 ± 17.8 | 6903.0 ± 40.9 | 6768.3 ± 8.2 |
| | | Vel.Disp | 178.9 ± 10.0 | 240.3 ± 13.6 | 273.8 ± 23.8 | 286.9 ± 8.5 |
| | low | Flux | 2.09E-16 ± 4.52E-18 | 1.50E-16 ± 9.73E-18 | 1.78E-16 ± 1.30E-17 | 1.15E-17 ± 4.91E-18 |
| | | Vlos | 6288.5 ± 4.5 | 6371.3 ± 14.5 | 6345.9 ± 17.8 | 6234.8 ± 29.2 |
| | | Vel.Disp | 247.0 ± 4.5 | 223.3 ± 10.7 | 236.3 ± 9.7 | 100.8 ± 32.7 |
| [OIII] 5008 | high | Flux | 1.90E-17 ± 3.73E-18 | 2.58E-17 ± 4.03E-18 | 1.54E-17 ± 3.09E-18 | 3.56E-17 ± 5.12E-18 |
| | | Vlos | 6712.8 ± 38.6 | 6863.0 ± 13.0 | 6890.4 ± 18.3 | 6771.0 ± 34.1 |
| | | Vel.Disp | 235.0 ± 38.9 | 117.8 ± 13.9 | 113.5 ± 18.8 | 296.2 ± 36.6 |
| | low | Flux | 3.17E-17 ± 3.59E-18 | 3.41E-17 ± 6.51E-18 | 2.37E-17 ± 4.94E-18 | 1.01E-17 ± 2.98E-18 |
| | | Vlos | 5999.4 ± 21.2 | 6287.0 ± 46.1 | 6212.7 ± 48.0 | 6226.9 ± 18.7 |
| | | Vel.Disp | 219.2 ± 20.8 | 296.2 ± 48.7 | 296.2 ± 53.6 | 95.4 ± 21.4 |
| [SII] 6718 | high | Flux | 1.15E-17 ± 4.14E-18 | 1.92E-17 ± 2.93E-18 | - | 4.66E-17 ± 5.88E-18 |
| | | Vlos | 6521.8 ± 84.1 | 6833.6 ± 31.2 | - | 6525.8 ± 26.3 |
| | | Vel.Disp | 220.1 ± 56.4 | 220.1 ± 29.0 | - | 195.7 ± 18.7 |
| | low | Flux | 7.19E-17 ± 4.07E-18 | 5.63E-17 ± 2.93E-18 | 8.18E-17 ± 4.17E-17 | 8.21E-18 ± 4.33E-18 |
| | | Vlos | 6008.0 ± 12.9 | 6158.4 ± 10.6 | 6118.6 ± 138.4 | 6201.5 ± 39.6 |
| | | Vel.Disp | 216.0 ± 8.6 | 220.1 ± 9.9 | 220.1 ± 55.9 | 111.8 ± 30.3 |
| [SII] 6732 | high | Flux | 8.83E-18 ± 3.18E-18 | 1.48E-17 ± 2.26E-18 | - | 3.59E-17 ± 4.52E-18 |
| | | Vlos | 6521.6 ± 83.9 | 6832.7 ± 31.2 | - | 6525.6 ± 26.3 |
| | | Vel.Disp | 219.6 ± 56.3 | 219.6 ± 28.9 | - | 195.3 ± 18.6 |
| | low | Flux | 5.53E-17 ± 3.13E-18 | 4.33E-17 ± 2.25E-18 | 6.29E-17 ± 3.20E-17 | 6.31E-18 ± 3.33E-18 |
| | | Vlos | 6008.9 ± 12.8 | 6159.0 ± 10.6 | 6119.3 ± 138.1 | 6202.0 ± 39.6 |
| | | Vel.Disp | 215.6 ± 8.5 | 219.6 ± 9.9 | 219.6 ± 55.8 | 111.6 ± 30.3 |

**Figure 6.51:** Continuation of the table in Fig.6.50, showing the values for region SF_5-8.

| | Vel comp | | SF_9 | SF_10 | SF_11 | SF_12 |
|---|---|---|---|---|---|---|
| Hß_NLR | high | Flux | 3.72E-17 ± 4.98E-18 | - | - | - |
| | | Vlos | 6460.5 ± 29.7 | - | - | - |
| | | Vel.Disp | 283.1 ± 32.9 | - | - | - |
| | low | Flux | 9.37E-18 ± 2.91E-18 | 1.34E-17 ± 6.81E-18 | 1.12E-17 ± 2.92E-18 | 1.84E-17 ± 1.59E-18 |
| | | Vlos | 5905.8 ± 19.4 | 6646.7 ± 99.7 | 5811.0 ± 47.0 | 5674.2 ± 6.6 |
| | | Vel.Disp | 85.6 ± 21.4 | 203.6 ± 41.1 | 210.7 ± 47.0 | 88.0 ± 6.6 |
| Hα_NLR | high | Flux | 1.44E-16 ± 6.53E-18 | 1.43E-16 ± 2.87E-18 | - | - |
| | | Vlos | 6425.7 ± 11.8 | 6714.0 ± 3.3 | - | - |
| | | Vel.Disp | 271.4 ± 10.2 | 163.6 ± 2.2 | - | - |
| | low | Flux | 4.79E-17 ± 2.45E-18 | 3.58E-17 ± 3.28E-18 | 7.11E-17 ± 3.00E-18 | 8.83E-17 ± 2.38E-18 |
| | | Vlos | 5753.0 ± 4.4 | 6317.5 ± 17.8 | 5890.5 ± 6.7 | 5630.9 ± 2.9 |
| | | Vel.Disp | 99.1 ± 4.2 | 225.3 ± 15.5 | 201.7 ± 7.3 | 128.8 ± 3.0 |
| [NII] 6550 | high | Flux | 2.12E-17 ± 1.52E-18 | 6.65E-18 ± 7.39E-19 | | |
| | | Vlos | 6425.6 ± 11.8 | 6714.6 ± 3.3 | | |
| | | Vel.Disp | 225.8 ± 13.1 | 124.3 ± 8.7 | | |
| | low | Flux | 2.56E-17 ± 2.05E-18 | 1.17E-17 ± 1.45E-18 | 2.58E-17 ± 1.44E-18 | 1.14E-17 ± 1.46E-18 |
| | | Vlos | 5751.4 ± 4.4 | 6317.2 ± 17.9 | 5839.6 ± 106.5 | 5691.3 ± 89.7 |
| | | Vel.Disp | 225.8 ± 15.8 | 225.8 ± 23.3 | 270.5 ± 5.4 | 272.1 ± 7.4 |
| [NII] 6585 | high | Flux | 6.36E-17 ± 3.80E-18 | 2.00E-17 ± 1.51E-18 | - | - |
| | | Vlos | 6425.7 ± 11.8 | 6713.1 ± 3.2 | - | - |
| | | Vel.Disp | 224.6 ± 13.1 | 123.6 ± 8.7 | - | - |
| | low | Flux | 7.68E-17 ± 5.47E-18 | 3.51E-17 ± 3.72E-18 | 1.46E-16 ± 3.35E-18 | 1.02E-16 ± 3.25E-18 |
| | | Vlos | 5755.1 ± 4.3 | 6317.9 ± 17.8 | 5842.8 ± 4.8 | 5695.4 ± 7.3 |
| | | Vel.Disp | 224.6 ± 15.7 | 224.6 ± 23.2 | 269.1 ± 5.3 | 270.6 ± 7.4 |
| [OI] 6302 | high | Flux | 3.09E-17 ± 4.90E-18 | 2.94E-17 ± 1.77E-18 | 2.14E-17 ± 2.91E-18 | 6.95E-18 ± 1.19E-18 |
| | | Vlos | 6531.7 ± 33.3 | 6723.9 ± 11.4 | 6958.0 ± 26.9 | 7103.9 ± 34.4 |
| | | Vel.Disp | 234.6 ± 30.4 | 234.6 ± 12.2 | 234.6 ± 27.3 | 234.6 ± 34.4 |
| | low | Flux | 1.89E-17 ± 4.86E-18 | 8.08E-18 ± 1.78E-18 | 3.47E-17 ± 2.88E-18 | 7.61E-18 ± 1.18E-18 |
| | | Vlos | 5847.2 ± 53.8 | 5821.1 ± 41.9 | 5873.2 ± 16.4 | 5664.8 ± 31.0 |
| | | Vel.Disp | 234.6 ± 49.1 | 234.6 ± 44.6 | 234.6 ± 16.7 | 234.6 ± 31.0 |
| [OII] 3727 | high | Flux | 1.27E-16 ± 5.01E-18 | 1.06E-16 ± 2.17E-18 | - | - |
| | | Vlos | 6560.9 ± 11.9 | 6879.8 ± 3.7 | - | - |
| | | Vel.Disp | 351.0 ± 11.9 | 209.4 ± 3.7 | - | - |
| | low | Flux | - | - | 3.48E-17 ± 2.93E-18 | 4.03E-17 ± 2.28E-18 |
| | | Vlos | - | - | 6073.8 ± 11.7 | 5877.6 ± 7.7 |
| | | Vel.Disp | - | - | 160.2 ± 11.7 | 157.8 ± 7.7 |
| [OIII] 5008 | high | Flux | 1.51E-17 ± 4.74E-18 | - | - | - |
| | | Vlos | 6671.4 ± 56.7 | - | - | - |
| | | Vel.Disp | 207.4 ± 52.2 | - | - | - |
| | low | Flux | 2.16E-17 ± 5.96E-18 | 5.70E-18 ± 1.95E-18 | 1.46E-17 ± 2.41E-18 | 7.90E-18 ± 1.40E-18 |
| | | Vlos | 5915.3 ± 68.2 | 6485.7 ± 35.6 | 5884.5 ± 19.5 | 5719.8 ± 10.5 |
| | | Vel.Disp | 296.2 ± 69.8 | 122.9 ± 32.9 | 137.8 ± 19.5 | 68.0 ± 10.5 |
| [SII] 6718 | high | Flux | 2.19E-17 ± 1.97E-18 | 2.09E-17 ± 8.20E-19 | - | - |
| | | Vlos | 6403.3 ± 9.6 | 6674.3 ± 4.9 | - | - |
| | | Vel.Disp | 135.0 ± 10.4 | 139.8 ± 4.7 | - | - |
| | low | Flux | 1.20E-17 ± 2.18E-18 | - | 2.76E-17 ± 2.88E-18 | 1.57E-17 ± 7.78E-19 |
| | | Vlos | 5791.2 ± 34.0 | - | 6379.3 ± 15.6 | 6087.4 ± 4.8 |
| | | Vel.Disp | 195.4 ± 30.8 | - | 176.9 ± 15.8 | 112.7 ± 4.7 |
| [SII] 6732 | high | Flux | 1.69E-17 ± 1.51E-18 | 1.60E-17 ± 6.31E-19 | - | - |
| | | Vlos | 6403.3 ± 9.6 | 6673.8 ± 4.9 | - | - |
| | | Vel.Disp | 134.7 ± 10.4 | 139.5 ± 4.7 | - | - |
| | low | Flux | 9.26E-18 ± 1.67E-18 | - | - | 8.70E-18 ± 5.26E-19 |
| | | Vlos | 5792.6 ± 33.9 | - | - | 6088.2 ± 4.8 |
| | | Vel.Disp | 195.0 ± 30.7 | - | - | 112.5 ± 4.7 |

**Figure 6.52:** Continuation of the table beginning in Fig.6.50, showing the values for region SF_9-12.

| | Vel comp | | SF_13 | SF_14 | SF_15 |
|---|---|---|---|---|---|
| Hß_NLR | high | Flux | - | - | - |
| | | Vlos | - | - | - |
| | | Vel.Disp | - | - | - |
| | low | Flux | 1.84E-17 ± 1.59E-18 | 1.84E-17 ± 1.59E-18 | 1.84E-17 ± 1.59E-18 |
| | | Vlos | 5674.2 ± 6.6 | 5674.2 ± 6.6 | 5674.2 ± 6.6 |
| | | Vel.Disp | 90.3 ± 10.3 | 84.1 ± 1.8 | 94.4 ± 4.8 |
| Hα_NLR | high | Flux | - | - | - |
| | | Vlos | - | - | - |
| | | Vel.Disp | - | - | - |
| | low | Flux | 1.43E-16 ± 2.27E-18 | 7.52E-16 ± 5.88E-18 | 1.86E-16 ± 3.76E-18 |
| | | Vlos | 5741.5 ± 1.8 | 5805.2 ± 0.8 | 5780.3 ± 2.1 |
| | | Vel.Disp | 137.4 ± 1.9 | 120.5 ± 0.8 | 124.8 ± 2.2 |
| [NII] 6550 | high | Flux | - | - | - |
| | | Vlos | - | - | - |
| | | Vel.Disp | - | - | - |
| | low | Flux | 1.61E-17 ± 1.35E-18 | 6.59E-17 ± 3.01E-18 | 1.47E-17 ± 2.28E-18 |
| | | Vlos | 5737.4 ± 55.1 | 5798.5 ± 19.8 | 5796.2 ± 67.2 |
| | | Vel.Disp | 272.1 ± 6.1 | 154.3 ± 2.9 | 272.1 ± 6.8 |
| [NII] 6585 | high | Flux | - | - | - |
| | | Vlos | - | - | - |
| | | Vel.Disp | - | - | - |
| | low | Flux | 1.17E-16 ± 3.05E-18 | 2.90E-16 ± 6.38E-18 | 1.81E-16 ± 5.27E-18 |
| | | Vlos | 5741.2 ± 5.9 | 5802.0 ± 2.9 | 5799.6 ± 6.6 |
| | | Vel.Disp | 270.6 ± 6.0 | 153.5 ± 2.9 | 270.6 ± 6.7 |
| [OI] 6302 | high | Flux | 1.35E-17 ± 2.01E-18 | 1.73E-17 ± 2.49E-18 | 1.21E-17 ± 1.87E-18 |
| | | Vlos | 6977.8 ± 29.8 | 6987.8 ± 28.7 | 6921.4 ± 18.7 |
| | | Vel.Disp | 234.6 ± 29.9 | 234.6 ± 28.8 | 234.6 ± 19.0 |
| | low | Flux | 1.71E-17 ± 1.99E-18 | 4.65E-17 ± 2.46E-18 | 1.98E-17 ± 1.88E-18 |
| | | Vlos | 5739.1 ± 23.2 | 5795.5 ± 10.6 | 5815.8 ± 30.9 |
| | | Vel.Disp | 234.6 ± 23.2 | 234.6 ± 10.6 | 234.6 ± 31.3 |
| [OII] 3727 | high | Flux | - | - | - |
| | | Vlos | - | - | - |
| | | Vel.Disp | - | - | - |
| | low | Flux | 5.83E-17 ± 3.03E-18 | 6.47E-16 ± 7.68E-18 | 1.27E-16 ± 3.33E-18 |
| | | Vlos | 5920.2 ± 6.9 | 5975.7 ± 1.7 | 5961.1 ± 3.6 |
| | | Vel.Disp | 153.5 ± 6.9 | 161.1 ± 1.7 | 158.6 ± 3.6 |
| [OIII] 5008 | high | Flux | - | - | |
| | | Vlos | - | - | - |
| | | Vel.Disp | - | - | |
| | low | Flux | 2.47E-17 ± 2.42E-18 | 3.44E-16 ± 4.70E-18 | 4.60E-17 ± 2.02E-18 |
| | | Vlos | 5755.5 ± 7.8 | 5790.6 ± 1.0 | 5779.5 ± 3.0 |
| | | Vel.Disp | 91.5 ± 7.8 | 82.1 ± 1.0 | 78.7 ± 3.0 |
| [SII] 6718 | high | Flux | - | - | - |
| | | Vlos | - | - | - |
| | | Vel.Disp | - | - | - |
| | low | Flux | 1.45E-17 ± 1.03E-18 | 1.02E-16 ± 1.78E-18 | 2.98E-17 ± 1.47E-18 |
| | | Vlos | 6187.8 ± 6.1 | 6249.5 ± 1.7 | 6228.5 ± 5.3 |
| | | Vel.Disp | 101.4 ± 6.1 | 114.7 ± 1.7 | 123.2 ± 5.0 |
| [SII] 6732 | high | Flux | - | - | - |
| | | Vlos | - | - | - |
| | | Vel.Disp | - | - | - |
| | low | Flux | 8.80E-18 ± 7.36E-19 | 5.93E-17 ± 1.24E-18 | 1.86E-17 ± 1.08E-18 |
| | | Vlos | 6188.4 ± 6.1 | 6249.9 ± 1.7 | 6229.0 ± 5.3 |
| | | Vel.Disp | 101.2 ± 6.1 | 114.5 ± 1.7 | 123.0 ± 5.0 |

**Figure 6.53:** Continuation of the table beginning in Fig.6.50, showing the values for region SF_13-15.

### 6.2.2 Gas Kinematics

As can be seen in the table in Fig.6.50-6.53 there are dual velocity components in several of the regions in the SF ridge, confirming the presence of dual components as suggested in Duarte Puertas et al. (2019). The fit of the H$\alpha$ − [NII] complex and the [OII]$\lambda3727$ line in region SF_1,2,5,7,8, are presented in Fig.6.54-6.58, clearly showing the presence and variety of the dual velocity components.

The velocity dispersion in the SF ridge spans $70 - 360$ km/s, while the line-of-sight velocities span $5670 - 7100$ km/s. The relation of the velocities and their connection to other galaxies and areas, is discussed in the Summary & Conclusions in Chapter 7.
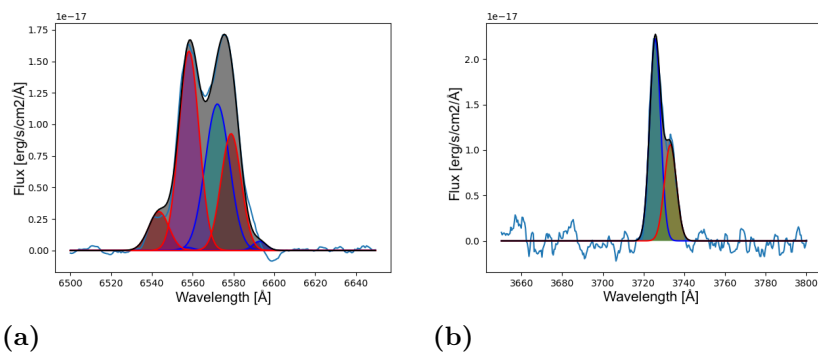


**Figure 6.54:** Illustrating the dual velocity components in the star-forming ridge, region SF_1. The black line is the best fit. (a) The fit of H$\alpha$−[NII] emission. In red are the lines that belong to one velocity component, while the other is blue; (b) The fit of the [OII]$\lambda3727$ line, the two different colours denote the different velocity components.
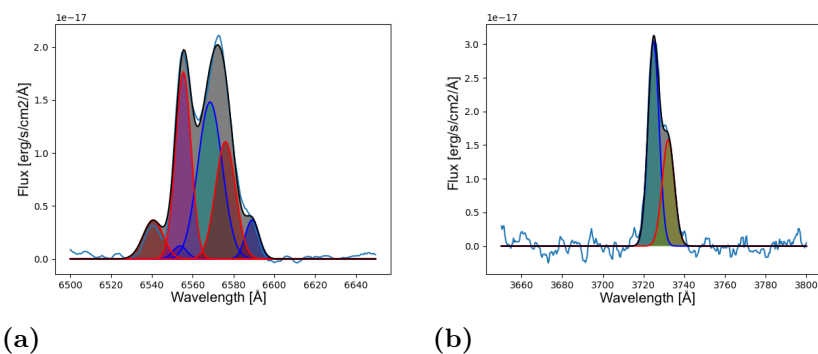


**Figure 6.55:** Illustrating the dual velocity components in the star-forming ridge, region SF_2. The black line is the best fit. (a) The fit of H$\alpha$−[NII] emission. In red are the lines that belong to one velocity component, while the other is blue; (b) The fit of the [OII]$\lambda3727$ line, the two different colours denote the different velocity components.
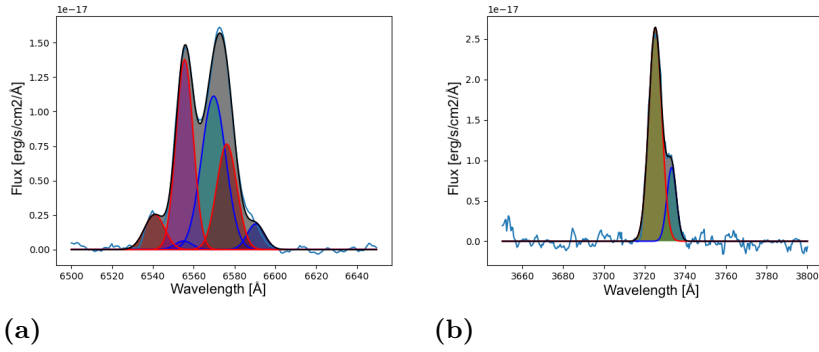
**Figure 6.56:** Illustrating the dual velocity components in the star-forming ridge, region SF_5. The black line is the best fit. (a) The fit of H$\alpha$−[NII] emission. In red are the lines that belong to one velocity component, while the other is blue; (b) The fit of the [OII]$\lambda$3727 line, the two different colours denote the different velocity components.
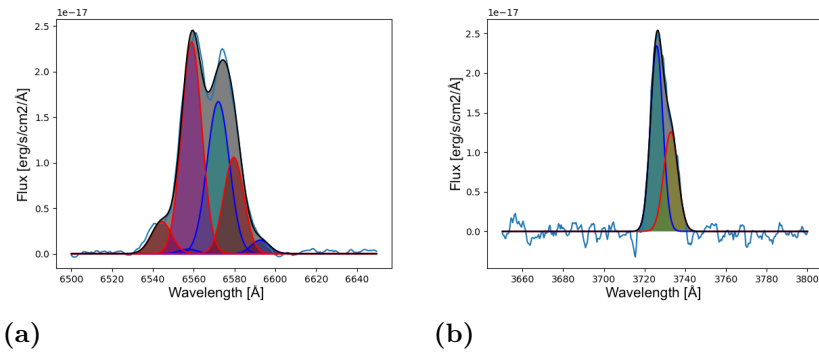


**Figure 6.57:** Illustrating the dual velocity components in the star-forming ridge, region SF_7. The black line is the best fit. (a) The fit of H$\alpha$−[NII] emission. In red are the lines that belong to one velocity component, while the other is blue; (b) The fit of the [OII]$\lambda$3727 line, the two different colours denote the different velocity components.
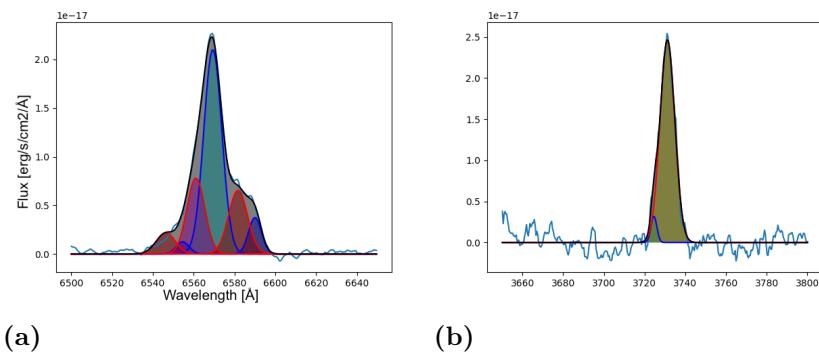


**Figure 6.58:** Illustrating the dual velocity components in the star-forming ridge, region SF_8. The black line is the best fit. (a) The fit of H$\alpha$−[NII] emission. In red are the lines that belong to one velocity component, while the other is blue; (b) The fit of the [OII]$\lambda$3727 line, the two different colours denote the different velocity components.

### 6.2.3 Excitation Mechanisms

Regarding the excitation mechanisms in the SF ridge, the low and high line-of-sight velocity components can be individually placed in the BPT diagrams. Fig.6.59, 6.60 and 6.61 present the [NII], [SII] and [OI] BPT emission line diagnostic diagrams, respectively. In general the regions are snugly placed in the area of the plots showing star-forming ionisation. However, there are several regions showing up in the AGN-parts of the diagrams. LINER-like emission-line ratios can be incited by shocks, and even Seyfert-like line ratios can be induced with a photoionised precursor, if the shock is travelling fast enough (Allen et al., 2008; Rodríguez-Baras et al., 2014). This is the case for region SF_14 in the west ridge, while region SF_15 leans more towards LINER-like line ratios. Furthermore, there are several regions positioned in the composite part of the diagnostic diagrams, Fig.6.59. It is clear that the shock front has a large impact on the ionisation of the gas in the star-forming ridge.
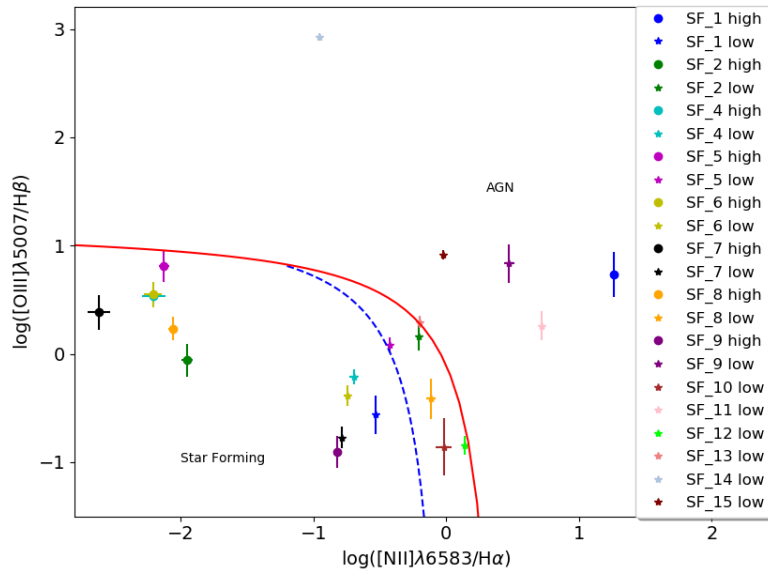


**Figure 6.59:** BPT diagnostic diagram, $\log([\text{NII}]\lambda 6585/\text{H}\alpha)$ vs $\log([\text{OIII}]\lambda 5008/\text{H}\beta)$, for the star-forming ridge, region SF_1-11, and the west ridge, region SF_12-15. The low velocity component is marked "low" and the high "high".
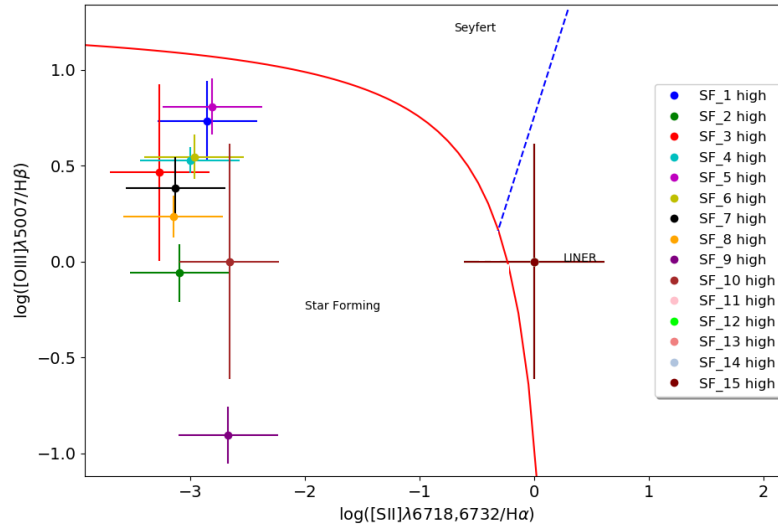
**Figure 6.60:** BPT diagnostic diagram, $\log([SII]\lambda 6718, 6732/H\alpha)$ vs $\log([OIII]\lambda 5008/H\beta)$, for the star-forming ridge, region SF_1-11, and the west ridge, region SF_12-15. The low velocity component is marked "low" and the high "high".
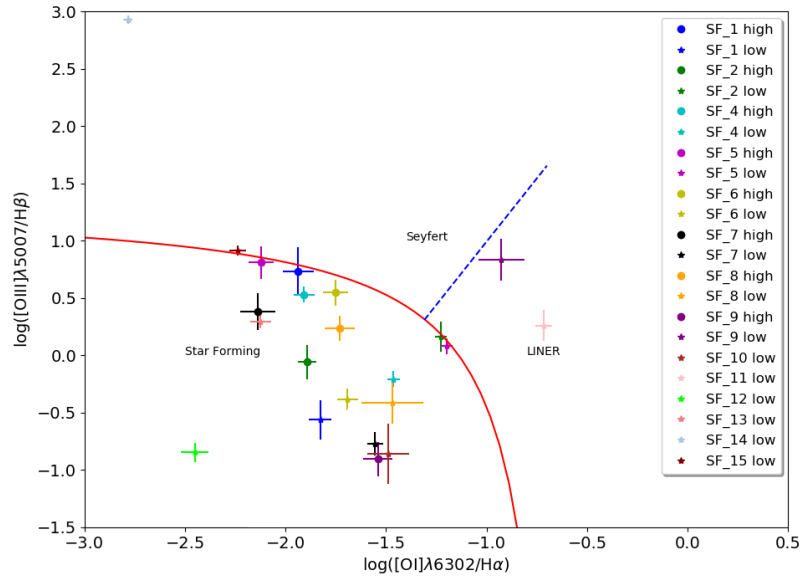


**Figure 6.61:** BPT diagnostic diagram, $\log([OI]\lambda 6302/H\alpha)$ vs $\log([OIII]\lambda 5008/H\beta)$, for the star-forming ridge, region SF_1-11, and the west ridge, region SF_12-15. The low velocity component is marked "low" and the high "high".

## 6.3 The NGC7318 Pair

The currently interacting galaxy pair contain two quiescent galaxies, NGC7318A and B. This chapter begins by presenting the stellar position-velocity maps and the spectra of the two galaxies. Thereafter the kinematics of each galaxy is discussed separately. Due to the lack of gaseous emission the excitation mechanisms cannot be analysed, and the discussion herein relies primarily on the stellar continuum and absorption.

### 6.3.1 Maps & Spectra

The spectrum of NGC7318A and B, presented in Fig.6.62 and 6.63 respectively, support the claim of quiescence and show clear stellar continuum and absorption features in both galaxies. While Rodríguez-Baras et al. (2014) find no emission in the NGC7318 pair, the data presented here indicates gaseous emission near the nuclei of both NGC7318A and B, as presented in the table in Fig.6.64. As far as possible the $H\alpha - [NII]$ complex has been fitted, displaying unusually large FWHMs as reflected in the velocity dispersions listed in table 6.64. [OIII], $H\beta$, [OI] and [SII] cannot be properly fitted, the [SII] doublet in NGC7318A has a very strange shape, and in NGC7318B there is only one line. These may be side effects of the stellar continuum subtraction.

Furthermore, Fig.6.65 displays the line-of-sight velocity and velocity dispersion as a function of position in the pair. To the top left, the line-of-sight velocity dispersion of NGC7318A is presented, where the 0 position is set to the centre as deduced from the peak stellar continuum and the 0 velocity is set to the mean line-of-sight velocity of the central 1.5″ (as deduced from the spectrum in Fig.6.62). The bottom left plot is the same as the top left but for NGC7318B. Whereas, to the right in Fig.6.65 the velocity dispersion for the pair is plotted in the same manner.
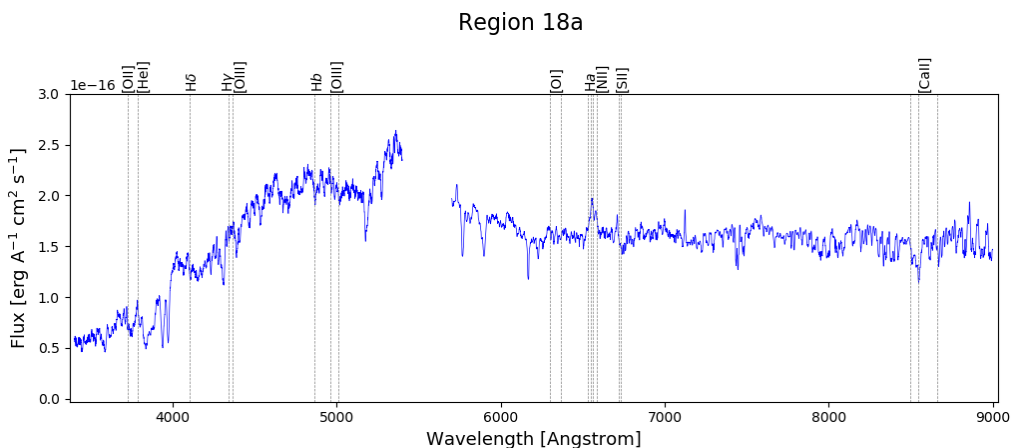


**Figure 6.62:** Spectrum of the central 1.5″ of NGC7318A, region 18a. Vertical dotted lines mark the expected line centres of different gas emission lines at the group average redshift of 0.0215, the spectrum is also corrected to this average redshift.
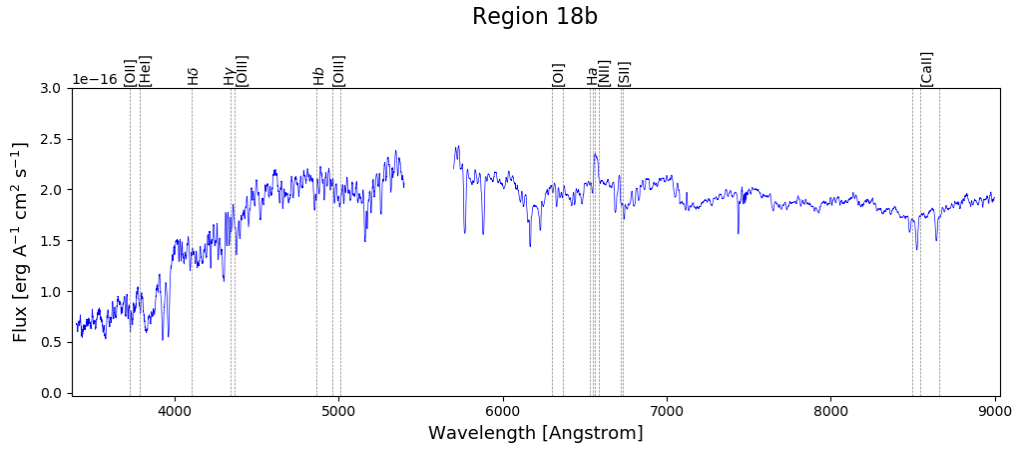
**Figure 6.63:** Spectrum of the central 1.5″ of NGC7318B, region 18b. Vertical dotted lines mark the expected line centres of different gas emission lines at the group average redshift of 0.0215, the spectrum is also corrected to this average redshift.



|  |  | NGC7318A | NGC7318B |
|---|---|---|---|
| **Hα_NLR** | Flux | 9.91E-16 ± 1.14E-16 | 7.41E-16 ± 6.12E-17 |
|  | Vlos | 6094.4 ± 52.6 | 6188.2 ± 34.3 |
|  | Vel.Disp | 408.5 ± 23.0 | 355.6 ± 23.1 |
| **[NII] 6550** | Flux | 1.26E-16 ± 2.07E-17 | 2.07E-16 ± 2.69E-17 |
|  | Vlos | 5962.1 ± 1164.1 | 6093.6 ± 612.5 |
|  | Vel.Disp | 456.0 ± 29.1 | 353.5 ± 27.0 |
| **[NII] 6585** | Flux | 1.08E-15 ± 1.25E-16 | 5.18E-16 ± 5.50E-17 |
|  | Vlos | 5964.6 ± 60.6 | 6095.5 ± 38.0 |
|  | Vel.Disp | 453.6 ± 28.9 | 351.6 ± 26.8 |
| **[OII] 3727** | Flux | 2.81E-17 ± 4.86E-18 | - |
|  | Vlos | 5949.1 ± 20.1 | - |
|  | Vel.Disp | 133.3 ± 20.1 | - |
|  |  |  |  |
| **stellar** | Vlos | 6787.3 ± 4.9 | 5973.2 ± 3.5 |
|  | Vel.Disp | 263.6 ± 10.7 | 168.9 ± 4.0 |

**Figure 6.64:** Table containing the flux in $ergcm^2s^{-1}$, line-of-sight velocity and velocity dispersion in km/s, of each atomic species, as well as the stellar component, in the inner 1.5″ of NGC7318A and B.
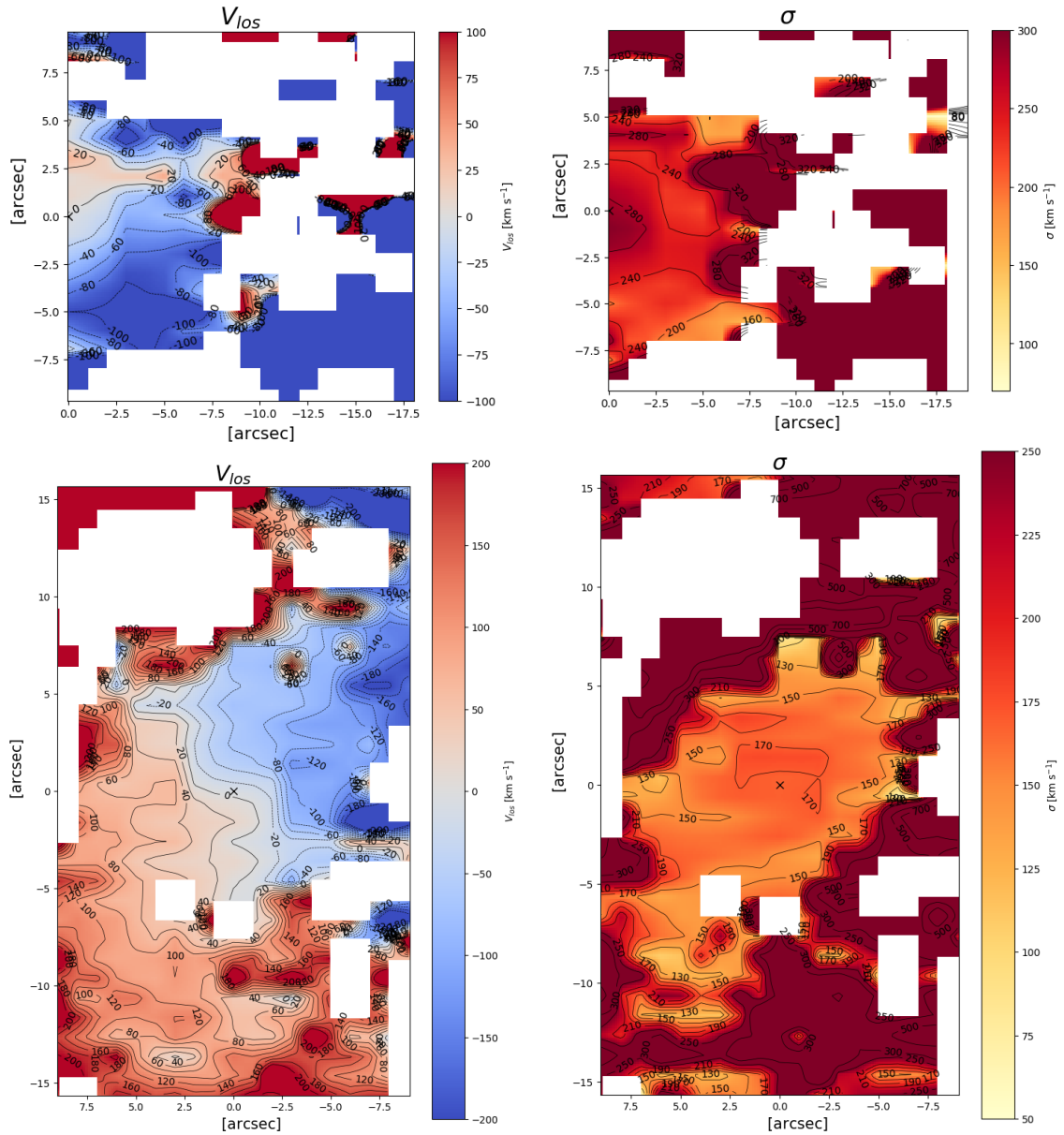
**Figure 6.65:** *Top left:* The line-of-sight velocity of NGC7318A, with 0 km/s set to the average of the central $1.5''$, i.e., $6787.3 \pm 4.9$ km/s. The cross marks at 0 RA, 0 Dec the centre of the galaxy as pinpointed by the peak stellar continuum emission;
*Bottom left:* The line-of-sight velocity of NGC7318B, with 0 km/s set to the average of the central $1.5''$, i.e., $5973.2 \pm 3.5$ km/s. The cross marks the centre of the galaxy as pinpointed by the peak stellar continuum emission;
*Top right:* The stellar velocity dispersion for the NGC7318A. The cross marks the centre of the galaxy as pinpointed by the peak stellar continuum emission;
*Bottom right:* The stellar velocity dispersion for the NGC7318B. The cross marks the centre of the galaxy as pinpointed by the peak stellar continuum emission.

### 6.3.2 NGC7318A: Kinematics & Rotation

The velocity dispersion shows a mean of $263.6 \pm 10.7$ km/s in the inner $1.5''$ of NGC7318A, thereafter the velocity dispersion decreases outwards near-circularly, after which it blends with the IGM and higher velocity dispersions, as seen in the top right image in Fig.6.65. The velocity dispersion as a function of radius is plotted in Fig.6.66. This shape of the velocity dispersion curve is as expected and common for elliptical galaxies (Romanowsky et al., 2004).

From the line-of-sight velocity map of NGC7318A, the top left plot in Fig.6.65, a general rotation of the galaxy can be noted. From the velocity field a position angle of 62° is obtained, considering the rotation of the telescope of 242°.
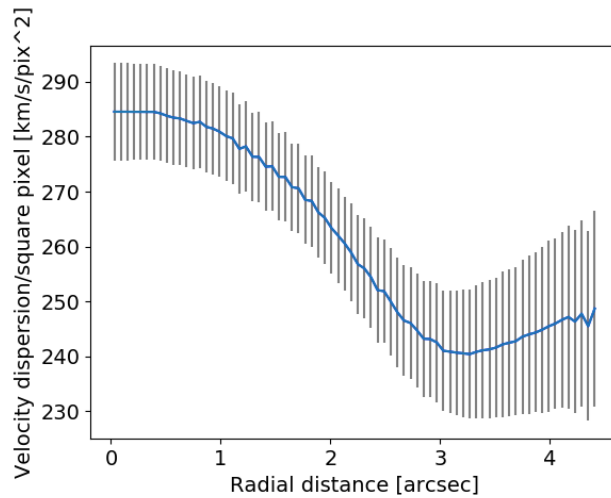


**Figure 6.66:** The velocity dispersion in NGC7318A as a function of radius.

### 6.3.3 NGC7318B: Kinematics & Rotation

The mean stellar velocity dispersion of NGC7318B in the central 1.5" is $168.9 \pm 4.0$ km/s, while an increased velocity dispersion follows the S-shape of the line-of-sight velocity field near the nucleus, as seen in Fig.6.65. In the outskirts of NGC7318B, towards the star-forming ridge, there is an increase in $H\alpha - [NII]$ emission, as shown in Fig.6.1.

Furthermore, the centre of the peak continuum emission is nicely located in the S-shape of the velocity field, as is clear in Fig.6.65. NGC7318B's velocity field is suitable for fitting a rotation field model and a function describing a rotation field, presented by Bertola et al. (1991), for a rotating disk assuming circular orbits in the galaxy plane is:

$$V_r = V_s + \frac{AR cos(\psi - \psi_0) sin(i) cos^p(i)}{(R^2 [sin^2(\psi - \psi_0) + cos^2(\psi - \psi_0)] + c_0^2 cos^2(i))^{p/2}} \quad (6.1)$$

where $V_r$ is the rotation velocity as a function of the polar coordinates R and $\psi$, $V_s$ is the systemic velocity, $A$ is the amplitude of the rotation field, $\psi_0$ is the position angle of the line-of-nodes, $i$ is the inclination of the disk, $p$ is a measure of the

slope of the rotation field at large radii, and $c_0$ is a concentration parameter. Using this equation to fit the rotation field in NGC7318B yields the results illustrated in Fig.6.67. A more stringent SNR is adopted to improve the fit, a SNR of 3 instead of 2. In Fig.6.67, plot (a) shows the velocity field, (b) the model used to fit the field and (c) the residual. As can be seen there are some residuals tracing the S-shape of the field, but apart from that this simple model fits the field well. The fit provides a systemic line-of-sight velocity of 5973.2$\pm$3.5km/s and an inclination, $i$, of 102.4$\pm$1.9° considering the 242° rotation of the telescope, using an amplitude of the rotation field, $A$, of 290 km/s and a position angle, $\psi_0$, of 25°.



**(a)**                                    **(b)**                                    **(c)**
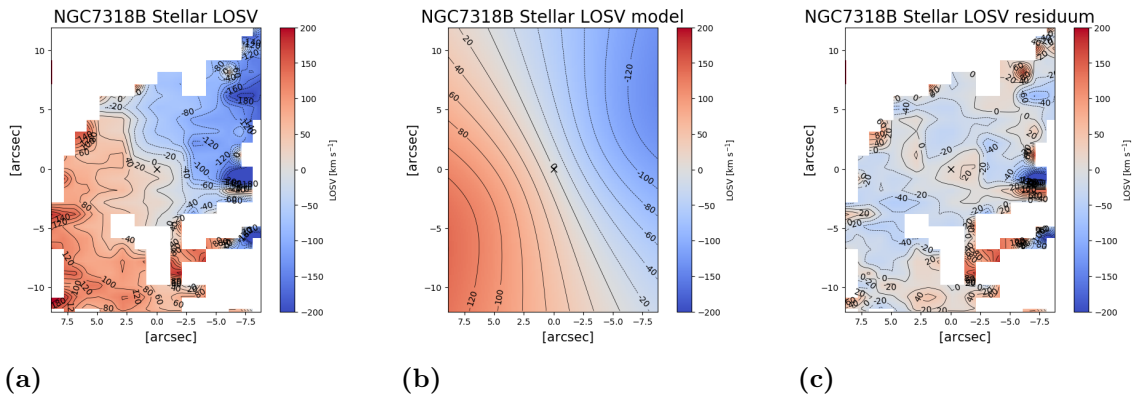
**Figure 6.67:** Rotation field fit of the stellar line-of-sight velocity field in NGC7318B. (a) Observed stellar line-of-sight velocity at a SNR> 3; (b) Model used to fit the rotation field; (c) Residual.

111

# 6.4 NGC7317

NGC7317 is the elliptical galaxy that may or may not have interacted with NGC7319 and/or NGC7318A in the past. This chapter presents the spectrum of NGC7317 as well as its line-of-sight velocity and velocity dispersion as a function of position along the slit (as only one slit has been positioned covering NGC7317).

## 6.4.1 Spectrum

The spectrum of NGC7317 is presented in Fig.6.68, showing a quiescent galaxy with significant lack of gaseous emission lines. This lack of gaseous content disables the possibility of an analysis of the excitation mechanisms using the BPT diagnostic diagrams. The removal of the gas from the galaxy may have been facilitated by a previous interaction, in which NGC7317 was stripped of its ISM. Due to the spectral content, the subsequent analysis and discussion is based on the stellar component. The values of the velocities of the central $1.5''$ of the nucleus are presented in the table in Fig.6.69.
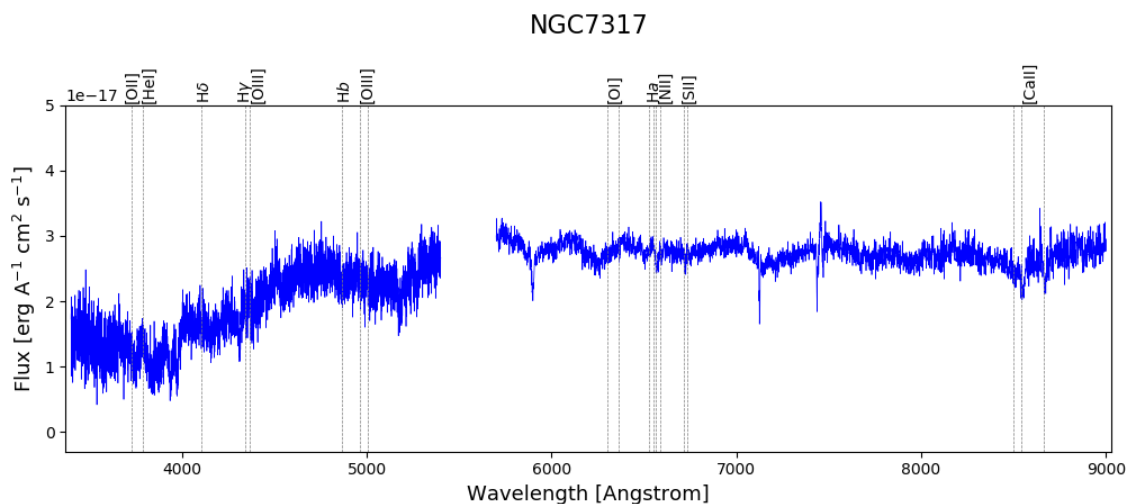


**Figure 6.68:** The spectrum of NGC7317. Vertical dotted lines mark the expected line centres of different gas emission lines at the group average redshift of 0.0215, the spectrum is also corrected to this average redshift.

|  |  | NGC7317 |
|---|---|---|
| **stellar** | Vlos | 6734.2 ± 5.2 |
|  | Vel.Disp | 262.7 ± 6.9 |

**Figure 6.69:** Table containing the line-of-sight velocity and velocity dispersion in km/s of the stellar component in the inner 1.5" of NGC7317.

## 6.4.2   Kinematics & Rotation

Fig.6.70 shows the line-of-sight velocity as a function of position along the slit with the 0 position as the stellar continuum peak, i.e., the galaxy centre. As can be seen the line-of-sight velocity increases slightly on each side of the nucleus before declining. While the velocity dispersion, displayed as a function of position along the slit in Fig.6.71, shows a slightly bumpy function quite steadily declining outwards. Together, the line-of-sight velocity and the velocity dispersion show a mildly rotating elliptical galaxy, potentially still in morphological transition.
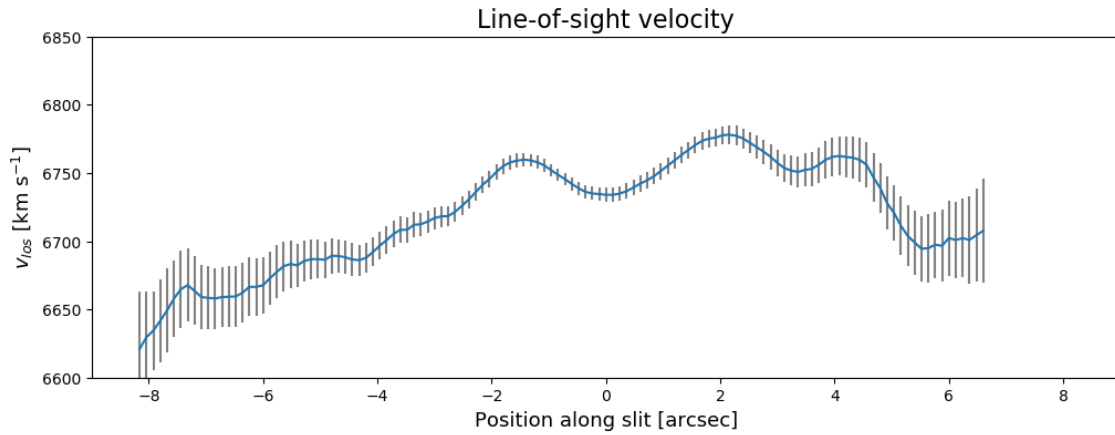


**Figure 6.70:** The line-of-sight velocity of the stellar component along the slit covering NGC7317. The 0 corresponds to the centre of the galaxy, set to the peak stellar continuum emission.
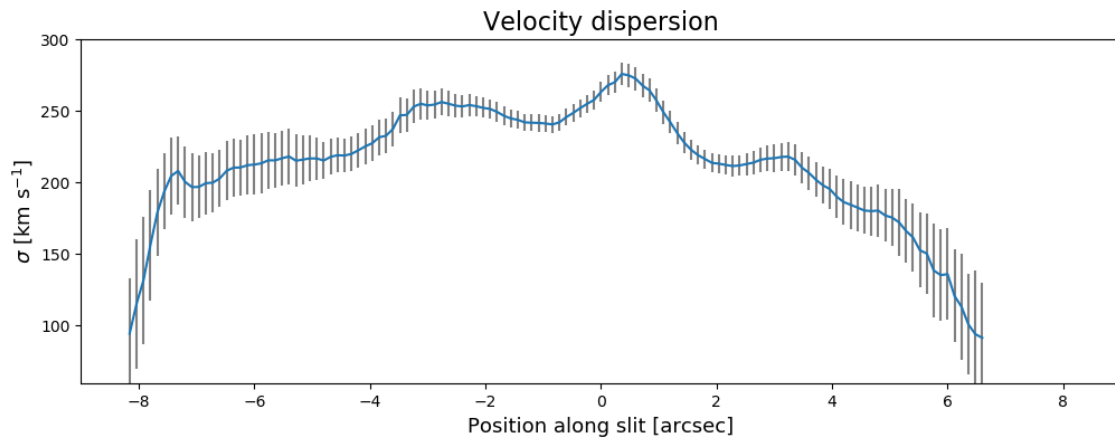


**Figure 6.71:** The velocity dispersion of the stellar component along the slit covering NGC7317. The 0 position corresponds to the centre of the galaxy.

# 7

# Summary & Conclusions

I have carried out optical long-slit spectroscopy observations of the compact galaxy group Stephan's Quintet, covering NGC7317 and an area of the group containing the active galaxy NGC7319, the currently interacting pair NGC7318A and B, as well as the star-forming ridge and the bridge connecting NGC7319 and the NGC7318 pair. Using several slit positions the area observed have been mapped with focus on the nucleus of the galaxies and the large-scale dynamics. An extensive analysis has been put forth in the previous chapters, presenting maps of the stellar continuum and gaseous emission, excitation mechanisms and velocities. As is expected of compact galaxy groups, large amounts of gas is present in the inter-galactic medium, facilitating shocks and star-formation as well as tracing the history of the group's interactions.

This chapter begins with a summary of the results specific to the individual galaxies and areas. Thereafter, I discuss the connections between the velocities of the different gas congregations in the regions (marked in Fig.6.1).

## 7.1 The Galaxies & the IGM

### NGC7319

The data presented in this work shows no indication that Stephan's Quintet would deviate from the claim by Hickson (1997), that only the first-ranked (most massive) galaxy of the group develops an AGN, as NGC7319 is the only galaxy showing AGN qualities in SQ. The high resolution data shows a BLR in this galaxy, revealing its Seyfert 1 nature. Furthermore, region 19_0-6, apart from 19_4, show AGN/Seyfert excitation mechanisms. Region 19_4 indicates stellar ionisation/LINER.

The velocity field of the stellar and gaseous components in NGC7319 are displaced, where the centre of the gas velocity field is shifted to the south-west (upper right in the maps presented in chapter 6.1) of the stellar continuum peak/galaxy centre, although the peak gas emission shows a tendency to extend towards the north-east (lower left). The displacement is such that, by studying the extension of the gas and stellar emission, it appears that the two disks are almost perpendicular to each other.

Furthermore, there is a significant difference between the average line-of-sight velocities of the gaseous and stellar disks. The outflow may prove to have an important role in this discrepancy. The data presented here provides values in the region of the outflow of $476.6 \pm 13.8$ km/s blue-shifted from the systemic stellar line-of-sight velocity of the galaxy, and the outflow is traced by shocked gas, as can be seen in the

[OIII]$\lambda$5008/H$\beta$ ratio in Fig.6.25b. We may be looking down an outflow funnel or at a large-scale nuclear wind. The BPT diagnostic diagrams, Fig.6.26-6.28, favour a nuclear wind.

A gaseous rotating disk without a stellar population is unlikely, and as the bar is undisturbed a tidal event can not have caused the discrepancy between the gas and stellar disks. The gas extension is perpendicular to the stellar disk, and though a significant contribution from star formation cannot be excluded, it is possible that all of the gas observed is in the form of a nuclear wind.

### NGC7318A & B
NGC7318A and B are both quiescent galaxies with low gas content. NGC7318A is an elliptical galaxy showing a velocity dispersion as a function of radius that is typical for elliptical galaxies. NGC7318B is a spiral galaxy with a beautiful velocity field suitable for fitting a model rotation field, Fig.6.67, which properly quantifies the galaxy's velocity field. There is slight gas emission in the nuclei of these galaxies, gas emission that show large velocity dispersions and line-of-sight velocities near the values of the intruder galaxy, NGC7318B.

### NGC7317
NGC7317 is another quiescent elliptical galaxy. The velocity dispersion as a function of radius is bumpy, as is the line-of-sight velocity as a function of radius, Fig.6.70 and 6.71, indicating a slightly rotating galaxy potentially still in morphological transition.

### The IGM: the Bridge, the Star-Forming Ridge & the West Ridge
There is extensive amount of gas in the shocked star-forming ridge and in the bridge connecting NGC7319 and the NGC7318 pair. The bridge shows strong [OII]$\lambda$3727, H$\alpha$, [NII]$\lambda$6550,6858 and [SII]$\lambda$6718,6732 emission and in several cases dual velocity components. The star-forming ridge, showing strong emission in these lines as well as in [OIII]$\lambda$5008 and [OI]$\lambda$6302, also exhibits multiple velocity components in several positions, as shown in the table in Fig.7.1, which confirms the results by Duarte Puertas et al. (2019).

The bridge is mainly ionised by star-formation processes, as is the star-forming ridge. But as the star-forming ridge is shocked, it reaches higher ionisation and in several regions displays LINER-like emission-line ratios.

The west ridge shows similar composition as the star-forming ridge, but with negligible [OI]$\lambda$6302 emission and significant H$\beta$ and [OIII]$\lambda$5008 emission. Indicating that the gas in the west ridge is more highly ionised, potentially enabled by higher metallicites in this area, as the oxygen content is higher in the west ridge compared to the SF ridge.

## 7.2 The Velocities & their Relation to the Galaxies

Fig.7.1 shows a table containing the galaxies and the regions, and their average velocities of different velocity congregations. Here I will discuss the particularities regarding these velocity congregations. Although note that considering the similar line-of-sight velocities of the core group, NGC7317 and NGC7318A/NGC7319, it is difficult to distinguish the origin based on velocities alone. Furthermore, gas deposits mix and interact, forming intermittent line-of-sight velocities. Deducing metallicities could be the next step to further our understanding of the gas congregations' origins.

**NGC7319**
The regions in NGC7319 show 2 or 3 velocity components. In general, one low in the [OI]$\lambda$6302 emission line at $\sim$ 5750 km/s and one high component at $\sim$ 6870 km/s in the combination of the [OII]$\lambda$3727 line and the stellar population. In the nuclear region, all gaseous components adhere to the higher velocity together with the stellar contribution, apart from the [OI]$\lambda$6302 line that shows the lower velocity, a velocity near that of NGC7320C. Region 19_6 and 19_7 lack the component at $\sim$6870 km/s, in these regions the stellar contribution is small and the velocities of the outflow dominate. Region 19_6 also lacks the low component at $\sim$ 5750 km/s, while 19_7's low velocity component may originate from NGC7320C at the creation of the inner tidal tail.

**The Bridge**
The regions in the bridge also display 2-3 velocity components. Furthermore, in the bridge there is a gradient, closer to NGC7319 the regions lean towards higher velocities and closer to the SF ridge the regions show a tendency towards lower velocities. Region b_3 and b_4 are likely part of the spiral arm originating from NGC7319, showing a superposition of velocities at $\sim$ 6450 km/s and that of the intruder galaxy NGC7318B at $\sim$ 5700 km/s. Region b_1 and b_2 are more snugly placed in the area of the inner tidal tail, showing velocities near that of NGC7319 at $\sim$ 6800 km/s, and somewhat lower at $\sim$ 6300 km/s.

**The Star-Forming Ridge**
Regions SF_1-10 are contained within what is commonly called the star-forming ridge, while SF_11 is closer to NGC7318B. Actually, regions SF_9-11 are located on the edge of the SF ridge closest to NGC7318B, which is clear from their velocity congregations. As we draw nearer to NGC7318B a separate component at $\sim$ 5840 km/s becomes clearer, while in region SF_1-8 the gas provides a low velocity component of $\sim$ 6100 km/s instead. Further, in the SF ridge the gas lines are often split into this low velocity component and a high velocity component at $\sim$ 6900 km/s. In SF_1-2 this high component is from the [OII]$\lambda$3727 line only, while in SF_3 the high velocity component is due to [OI]$\lambda$6302, [OII]$\lambda$3727 and [OIII]$\lambda$5008.

**NGC7318A**
For NGC7318A the high velocity component at 6734 km/s is from the stellar disk,

while the lower velocity component at 6002 km/s is the gaseous emission. The gas emission is weak in this galaxy, meaning that much weight cannot be put upon the lower velocity component. However, if this value is accurate it indicates that we are either detecting the gas emission extracted from NGC7318B or a gas congregation deposited in this location during the previous interaction with NGC7320C.

**NGC7318B**

NGC7318B also shows two velocity congregations, the lower one from the stellar population at 5973 km/s and the higher one at 6142 km/s for the gas. The gas detected here may be a combination of gas originating from NGC7318B, gas near NGC7318A and gas in the IGM. But it is also possible that the gas detection is the NGC7318B gas disk decoupled from the stellar disk through NGC7318B's interaction with the IGM and NGC7318A.

**The West Ridge**

The west ridge, regions SF_12-15, shows 3 velocity congregations at $\sim 5770$ km/s, $\sim 6180$ km/s and $\sim 7000$ km/s. The high velocity component corresponds to the [OI]$\lambda 6302$ line, the middle one to the [SII]$\lambda 6718, 6732$ doublet and the low component consist of the rest of the gas emission lines. The west ridge can be further split into two areas, one that extends the western NW tail (the tails are marked in Fig.3.2), regions SF_14-15, and one that follows the dust trail connecting the SW tail to the western NW tail, SF_12-13. Regions SF_14-15, in the extension of the NW tail, show slightly higher velocities of the low and middle component, i.e., $\sim 5800$ km/s and $\sim 6240$ km/s, compared to that of SF_12-13 at $\sim 5730$ km/s and $\sim 6130$ km/s, while the high component remains approximately stable throughout the west ridge.

| | | 5600-5800 | 5800-6000 | 6000-6200 | 6200-6400 | 6400-6600 | 6600-6800 | 6800-7000 |
|---|---|---|---|---|---|---|---|---|
| NGC7317 | Vlos | | | | | | 6734.2 ± 5.2 | |
| | Vel.Disp | | | | | | 262.7 ± 6.9 | |
| NGC7318A | Vlos | | | 6002.7 ± 27.6 | | | 6787.3 ± 4.9 | |
| | Vel.Disp | | | 331.8 ± 14.0 | | | 263.6 ± 10.7 | |
| NGC7318B | Vlos | | 5973.2 ± 3.5 | 6141.9 ± 25.6 | | | | |
| | Vel.Disp | | 168.9 ± 4.0 | 353.6 ± 17.7 | | | | |
| NGC7319 (19_0) | Vlos | | 5837.6 ± 25.6 | | | | 6745.8 ± 1.8 | |
| | Vel.Disp | | 234.6 ± 27.3 | | | | 205.2 ± 18.0 | |
| 19_1 | Vlos | 5720.3 ± 39.7 | | | | 6447.5 ± 4.8 | | 6919.6 ± 54.3 |
| | Vel.Disp | 234.6 ± 41.2 | | | | 196.9 ± 2.3 | | 402.9 ± 56.5 |
| 19_2 | Vlos | 5685.8 ± 24.6 | | | | 6585.1 ± 4.4 | | 6862.1 ± 9.1 |
| | Vel.Disp | 234.6 ± 26.1 | | | | 221.7 ± 1.7 | | 216.8 ± 10.0 |
| 19_3 | Vlos | | 5811.1 ± 24.3 | | | | 6662.4 ± 4.6 | 6827.9 ± 8.0 |
| | Vel.Disp | | 234.6 ± 25.9 | | | | 236.5 ± 1.3 | 219.8 ± 7.9 |
| 19_4 | Vlos | 5731.4 ± 24.9 | | 6130.8 ± 28.9 | | 6592.3 ± 10.7 | | 6819.2 ± 28.0 |
| | Vel.Disp | 234.6 ± 26.4 | | 185.1 ± 26.9 | | 183.9 ± 5.7 | | 154.6 ± 21.5 |
| 19_5 | Vlos | 5639.6 ± 31.4 | | | 6350.5 ± 143.8 | | | 6819.0 ± 21.6 |
| | Vel.Disp | 234.6 ± 33.3 | | | 152.7 ± 66.3 | | | 245.4 ± 18.4 |
| 19_6 | Vlos | | | | 6386.4 ± 15.6 | | 6650.4 ± 31.4 | |
| | Vel.Disp | | | | 220.3 ± 8.7 | | 329.0 ± 31.6 | |
| 19_7 | Vlos | | 5874.0 ± 43.1 | | 6327.8 ± 9.7 | | 6644.2 ± 6.6 | |
| | Vel.Disp | | 234.6 ± 45.8 | | 181.7 ± 8.6 | | 180.2 ± 6.5 | |
| b_1 | Vlos | | | | 6350.4 ± 5.1 | 6569.8 ± 4.5 | | 6924.3 ± 23.7 |
| | Vel.Disp | | | | 152.9 ± 5.2 | 158.7 ± 4.0 | | 198.1 ± 21.5 |
| b_2 | Vlos | | | | 6229.0 ± 18.4 | | 6784.3 ± 11.3 | |
| | Vel.Disp | | | | 182.3 ± 32.1 | | 169.2 ± 11.3 | |
| b_3 | Vlos | 5648.2 ± 40.6 | | | 6386.4 ± 7.4 | | 6623.3 ± 5.4 | |
| | Vel.Disp | 232.6 ± 43.6 | | | 184.0 ± 4.0 | | 191.8 ± 5.4 | |
| b_4 | Vlos | 5740.6 ± 32.2 | | | | 6418.2 ± 9.4 | | |
| | Vel.Disp | 234.6 ± 31.1 | | | | 232.7 ± 3.9 | | |
| SF_1 | Vlos | | | 6115.7 ± 13.4 | | 6518.0 ± 21.0 | 6751.7 ± 16.2 | 6925.0 ± 21.8 |
| | Vel.Disp | | | 225.5 ± 10.4 | | 167.0 ± 14.0 | 190.1 ± 17.7 | 233.0 ± 18.1 |
| SF_2 | Vlos | | | 6022.8 ± 5.2 | 6259.4 ± 8.9 | | 6606.8 ± 13.8 | 6842.8 ± 18.7 |
| | Vel.Disp | | | 193.2 ± 4.8 | 210.4 ± 6.6 | | 232.0 ± 12.3 | 233.5 ± 14.5 |
| SF_3 | Vlos | | | 6047.8 ± 7.1 | 6366.8 ± 32.3 | | | 6839.1 ± 29.0 |
| | Vel.Disp | | | 146.2 ± 14.2 | 211.8 ± 12.7 | | | 267.6 ± 21.9 |
| SF_4 | Vlos | | | 6123.7 ± 5.1 | 6349.5 ± 6.0 | | | 6869.6 ± 4.9 |
| | Vel.Disp | | | 238.4 ± 5.9 | 251.6 ± 6.2 | | | 194.1 ± 8.0 |
| SF_5 | Vlos | | | 6046.5 ± 4.3 | | | 6674.7 ± 14.8 | |
| | Vel.Disp | | | 255.5 ± 4.2 | | | 208.6 ± 11.2 | |
| SF_6 | Vlos | | | | 6228.2 ± 6.9 | | | 6837.6 ± 6.7 |
| | Vel.Disp | | | | 238.4 ± 7.1 | | | 193.3 ± 8.0 |
| SF_7 | Vlos | | | 6189.5 ± 22.7 | | | | 6817.4 ± 10.0 |
| | Vel.Disp | | | 239.7 ± 11.2 | | | | 198.0 ± 10.8 |
| SF_8 | Vlos | | | | 6231.3 ± 12.8 | | 6658.4 ± 8.2 | |
| | Vel.Disp | | | | 156.3 ± 9.9 | | 207.7 ± 6.9 | |
| SF_9 | Vlos | | 5814.0 ± 12.7 | | | 6478.7 ± 8.6 | | |
| | Vel.Disp | | 194.5 ± 12.6 | | | 229.7 ± 8.3 | | |
| SF_10 | Vlos | | 5821.1 ± 41.9 | | 6359.6 ± 11.0 | | 6717.5 ± 12.6 | |
| | Vel.Disp | | 234.6 ± 44.6 | | 199.6 ± 12.3 | | 167.3 ± 5.7 | |
| SF_11 | Vlos | | 5888.0 ± 17.1 | | | | | 6958.0 ± 26.9 |
| | Vel.Disp | | 212.1 ± 8.0 | | | | | 234.6 ± 27.3 |
| SF_12 | Vlos | 5707.7 ± 13.8 | | 6087.8 ± 3.4 | | | | 7103.9 ± 34.4 |
| | Vel.Disp | 174.3 ± 5.1 | | 112.6 ± 3.3 | | | | 234.6 ± 34.4 |
| SF_13 | Vlos | 5758.4 ± 8.8 | | 6188.1 ± 4.3 | | | | 6977.8 ± 29.8 |
| | Vel.Disp | 178.6 ± 4.1 | | 101.3 ± 4.3 | | | | 234.6 ± 29.9 |
| SF_14 | Vlos | | 5806.0 ± 3.4 | | 6249.7 ± 1.2 | | | 6987.8 ± 28.7 |
| | Vel.Disp | | 141.4 ± 1.7 | | 114.6 ± 1.2 | | | 234.6 ± 28.8 |
| SF_15 | Vlos | | 5801.0 ± 10.7 | | 6228.8 ± 3.8 | | | 6921.4 ± 18.7 |
| | Vel.Disp | | 176.3 ± 4.8 | | 123.1 ± 3.6 | | | 234.6 ± 19.0 |

**Figure 7.1:** Table containing the velocity components in km/s present in the regions.

# Part II

# Molecular Gas Kinematics in Stephan's Quintet

# 8

# Radio Astronomy

The field of radio astronomy went from theory to practise when Karl Jansky, in the early 1930s, serendipitously detected radio emission coming from the centre of the Milky Way. Jansky detected a reoccurring signal repeating once every sidereal day while working at Bell Telephone Laboratories investigating static interference with transatlantic voice transmissions. This source was later designated Sagittarius A and is a complex radio source at the centre of our galaxy. Through radio observations astronomers have not only detected known objects such as stars and galaxies, but have also found several new classes of objects including radio galaxies, quasars and pulsars invisible to the optical telescopes. The astronomical objects found through radio astronomy show some of the most extreme and energetic processes in the Universe.

Contrary to optical telescopes, radio telescopes can be used both during nighttime as well as daytime, and clouds are not as much of a hindrance. Certain molecules in the atmosphere do interfere with radio observations by decreasing the atmospheric transmission and increasing noise levels, such as water vapour with strong bands at 22.2GHz ($\lambda = 1.35$ cm) and 183GHz ($\lambda = 1.63$ mm), and $O_2$ with a strong band at 60GHz ($\lambda = 5$ mm). To minimise the water vapour in the line of sight, radio observatories are built on high and dry sites.

## 8.1   Radio Telescopes

Grote Reber built a parabolic 9m radio telescope in the late 1930s, and carried out the first sky survey in radio frequencies (**?**). The configuration of radio telescopes, design and size, varies widely depending on which part of the radio spectrum it is designed for. The radio spectrum spans a large range of frequencies, 3 kHz to 300 GHz ($\lambda = 100$ km - 1 mm), and there are different configurations that are more advantageous in different wavelength regions.

In general terms, a radio telescope consists of a large radio antenna and a sensitive radiometer or radio receiver. At $10 - 100$ MHz ($\lambda = \sim 30 - 3$ m) the radio antennas are either directional antennas or stationary reflectors with movable focal points. At these long wavelengths the reflector surface can be made out of a coarse wire mesh. At shorter wavelengths the parabolic dish antennas dominate. The incoming radiation is reflected by the parabolic dish, either directly or via a subreflector, into a receiver where it is virtually stored to later be analysed. To build radio images of astronomical targets, the telescope is moved over the source, and the image is constructed by scanning and tracking across the target.
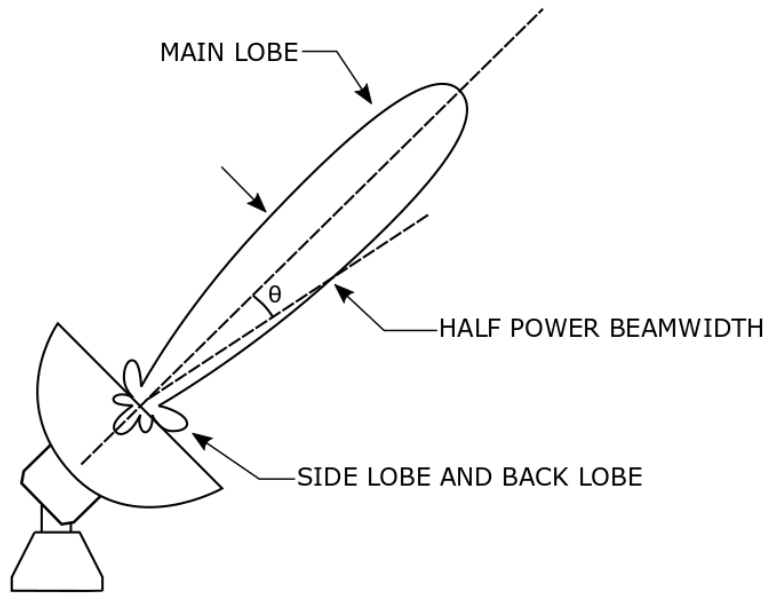
**Figure 8.1:** The reception pattern of a single dish antenna.

When carrying out radio observations, it is the temperature of the receiver that provides the astronomer with the required information. However, it is not only the direct emission from the astronomical object of interest that is picked up by the receiver. Fig.8.1 shows the reception pattern of a single dish antenna. The receiver detects emission from the target, i.e., in the main lobe, but also a certain amount of emission from the side lobes and back lobe. So, while the total beam temperature, $T_A$, is what is being registered by the telescope, it is the main beam temperature, $T_{mb}$, that provides information of the target. The main beam temperature can be calculated from the total beam temperature using two telescope specific parameters: the main beam efficiency and the forward efficiency.

As Wilson et al. (2009) details, the main beam efficiency, $B_{eff}$, describes how well the power pattern is concentrated in the main beam and is calculated as the ratio between the total beam solid angle, $\Omega_A$, and the main beam solid angle, $\Omega_{mb}$:

$$B_{eff} = \frac{\Omega_{mb}}{\Omega_A} \tag{8.1}$$

where the beam solid angle, $\Omega_A$, and the main beam solid angle, $\Omega_{mb}$, are defined as:

$$\Omega_A \ [rad^2] = \int\!\!\int_{4\pi} P_n(\nu, \theta, \phi) d\Omega \tag{8.2}$$

$$\Omega_{mb} \ [rad^2] = \int\!\!\int_{mainlobe} P_n(\nu, \theta, \phi) d\Omega \tag{8.3}$$

$P_n$ is the normalised reception/power pattern, $\nu$ the frequency, $\phi$ is the azimuth angle, $\theta$ the angle between the normal to the dish and the direction to $d\Omega$, and $d\Omega$ is the position observed measured in $Wm^{-1}Hz^{-1}rad^2$.

The forward efficiency, $F_{eff}$, is a measure of how well the receiver couples with the cold sky. The main beam efficiency and forward efficiency are telescope specific
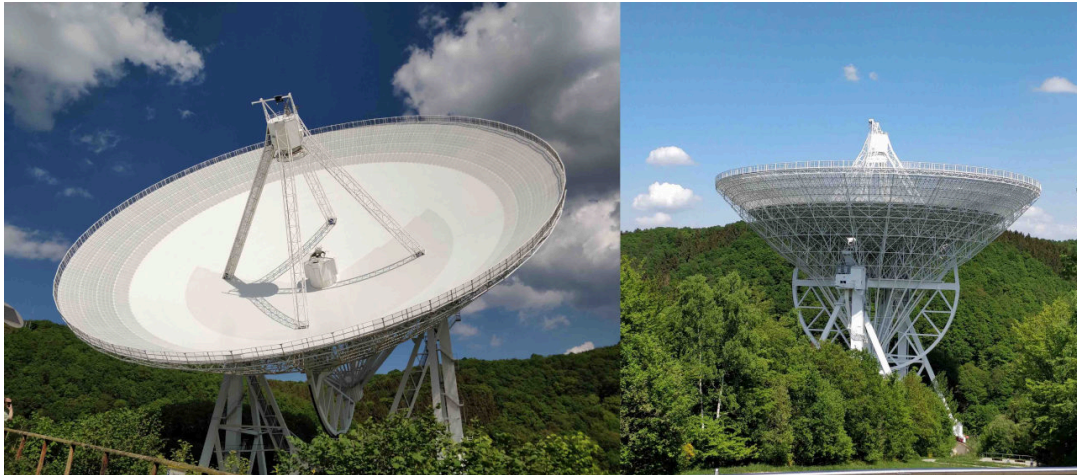
**Figure 8.2:** The 100m Effelsberg telescope covers a frequency range of 800 MHz$-$86 GHz ($\lambda = 50$ cm$-$3 mm). To ensure that the parabolic shape of the dish remains under the effect of gravity, a complex support structure is in place, shown to the right. Pictures taken by the author.

parameters, obtained through measurements and made available by IRAM. Using these two efficiencies together with the observed total beam temperature, $T_A$, the main beam temperature can be obtained as:

$$T_{mb} = \frac{F_{eff}}{B_{eff}} \, T_A.$$  (8.4)

The spatial resolution, i.e., the half-power beam width, of a radio antenna can be described as:

$$\Theta_{FWHM} \, [rad] = 1.02 \frac{\lambda}{D},$$  (8.5)

where $D$ is the diameter of the telescope and $\lambda$ the observed wavelength. It is, therefore, clear that a radio telescope has to have a much larger diameter than an optical telescope to reach the same resolution. This introduces particular issues with the shear weight of the radio telescope and gravitational deformations of the parabolic dish. The largest freely steerable telescopes have a diameter of $\sim 100$ m. The Effelsberg telescope is a 100 m freely steerable telescope located near Effelsberg, between Köln and Bonn in Germany, depicted in Fig.8.2. This telescope is a good example of the complexity and engineering effort required to build radio telescopes with good resolution for longer wavelengths. The Effelsberg telescope covers the frequency range 800 MHz$-$86 GHz ($\lambda =$ 50 cm$-$3 mm) and compensates for the gravitational deformation of the parabolic shape of the dish by a complex support structure (shown to the right in Fig.8.2), which ensures that the dish retains a parabolic shape.

Due to the immense telescope size required for higher resolution radio astronomy, astronomers and scientists developed radio interferometry in the 1940s. Interferometry combines the simultaneous effort of several telescopes, to increase the resolution by synthetically increasing the "diametre" of the telescope. By using a large number of telescopes an observation can be produced that has a resolution of a single

telescope with a diameter equivalent to the maximum physical separation of the telescopes (the baseline). To ensure a high quality image, a multitude of telescopes with a large number of different separations between the telescopes must be used. In the 1970s, very-long-baseline interferometry came to light. Very-long-baseline interferometry combines the effort of radio telescopes all around the world to reach a baseline as large as the diameter of the Earth. In the 2010s, astronomers used telescopes all around the world as well as a space based telescope, to obtain the largest radio interferometer to date, RadioAstron, which has a 8 microarcsecond resolution and operates at $1.19 - 1.63$ cm (K-band), 6.2 cm (C-band), 18 cm (L-band), and 92 cm (P-band)[1].



**Figure 8.3:** The IRAM 30m telescope. Picture taken by the author.

## 8.2 IRAM 30m

The Institut de Radioastronomie Millimétrique (IRAM) 30m telescope, depicted in Fig.8.3 and constructed in the 1980s, is located at an altitude of 2850 m on Pico Veleta in the Spanish Sierra Nevada. Consisting of a 30 m classic single dish parabolic antenna, the telescope contains continuum cameras and heterodyne receivers operating at 3, 2, 1 and 0.9 mm, covering the range of $70 - 375$ GHz

---

[1]RadioAstron operational wavelengths provided by the RADIOASTRON USER HANDBOOK, prepared by the RadioAstron Science and Technical Operations Group Version 2.94; 10 December 2019.

($\lambda = 4.3 - 0.8$ mm). In addition, the IRAM 30m can observe simultaneously at several wavelengths, thus enabling the production of multiple images at once.

The parabolic dish collects the signal and reflects it to the sub-reflector, which directs the signal into the antenna cabin where the receivers are located. There is a number of different receivers available in the antenna cabin, and the signal is distributed to the chosen receiver using a series of carefully placed high precision mirrors. The 30m telescope has great potential and can be used in a multitude of different configurations, depending on the requirements of the science and the observation. Currently active at the telescope are the frontends EMIR (Eight MIxer Receiver), HERA (a 3x3 dual-polarisation 1mm receiver) and NIKA-2 (a wide field-of-view camera). Older receivers/cameras include ABCD, NIKA-1 and MAMBO2. The available backends are WILMA, VESPA, FTS50 and FTS200, chosen depending on the requirements of the individual observation. A short intro to EMIR will be provided in the subsequent chapter, since this is the instrument used for the observations carried out in this part of the thesis. The tracking precision of IRAM 30m is $1''$, while the angular resolution of the telescope ranges from approximately $9''$ at 1 mm to $20 - 30''$ at 3 mm.
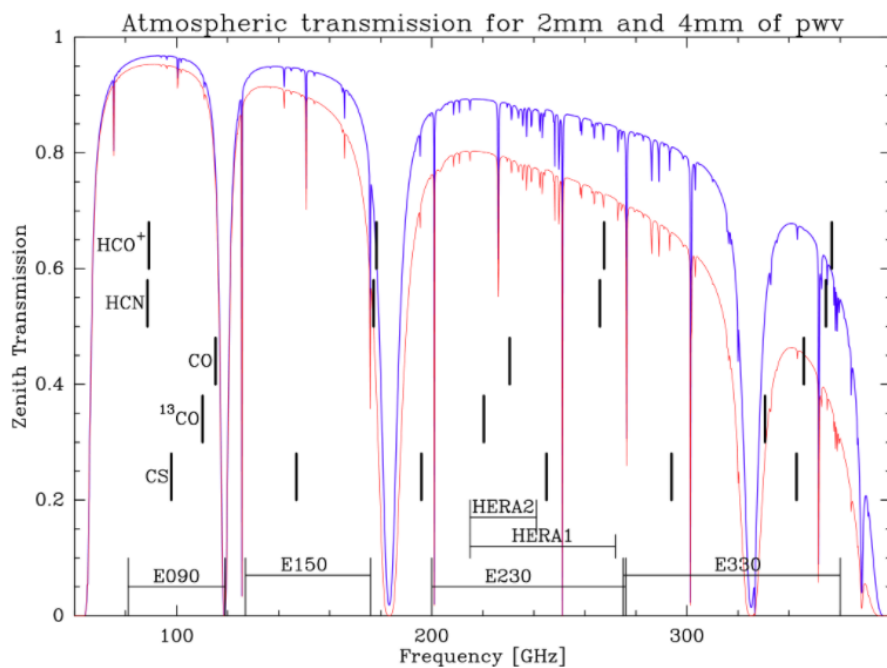


**Figure 8.4:** Atmospheric transmission in the frequency range covered by IRAM 30m and EMIR. Pinpointed in the graph are the extension of the EMIR bands as well as some of the more important molecular emission lines. Credit: IRAM wiki EMIRforAstronomers.

## 8.2.1 EMIR[2]

The frontend Eight MIxer Receiver (EMIR) was installed on the IRAM 30m telescope in 2009, it has four bands: E090, E150, E230, E330, named so according to their respective approximate centre of frequency. The atmospheric transmission in the frequency range covered by IRAM 30m and EMIR is depicted in Fig.8.4. The EMIR bands are pinpointed as well as a selection of molecular emission lines. EMIR is the first instrument on the 30m that enables permanent high sensitivity observations in the E330 band.

Each band outputs 2 sidebands, lower (L) and upper (U), as well as 2 polarisations (H and V), see Fig.8.5 which shows an overview of the band combinations available. In addition, each sideband is split into two blocks, inner (I) and outer (O), of 4GHz each. The signals are sent through 8 coaxial cables. The older WILMA and VESPA backends can only be connected to the first 4 cables, while the newer FTS backends can be connected to all 8 cables. While EMIR allows dual band observations, it is only possible in certain combinations of the bands, i.e., only the E0/E1, E0/E2 and E1/E3 combinations are allowed by the receiver optics. Dual band observations use dichroics which introduce losses, and each percent of loss increases the receiver temperature by approximately 4K. Thereafter, the choice of backend can be done freely, considering the required frequency coverage and resolution. The frequency ranges of VESPA, FTS50 and FTS200 are shown in Fig.8.6.

---

[2]Unless stated otherwise, the information detailed in this chapter relies on the IRAM EMIR-forAstronomers wiki pages maintained by C.Kramer: `http://www.iram.es/IRAMES/mainWiki/EmirforAstronomers`.
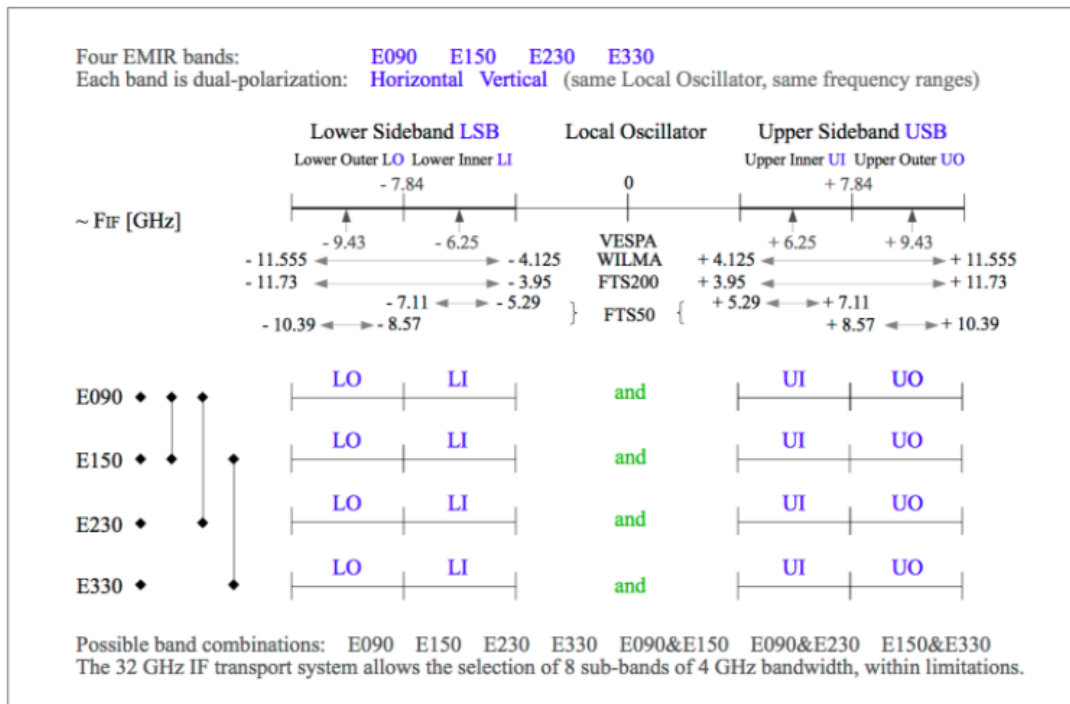
**Figure 8.5:** Overview of the EMIR band combinations and frequencies, including the frequency ranges for the backends VESPA, WILMA, FTS200 and FTS50. Credit: IRAM wiki EMIRforAstronomers and Backends.
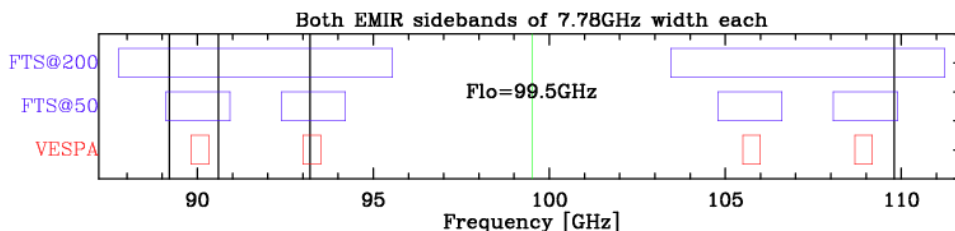


**Figure 8.6:** The frequency ranges of the backends FTS200, FTS50 and VESPA for EMIR, with the local oscillator set to 99.5GHz. Credit: IRAM wiki EMIRforAstronomers.

# 9

# Observational Setup & Data Treatment[1]

The study of the molecular gas content and kinematics in Stephan's Quintet carried out in this thesis, relies on data obtained with the IRAM 30m telescope, Sierra Nevada, Spain, on the 14-18th of September 2018. The observations cover the 4 main galaxies, NGC7317, NGC7318A, NGC7318B and NGC7319, as well as the shocked star-forming ridge and the extended IGM between the 4 galaxies. The aim of this project was to map the emission of three different CO isotopologues: $^{12}$CO$(1 \rightarrow 0)$, $^{13}$CO$(1 \rightarrow 0)$ and $^{12}$CO$(2 \rightarrow 1)$ - the transition frequencies are stated in Table 9.1. This chapter details the setup of the observations, the data reduction and the initial analysis.

| Molecular transition | Frequency (wavelength) |
|:---:|:---:|
| $^{12}$CO$(1 \rightarrow 0)$ | 115271.2018 MHz (2.6 mm) |
| $^{12}$CO$(2 \rightarrow 1)$ | 230538.0000 MHz (1.3 mm) |
| $^{13}$CO$(1 \rightarrow 0)$ | 110201.3543 MHz (2.7 mm) |

**Table 9.1:** Molecular emission line frequencies of interest.

## 9.1 Observational Setup & Exposure Times

The observations were carried out using the IRAM 30m telescope with the frontend EMIR and backend FTS200. A 5.67 $arcmin^2$ region covering SQ, depicted in Fig.9.1, was observed using on-the-fly (OTF) mapping. On-the-fly mapping is a method where the beam moves continuously over the chosen area, vertically and horizontally respectively, proving a 3D map with the spectrum as a function of position. The green boxes in Fig.9.1 show how the area was separated into square submaps with sizes of $80 \times 80$ $arcsec^2$, $60 \times 60$ $arcsec^2$ and $40 \times 40$ $arcsec^2$ for separate OTF mapping. The centres of the boxes and the number of scans performed are stated in table 9.2.

Each submap was scanned horizontally and vertically, and after each scanned line, back and forth along one RA/Dec, a reference/offset position was observed. Observing this offset position, a method called position switching, during the OTF

---

mapping, is required to enable accurate background subtraction for extended targets such as Stephan's Quintet.

| Box | Centre (RA Dec) | No. of scans |
|---|---|---|
| 1: $80'' \times 80''$ | 22:36:04.747 +33:58:30.523 | 10 |
| 2: $60'' \times 60''$ | 22:35:59.105 +33:57:49.127 | 12 |
| 3: $60'' \times 60''$ | 22:35:59.121 +33:58:48.896 | 12 |
| 4: $40'' \times 40''$ | 22:35:55.096 +33:57:43.061 | 12 |
| 5: $40'' \times 40''$ | 22:35:55.093 +33:58:22.909 | 12 |
| 6: $60'' \times 60''$ | 22:35:52.459 +33:56:53.152 | 11 |

**Table 9.2:** The boxes being scanned using on-the-fly mapping, their centres and the number of scans (in this case 1 scan is a scan of a full box, both vertically and horizontally) carried out per box.
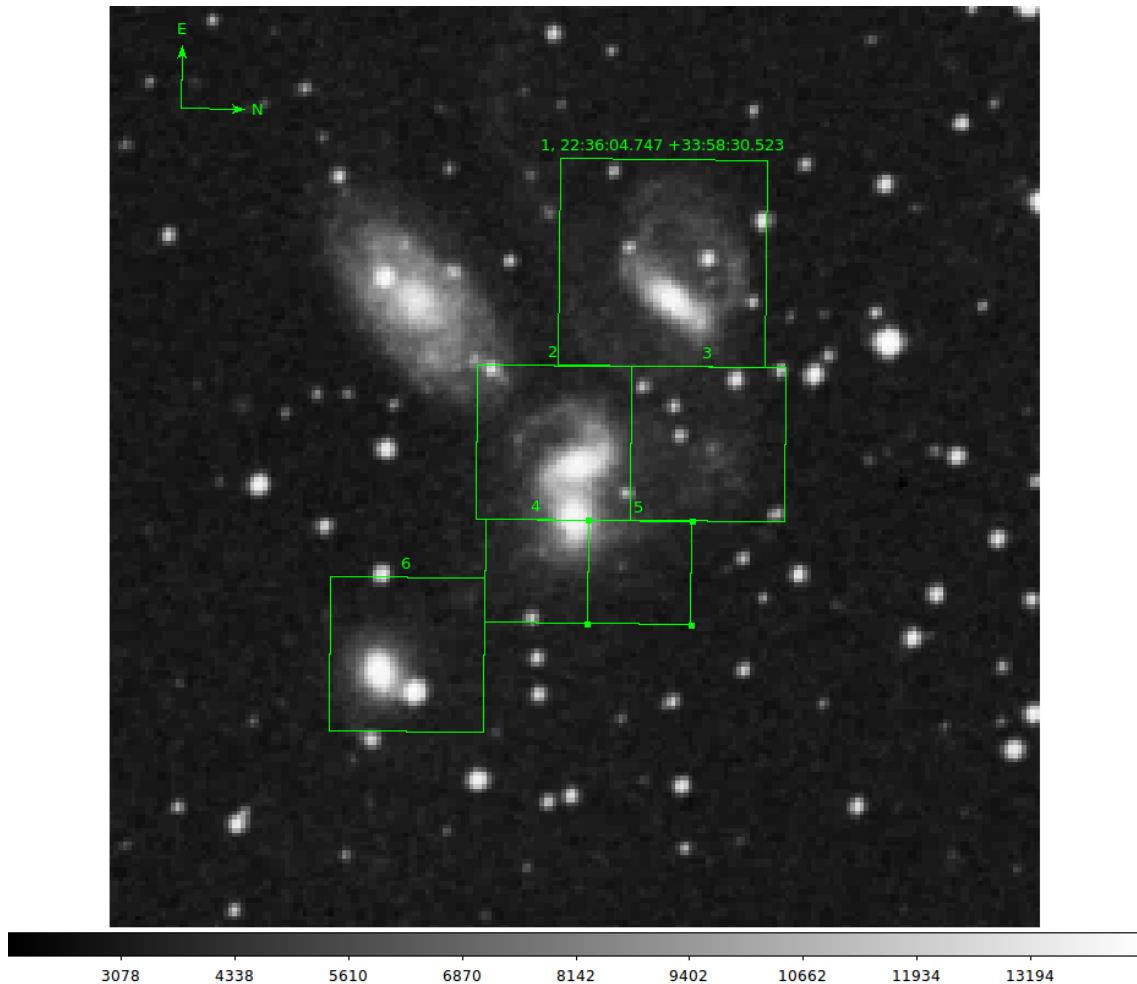


**Figure 9.1:** The boxes adopted for on-the-fly mapping of Stephan's Quintet using IRAM 30m.

A combined E090: UI+UO & E230: UI+UO mode efficiently trace the $^{12}CO(1 \to 0)$, $^{12}CO(2 \to 1)$ and $^{13}CO(1 \to 0)$ emission simultaneously, and was adopted for the observations. The frontend and backend setup, including the target sensitivity are stated in the table in Fig.9.2. The backend FTS200 was chosen since its frequency range allows both $^{12}CO(1 \to 0)$ and $^{13}CO(1 \to 0)$ to be observed within the same sideband. In addition, the FTS200 has a sufficient resolution of $\sim$1 km/s, for the expected line widths in SQ of >100 km/s.

Frontend/Backend setups:

| Setup | Band | Species/Transition | Frequency | Receiver band | $T_A^*$ | Rms | ΔV | Backends |
|-------|------|--------------------|-----------|---------------|---------|-----|-----|----------|
| 1 | E0 (3mm) | 12CO(1-0), 13CO(1-0) | 110.95 | UI | 10.0 | 1.4 - 3.0 | 30.0 | FTS200 |
| 1 | E2 (1.3mm) | 12CO(2-1) | 230.54 | UI | 15.0 | 3.0 - 6.0 | 30.0 | FTS200 |

**Figure 9.2:** EMIR technical setup, frontend and backend, including expected receiver temperatures in mK as well as target rms and ΔV. The frequency stated is the one to which the UI local oscillator is tuned to.

The expected line strengths in SQ are 15 mK & 10 mK for $^{12}CO(1 \to 0)$ and $^{12}CO(2 \to 1)$ respectively, in the intra group medium (Guillard et al., 2012). The integration time was calculated prior to the observations using the 30m EMIR Time/Sensitivity Estimator to reach a rms sensitivity of $\sim 1/3$ of the line strength, and found to be 20.5 h. I was granted 30 h of observation time, unfortunately with the weather conditions present during the observation run, more than double that time would have been needed to reach the requested rms.

A planet (Saturn and Mars interchangeably) was used for general pointing and focusing, and a nearby calibrator, chosen from the catalogues available at the telescope, was adopted for pointing corrections close to the source - according to common practise. Furthermore, a line calibrator, a bright source for which IRAM has an accurate catalogue of its lines, was observed to determine possible problems in the system.

The average line-of-sight velocity of Stephan's Quintet is so large that the redshifted frequencies had to be calculated by hand and all velocities in the scripts set to 0. To ensure that the expected emission would stay within the frequency range of the backends, an average velocity of 6200 km/s was adopted and the position of the Upper-Inner (UI) local oscillator (LO) for the E0 and E3 band was put to 108.8942391 GHz and 225.8668535 GHz respectively, which includes an extra 200 MHz shift to avoid instrument specific aberrations in the sensitivity function. Adopting the redshifted velocitites in this manner introduces a difficulty with the line calibrator, since the calibrator is not at a line-of-sight velocity of 6200 km/s. Together with the astronomer on duty a line calibrator that emits a multitude of lines was chosen, to enable mitigation of this potential issue.

## 9.2 Data Reduction[2]

The data was reduced using GILDAS and the software packages CLASS (the Continuum and Line Analysis Single-dish Software) and GreG (Grenoble Graphic software)[3]. GILDAS is the IRAM standard data reduction package and contains a collection of state-of-the-art software aimed at sub-millimetre/millimetre radio astronomical applications, suitable for both single-dish and interferometer data. Written in Fortran-90/95 and C/C++, different subprograms can be chosen and used independently, and as stated, CLASS and GreG were the required packages for the reduction carried out here. CLASS is a software package for reducing single-dish spectroscopic data and GreG is an all purpose 1-D and 2-D graphic program, suitable for preparing plots, as well as manipulating and analysing data.

First, the observed spectra were combined into a map. Then, following standard reduction practises, platforms in the spectra were corrected for. Platforms occur due to power fluctuations of the telescope. To illustrate the platforms present, see the example in Fig.9.3a, this spectrum is smoothed by averaging every 10 channels to decrease the noise to enable a clearer view of the platforms and is only used for illustration of the platforming reduction step. By fitting baselines to the spectrum the platforms were removed, ensuring that post-platforming the spectrum was flat, as depicted in the smoothed example Fig.9.3b.



(a)                                                    (b)
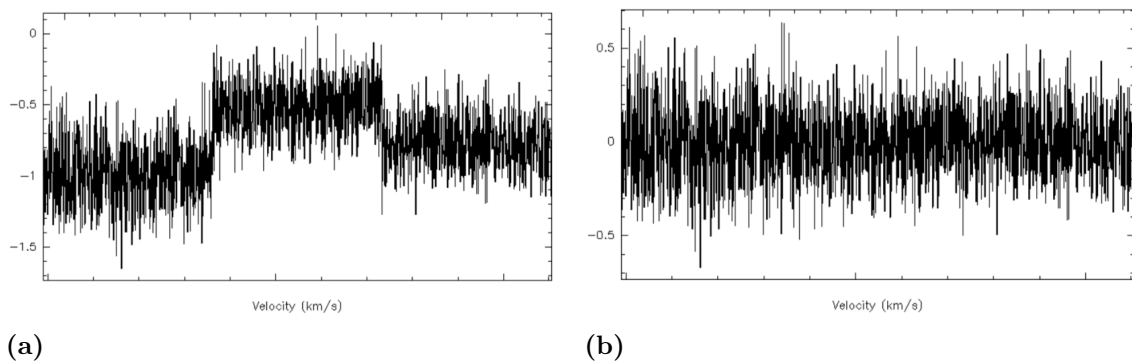
**Figure 9.3:** The need and effect of the correction for platforms in the spectra are illustrated using this example of a smoothed spectrum. The x-axis is frequency/line-of-sight velocity scale and the y-axis the receiver temperature in mK. (a) Prior to platforming; (b) Post platforming. (Images in collaboration with Timo Peitl-Thiesen, a BSc student I supervised.)

---

[2]The IRAM 30m data reduction detailed in this sub-chapter was carried out in collaboration with Timo Peitl-Thiesen, a Bachelor thesis student I supervised. Further reduction and analysis, including calculations and higher level interpretation, as detailed in the subsequent sub-chapters, was thereafter carried out by me alone. For a more detailed description of the basic data reduction detailed in this sub-chapter see Timo Peitl-Thiesen's thesis titled: Molecular gas in Stephan's Quintet - Radio observations and data reduction, searching for CO emission.

[3]GILDAS software and manual is available at `http://www.iram.fr/IRAMFR/GILDAS`, as is the GreG and CLASS software packages.

Thereafter, the emission lines of interest were split into separate datasets, with the expected line centre as the 0 velocity. The velocity channel width was set to 40 km/s and data outside of the expected velocity range was cut. Due to the poor weather conditions during the observations the data had to be filtered. Considering the root mean square (rms) of the spectra and removing the spectra with too large rms values, a rigorous investigation resulted in rms levels used for filtering for each emission line dataset as listed in Table 9.3. Note that this also means that only scans that fulfill the rms level requirements are included in the final maps, contrary to the number of scans carried out as listed in Table 9.2. The $^{12}CO(2 \rightarrow 1)$ emission was highly affected by the poor weather conditions and showed high noise levels, any filtering carried out made no noticeable effect on the data. Table 9.3 also lists the beam efficiencies, $B_{eff}$, and forward efficiencies, $F_{eff}$, of the telescope for the observed lines, as these were used to obtain the main beam temperature, $T_{mb}$.

| Molecular transition | Filter rms limit | $B_{eff}$ | $F_{eff}$ |
|---|---|---|---|
| $^{12}CO(1 \rightarrow 0)$ | 0.0585 | 0.78 | 0.94 |
| $^{12}CO(2 \rightarrow 1)$ | none | 0.59 | 0.92 |
| $^{13}CO(1 \rightarrow 0)$ | 0.4 | 0.78 | 0.94 |

**Table 9.3:** Rms levels adopted for filtering the individual CO emission line maps.

Spikes, very narrow high peaks, caused by errors occurring in the telescope or electronics were removed using the following requirement: if the peak is higher then five times rms of the spectrum and if the intensity of the neighbouring channels are four times lower than the channel of interest, the peak is deemed a spike and thereby removed. In addition, the spectra are affected by a non-flat baseline caused by background radiation. This baseline must be subtracted and an example of the effect of the baseline subtraction is displayed in Fig.9.4.



(a)                                                    (b)
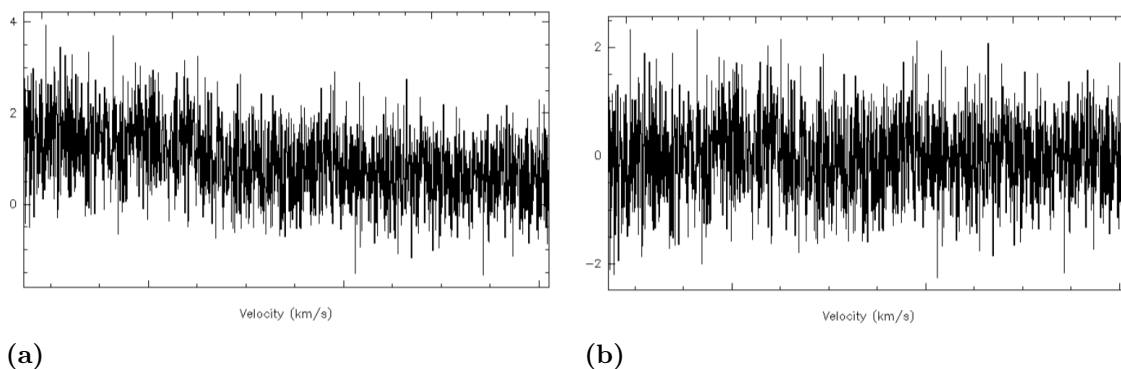
**Figure 9.4:** The need and effect of the subtraction of the baseline is illustrated in this example. The x-axis is frequency/line-of-sight velocity scale and the y-axis the receiver temperature in mK. (a) Showing the non-flat baseline; (b) The spectrum post baseline subtraction. (Images in collaboration with Timo Peitl-Thiesen, a BSc student I supervised.)

Lastly, maps of the observed area were created for each emission line. For these maps a $2'' \times 2''$ pixel size was adopted and smoothed versions of these maps were created using a half power beamwidth of $50''$, to eliminate noise and increase the likelihood that the final maps only contain real emission.

## 9.2.1 Challenges

There is a challenge regarding the setup of the observations. Due to the large span of line-of-sight velocities in SQ, the pinpointing of the tuning of the E090 UI local oscillator was particularly important and delicate. The goal is to ensure that despite the shifting of the line due to the varying line-of-sight velocities in SQ, the $^{12}CO(1 \to 0)$ and $^{13}CO(1 \to 0)$ lines would remain within the sideband throughout the mapped area.

The weather conditions were quite poor throughout the whole observation run. The amount of water vapour in the atmosphere and the atmospheric turbulence had large impacts on the observations. For example, one night the conditions were very poor and we were unable to achieve an accurate pointing on Saturn, since the planet was moving around to much in the plane of the sky.

In particular, the filters highly affect the data. A filter reduces not only the noise but also the number of spectra included in the final map. This results in less data which decreases the chances of a proper analysis. However, too much noise makes the signal highly difficult to distinguish, i.e., too stringent limitations remove a lot of noise but also decrease the signal, while too loose limitations leave too much noise which can drown out the signal. It is a fine line to tread and a particularly tricky one considering the weather conditions present during these observations.

## 9.3 Initial Scientific Analysis

CO emission lines provide information regarding abundances, line-of-sight velocities, velocity dispersions, estimations of molecular gas mass, excitation temperatures and optical depth. To obtain this information the CO emission lines must be fitted and the quantities deduced as described in this chapter.

### 9.3.1 CO Lines

The fitting of the CO emission lines was carried out using manually defined multiple Gaussian functions and Python's SciPy curvefit optimisation module. Manually defining the function used for fitting the spectrum enables the choice of the number of components, expected line centres and expected amplitudes. Python's curvefit module optimises the fit of the function to the spectrum, and allows stringent boundary conditions to be put on the parameters to ensure a good and true fit. Fig.9.5 shows two examples of how such a fit looks. While the respective shifts of the central velocities and line widths are derived directly from the fitted Gaussians, the integrated intensities $I_{CO}$, in K km/s, are derived using two different methods. In the first method the integrated flux is obtained from integration of the respective Gaussian functions, while in the second the flux is obtained as:

$$I_{CO}[K\ km/s] = \int_{\langle v \rangle - v_{min}}^{v_{max} - \langle v \rangle} \tau_{mb} dv, \tag{9.1}$$

to better account for potential asymmetry in the line profile. $\tau_{mb}$ is the CO main beam temperature over the velocity range $v_{min}$ to $v_{max}$, and $\langle v \rangle$ is the first moment mean intensity-weighted velocity over the velocity range (Guillard et al., 2012).



**(a)**                    **(b)**
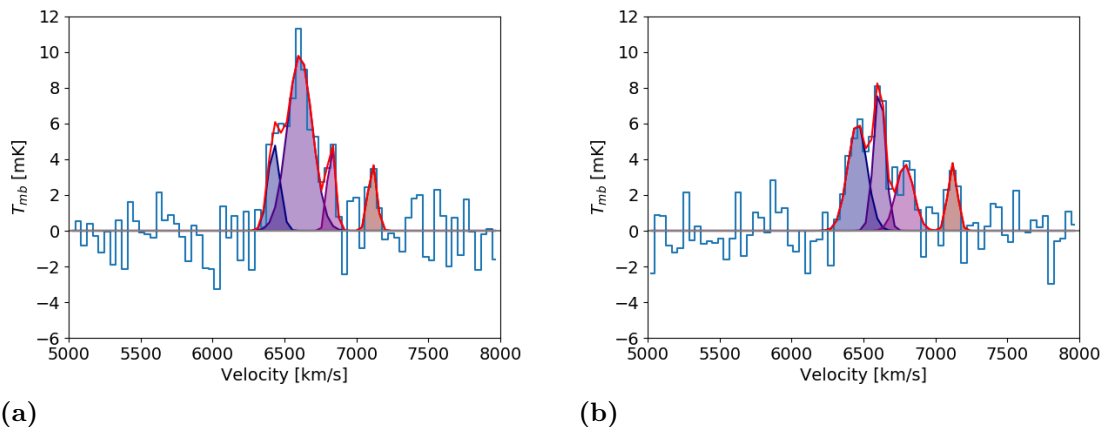
**Figure 9.5:** Two examples of the $^{12}$CO$(1 \to 0)$ emission line fit using Python's curvefit and manually defined Gaussian functions with multiple velocity components. The red line follows the full fit, while the individual Gaussian functions are shaded in different colours. (a) The fit of the NGC7319 centre, i.e., region 19; (b) The fit of the bridge, i.e., region b_i.

## 9.3.2 Molecular Hydrogen Gas Mass

The column density of molecular hydrogen, $N(\mathrm{H_2})$, can be obtained directly from the $^{12}\mathrm{CO}(1 \to 0)$ flux using the Galactic conversion factor of

$$\frac{N(\mathrm{H_2})}{I_{CO}} = 2 \times 10^{20} cm^{-2} \ [K \ km/s] \tag{9.2}$$

(Guillard et al., 2009). Enabling the mass of the $\mathrm{H_2}$ gas to be calculated as

$$M_{H_2} = 75 I_{CO} D^2 \Omega \ [M_\odot], \tag{9.3}$$

where $I_{CO}$ is the velocity integrated $^{12}\mathrm{CO}(1 \to 0)$ line intensity in Kkm/s, $D$ is the distance expressed in Mpc and $\Omega$ is the area covered in $arcsec^2$ (Braine et al., 2001; Lisenfeld et al., 2002). For a single pointing with a Gaussian beam of FWHM $\Theta$, $\Omega = 1.13\Theta^2$. In the calculations presented in the subsequent chapters a distance of 88.6 Mpc (Duarte Puertas et al., 2019) has been adopted, and the single pointing beamwidth for our regions is 22".

## 9.3.3 Excitation Temperature & Optical Depth

The excitation temperature of the CO gas, as well as the optical depth can be estimated from the $^{12}\mathrm{CO}(1 \to 0)$, $^{12}\mathrm{CO}(2 \to 1)$ and $^{13}\mathrm{CO}(1 \to 0)$ lines (Eckart et al., 1990; Nishimura et al., 2015; Zschaechner et al., 2018), where the typical temperature of $^{12}\mathrm{CO}$ is 5-100 K. Assuming local thermal equilibrium allows the excitation temperature, $T_{ex}$, to be estimated from the main beam brightness temperature, $T_{mb}$, ratio of the 12CO lines:

$$\frac{T_{mb}^{21}}{T_{mb}^{10}} = \frac{1 - e^{-\tau_{21}}}{1 - e^{-\tau_{21}}} \frac{((h\nu_{21}/k)[exp(h\nu_{21}/kT_{ex}) - 1]^{-1} - T_{bg}^{21})}{((h\nu_{10}/k)[exp(h\nu_{10}/kT_{ex}) - 1]^{-1} - T_{bg}^{10})} \tag{9.4}$$

Where $\nu$ and $\tau$ is the transitional frequency and optical depth of the respective lines, and $T_{bg}$ is the contribution from the CMB at the frequency in question. Furthermore, local thermal equilibrium means that the distribution of the population among energy levels will follow the Boltzmann equation at the physical temperature of the system, the excitation temperature is actually the kinetic temperature of the gas and $T_{ex}^{12CO(1\to0)} = T_{ex}^{12CO(2\to1)} = T_{kin}$.

In the optically thick case $\tau \gg 1$ and Eq.9.4 can be stated as

$$\frac{T_{mb}^{12CO(2\to1)}}{T_{mb}^{12CO(1\to0)}} = \frac{11.03[\exp(11.03/T_{ex}) - 1]^{-1} - 0.20}{5.52[\exp(5.52/T_{ex}) - 1]^{-1} - 0.85}, \tag{9.5}$$

and for optically thin gas the equation can be simplified to

$$\frac{T_{mb}^{12CO(2\to1)}}{T_{mb}^{12CO(1\to0)}} \approx 4 \ \exp\left(-\frac{11.03}{T_{ex}}\right). \tag{9.6}$$

Meaning that for dense, warm, optically thick gas (2-1)/(1-0)-line ratios near 1 are expected, while dense, warm, optically thin gas provides a line ratio near 4. Whereas a line ratio value below 1 can indicate low temperatures for optically thick lines.

Using the excitation temperature, $T_{ex}$, the optical depth, $\tau$, can be derived from the main beam temperature of $^{13}CO(1 \rightarrow 0)$ (Nishimura et al., 2015):

$$\tau(\nu) = -\ln\left(1 - \frac{T_{mb}^{13CO(1\rightarrow 0)}(\nu)}{5.29}\left[\frac{1}{\exp(5.29/T_{ex}) - 1} - 0.17\right]^{-1}\right). \qquad (9.7)$$

Further, assuming that the $^{13}CO$ line is in the optically thin limit and that the $^{12}CO$ line is optically thick, their ratio, being proportional to the optical depth of the CO gas (Vantyghem et al., 2017), can be estimated as:

$$\tau \approx -\ln\left(1 - \frac{T_{mb}^{13CO}}{T_{mb}^{12CO}}\right). \qquad (9.8)$$

Saying that a value of the ratio $^{13}CO(1 \rightarrow 0)/^{12}CO(1 \rightarrow 0)$ near 1 indicates that the gas is infinitely opaque, while a ratio value closer to 0 indicates an optically thin medium and the ratio value near 0.63 denotes the limit of optically thick, i.e., $\tau = 1$.

Note that the resolution of the $CO(1 \rightarrow 0)$ lines and the $CO(2 \rightarrow 1)$ line is not the same. All three line maps have been smoothed and the regions chosen for closer analysis use a beam size matching the larger $CO(1 \rightarrow 0)$ beam. The discrepancy introduced in the line ratios by the difference in resolution is expected to be small compared to the discrepancies originating from the mixed, multiple velocity component, gas and poor weather conditions.

## 9.3.4 Particularly Challenging Aspects

The weather conditions proved to be the biggest enemy. Due to the poor weather conditions at the time of the observations, the amount of noise and poor signal in many parts of the mapped area were overwhelming any possible emission in one or several of the three CO lines. Therefore, fitting complete maps of the entire region is futile. In addition, there are large variations between the regions that show emission, in terms of both the number of velocity components as well as the ratios between these components. This means that any attempt in finding one algorithm that works satisfactorily across the entire observed area is highly difficult.

If it was not already immensely difficult to find an algorithm that works across the entire map for each respective CO line, the large variations in line-of-sight velocity would add an additional obstacle. The line-of-sight velocities in SQ spans $5600 - 7200$ km/s, and this is of course reflected in the large shifts of the emission lines across the different regions of the mapped area. To be able to fit all regions properly, strict region-specific restrictions on the fitting parameters would have had to have been implemented (if there would have been sufficient emission).

Further considering the different line-of-sight velocities, it is uncommon that a velocity component is present in two CO lines, let alone all three. This makes obtaining line ratios difficult as I cannot ensure that the gas originates from the same gas deposit. And therefore, the estimation of excitation temperatures and optical depths are in many cases more arbitrary than requested. The $^{13}CO(1 \rightarrow 0)$ is too weak in most regions and a proper value of the optical depth often eludes.

In conclusion, full maps were not fitted. Partially, due to the large variation in number of velocity components, ratios between the velocity components and the

large span of line-of-sight velocities, but mainly due to the lack of distinct emission worsened and caused by the poor weather conditions. Individual regions, have been handpicked and fitted with individual boundary conditions and a suitable number of velocity components. Although in many of the regions line ratios cannot be obtained due to the low emission and non-coincidence of line-of-sight velocities across the CO lines.

# 10

# Results & Discussion

This chapter details the results of the analysis of the radio data obtained with the IRAM 30m telescope, as outlined in the previous chapter. Several regions have been chosen for closer analysis, marked with $22''$ diameter circles in Fig.10.1. The $22''$ diameter reflects the beamwidth at 3 mm, while the beamwidth at 1 mm is $11''$. 22 such circles/regions have been chosen, the spectrum from each region has been averaged to increase SNR while retaining flux values.

This chapter begins by displaying intensity maps of the $^{12}CO(1 \rightarrow 0)$, $^{12}CO(2 \rightarrow 1)$ and $^{13}CO(1 \rightarrow 0)$ lines. Thereafter it is split into 3 main parts, related to the area of focus: regions in/near NGC7319, regions in the star-forming ridge and the bridge, as well as regions in/near the NGC7318 pair and NGC7317. In each area I present the spectra together with the results of the Gaussian decompositions, including the alternative method of calculating the fluxes as described by Eq.9.1. I discuss velocities and flux distribution, molecular hydrogen gas mass, temperatures and optical depth.
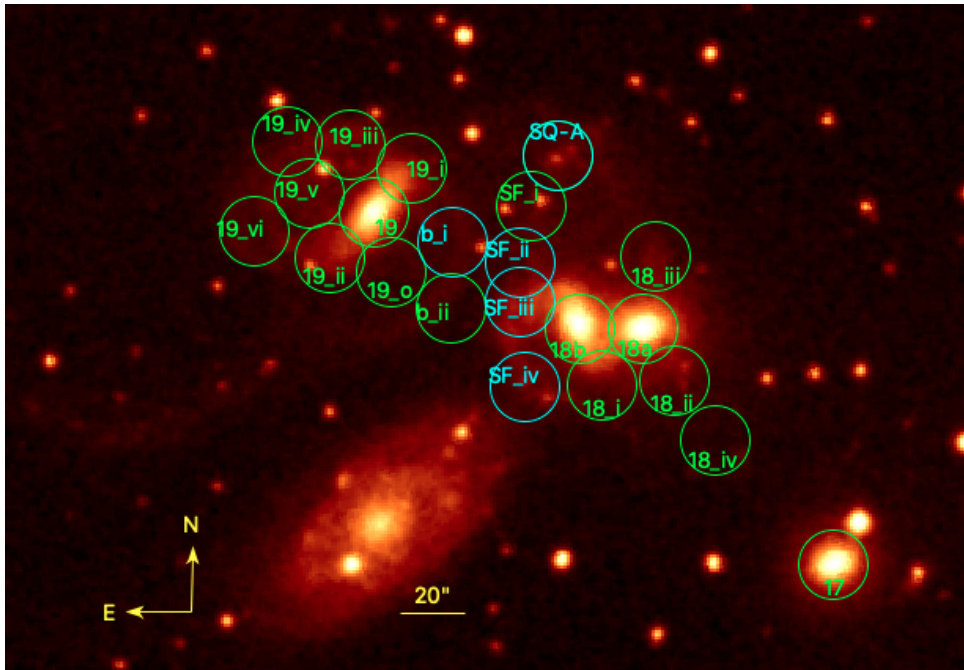


**Figure 10.1:** The 22 regions chosen for closer analysis, marked with $22''$ diameter circles containing their naming convention within. Displayed on a DSS2 red image. The regions in cyan coincide with the single beam IRAM 30m observations carried out by Guillard et al. (2012).

## 10.1 Maps of Overall CO Emission

The emission in the three CO lines summed over a velocity range of $5100 - 7500$ km/s, to ensure inclusion of all the emission present in Stephan's Quintet, is shown in Fig.10.2-10.4. Note that the $^{12}CO(2 \rightarrow 1)$ map appears a bit more compact, this is due to the smaller beam size at this frequency, $11''$ at 1 mm compared to $22''$ at 3 mm. Furthermore, the $^{12}CO(1 \rightarrow 0)$ line in Fig.10.2 shows clear preference to the area of NGC7319, extending towards the bridge and the star-forming ridge. As the 1.3 mm line, i.e., the $^{12}CO(2 \rightarrow 1)$ line, is more affected by the amount of water vapour in the atmosphere the map in Fig.10.3 is subjected to significant noise levels. The map of the $^{13}CO(1 \rightarrow 0)$ line in Fig.10.4 shows negligible emission apart from in two general areas, an edge defect to the left and a slight increase in/near NGC7319 and the NGC7318 pair. As can be seen the main emission is in the $^{12}CO(1 \rightarrow 0)$ line and the brunt of the CO emission in Stephan's Quintet is located in/near NGC7319, with a significant amount spread out in the bridge, the star-forming ridge and SQ-A as well.
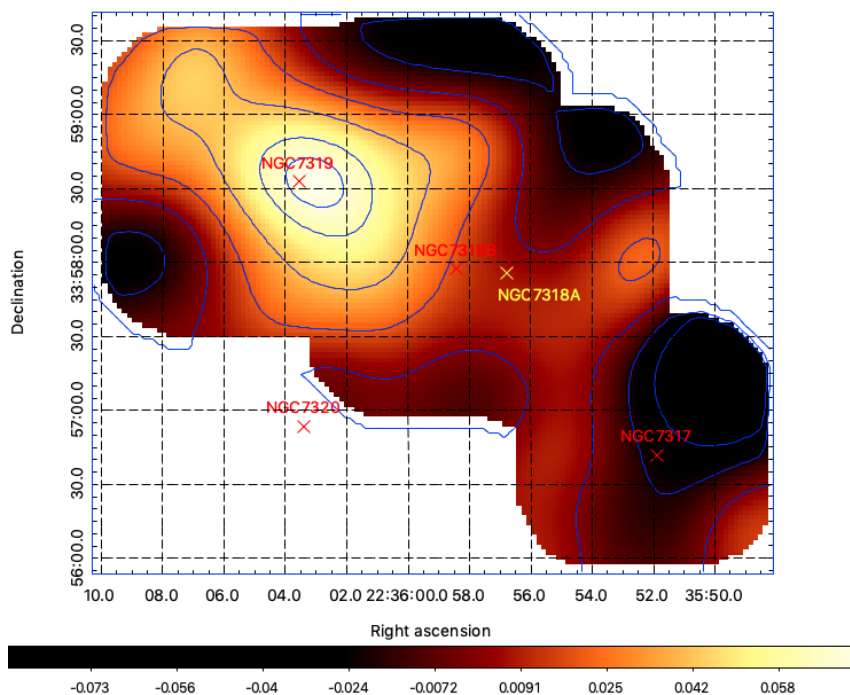


**Figure 10.2:** The map showing the summed emission of the $^{12}CO(1 \rightarrow 0)$ line over the velocity range $5100 - 7500$ km/s. Arbitrary contours in blue show the flux variations, while the red/yellow crosses pinpoint the galaxies.
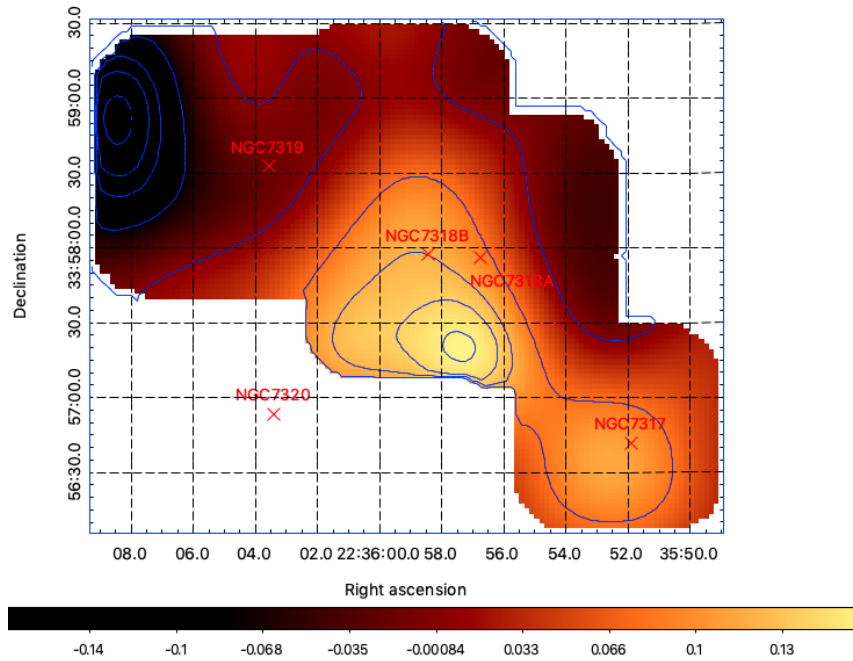
**Figure 10.3:** The map showing the summed emission of the $^{12}$CO$(2 \to 1)$ line over the velocity range $5100 - 7500$ km/s. Arbitrary contours in blue show the flux variations, while the red crosses pinpoint the galaxies.
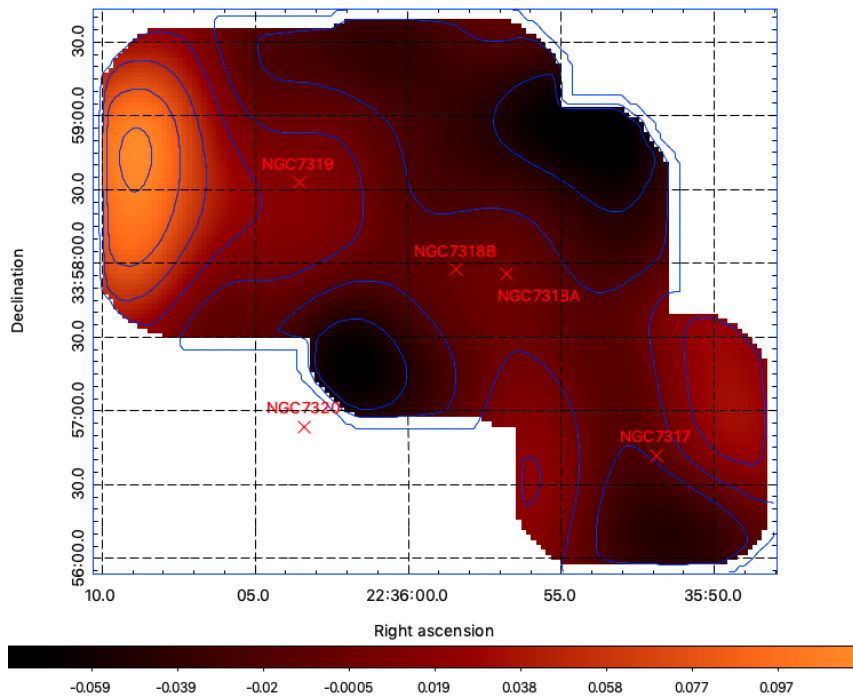


**Figure 10.4:** The map showing the summed emission of the $^{13}$CO$(1 \to 0)$ line over the velocity range $5100 - 7500$ km/s. Arbitrary contours in blue show the flux variations, while the red crosses pinpoint the galaxies.

143

## 10.2   The Active Galaxy NGC7319

The active galaxy in Stephan's Quintet, NGC7319, shows beautiful spiral arms pulled out in the previous interaction with NGC7320C and potentially NGC7317. This chapter details the results of the radio observations near and in NGC7319, presenting spectra, velocities, fluxes, molecular hydrogen gas masses as well as discussing excitation temperatures and optical depth.

### 10.2.1   Spectra

Fig.10.5-10.12 show the emission in each of the CO lines in region 19, 19_o and 19_i-vi as marked in Fig.10.1. In each plot the blue line shows the observed spectrum and the red line shows the multiple Gaussian fit (fitted as explained in Chapter 9.3) whenever a fit is possible. Note that the y-axis of the $^{12}CO(1 \to 0)$ and the $^{13}CO(1 \to 0)$ lines in (a) and (c) spans -6 to 12 mK, while the y-axis of the $^{12}CO(2 \to 1)$ line in (b) spans -15 to 20 mK.

The spectra in Fig.10.5-10.12 clearly show the complexity of the CO gas in Stephan's Quintet, via the multiple and broad velocity components present. The result of the Gaussian decomposition of these spectra are presented in the table in Fig.10.13, including the $H_2$ gas mass, for a SNR> 2. Furthermore, Fig.10.14 displays a table of the $H_2$ gas mass and fluxes of the three CO lines in velocity ranges of 200 km/s as derived using Eq.9.1, illustrating the distribution of matter while including more diffuse gas as well. Although absorption is unlikely, the values have been included shaded in grey for completeness. Included in this table is also the flux ratios of $^{12}CO(2 \to 1)/^{12}CO(1 \to 0)$, as well as $^{13}CO(1 \to 0)/^{12}CO(1 \to 0)$.



(a)                          (b)                          (c)
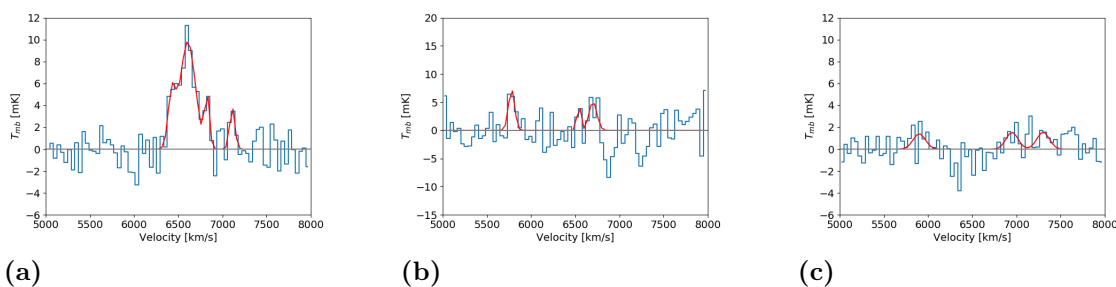
**Figure 10.5:** CO emission in the centre of NGC7319, i.e., region 19, shown in blue, and the fit is shown in red. The fits that result in a SNR> 2 are presented in the tables in Fig.10.13. (a) The $^{12}CO(1 \to 0)$ line; (b) The $^{12}CO(2 \to 1)$ line; (c) The $^{13}CO(1 \to 0)$ line.
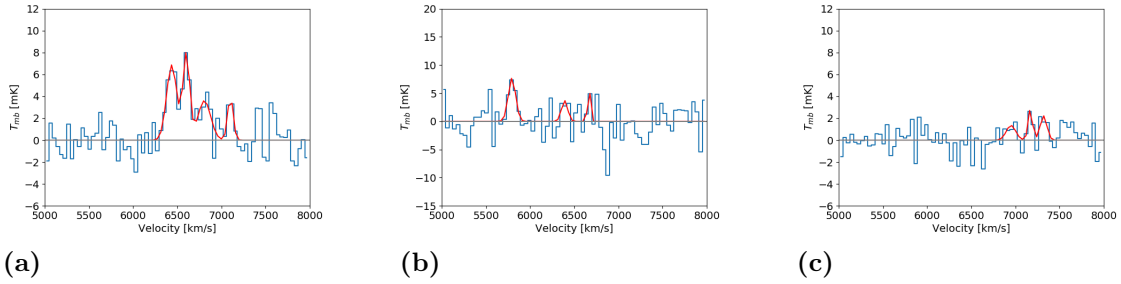
**Figure 10.6:** CO emission in region 19_o shown in blue, and the fit is shown in red. The fits that result in a SNR> 2 are presented in the tables in Fig.10.13. (a) The $^{12}$CO$(1 \rightarrow 0)$ line; (b) The $^{12}$CO$(2 \rightarrow 1)$ line; (c) The $^{13}$CO$(1 \rightarrow 0)$ line.
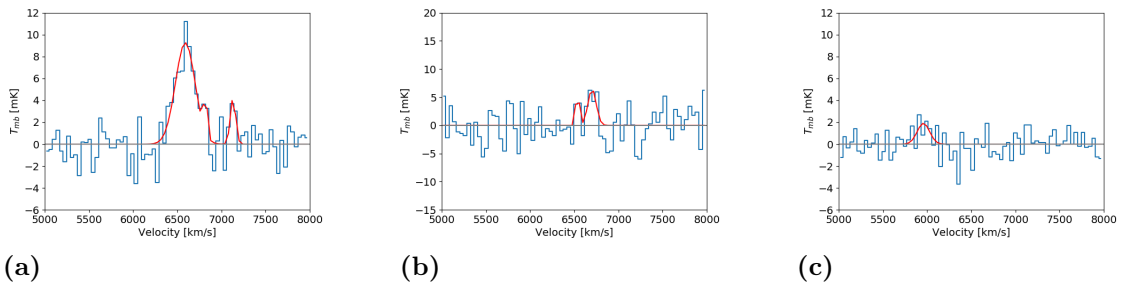


**Figure 10.7:** CO emission in region 19_i shown in blue, and the fit is shown in red. The fits that result in a SNR> 2 are presented in the tables in Fig.10.13. (a) The $^{12}$CO$(1 \rightarrow 0)$ line; (b) The $^{12}$CO$(2 \rightarrow 1)$ line; (c) The $^{13}$CO$(1 \rightarrow 0)$ line.
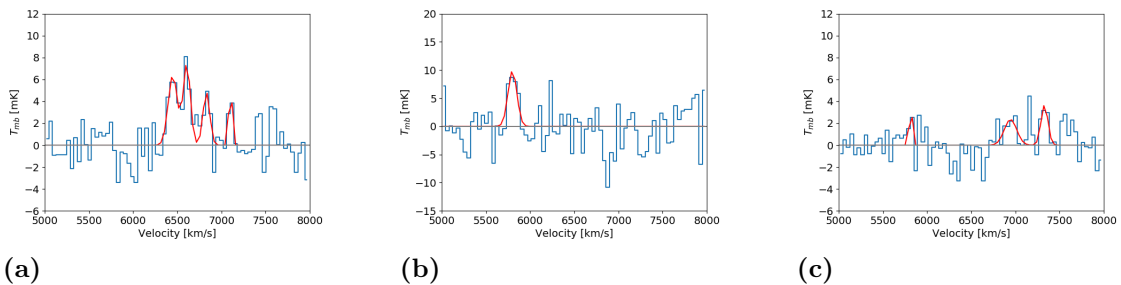


**Figure 10.8:** CO emission in region 19_ii shown in blue, and the fit is shown in red. The fits that result in a SNR> 2 are presented in the tables in Fig.10.13. (a) The $^{12}$CO$(1 \rightarrow 0)$ line; (b) The $^{12}$CO$(2 \rightarrow 1)$ line; (c) The $^{13}$CO$(1 \rightarrow 0)$ line.

**(a)**　　　　　　　　**(b)**　　　　　　　　**(c)**
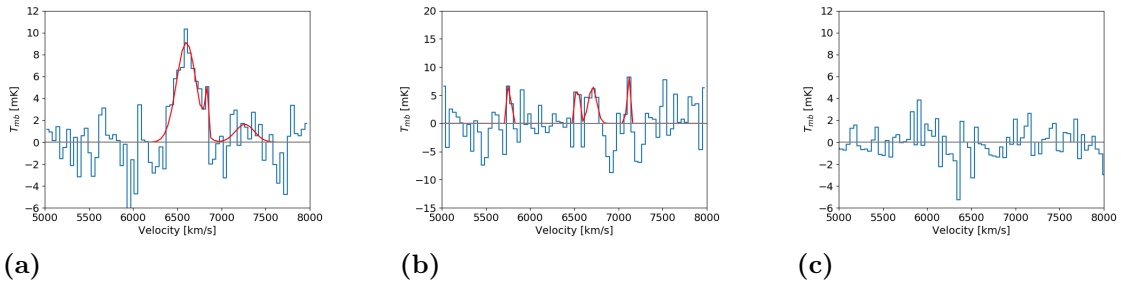
**Figure 10.9:** CO emission in region 19_iii shown in blue, and the fit is shown in red (wherever a fit is possible). The fits that result in a SNR> 2 are presented in the tables in Fig.10.13. (a) The $^{12}$CO(1 → 0) line; (b) The $^{12}$CO(2 → 1) line; (c) The $^{13}$CO(1 → 0) line.



**(a)**　　　　　　　　**(b)**　　　　　　　　**(c)**
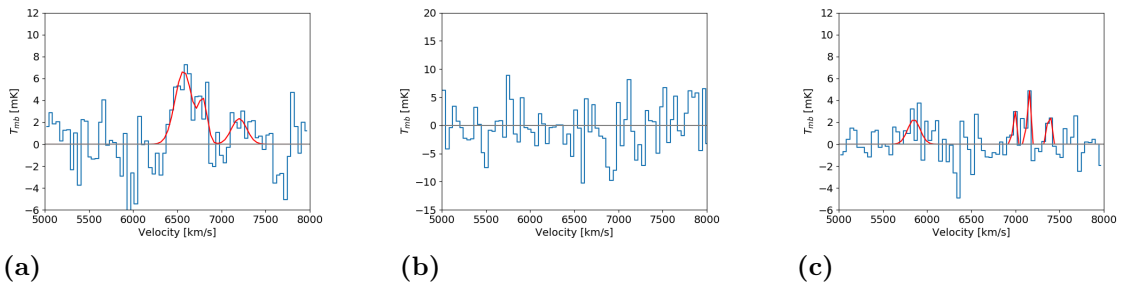
**Figure 10.10:** CO emission in region 19_iv shown in blue, and the fit is shown in red (wherever a fit is possible). The fits that result in a SNR> 2 are presented in the tables in Fig.10.13. (a) The $^{12}$CO(1 → 0) line; (b) The $^{12}$CO(2 → 1) line; (c) The $^{13}$CO(1 → 0) line.



**(a)**　　　　　　　　**(b)**　　　　　　　　**(c)**
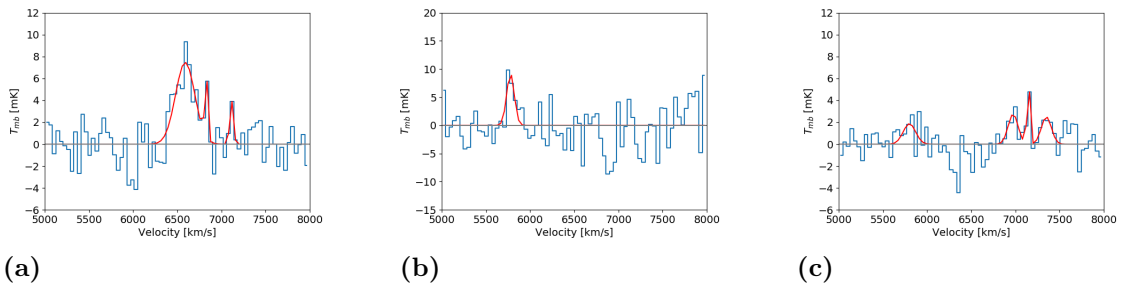
**Figure 10.11:** CO emission in region 19_v shown in blue, and the fit is shown in red. The fits that result in a SNR> 2 are presented in the tables in Fig.10.13. (a) The $^{12}$CO(1 → 0) line; (b) The $^{12}$CO(2 → 1) line; (c) The $^{13}$CO(1 → 0) line.

146

**(a)**　　　　　　　　　　**(b)**　　　　　　　　　　**(c)**
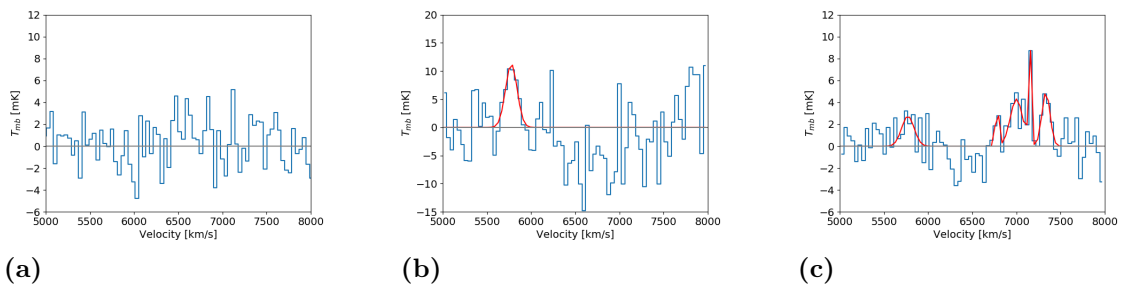
**Figure 10.12:** CO emission in region 19_vi shown in blue, and the fit is shown in red (wherever a fit is possible). The fits that result in a SNR> 2 are presented in the tables in Fig.10.13. (a) The $^{12}$CO$(1 \rightarrow 0)$ line; (b) The $^{12}$CO$(2 \rightarrow 1)$ line; (c) The $^{13}$CO$(1 \rightarrow 0)$ line.

| Region | 12CO(1-0) Vlos [km/s] | Vel.Disp [km/s] | Flux [K km/s] | $M(H_2)$ $[10^8 M_\odot]$ |
|---|---|---|---|---|
| 19_ | 6427.0 ± 16.3 | 41.4 ± 16.1 | 0.36 ± 0.14 | 1.15 ± 0.44 |
| | 6607.0 ± 13.1 | 85.6 ± 15.7 | 1.49 ± 0.21 | 4.81 ± 0.67 |
| | 6826.1 ± 10.2 | 26.4 ± 11.6 | 0.23 ± 0.10 | 0.75 ± 0.32 |
| | 7111.1 ± 13.5 | 29.5 ± 12.8 | 0.20 ± 0.09 | 0.64 ± 0.29 |
| 19_o | 6437.0 ± 12.6 | 58.0 ± 13.9 | 0.71 ± 0.15 | 2.27 ± 0.49 |
| | 6602.8 ± 9.3 | 38.1 ± 9.9 | 0.53 ± 0.12 | 1.72 ± 0.39 |
| | 6806.5 ± 24.4 | 71.4 ± 26.6 | 0.46 ± 0.16 | 1.47 ± 0.52 |
| | 7101.4 ± 13.2 | 31.0 ± 15.8 | 0.22 ± 0.11 | 0.71 ± 0.36 |
| 19_i | 6590.9 ± 12.2 | 111.0 ± 13.4 | 1.82 ± 0.21 | 5.87 ± 0.67 |
| | 7131.0 ± 12.9 | 30.1 ± 13.4 | 0.23 ± 0.10 | 0.73 ± 0.33 |
| 19_ii | 6449.2 ± 15.0 | 52.0 ± 16.4 | 0.59 ± 0.17 | 1.90 ± 0.53 |
| | 6607.9 ± 11.5 | 40.4 ± 11.9 | 0.53 ± 0.14 | 1.72 ± 0.46 |
| | 6829.5 ± 14.4 | 38.4 ± 14.3 | 0.33 ± 0.13 | 1.06 ± 0.41 |
| 19_iii | 6602.3 ± 17.0 | 110.6 ± 18.6 | 1.79 ± 0.29 | 5.75 ± 0.92 |
| 19_iv | 6571.0 ± 30.2 | 96.6 ± 33.1 | 1.14 ± 0.33 | 3.68 ± 1.06 |
| 19_v | 6590.0 ± 16.5 | 109.2 ± 17.7 | 1.45 ± 0.23 | 4.66 ± 0.74 |
| 19_vi | | | | |

| Region | 12CO(2-1) Vlos [km/s] | Vel.Disp [km/s] | Flux [K km/s] | 13CO(1-0) Vlos [km/s] | Vel.Disp [km/s] | Flux [K km/s] |
|---|---|---|---|---|---|---|
| 19_ | 5778.7 ± 16.5 | 34.6 ± 16.6 | 0.45 ± 0.22 | | | |
| 19_o | 5794.6 ± 16.3 | 41.7 ± 16.2 | 0.57 ± 0.23 | | | |
| | | | | 7168.5 ± 15.0 | 24.7 ± 13.4 | 0.13 ± 0.07 |
| | | | | 7318.2 ± 20.1 | 37.7 ± 19.8 | 0.15 ± 0.08 |
| 19_i | | | | 5958.2 ± 31.9 | 70.0 ± 31.9 | 0.24 ± 0.11 |
| | 6701.7 ± 21.3 | 46.5 ± 22.0 | 0.53 ± 0.25 | | | |
| 19_ii | 5800.0 ± 17.5 | 49.8 ± 17.5 | 0.87 ± 0.32 | | | |
| | | | | 6944.1 ± 34.1 | 70.0 ± 34.1 | 0.29 ± 0.15 |
| | | | | 7328.6 ± 16.3 | 39.0 ± 16.3 | 0.25 ± 0.11 |
| 19_iii | | | | | | |
| 19_iv | | | | 5850.8 ± 36.5 | 70.0 ± 36.5 | 0.28 ± 0.15 |
| 19_v | 5777.9 ± 18.0 | 42.9 ± 18.0 | 0.70 ± 0.30 | | | |
| | | | | 6973.7 ± 23.9 | 55.7 ± 24.3 | 0.27 ± 0.12 |
| | | | | 7349.8 ± 26.4 | 56.5 ± 26.8 | 0.25 ± 0.12 |
| 19_vi | 5776.2 ± 28.3 | 65.4 ± 28.3 | 1.31 ± 0.59 | 5771.2 ± 33.2 | 70.0 ± 33.2 | 0.34 ± 0.17 |
| | | | | 7000.0 ± 23.4 | 70.0 ± 27.5 | 0.53 ± 0.19 |
| | | | | 7334.0 ± 14.9 | 45.7 ± 14.9 | 0.40 ± 0.14 |

**Figure 10.13:** Table containing the line-of-sight velocity, velocity dispersion and the integrated flux of the fits of the $^{12}$CO(1 → 0), $^{12}$CO(2 → 1) and $^{13}$CO(1 → 0) lines, as well as the $H_2$ molecular gas mass, whenever the SNR> 2, in the regions in/near NGC7319, as marked in Fig.10.1.

148

| Region | Vel. Range [km/s] | M(H₂) [$10^8 M_\odot$] | 12CO(1-0) Flux [K km/s] | 12CO(2-1) Flux [K km/s] | 13CO(1-0) Flux [K km/s] | I(12CO(2-1))/ I(12CO(1-0)) | I(13CO(1-0))/ I(12CO(1-0)) |
|---|---|---|---|---|---|---|---|
| 19_ | 5600-5800 | 0.47 ± 0.11 | 0.15 ± 0.03 | **0.45 ± 0.13** | 0.10 ± 0.02 | 3.10 ± 1.15 | 0.70 ± 0.22 |
| | 5800-6000 | | -0.24 ± 0.04 | | **0.24 ± 0.05** | | |
| | 6200-6400 | 0.65 ± 0.29 | 0.20 ± 0.09 | | -0.28 ± 0.06 | | |
| | 6400-6600 | **4.64 ± 0.28** | **1.44 ± 0.09** | | -0.12 ± 0.04 | | |
| | 6600-6800 | 3.37 ± 0.28 | **1.05 ± 0.09** | **0.54 ± 0.12** | -0.11 ± 0.03 | 0.51 ± 0.12 | |
| | 6800-7000 | 0.86 ± 0.30 | 0.27 ± 0.09 | -0.85 ± 0.08 | **0.21 ± 0.04** | | 0.80 ± 0.31 |
| | 7000-7200 | 0.80 ± 0.21 | 0.25 ± 0.07 | | 0.16 ± 0.06 | | 0.66 ± 0.28 |
| 19_o | 5600-5800 | 0.65 ± 0.15 | 0.20 ± 0.05 | **0.55 ± 0.12** | 0.06 ± 0.02 | 2.72 ± 0.87 | 0.29 ± 0.12 |
| | 5800-6000 | | -0.20 ± 0.03 | 0.25 ± 0.09 | **0.15 ± 0.06** | | |
| | 6000-6200 | | -0.17 ± 0.05 | | 0.03 ± 0.02 | | |
| | 6200-6400 | 1.24 ± 0.27 | 0.38 ± 0.09 | 0.24 ± 0.11 | -0.19 ± 0.04 | 0.63 ± 0.32 | |
| | 6400-6600 | **3.61 ± 0.22** | **1.12 ± 0.07** | | | | |
| | 6600-6800 | 1.95 ± 0.17 | **0.61 ± 0.05** | **0.38 ± 0.10** | | 0.62 ± 0.18 | |
| | 6800-7000 | 1.11 ± 0.26 | 0.34 ± 0.08 | -0.71 ± 0.14 | **0.17 ± 0.03** | | 0.49 ± 0.14 |
| | 7000-7200 | 0.99 ± 0.17 | 0.31 ± 0.05 | | | | |
| 19_i | 5600-5800 | 0.43 ± 0.13 | 0.13 ± 0.04 | | | | |
| | 5800-6000 | | | | **0.28 ± 0.04** | | |
| | 6000-6200 | | -0.18 ± 0.08 | | | | |
| | 6200-6400 | | | -0.15 ± 0.04 | -0.19 ± 0.06 | | |
| | 6400-6600 | **4.41 ± 0.31** | **1.37 ± 0.10** | | -0.11 ± 0.04 | | |
| | 6600-6800 | 3.48 ± 0.27 | **1.08 ± 0.08** | **0.71 ± 0.12** | | 0.66 ± 0.12 | |
| | 6800-7000 | | | -0.45 ± 0.09 | -0.08  0.04 | | |
| | 7000-7200 | 0.76 ± 0.30 | 0.24 ± 0.09 | | 0.12 ± 0.04 | | 0.53 ± 0.28 |
| 19_ii | 5600-5800 | 0.60 ± 0.11 | 0.19 ± 0.03 | **0.58 ± 0.17** | 0.19 ± 0.01 | 3.09 ± 1.08 | 0.99 ± 0.19 |
| | 5800-6000 | | -0.38 ± 0.04 | 0.37 ± 0.17 | 0.20 ± 0.07 | | |
| | 6000-6200 | | | | -0.08 ± 0.03 | | |
| | 6200-6400 | 0.74 ± 0.25 | 0.23 ± 0.08 | 0.32 ± 0.14 | -0.32 ± 0.05 | 1.42 ± 0.78 | |
| | 6400-6600 | **3.42 ± 0.22** | **1.06 ± 0.07** | | -0.14 ± 0.03 | | |
| | 6600-6800 | 1.84 ± 0.15 | **0.57 ± 0.05** | | | | |
| | 6800-7000 | 0.83 ± 0.32 | 0.26 ± 0.10 | -1.11 ± 0.09 | **0.33 ± 0.04** | | 1.29 ± 0.51 |
| | 7000-7200 | 0.85 ± 0.23 | 0.26 ± 0.07 | | 0.20 ± 0.07 | | 0.77 ± 0.35 |
| 19_iii | 5600-5800 | 0.93 ± 0.15 | 0.29 ± 0.05 | | 0.06 ± 0.01 | | 0.20 ± 0.05 |
| | 5800-6000 | | -0.42 ± 0.10 | | **0.31 ± 0.07** | | |
| | 6200-6400 | | -0.18 ± 0.09 | | -0.29 ± 0.09 | | |
| | 6400-6600 | **4.24 ± 0.29** | **1.32 ± 0.09** | | | | |
| | 6600-6800 | 3.64 ± 0.22 | **1.13 ± 0.07** | **0.79 ± 0.08** | -0.18 ± 0.02 | 0.70 ± 0.09 | |
| | 6800-7000 | | | -0.87 ± 0.09 | | | |
| | 7000-7200 | | | 0.33 ± 0.14 | 0.17 ± 0.04 | | |
| 19_iv | 5600-5800 | 0.83 ± 0.20 | 0.26 ± 0.06 | **0.51 ± 0.15** | 0.19 ± 0.02 | 2.00 ± 0.77 | 0.75 ± 0.20 |
| | 5800-6000 | | -0.51 ± 0.10 | | **0.32 ± 0.08** | | |
| | 6000-6200 | | | -0.23 ± 0.09 | 0.10 ± 0.05 | | |
| | 6200-6400 | | -0.22 ± 0.07 | -0.16 ± 0.05 | -0.28 ± 0.09 | | |
| | 6400-6600 | **3.34 ± 0.17** | **1.04 ± 0.05** | -0.60 ± 0.18 | | | |
| | 6600-6800 | 2.53 ± 0.20 | **0.78 ± 0.06** | | -0.19 ± 0.01 | | |
| | 6800-7000 | | | -1.10 ± 0.11 | 0.15 ± 0.05 | | |
| | 7000-7200 | | | 0.35 ± 0.16 | **0.34 ± 0.07** | | |
| 19_v | 5600-5800 | 0.52 ± 0.14 | 0.16 ± 0.04 | **0.69 ± 0.17** | 0.24 ± 0.01 | 4.28 ± 1.58 | 1.48 ± 0.41 |
| | 5800-6000 | | -0.40 ± 0.06 | 0.30 ± 0.10 | 0.24 ± 0.06 | | |
| | 6200-6400 | | | | -0.37 ± 0.07 | | |
| | 6400-6600 | **3.72 ± 0.23** | **1.16 ± 0.07** | -0.40 ± 0.13 | -0.16 ± 0.04 | | |
| | 6600-6800 | 2.66 ± 0.24 | **0.83 ± 0.07** | 0.14 ± 0.07 | -0.13 ± 0.04 | 0.17 ± 0.08 | |
| | 6800-7000 | | | -1.15 ± 0.05 | **0.32 ± 0.05** | | |
| | 7000-7200 | 0.51 ± 0.24 | 0.16 ± 0.07 | 0.25 ± 0.12 | **0.32 ± 0.07** | 1.56 ± 1.06 | 1.98 ± 1.01 |
| 19_vi | 5600-5800 | | | **1.25 ± 0.16** | 0.38 ± 0.04 | | |
| | 5800-6000 | | -0.28 ± 0.07 | 0.38 ± 0.17 | 0.26 ± 0.08 | | |
| | 6200-6400 | | | | -0.38 ± 0.06 | | |
| | 6400-6600 | **1.70 ± 0.21** | **0.53 ± 0.06** | -1.59 ± 0.17 | -0.24 ± 0.02 | | |
| | 6600-6800 | 0.63 ± 0.15 | 0.20 ± 0.05 | -0.81 ± 0.11 | | | |
| | 6800-7000 | | | -1.41 ± 0.10 | 0.47 ± 0.08 | | |
| | 7000-7200 | | | | **0.66 ± 0.11** | | |

**Figure 10.14:** Table containing the flux of the $^{12}$CO($1 \to 0$), $^{12}$CO($2 \to 1$) and $^{13}$CO($1 \to 0$) emission summed over 200 km/s velocity ranges, including the H$_2$ molecular gas mass and flux ratios, in each region as marked in Fig.10.1. Peak emission velocity ranges in each region have been highlighted in boldface, while negative values have been shaded in grey. The error here is the standard deviation in that velocity range.

## 10.2.2  Molecular Hydrogen Gas Mass & Kinematics

As can be seen in the table in Fig.10.14 the main $H_2$ gas mass and $^{12}CO(1 \rightarrow 0)$ emission in/near NGC7319 is in the $6400 - 6600$ km/s velocity range. But the regions along the bar, region 19, 19_i and 19_ii, and region 19_o that covers the starting point of the inner tidal tail, show higher velocity components as well, as clear in the table in Fig.10.13. Furthermore, region 19_o and 19_ii have the main part of their $H_2$ gas content at the lower $\sim 6400$ km/s velocity component and a significant amount spread into the $\sim 6600$ and $\sim 6800$ km/s components. While the other regions in/near NGC7319 show a proclivity toward keeping the main part of the gas in the $\sim 6600$ km/s velocity region.

The $^{12}CO(2 \rightarrow 1)$ and $^{13}CO(1 \rightarrow 0)$ can be detected in nearly all of the regions in/near NGC7319, but they can rarely be fitted with Gaussians at similar velocities, see the tables in Fig.10.13 and Fig.10.14.

The velocity dispersion in/near NGC7319 ranges $\sim 25-110$ km/s for the $^{12}CO(1 \rightarrow 0)$ line, with one broad main component, while for the $^{12}CO(2 \rightarrow 1)$ and $^{13}CO(1 \rightarrow 0)$ it is slightly more contained at $\sim 35 - 65$ km/s and $\sim 25 - 70$ km/s respectively. In the southern parts of NGC7319, i.e., region 19, 19_o, 19_ii, 19_v-vi, a low velocity component in $^{12}CO(2 \rightarrow 1)$ at $\sim 5800$ km/s is consistently present, potentially connecting to a lower velocity gas deposit left during the previous interaction with NGC7320C. Only in region 19_i does the $^{12}CO(2 \rightarrow 1)$ show a high velocity component at $\sim 6700$ km/s. The $^{13}CO(1 \rightarrow 0)$ emission is quite faint, and favours a higher line-of-sight velocity, of $\sim 6900 - 7300$ km/s, compared to the systemic line-of-sight velocity of this galaxy of $\sim 6750$ km/s.

## 10.2.3  Line Ratios; Excitation Temperature & Optical Depth

From the table in Fig.10.13 it is clear that there are few $^{12}CO(1 \rightarrow 0)$, $^{12}CO(2 \rightarrow 1)$ and $^{13}CO(1 \rightarrow 0)$ lines co-existing at the same line-of-sight velocity in the same region. Therefore calculating the excitation temperature, Eq.9.4, and the optical depth, Eq.9.7/9.8, is not straight forward - as the equations rely on the lines originating from the same gas congregation at the same resolution. But, from the tables in Fig.10.13 and 10.14 it can be assumed that in region 19_v, the gas content at a line-of-sight velocity of $\sim 5770$ km/s is most likely at high temperature and probably optically thick.

Looking at the $^{12}CO(2 \rightarrow 1)/^{12}CO(1 \rightarrow 0)$ main beam temperature line ratios provide only two regions with values at a SNR$> 2$. Region 19_i at a velocity of $\sim 6645$ km/s at a ratio value of $0.70 \pm 0.28$ and region 19_iii at a velocity of $\sim 6655$ km/s at $0.73 \pm 0.36$. Remember that ratio values of $^{12}CO(2 \rightarrow 1)/^{12}CO(1 \rightarrow 0)$ near 1 denotes dense, warm, optically thick gas, values near 4 indicates dense, warm, optically thin and a value below 1 can indicate low temperature thick gas. Both of the ratio values in region 19_i and region 19_ii therefore indicate low temperature optically thick gas.

However, if a leap is taken and the assumption made that all gas in a 200 km/s velocity range originates from the same gas deposit, more flux ratio values can be obtained. See the two right columns in the table in Fig.10.14, where such values are presented. Since a line ratio value of $^{13}CO(1 \rightarrow 0)/^{12}CO(1 \rightarrow 0) > 0.63$ means

optically thick gas, interesting opposition in the values presented in the table in Fig.10.14 is seen. For example, observe the velocity range of $5600 - 5800$ km/s in region 19, the $^{12}$CO$(2 \rightarrow 1)/^{12}$CO$(1 \rightarrow 0)$ line ratio states near dense, warm, optically thin gas, while the $^{13}$CO$(1 \rightarrow 0)/^{12}$CO$(1 \rightarrow 0)$ line ratio indicates optically thick gas - however, the errors are too large to exclude either case.

Region 19_o, on the other hand, shows agreement in the two line ratios in the low velocity range, indicating dense, warm, optically thin gas. While the velocity range $6200 - 6800$ km/s shows a tendency towards lower temperature optically thick gas. The velocity range $6800 - 7000$ km/s line ratio indicates optically thin gas, but if the peak temperature values of the two peaks is used, a value of $T_{mb}^{13CO(1 \rightarrow 0)}/T_{mb}^{12CO(1 \rightarrow 0)} = 0.79 \pm 0.43$ is obtained, i.e., with too large error to be able to state if the gas is optically thick or thin. Unfortunately, no $^{13}$CO$(1 \rightarrow 0)/^{12}$CO$(1 \rightarrow 0)$ line ratios provide a SNR$> 2$ using the Gaussian fit values, and as they vary in $0.49 - 0.79 \pm 0.26 - 0.43$ they cannot provide any clear statement regarding the optical depth.

Further observing the table in Fig.10.14, reveals a general indication of the gas in/near NGC7319 to be dense, warm and optically thick, albeit sometimes a bit colder. The exception is the lowest velocity range, $5600 - 5800$ km/s, where the gas in several cases borders on optically thin or low density.

## 10.3 The Star-Forming Ridge & the Bridge

The IGM in Stephan's Quintet contains large amounts of gas, deposited there during the previous interactions in the group. This chapter details the results of the radio observations in the regions chosen in the bridge, the star-forming ridge and SQ-A. Presenting spectra, velocities, fluxes, molecular hydrogen gas masses as well as a discussion of excitation temperatures and optical depth.

### 10.3.1 Spectra

Fig.10.15-10.21 show the emission in each of the CO lines in region b_i-ii, SQ-A and SF_i-iv as marked in Fig.10.1. In each plot the blue line shows the observed spectrum and the red line shows the fit (fitted as explained in Chapter 9.3) whenever a fit is possible. Note that while the y-axis of the $^{12}CO(1 \rightarrow 0)$ and the $^{13}CO(1 \rightarrow 0)$ lines in (a) and (c) spans -6 to 12 mK, the y-axis of the $^{12}CO(2 \rightarrow 1)$ line in (b) spans -15 to 20 mK.

The spectra in Fig.10.15-10.21 show the complexity of the CO gas in the IGM, via the multiple velocity components present and the effect of the ongoing shock. As can be seen the main emission is in the $^{12}CO(1 \rightarrow 0)$ and $^{12}CO(2 \rightarrow 1)$ lines, with emission present in all of the regions, i.e., the bridge, the star-forming ridge and SQ-A. Furthermore, there is no clear emission in the $^{13}CO(1 \rightarrow 0)$ line detected in any of these regions.

The results of the Gaussian decomposition of these spectra are presented in the table in Fig.10.22, including the $H_2$ gas mass f, for SNR> 2. The table in Fig.10.23 displays the $H_2$ gas mass and fluxes of the three CO lines in velocity ranges of 200 km/s as derived using Eq.9.1, illustrating the distribution of matter while including more diffuse gas as well. Although absorption is unlikely, the values have been included shaded in grey for completeness. Included in this table is also the flux ratios of $^{12}CO(2 \rightarrow 1)/^{12}CO(1 \rightarrow 0)$, as well as $^{13}CO(1 \rightarrow 0)/^{12}CO(1 \rightarrow 0)$.



(a)    (b)    (c)
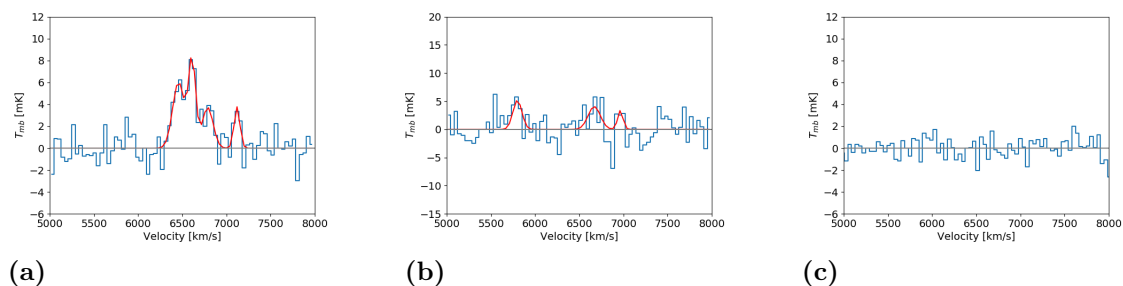
**Figure 10.15:** CO emission in region b_i shown in blue, and the fit is shown in red (wherever a fit is possible). The fits that result in a SNR> 2 are presented in the tables in Fig.10.22. (a) The $^{12}CO(1 \rightarrow 0)$ line; (b) The $^{12}CO(2 \rightarrow 1)$ line; (c) The $^{13}CO(1 \rightarrow 0)$ line.
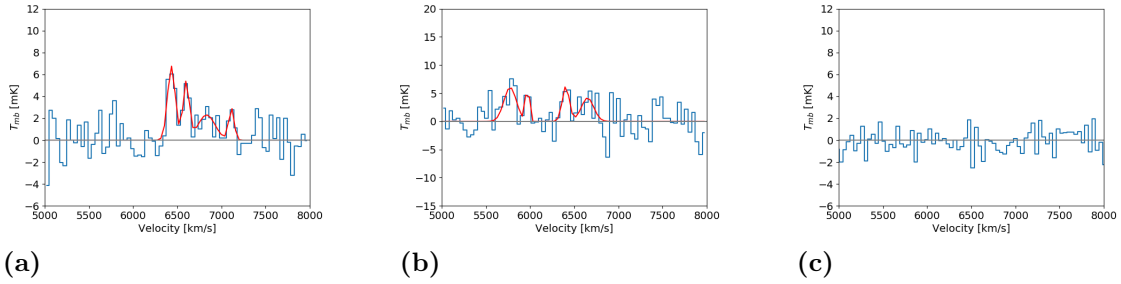
**Figure 10.16:** CO emission in region b_ii shown in blue, and the fit is shown in red (wherever a fit is possible). The fits that result in a SNR> 2 are presented in the tables in Fig.10.22. (a) The $^{12}CO(1 \to 0)$ line; (b) The $^{12}CO(2 \to 1)$ line; (c) The $^{13}CO(1 \to 0)$ line.
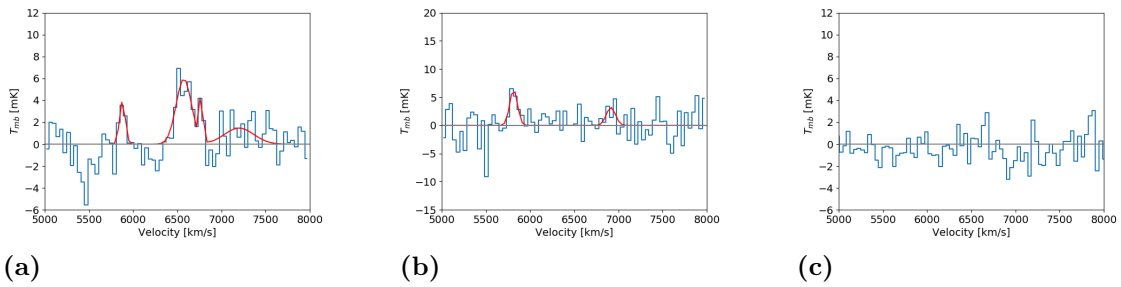


**Figure 10.17:** CO emission in region SQ-A shown in blue, and the fit is shown in red (wherever a fit is possible). The fits that result in a SNR> 2 are presented in the tables in Fig.10.22. (a) The $^{12}CO(1 \to 0)$ line; (b) The $^{12}CO(2 \to 1)$ line; (c) The $^{13}CO(1 \to 0)$ line.
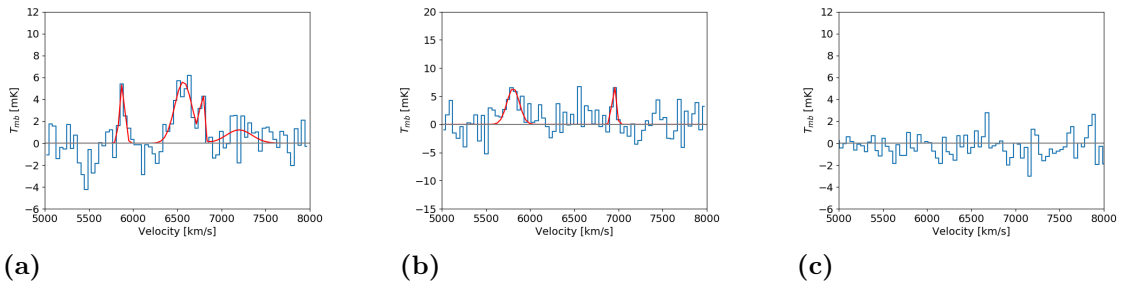


**Figure 10.18:** CO emission in region SF_i shown in blue, and the fit is shown in red (wherever a fit is possible). The fits that result in a SNR> 2 are presented in the tables in Fig.10.22. (a) The $^{12}CO(1 \to 0)$ line; (b) The $^{12}CO(2 \to 1)$ line; (c) The $^{13}CO(1 \to 0)$ line.

153
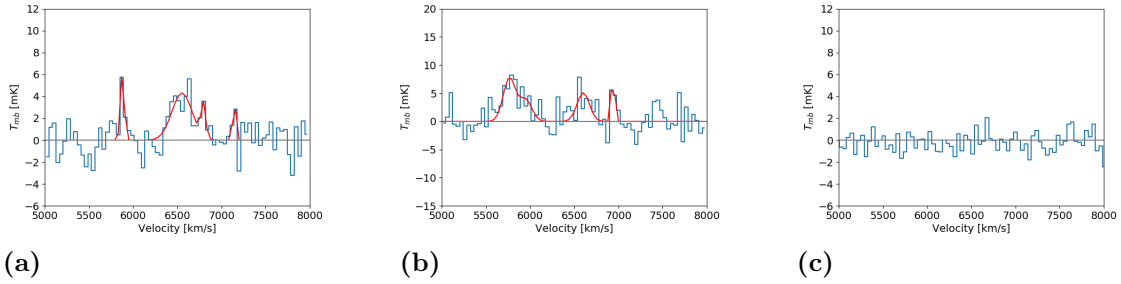
**Figure 10.19:** CO emission in region SF_ii shown in blue, and the fit is shown in red (wherever a fit is possible). The fits that result in a SNR$> 2$ are presented in the tables in Fig.10.22. (a) The $^{12}$CO$(1 \rightarrow 0)$ line; (b) The $^{12}$CO$(2 \rightarrow 1)$ line; (c) The $^{13}$CO$(1 \rightarrow 0)$ line.
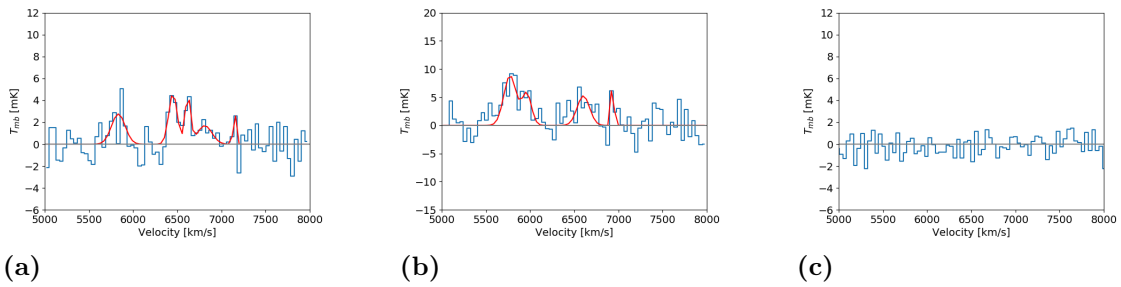


**Figure 10.20:** CO emission in region SF_iii shown in blue, and the fit is shown in red (wherever a fit is possible). The fits that result in a SNR$> 2$ are presented in the tables in Fig.10.22. (a) The $^{12}$CO$(1 \rightarrow 0)$ line; (b) The $^{12}$CO$(2 \rightarrow 1)$ line; (c) The $^{13}$CO$(1 \rightarrow 0)$ line.
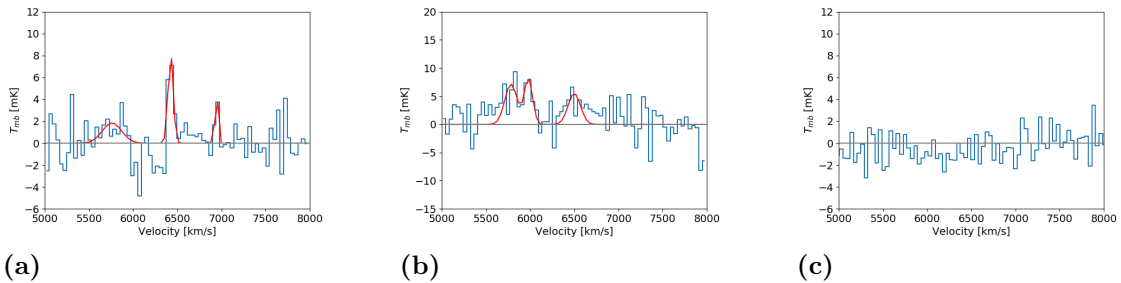


**Figure 10.21:** CO emission in region SF_iv shown in blue, and the fit is shown in red (wherever a fit is possible). The fits that result in a SNR$> 2$ are presented in the tables in Fig.10.22. (a) The $^{12}$CO$(1 \rightarrow 0)$ line; (b) The $^{12}$CO$(2 \rightarrow 1)$ line; (c) The $^{13}$CO$(1 \rightarrow 0)$ line.

| Region | 12CO(1-0) Vlos [km/s] | Vel.Disp [km/s] | Flux [K km/s] | M(H$_2$) [$10^8$M$_\odot$] |
|---|---|---|---|---|
| b_i | 6457.9 ± 17.8 | 66.4 ± 18.3 | 0.71 ± 0.15 | 2.30 ± 0.49 |
|  | 6611.6 ± 9.6 | 39.9 ± 10.5 | 0.57 ± 0.12 | 1.85 ± 0.40 |
|  | 6787.9 ± 20.0 | 61.2 ± 22.1 | 0.40 ± 0.13 | 1.30 ± 0.42 |
|  | 7119.7 ± 12.7 | 32.8 ± 11.5 | 0.22 ± 0.08 | 0.71 ± 0.26 |
| b_ii | 6433.7 ± 10.3 | 43.8 ± 10.7 | 0.52 ± 0.13 | 1.69 ± 0.41 |
|  | 6600.7 ± 12.6 | 35.2 ± 12.7 | 0.33 ± 0.12 | 1.07 ± 0.37 |
|  | 6831.5 ± 47.2 | 96.1 ± 53.7 | 0.39 ± 0.20 | 1.27 ± 0.65 |
| SQ-A | 5879.2 ± 16.5 | 32.4 ± 15.8 | 0.23 ± 0.12 | 0.73 ± 0.37 |
|  | 6574.2 ± 19.5 | 87.1 ± 21.8 | 0.92 ± 0.21 | 2.97 ± 0.68 |
| SF_i | 5877.1 ± 9.9 | 29.1 ± 8.6 | 0.28 ± 0.09 | 0.90 ± 0.28 |
|  | 6568.5 ± 17.4 | 97.3 ± 18.8 | 0.97 ± 0.18 | 3.12 ± 0.58 |
| SF_ii | 5879.6 ± 10.3 | 22.1 ± 8.4 | 0.24 ± 0.09 | 0.78 ± 0.29 |
|  | 6553.7 ± 24.1 | 114.5 ± 26.4 | 0.87 ± 0.19 | 2.81 ± 0.61 |
|  | 6794.6 ± 17.2 | 26.3 ± 13.1 | 0.15 ± 0.08 | 0.47 ± 0.25 |
| SF_iii | 5832.8 ± 28.2 | 76.7 ± 28.2 | 0.38 ± 0.14 | 1.21 ± 0.46 |
|  | 6451.0 ± 13.4 | 47.6 ± 13.9 | 0.39 ± 0.12 | 1.27 ± 0.37 |
|  | 6619.8 ± 12.1 | 31.1 ± 15.4 | 0.24 ± 0.11 | 0.79 ± 0.35 |
| SF_iv | 6425.2 ± 7.9 | 29.5 ± 7.9 | 0.43 ± 0.12 | 1.38 ± 0.38 |

| Region | 12CO(2-1) Vlos [km/s] | Vel.Disp [km/s] | Flux [K km/s] | 13CO(1-0) Vlos [km/s] | Vel.Disp [km/s] | Flux [K km/s] |
|---|---|---|---|---|---|---|
| b_i | 5800.0 ± 22.3 | 50.5 ± 22.3 | 0.46 ± 0.21 |  |  |  |
|  | 6669.3 ± 33.4 | 69.1 ± 33.4 | 0.50 ± 0.25 |  |  |  |
| b_ii | 5774.2 ± 24.2 | 70.0 ± 25.5 | 0.75 ± 0.27 |  |  |  |
|  | 6403.8 ± 17.5 | 39.8 ± 17.7 | 0.44 ± 0.20 |  |  |  |
|  | 6650.0 ± 34.7 | 70.0 ± 35.5 | 0.52 ± 0.27 |  |  |  |
| SQ-A | 5813.0 ± 18.1 | 43.2 ± 18.1 | 0.49 ± 0.21 |  |  |  |
| SF_i | 5808.1 ± 20.9 | 70.0 ± 20.9 | 0.80 ± 0.25 |  |  |  |
| SF_ii | 5766.4 ± 42.8 | 70.0 ± 33.7 | 0.96 ± 0.35 |  |  |  |
|  | 6601.3 ± 25.2 | 70.0 ± 25.2 | 0.63 ± 0.23 |  |  |  |
| SF_iii | 5773.1 ± 21.8 | 70.0 ± 22.7 | 1.10 ± 0.29 |  |  |  |
|  | 5961.8 ± 29.6 | 53.0 ± 28.2 | 0.53 ± 0.24 |  |  |  |
|  | 6602.6 ± 25.1 | 70.0 ± 25.1 | 0.65 ± 0.24 |  |  |  |
| SF_iv | 5783.8 ± 27.2 | 70.0 ± 30.1 | 0.89 ± 0.34 |  |  |  |
|  | 5981.5 ± 19.6 | 46.0 ± 19.8 | 0.67 ± 0.26 |  |  |  |
|  | 6500.0 ± 30.3 | 70.0 ± 30.3 | 0.68 ± 0.30 |  |  |  |

**Figure 10.22:** Table containing the line-of-sight velocity, velocity dispersion and the integrated flux of the fits of the $^{12}$CO($1 \to 0$), $^{12}$CO($2 \to 1$) and $^{13}$CO($1 \to 0$) lines, as well as the H$_2$ molecular gas mass, whenever the SNR$> 2$, in the regions in the star-forming ridge and the bridge, as marked in Fig.10.1.

| Region | Vel. Range [km/s] | M(H₂) [10⁸M_⊙] | 12CO(1-0) Flux [K km/s] | 12CO(2-1) Flux [K km/s] | 13CO(1-0) Flux [K km/s] | I(12CO(2-1))/ I(12CO(1-0)) | I(13CO(1-0))/ I(12CO(1-0)) |
|---|---|---|---|---|---|---|---|
| b_i | 5600-5800 | | | **0.64 ± 0.07** | | | |
| | 5800-6000 | 0.54 ± 0.16 | 0.17 ± 0.05 | 0.21 ± 0.08 | **0.10 ± 0.04** | 1.25 ± 0.59 | 0.59 ± 0.28 |
| | 6000-6200 | | -0.18 ± 0.03 | | | | |
| | 6200-6400 | 0.76 ± 0.26 | 0.24 ± 0.08 | | -0.11 ± 0.02 | | |
| | 6400-6600 | **3.75 ± 0.16** | **1.17 ± 0.05** | 0.26 ± 0.07 | | 0.22 ± 0.06 | |
| | 6600-6800 | 2.45 ± 0.24 | **0.76 ± 0.08** | 0.52 ± 0.12 | | 0.69 ± 0.17 | |
| | 6800-7000 | 0.69 ± 0.20 | 0.21 ± 0.06 | | | | |
| | 7000-7200 | 0.94 ± 0.20 | 0.29 ± 0.06 | | | | |
| b_ii | 5600-5800 | 0.88 ± 0.25 | 0.27 ± 0.08 | **0.79 ± 0.08** | | 2.87 ± 0.86 | |
| | 5800-6000 | | | **0.64 ± 0.10** | | | |
| | 6000-6200 | | -0.13 ± 0.04 | | **0.06 ± 0.02** | | |
| | 6200-6400 | | | 0.30 ± 0.12 | -0.10 ± 0.01 | | |
| | 6400-6600 | **2.58 ± 0.22** | **0.80 ± 0.07** | 0.51 ± 0.08 | | 0.63 ± 0.12 | |
| | 6600-6800 | **1.20 ± 0.16** | **0.37 ± 0.05** | 0.56 ± 0.09 | -0.13 ± 0.03 | 1.49 ± 0.31 | |
| | 6800-7000 | 1.02 ± 0.15 | 0.32 ± 0.05 | | -0.12 ± 0.02 | | |
| | 7000-7200 | 0.76 ± 0.12 | 0.23 ± 0.04 | | | | |
| SQ-A | 5600-5800 | | | 0.28 ± 0.11 | -0.17 ± 0.03 | | |
| | 5800-6000 | 1.08 ± 0.18 | 0.33 ± 0.05 | **0.50 ± 0.07** | | 1.49 ± 0.32 | |
| | 6000-6200 | | -0.16 ± 0.03 | 0.15 ± 0.05 | -0.20 ± 0.02 | | |
| | 6200-6400 | | -0.18 ± 0.05 | 0.22 ± 0.05 | | | |
| | 6400-6600 | 2.58 ± 0.27 | **0.80 ± 0.08** | | | | |
| | 6600-6800 | 2.16 ± 0.19 | **0.67 ± 0.06** | 0.12 ± 0.03 | | 0.17 ± 0.05 | |
| | 6800-7000 | | | **0.40 ± 0.07** | -0.35 ± 0.04 | | |
| | 7000-7200 | 0.54 ± 0.19 | 0.17 ± 0.06 | | -0.22 ± 0.04 | | |
| SF_i | 5600-5800 | | | **0.65 ± 0.08** | -0.13 ± 0.04 | | |
| | 5800-6000 | 1.43 ± 0.22 | 0.44 ± 0.07 | **0.70 ± 0.08** | | 1.57 ± 0.30 | |
| | 6000-6200 | | -0.15 ± 0.04 | 0.21 ± 0.05 | -0.13 ± 0.04 | | |
| | 6200-6400 | | | | -0.12 ± 0.03 | | |
| | 6400-6600 | **2.65 ± 0.17** | **0.82 ± 0.05** | 0.32 ± 0.11 | | 0.38 ± 0.13 | |
| | 6600-6800 | **2.24 ± 0.21** | **0.70 ± 0.07** | 0.32 ± 0.06 | **0.10 ± 0.05** | 0.46 ± 0.10 | 0.15 ± 0.07 |
| | 6800-7000 | | | 0.40 ± 0.11 | -0.15 ± 0.03 | | |
| | 7000-7200 | 0.59 ± 0.18 | 0.18 ± 0.06 | -0.13 ± 0.04 | -0.19 ± 0.05 | | |
| SF_ii | 5600-5800 | 0.55 ± 0.12 | 0.17 ± 0.04 | **0.98 ± 0.10** | -0.10 ± 0.04 | 5.73 ± 1.33 | |
| | 5800-6000 | 1.25 ± 0.26 | 0.39 ± 0.08 | **0.93 ± 0.08** | -0.05 ± 0.02 | 2.40 ± 0.54 | |
| | 6000-6200 | | -0.11 ± 0.05 | 0.18 ± 0.06 | -0.07 ± 0.03 | | |
| | 6200-6400 | | | | -0.11 ± 0.03 | | |
| | 6400-6600 | **2.29 ± 0.07** | **0.71 ± 0.02** | 0.59 ± 0.10 | | 0.83 ± 0.15 | |
| | 6600-6800 | **1.78 ± 0.21** | **0.55 ± 0.07** | 0.51 ± 0.07 | | 0.92 ± 0.17 | |
| | 6800-7000 | 0.20 ± 0.09 | 0.06 ± 0.03 | | | | |
| | 7000-7200 | 0.54 ± 0.16 | 0.17 ± 0.05 | | -0.12 ± 0.03 | | |
| SF_iii | 5600-5800 | 0.96 ± 0.14 | 0.30 ± 0.04 | **1.09 ± 0.11** | -0.07 ± 0.04 | 3.66 ± 0.66 | |
| | 5800-6000 | 0.84 ± 0.26 | 0.26 ± 0.08 | **1.15 ± 0.08** | -0.09 ± 0.02 | 4.44 ± 1.41 | |
| | 6000-6200 | | | 0.20 ± 0.05 | -0.07 ± 0.02 | | |
| | 6200-6400 | | | | -0.10 ± 0.03 | | |
| | 6400-6600 | **1.92 ± 0.13** | **0.60 ± 0.04** | 0.70 ± 0.08 | | 1.16 ± 0.16 | |
| | 6600-6800 | **1.24 ± 0.17** | **0.39 ± 0.05** | 0.55 ± 0.06 | | 1.42 ± 0.25 | |
| | 6800-7000 | 0.47 ± 0.07 | 0.15 ± 0.02 | | | | |
| | 7000-7200 | 0.44 ± 0.13 | 0.14 ± 0.04 | | -0.05 ± 0.02 | | |
| SF_iv | 5600-5800 | 0.81 ± 0.08 | 0.25 ± 0.03 | **0.87 ± 0.08** | | 3.48 ± 0.48 | |
| | 5800-6000 | | | **1.25 ± 0.10** | -0.23 ± 0.02 | | |
| | 6000-6200 | | -0.29 ± 0.08 | 0.24 ± 0.08 | -0.23 ± 0.04 | | |
| | 6200-6400 | | | 0.28 ± 0.12 | -0.20 ± 0.02 | | |
| | 6400-6600 | **1.70 ± 0.31** | **0.53 ± 0.09** | 0.79 ± 0.07 | -0.14 ± 0.04 | 1.51 ± 0.30 | |
| | 6600-6800 | 0.41 ± 0.03 | 0.13 ± 0.01 | 0.48 ± 0.03 | | 3.83 ± 0.34 | |
| | 6800-7000 | 0.52 ± 0.22 | 0.16 ± 0.07 | 0.29 ± 0.09 | -0.23 ± 0.03 | 1.80 ± 0.96 | |
| | 7000-7200 | | | 0.43 ± 0.10 | | | |

**Figure 10.23:** Table containing the flux of the $^{12}$CO$(1 \rightarrow 0)$, $^{12}$CO$(2 \rightarrow 1)$ and $^{13}$CO$(1 \rightarrow 0)$ emission summed over 200 km/s velocity ranges, including the H$_2$ molecular gas mass and flux ratios, in each region as marked in Fig.10.1. Peak emission velocity ranges in each region have been highlighted in boldface, while negative values have been shaded in grey. The error here is the standard deviation in that velocity range.

## 10.3.2 Molecular Hydrogen Gas Mass & Kinematics

Studying the spectra in Fig.10.15-10.21 and the table in Fig.10.22 reveal gas of multiple velocity components, as detected in this area in previous observations (Guillard et al. (2012) amongst others). The velocity dispersion of the $^{12}CO(1 \rightarrow 0)$ line spans $\sim 20-115$ km/s, while the $^{12}CO(2 \rightarrow 1)$ line shows velocity dispersions of $\sim 40-70$ km/s.

The $^{12}CO(2 \rightarrow 1)$ line shows a slight predisposition towards lower velocities compared to the $^{12}CO(1 \rightarrow 0)$. But the effect of the ongoing shock in the star-forming ridge is clear in the high amount of $^{12}CO(2 \rightarrow 1)$ present in the region.

In general the CO in the bridge, region b_i, favours a higher velocity component, closer to that of its closest galaxy, NGC7319. However, in $^{12}CO(2 \rightarrow 1)$ a low velocity component is also prominent, relating to NGC7320C or NGC7318B. The star-forming ridge shows multiple velocity components, centering on one at $\sim 5800$ km/s and one at $\sim 6600$ km/s, relating it to the line-of-sight velocities of NGC7318B and NGC7317/NGC7318A respectively.

This data question the discovery by Guillard et al. (2012) of a $\sim 6900$ km/s velocity component in the SQ-A, however, a significant amount of $^{12}CO(2 \rightarrow 1)$ gas is found in this region in the $6800 - 7000$ km/s velocity range, see the table in Fig.10.23. While the main portion of the $^{12}CO(1 \rightarrow 0)$ gas in SQ-A is in the $6400 - 6800$ km/s velocity range, the $^{12}CO(2 \rightarrow 1)$ collects in the $5800 - 6000$ km/s and $6800 - 7000$ km/s ranges.

## 10.3.3 Line Ratios; Excitation Temperature & Optical Depth

The table in Fig.10.22 shows that there is not sufficient $^{13}CO(1 \rightarrow 0)$ emission in the bridge and star-forming ridge to warrant proper fitting, but it does show that there are several regions where there is emission in both $^{12}CO(1 \rightarrow 0)$ and $^{12}CO(2 \rightarrow 1)$ simultaneously at a similar line-of-sight velocity.

The table in Fig.10.24 presents the values of the main beam brightness temperature and the line ratios at all velocities in the bridge and star-forming ridge where the lines are within 120 km/s from each other (i.e., 3 velocity channels) - generally they are only $\sim 50$ km/s apart. As can be seen in the table, the bridge is optically thick but at low temperature (ratio values below 1), while the SQ-A and the star-forming ridge is in general dense, warm and optically thick. There are two exceptions, the low velocity component in SF_iii that is potentially warm, dense and optically thin, and SF_iv that may be at lower temperatures, but still optically thick.

If the assumption is made that all the gas in one region in a 200 km/s velocity range originates from the same gas congregation, the flux ratio values are as presented in the table in Fig.10.23. In general these values agree with the statement made by the main beam temperature line ratios of the gas being optically thick. There are only a couple of outliers, particularly the lower velocity ranges of region SF_ii, SF_iii and SF_iv, which are bordering on warm, dense and optically thin.

| Region | Vlos average [km/s] | 12CO(1-0) T$_{mb}$ [mK] | 12CO(2-1) T$_{mb}$ [mK] | T$_{mb}$ ratio 12CO(2-1)/ 12CO(1-0) |
|--------|---------|-----------|-----------|------------|
| b_i    | 6640 | 8.11 ± 1.28 | 4.06 ± 1.70 | 0.50 ± 0.22 |
| b_ii   | 6420 | 6.76 ± 1.36 | 6.25 ± 2.35 | 0.93 ± 0.39 |
| SQ-A   | 5845 | 3.94 ± 1.69 | 6.42 ± 2.33 | 1.63 ± 0.92 |
| SF_i   | 5845 | 5.42 ± 1.45 | 6.43 ± 1.66 | 1.19 ± 0.44 |
| SF_ii  | 5825 | 6.16 ± 1.90 | 7.70 ± 1.95 | 1.25 ± 0.50 |
|        | 6575 | 4.30 ± 0.75 | 5.09 ± 1.59 | 1.18 ± 0.42 |
| SF_iii | 5805 | 2.76 ± 0.88 | 8.88 ± 1.67 | 3.22 ± 1.19 |
|        | 6610 | 4.44 ± 1.50 | 5.25 ± 1.63 | 1.18 ± 0.54 |
| SF_iv  | 6465 | 8.18 ± 1.87 | 5.49 ± 2.06 | 0.67 ± 0.29 |

**Figure 10.24:** Table containing the main beam brightness temperature of the $^{12}$CO(1 → 0) and $^{12}$CO(2 → 1) lines and their ratio, in the intergalactic medium between NGC7319 and the NGC7318 pair, i.e., including the bridge and the star-forming ridge. The velocity stated is the average of the velocity centres of $^{12}$CO(1 → 0) and $^{12}$CO(2 → 1), where the lines are separated by $\sim$ 50 km/s, maximum 120 km/s (3 velocity channels).

# 10.4   The NGC7318 Pair & NGC7317

NGC7318B, the intruder, is currently entering the group from behind at a relative velocity of $\sim 000$ km/s and is creating intense activity by interacting with both NGC7318A and the SQ IGM. NGC7318A is a quiescent elliptical galaxy, as is the gas poor NGC7317. NGC7317 may have passed through the group in the past, an interaction in which it deposited most of its ISM into the IGM.

This chapter details the results of the radio observations in regions chosen in/near the NGC7318 pair as well as in NGC7317. Presenting spectra, velocities, fluxes, molecular hydrogen gas masses as well as discussing of excitation temperatures and optical depth.

## 10.4.1   Spectra

Fig.10.25-10.31 show the emission in each of the CO lines in region 18a, 18b, 18_i-iv and 17 as marked in Fig.10.1. In each plot the blue line shows the observed spectrum and the red line shows the fit, as detailed in Chapter 9.3, whenever a fit is possible. Note that while the y-axis of the $^{12}CO(1 \rightarrow 0)$ and the $^{13}CO(1 \rightarrow 0)$ lines in (a) and (c) spans -6 to 12 mK, the y-axis of the $^{12}CO(2 \rightarrow 1)$ line in (b) spans -15 to 20 mK.

As can be seen in the spectra, there is not excessive CO emission present in these regions. NGC7318A show slight emission in $^{12}CO(2 \rightarrow 1)$ and $^{13}CO(1 \rightarrow 0)$, while the spiral galaxy, NGC7318B, display $^{12}CO(1 \rightarrow 0)$ and $^{12}CO(2 \rightarrow 1)$ content. Region 18_i, that contains the dust trail seen to the south-west of NGC7318A (see Fig.3.1) displays CO gas emission in all three lines. The west NW-arm, region 18_iii, displays $^{12}CO(1 \rightarrow 0)$ as well as $^{12}CO(2 \rightarrow 1)$ emission. Furthermore, region 17, NGC7317, shows $^{12}CO(2 \rightarrow 1)$ emission only and at lower line-of-sight velocity than the systematic line-of-sight velocity of the galaxy itself.

The results of the Gaussian decomposition of these spectra are presented in the table in Fig.10.32, including the $H_2$ gas mass, for a SNR$> 2$. The table in Fig.10.33 displays the $H_2$ gas mass and fluxes of the three CO lines in velocity ranges of 200 km/s as derived using Eq.9.1, illustrating the distribution of matter while including more diffuse gas as well. Although absorption is unlikely, the values have been included shaded in grey for completeness. Included in this table are also the flux ratios of $^{12}CO(2 \rightarrow 1)/^{12}CO(1 \rightarrow 0)$, as well as $^{13}CO(1 \rightarrow 0)/^{12}CO(1 \rightarrow 0)$.
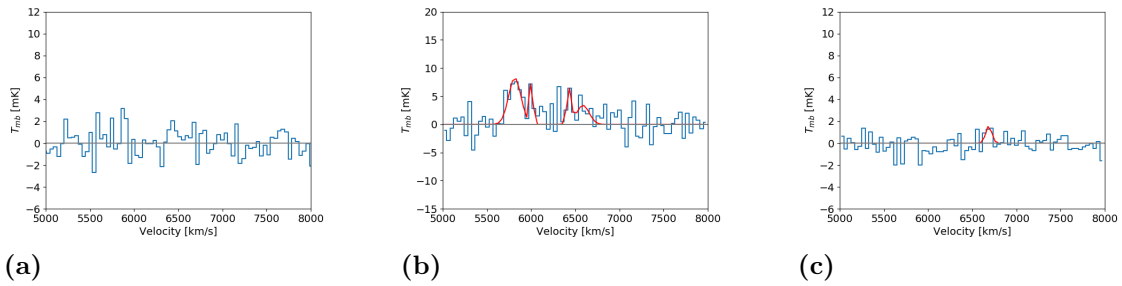
**Figure 10.25:** CO emission in NGC7318A, i.e., region 18a, shown in blue, and the fit is shown in red (wherever a fit is possible). The fits that result in a SNR$> 2$ are presented in the tables in Fig.10.32. (a) The $^{12}CO(1 \rightarrow 0)$ line; (b) The $^{12}CO(2 \rightarrow 1)$ line; (c) The $^{13}CO(1 \rightarrow 0)$ line.
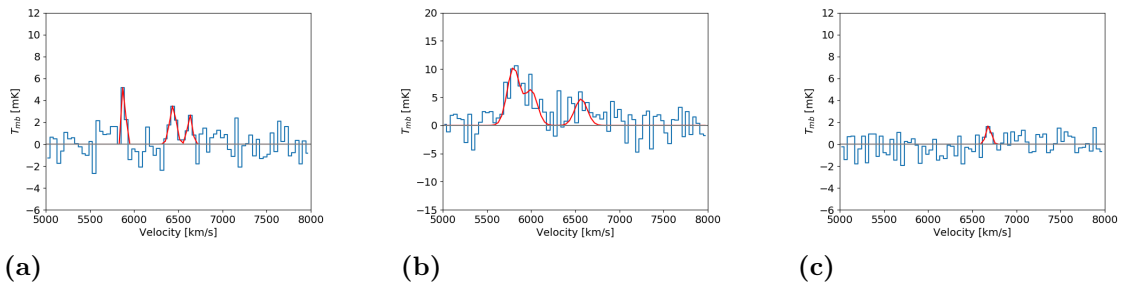


**Figure 10.26:** CO emission in NGC7318B, i.e., region 18b, shown in blue, and the fit is shown in red. The fits that result in a SNR$> 2$ are presented in the tables in Fig.10.32. (a) The $^{12}CO(1 \rightarrow 0)$ line; (b) The $^{12}CO(2 \rightarrow 1)$ line; (c) The $^{13}CO(1 \rightarrow 0)$ line.
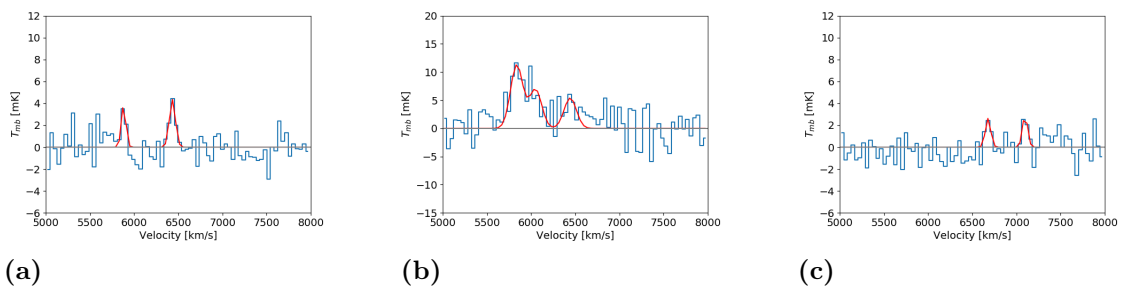


**Figure 10.27:** CO emission in region 18_i shown in blue, and the fit is shown in red. The fits that result in a SNR$> 2$ are presented in the tables in Fig.10.32. (a) The $^{12}CO(1 \rightarrow 0)$ line; (b) The $^{12}CO(2 \rightarrow 1)$ line; (c) The $^{13}CO(1 \rightarrow 0)$ line.
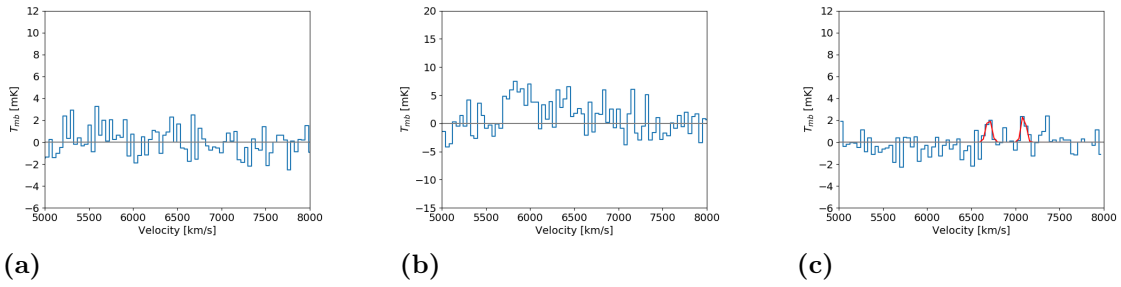
**Figure 10.28:** CO emission in region 18_ii shown in blue, and the fit is shown in red (wherever a fit is possible). The fits that result in a SNR> 2 are presented in the tables in Fig.10.32. (a) The $^{12}CO(1 \rightarrow 0)$ line; (b) The $^{12}CO(2 \rightarrow 1)$ line; (c) The $^{13}CO(1 \rightarrow 0)$ line.
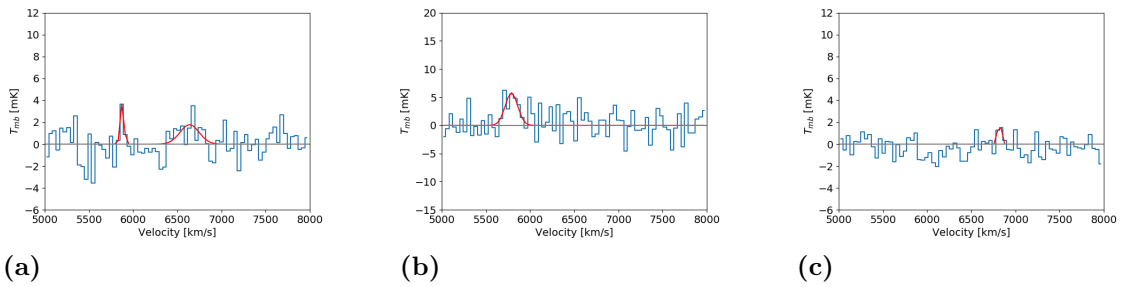


**Figure 10.29:** CO emission in region 18_iii shown in blue, and the fit is shown in red. The fits that result in a SNR> 2 are presented in the tables in Fig.10.32. (a) The $^{12}CO(1 \rightarrow 0)$ line; (b) The $^{12}CO(2 \rightarrow 1)$ line; (c) The $^{13}CO(1 \rightarrow 0)$ line.
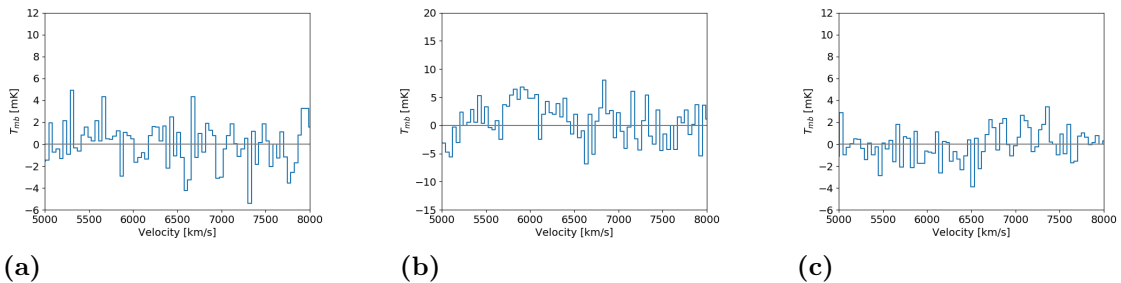


**Figure 10.30:** CO emission in region 18_iv shown in blue, and the fit is shown in red (wherever a fit is possible). The fits that result in a SNR> 2 are presented in the tables in Fig.10.32. (a) The $^{12}CO(1 \rightarrow 0)$ line; (b) The $^{12}CO(2 \rightarrow 1)$ line; (c) The $^{13}CO(1 \rightarrow 0)$ line.

161

(a)  (b)  (c)
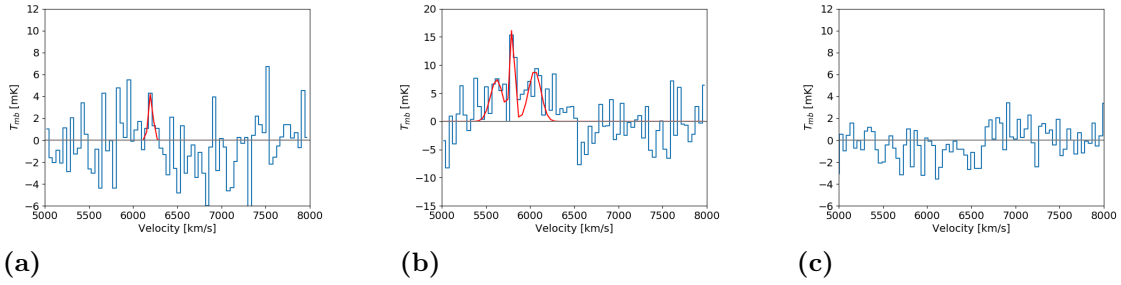
**Figure 10.31:** CO emission in NGC7317, i.e., region 17, shown in blue, and the fit is shown in red (wherever a fit is possible). The fits that result in a SNR> 2 are presented in the tables in Fig.10.32. (a) The $^{12}$CO$(1 \rightarrow 0)$ line; (b) The $^{12}$CO$(2 \rightarrow 1)$ line; (c) The $^{13}$CO$(1 \rightarrow 0)$ line.

| Region | 12CO(1-0) Vlos [km/s] | Vel.Disp [km/s] | Flux [K km/s] | M(H$_2$) [$10^8$M$_\odot$] |
|---|---|---|---|---|
| 18a | | | | |
| 18b | 6439.0 ± 13.8 | 37.3 ± 13.5 | 0.23 ± 0.09 | 0.75 ± 0.28 |
| | 6631.0 ± 16.5 | 27.7 ± 13.6 | 0.13 ± 0.07 | 0.43 ± 0.23 |
| 18_i | 5881.8 ± 11.5 | 25.8 ± 11.7 | 0.18 ± 0.08 | 0.57 ± 0.26 |
| | 6433.6 ± 10.8 | 34.3 ± 10.1 | 0.27 ± 0.08 | 0.85 ± 0.27 |
| 18_iii | 5876.6 ± 18.3 | 20.6 ± 11.6 | 0.14 ± 0.07 | 0.44 ± 0.24 |
| | 6639.0 ± 51.0 | 107.9 ± 51.0 | 0.34 ± 0.17 | 1.10 ± 0.54 |
| 17_ | | | | |

| Region | 12CO(2-1) Vlos [km/s] | Vel.Disp [km/s] | Flux [K km/s] | 13CO(1-0) Vlos [km/s] | Vel.Disp [km/s] | Flux [K km/s] |
|---|---|---|---|---|---|---|
| 18a | 5815.2 ± 15.6 | 70.0 ± 16.9 | 1.03 ± 0.24 | | | |
| | 6429.6 ± 16.5 | 25.3 ± 13.2 | 0.28 ± 0.14 | | | |
| | | | | 6686.6 ± 18.6 | 34.0 ± 18.5 | 0.10 ± 0.05 |
| 18b | 5800.0 ± 24.5 | 70.0 ± 22.3 | 1.27 ± 0.31 | | | |
| | 6001.0 ± 40.5 | 70.0 ± 36.9 | 0.77 ± 0.31 | | | |
| | 6564.8 ± 28.6 | 70.0 ± 28.6 | 0.58 ± 0.25 | | | |
| 18_i | 5837.0 ± 21.6 | 70.0 ± 21.2 | 1.40 ± 0.34 | | | |
| | 6050.0 ± 35.4 | 70.0 ± 34.7 | 0.86 ± 0.34 | | | |
| | 6442.7 ± 28.9 | 70.0 ± 28.9 | 0.67 ± 0.29 | | | |
| | | | | 6678.8 ± 16.4 | 30.7 ± 14.1 | 0.14 ± 0.07 |
| 18_iii | 5789.1 ± 22.1 | 70.0 ± 22.1 | 0.72 ± 0.23 | | | |
| 17_ | 5621.1 ± 31.0 | 70.0 ± 34.2 | 0.92 ± 0.42 | | | |
| | 5800.0 ± 9.5 | 26.0 ± 9.9 | 0.79 ± 0.27 | | | |
| | 6052.1 ± 23.7 | 70.0 ± 23.8 | 1.12 ± 0.39 | | | |

**Figure 10.32:** Table containing the line-of-sight velocity, velocity dispersion and the integrated flux of the fits of the $^{12}$CO$(1 \rightarrow 0)$, $^{12}$CO$(2 \rightarrow 1)$ and $^{13}$CO$(1 \rightarrow 0)$ lines, as well as the H$_2$ molecular gas mass, whenever the SNR> 2, in the regions in/near the NGC7318 pair and NGC7317, as marked in Fig.10.1.

| Region | Vel. Range [km/s] | M(H$_2$) [$10^8$M$_\odot$] | 12CO(1-0) Flux [K km/s] | 12CO(2-1) Flux [K km/s] | 13CO(1-0) Flux [K km/s] | I(12CO(2-1))/ I(12CO(1-0)) | I(13CO(1-0))/ I(12CO(1-0)) |
|---|---|---|---|---|---|---|---|
| 18a | 5600-5800 | 0.33 ± 0.13 | 0.10 ± 0.04 | **0.72 ± 0.12** | -0.11 ± 0.05 | 6.91 ± 2.91 | |
| | 5800-6000 | 0.49 ± 0.23 | **0.15 ± 0.07** | **1.07 ± 0.10** | -0.10 ± 0.04 | 6.96 ± 3.26 | |
| | 6000-6200 | | -0.09 ± 0.03 | 0.36 ± 0.06 | -0.14 ± 0.01 | | |
| | 6200-6400 | | | 0.48 ± 0.11 | | | |
| | 6400-6600 | **0.62 ± 0.08** | **0.19 ± 0.02** | 0.67 ± 0.08 | | 3.53 ± 0.63 | |
| | 6600-6800 | | | 0.28 ± 0.04 | **0.12 ± 0.03** | | |
| | 6800-7000 | | | 0.24 ± 0.06 | 0.05 ± 0.02 | | |
| 18b | 5600-5800 | 0.80 ± 0.04 | **0.25 ± 0.01** | 1.03 ± 0.13 | | 4.16 ± 0.57 | |
| | 5800-6000 | 0.71 ± 0.30 | 0.22 ± 0.09 | **1.51 ± 0.09** | -0.10 ± 0.03 | 6.83 ± 2.95 | |
| | 6000-6200 | | | 0.49 ± 0.07 | -0.16 ± 0.03 | | |
| | 6200-6400 | | | 0.28 ± 0.11 | -0.10 ± 0.03 | | |
| | 6400-6600 | **0.99 ± 0.15** | **0.31 ± 0.05** | 0.72 ± 0.08 | -0.07 ± 0.03 | 2.33 ± 0.44 | |
| | 6600-6800 | 0.52 ± 0.19 | 0.16 ± 0.06 | 0.42 ± 0.04 | **0.11 ± 0.03** | 2.61 ± 0.97 | 0.68 ± 0.31 |
| | 6800-7000 | 0.34 ± 0.09 | 0.10 ± 0.03 | 0.27 ± 0.08 | 0.10 ± 0.02 | 2.60 ± 1.00 | 0.94 ± 0.31 |
| 18_i | 5600-5800 | 0.59 ± 0.05 | 0.18 ± 0.02 | **0.85 ± 0.13** | | 4.68 ± 0.79 | |
| | 5800-6000 | 0.58 ± 0.22 | 0.18 ± 0.07 | **1.79 ± 0.10** | -0.07 ± 0.03 | 10.05 ± 3.96 | |
| | 6000-6200 | | -0.15 ± 0.04 | 0.69 ± 0.08 | -0.16 ± 0.04 | | |
| | 6200-6400 | | | 0.56 ± 0.10 | -0.12 ± 0.03 | | |
| | 6400-6600 | **0.81 ± 0.23** | **0.25 ± 0.07** | 0.76 ± 0.06 | -0.18 ± 0.03 | 3.00 ± 0.89 | |
| | 6600-6800 | | | 0.33 ± 0.02 | 0.19 ± 0.04 | | |
| | 6800-7000 | | | 0.37 ± 0.10 | | | |
| | 7000-7200 | | | 0.28 ± 0.12 | **0.22 ± 0.04** | | |
| 18_ii | 5600-5800 | **0.64 ± 0.11** | **0.20 ± 0.03** | 0.57 ± 0.11 | -0.12 ± 0.05 | 2.83 ± 0.74 | |
| | 5800-6000 | 0.34 ± 0.14 | 0.11 ± 0.04 | **1.18 ± 0.06** | -0.11 ± 0.03 | 11.20 ± 4.56 | |
| | 6000-6200 | | -0.14 ± 0.04 | 0.43 ± 0.08 | -0.12 ± 0.03 | | |
| | 6200-6400 | 0.33 ± 0.10 | 0.10 ± 0.03 | **0.65 ± 0.09** | -0.08 ± 0.03 | 6.39 ± 2.14 | |
| | 6400-6600 | 0.36 ± 0.15 | 0.11 ± 0.05 | 0.55 ± 0.08 | -0.15 ± 0.04 | 4.95 ± 2.23 | |
| | 6600-6800 | | | | 0.17 ± 0.03 | | |
| | 6800-7000 | | -0.12 ± 0.01 | 0.32 ± 0.10 | | | |
| | 7000-7200 | 0.25 ± 0.06 | 0.08 ± 0.02 | | **0.19 ± 0.03** | | 2.40 ± 0.68 |
| 18_iii | 5600-5800 | | -0.13 ± 0.04 | **0.56 ± 0.12** | -0.11 ± 0.03 | | |
| | 5800-6000 | 0.47 ± 0.20 | 0.15 ± 0.06 | **0.58 ± 0.08** | -0.11 ± 0.04 | 3.95 ± 1.80 | |
| | 6000-6200 | | -0.09 ± 0.02 | | -0.25 ± 0.02 | | |
| | 6200-6400 | | -0.17 ± 0.05 | | -0.10 ± 0.02 | | |
| | 6400-6600 | 0.62 ± 0.08 | 0.19 ± 0.03 | 0.25 ± 0.10 | | 1.30 ± 0.55 | |
| | 6600-6800 | **1.04 ± 0.13** | **0.32 ± 0.04** | | | | |
| | 6800-7000 | | -0.10 ± 0.04 | 0.18 ± 0.08 | **0.09 ± 0.03** | | |
| | 7000-7200 | 0.30 ± 0.15 | 0.09 ± 0.05 | | -0.17 ± 0.02 | | |
| 18_iv | 5600-5800 | **0.82 ± 0.20** | **0.25 ± 0.06** | 0.43 ± 0.11 | | 1.70 ± 0.60 | |
| | 5800-6000 | | | **1.16 ± 0.04** | -0.20 ± 0.05 | | |
| | 6000-6200 | | -0.17 ± 0.03 | 0.56 ± 0.12 | -0.11 ± 0.05 | | |
| | 6200-6400 | | | 0.58 ± 0.05 | -0.23 ± 0.03 | | |
| | 6400-6600 | | | | -0.25 ± 0.07 | | |
| | 6600-6800 | | | | 0.14 ± 0.05 | | |
| | 6800-7000 | | | 0.42 ± 0.15 | 0.12 ± 0.05 | | |
| | 7000-7200 | 0.29 ± 0.11 | 0.09 ± 0.03 | | **0.28 ± 0.03** | | 3.05 ± 1.20 |
| 17_ | 5600-5800 | | | **1.40 ± 0.20** | -0.20 ± 0.06 | | |
| | 5800-6000 | **1.54 ± 0.30** | **0.48 ± 0.09** | 1.31 ± 0.11 | -0.20 ± 0.06 | 2.74 ± 0.58 | |
| | 6000-6200 | 0.92 ± 0.22 | 0.29 ± 0.07 | 1.16 ± 0.12 | -0.30 ± 0.05 | 4.05 ± 1.03 | |
| | 6200-6400 | | | 0.62 ± 0.11 | -0.13 ± 0.01 | | |
| | 6400-6600 | | -0.28 ± 0.11 | | -0.41 ± 0.03 | | |
| | 6600-6800 | | -0.38 ± 0.05 | -0.39 ± 0.12 | 0.19 ± 0.04 | | |
| | 6800-7000 | | | | 0.18 ± 0.06 | | |
| | 7000-7200 | | -0.46 ± 0.07 | | **0.22 ± 0.03** | | |

**Figure 10.33:** Table containing the flux of the $^{12}$CO(1 → 0), $^{12}$CO(2 → 1) and $^{13}$CO(1 → 0) emission summed over 200 km/s velocity ranges, including the H$_2$ molecular gas mass and flux ratios, in each region as marked in Fig.10.1. Peak emission velocity ranges in each region have been highlighted in boldface, while negative values have been shaded in grey. The error here is the standard deviation in that velocity range.

## 10.4.2 Molecular Hydrogen Gas Mass & Kinematics

The table in Fig.10.33 shows that the main CO flux is in the $^{12}CO(2 \to 1)$ line throughout the NGC7318 and NGC7317 regions. There is a significant amount of $^{12}CO$ in the $6400 - 6600$ km/s velocity range in NGC7318B, although the largest amount of CO is in the $5600 - 6000$ km/s velocity range, as expected considering the systematic line-of-sight velocity of the galaxy of $\sim 5770$ km/s.

NGC7318A also shows a clear low velocity component in the $^{12}CO(2 \to 1)$ line. This is either gas from NGC7318B that is detected in this region or gas deposited in front of NGC7318A at a previous interactions with NGC7320C. Interestingly NGC7317 also shows a low velocity component in $^{12}CO(2 \to 1)$, the origin of this is unknown. Furthermore, NGC7317 shows negligible CO emission in the velocities near its systematic line-of-sight velocity, $\sim 6600$ km/s, confirming that this is a gas-poor galaxy.

The region containing the dust trail to the south-east of NGC7318A, i.e., region 18_i, shows velocity components matching both NGC7318A as well as NGC7318B, and even shows a $^{13}CO(1 \to 0)$ gas deposit at a velocity of $\sim 6680$ km/s. Region 18_i is the only region in the NGC7318-NGC7317 region showing clear $^{13}CO(1 \to 0)$ emission, at a line-of-sight velocity of $\sim 6680$ km/s.

The NW-tail in region 18_iii shows two main gas deposits, one at the $^{12}CO(1 \to 0)$ line at $6400 - 6800$ km/s and one at the $^{12}CO(2 \to 1)$ line at $5600 - 6000$ km/s. Indicating that there is gas from NGC7318A present in the region at lower temperature, co-existing with gas from the intruder, NGC7318B, at a higher temperature.

## 10.4.3 Line Ratios; Excitation Temperature & Optical Depth

The table in Fig.10.32 shows that there is no region where there is simultaneous clear line emission in $^{13}CO(1 \to 0)$ and $^{12}CO(1 \to 0)$ at a similar velocity. Fortunately there are a couple of regions where there is emission in $^{12}CO(1 \to 0)$ and $^{12}CO(2 \to 1)$ at a similar velocity. Albeit with a large error, NGC7318B, region 18b, has a main beam temperature line ratio of $1.73 \pm 0.99$ at a velocity of $\sim 6625$ km/s, indicating warm, dense, optically thick gas. And in region 18_i the main beam temperature ratios at the respective velocities are: $2.90 \pm 1.20$ at $\sim 5860$ km/s and $1.24 \pm 0.55$ at $\sim 6440$ km/s - i.e., mainly warm, dense, optically thick gas.

Assuming all gas in the same 200 km/s velocity range originates from the same gas deposit results in the ratio values presented in the table in Fig.10.33. In region 18b this table provides a similar value of the $^{12}CO(2 \to 1)/^{12}CO(1 \to 0)$ flux ratio as the main beam temperature ratio. However, the value in region 18_iii, in the velocity range of $5800 - 6000$ km/s, is $3.95 \pm 1.80$, while the main beam temperature ratio is $1.54 \pm 0.79$ at the velocity of $\sim 5835$ km/s.

In general, the regions in/near the NGC7318 pair and NGC7317, have an inclination toward higher $^{12}CO(2 \to 1)/^{12}CO(1 \to 0)$-ratio values than in the regions in the SF ridge, in the bridge and in/near NGC7319. The main beam temperature line ratios in/near the NGC7318 pair and NGC7317 keep the gas at dense, warm and optically thick, in some cases the gas deposits border on optically thin, while the ratios of the summed fluxes in the table in Fig.10.33 in several cases prefer optically thin. Whereas the $^{13}CO(1 \to 0)/^{12}CO(1 \to 0)$ ratio of the summed fluxes

consistently indicate optically thick in all regions and velocities in which there is detection.

# 11

# Summary & Conclusions

I have carried out radio observations using the IRAM 30m telescope in Sierra Nevada, Spain. By using an on-the-fly observing technique I have mapped the $^{12}$CO$(1 \rightarrow 0)$, $^{12}$CO$(2 \rightarrow 1)$ and $^{13}$CO$(1 \rightarrow 0)$ emission in the compact galaxy group Stephan's Quintet, and thereafter choosing 22 regions for closer analysis. The weather conditions during the observations severely impacted the data quality, but nonetheless many fascinating aspects of the molecular gas content in the galaxy group has been revealed and highlighted. Fig.10.2-10.4, show that the brunt of the CO emission is in/near NGC7319 extending towards and into the bridge, the star-forming ridge and SQ-A. Furthermore, the tables in Fig.10.13, 10.14, 10.22, 10.23, 10.32 and 10.33, show that the CO emission extend over a very large range of velocities $\sim 5600 - 7200$ km/s.

In this chapter I will summarise the results of the observations, discussing the flux and velocity distribution, the molecular hydrogen gas content and the multiple velocity components present. Lastly, I will summarise the discussion of the excitation temperatures and optical depths.

## 11.1 The Flux Distribution

The table in Fig.11.1 presents summed fluxes and masses over all line-of-sight velocities in the regions, further claryfing that most of the molecular gas in Stephan's Quintet is in/near NGC7319. The total molecular hydrogen in Stephan's Quintet measures $69.63 \pm 3.06 \cdot 10^8 M_{\odot}/101.82 \pm 1.38 \cdot 10^8 M_{\odot}$, obtained from the Gaussian fits and the summing across the whole spectra respectively, the amount of molecular hydrogen in/near NGC7319 thereby encompasses 56%/52% of the total H$_2$ mass. The star-forming ridge and the bridge contain 38%/40%, as provided by the Gaussian fits and the summed spectra respectively. A very small amount of molecular gas is present in/near the NGC7318 pair and in NGC7317.

However, the molecular hydrogen gas mass has been calculated from the $^{12}$CO$(1 \rightarrow 0)$ line emission and as can be seen in the table in Fig.11.1, most of the $^{12}$CO$(2 \rightarrow 1)$ emission is in/near the NGC7318 pair, NGC7317 and the SF ridge, with only a very small amount in/near NGC7319, i.e., only 18%/4% (obtained from the summed Gaussian fits/the summed spectra). While the NGC7318 pair and NGC7317 maintain 42%/55%, and the rest of the $^{12}$CO$(2 \rightarrow 1)$ is in SQ-A and the bridge. Furthermore, NGC7319 retains almost all of the $^{13}$CO$(1 \rightarrow 0)$ emission in SQ.

## 11.2 The Velocity Distribution

Studying the table in Fig.10.23 shows how the gas in the IGM between NGC7319 and the NGC7318 pair relates to the other galaxies line-of-sight velocities. Indicating that the star-forming ridge contains a mixture of gas from NGC7319, NGC7320C, NGC7317 as well as NGC7318B. The gas deposited during the previous passage of NGC7320C appears to be the most important for the $^{12}$CO($2 \rightarrow 1$) emission.

The main CO flux in Stephan's Quintet is in/near NGC7319 and in the $^{12}$CO($1 \rightarrow 0$) line, but it is not only at one line-of-sight velocity. In general 3-4 velocity components compose the flux in/near NGC7319 spanning $6400 - 7200$ km/s. The same is true in the bridge and the SF ridge, which also exhibit 3-4 velocity components ranging $5700 - 6900$ km/s. This data questions Guillard et al. (2012) detection of a $\sim 6900$ km/s velocity component in SQ-A, as it is only $^{12}$CO($2 \rightarrow 1$) that has significant emission detected in the $6800 - 7000$ km/s velocity range in this region. Furthermore, the velocity components of the star-forming ridge may be centred at $\sim 5800$ km/s and $\sim 6600$ km/s, and can thereby be directly related to the intruder galaxy, NGC7318B, and gas deposited during a previous passage of NGC7317.

Contrary to the regions in/near NGC7319, the regions in/near the NGC7318 pair and NGC7317 have their main CO flux in the $^{12}$CO($2 \rightarrow 1$) line instead of the $^{12}$CO($1 \rightarrow 0$) line. Indicating that the gas in this region exists at a higher temperature. The spectra here exhibit 1-3 velocity components ranging $5800 - 6700$ km/s.

## 11.3 The Line Ratios; Excitation Temperature & Optical Depth

Unfortunately no $T_{mb}^{13CO(1 \rightarrow 0)}/T_{mb}^{12CO(1 \rightarrow 0)}$ ratio with a SNR$> 2$ can be obtained in the same region for a similar velocity. However, for the $T_{mb}^{12CO(2 \rightarrow 1)}/T_{mb}^{12CO(1 \rightarrow 0)}$ ratio several regions are amenable and presented in the table in Fig.11.2. As a ratio value below 1 indicates an optically thick medium at low temperature, it can be seen from the table that this is clearly the case in the regions in/near NGC7319 and the bridge. While the star-forming ridge, SQ-A and 18_i favour warm, dense, optically thick gas. Furthermore, the low velocity component at $\sim 5800$ km/s in SF_iii and 18_i is closing in on a value of 4, indicating that this velocity component in these regions is not as optically thick as the other regions, and may even be warm, dense and optically thin.

| Region | | Total M(H$_2$) [$10^8$M$_\odot$] | 12CO(1-0) Flux [K km/s] | 12CO(2-1) Flux [K km/s] | 13CO(1-0) Flux [K km/s] | I(12CO(2-1))/ I(12CO(1-0)) | I(13CO(1-0))/ I(12CO(1-0)) |
|---|---|---|---|---|---|---|---|
| 19_ | Integrated fits | 7.35 ± 0.91 | 2.28 ± 0.28 | 0.45 ± 0.22 | | 0.20 ± 0.10 | |
| | Sum 5600-7200 km/s | 9.62 ± 0.42 | 2.99 ± 0.13 | | 0.22 ± 0.06 | | 0.07 ± 0.02 |
| 19_o | Integrated fits | 6.17 ± 0.89 | 1.92 ± 0.28 | 0.57 ± 0.23 | 0.27 ± 0.11 | 0.30 ± 0.13 | 0.14 ± 0.06 |
| | Sum 5600-7200 km/s | 8.37 ± 0.33 | 2.60 ± 0.10 | 0.64 ± 0.13 | 0.14 ± 0.05 | 0.25 ± 0.05 | 0.06 ± 0.02 |
| 19_i | Integrated fits | 6.61 ± 0.75 | 2.05 ± 0.23 | 0.53 ± 0.25 | 0.24 ± 0.11 | 0.26 ± 0.13 | 0.12 ± 0.06 |
| | Sum 5600-7200 km/s | 8.73 ± 0.43 | 2.71 ± 0.13 | 0.34 ± 0.12 | | 0.13 ± 0.05 | |
| 19_ii | Integrated fits | 4.69 ± 0.81 | 1.46 ± 0.25 | 0.87 ± 0.32 | 0.55 ± 0.18 | 0.60 ± 0.24 | 0.37 ± 0.14 |
| | Sum 5600-7200 km/s | 6.61 ± 0.34 | 2.05 ± 0.11 | | 0.33 ± 0.07 | | 0.16 ± 0.03 |
| 19_iii | Integrated fits | 5.75 ± 0.92 | 1.79 ± 0.29 | | | | |
| | Sum 5600-7200 km/s | 6.97 ± 0.48 | 2.16 ± 0.15 | 0.69 ± 0.15 | | 0.32 ± 0.07 | |
| 19_iv | Integrated fits | 3.68 ± 1.06 | 1.14 ± 0.33 | | | | |
| | Sum 5600-7200 km/s | 4.34 ± 0.42 | 1.35 ± 0.13 | | 0.66 ± 0.08 | | 0.49 ± 0.07 |
| 19_v | Integrated fits | 4.66 ± 0.74 | 1.45 ± 0.23 | 0.70 ± 0.30 | 0.52 ± 0.17 | 0.49 ± 0.22 | 0.36 ± 0.13 |
| | Sum 5600-7200 km/s | 6.28 ± 0.40 | 1.95 ± 0.12 | | 0.42 ± 0.07 | | 0.22 ± 0.04 |
| 19_vi | Integrated fits | | | 1.31 ± 0.59 | 1.28 ± 0.29 | | |
| | Sum 5600-7200 km/s | 1.93 ± 0.30 | 0.60 ± 0.09 | | 1.23 ± 0.10 | | 2.05 ± 0.36 |
| **Sum 7319** | Integrated fits | 38.91 ± 2.31 | 12.08 ± 0.72 | 4.43 ± 0.84 | 2.86 ± 0.41 | 0.37 ± 0.07 | 0.24 ± 0.04 |
| | Sum 5600-7200 km/s | 52.86 ± 1.11 | 16.42 ± 0.35 | 1.67 ± 0.24 | 3.01 ± 0.17 | 0.10 ± 0.01 | 0.18 ± 0.01 |
| b_i | Integrated fits | 6.15 ± 0.81 | 1.91 ± 0.25 | 0.96 ± 0.33 | | 0.50 ± 0.18 | |
| | Sum 5600-7200 km/s | 8.84 ± 0.32 | 2.75 ± 0.10 | 1.18 ± 0.11 | | 0.43 ± 0.04 | |
| b_ii | Integrated fits | 4.02 ± 0.86 | 1.25 ± 0.27 | 1.71 ± 0.43 | | 1.37 ± 0.45 | |
| | Sum 5600-7200 km/s | 6.57 ± 0.26 | 2.04 ± 0.08 | 2.58 ± 0.12 | | 1.26 ± 0.08 | |
| **SQ-A** | Integrated fits | 3.70 ± 0.78 | 1.15 ± 0.24 | 0.49 ± 0.21 | | 0.43 ± 0.21 | |
| | Sum 5600-7200 km/s | 4.64 ± 0.30 | 1.44 ± 0.09 | 1.72 ± 0.08 | | 1.20 ± 0.10 | |
| SF_i | Integrated fits | 4.02 ± 0.65 | 1.25 ± 0.20 | 0.80 ± 0.25 | | 0.64 ± 0.22 | |
| | Sum 5600-7200 km/s | 6.32 ± 0.28 | 1.96 ± 0.09 | 2.50 ± 0.10 | | 1.27 ± 0.08 | |
| SF_ii | Integrated fits | 4.06 ± 0.72 | 1.26 ± 0.23 | 1.59 ± 0.43 | | 1.26 ± 0.41 | |
| | Sum 5600-7200 km/s | 6.27 ± 0.24 | 1.95 ± 0.07 | 3.44 ± 0.12 | | 1.77 ± 0.09 | |
| SF_iii | Integrated fits | 3.26 ± 0.68 | 1.01 ± 0.21 | 2.28 ± 0.45 | | 2.25 ± 0.65 | |
| | Sum 5600-7200 km/s | 5.45 ± 0.22 | 1.69 ± 0.07 | 4.05 ± 0.12 | | 2.39 ± 0.12 | |
| SF_iv | Integrated fits | 1.38 ± 0.38 | 0.43 ± 0.12 | 2.23 ± 0.53 | | 5.22 ± 1.89 | |
| | Sum 5600-7200 km/s | 2.63 ± 0.29 | 0.82 ± 0.09 | 4.64 ± 0.11 | | 5.69 ± 0.64 | |
| **Sum SF** | Integrated fits | 12.72 ± 1.25 | 3.95 ± 0.39 | 6.90 ± 0.85 | | 1.75 ± 0.27 | |
| | Sum 5600-7200 km/s | 20.68 ± 0.52 | 6.42 ± 0.16 | 14.64 ± 0.22 | | 2.28 ± 0.07 | |
| 7318A | Integrated fits | | | 1.31 ± 0.28 | 0.10 ± 0.05 | | |
| | Sum 5600-7200 km/s | 1.47 ± 0.15 | 0.46 ± 0.05 | 3.94 ± 0.11 | | 8.64 ± 0.92 | |
| 7318B | Integrated fits | 1.18 ± 0.36 | 0.36 ± 0.11 | 2.62 ± 0.51 | | 7.17 ± 2.60 | |
| | Sum 5600-7200 km/s | 3.10 ± 0.19 | 0.96 ± 0.06 | 4.85 ± 0.12 | | 5.04 ± 0.34 | |
| 18_i | Integrated fits | 1.43 ± 0.37 | 0.44 ± 0.12 | 2.93 ± 0.56 | 0.14 ± 0.07 | 6.60 ± 2.14 | |
| | Sum 5600-7200 km/s | 1.65 ± 0.18 | 0.51 ± 0.06 | 5.64 ± 0.13 | | 10.99 ± 1.21 | |
| 18_ii | Integrated fits | | | | | | |
| | Sum 5600-7200 km/s | 1.17 ± 0.15 | 0.36 ± 0.05 | 4.05 ± 0.11 | | 11.16 ± 1.44 | |
| 18_iii | Integrated fits | 1.54 ± 0.46 | 0.48 ± 0.14 | 0.72 ± 0.23 | | 1.50 ± 0.66 | |
| | Sum 5600-7200 km/s | 0.85 ± 0.17 | 0.26 ± 0.05 | 1.90 ± 0.10 | | 7.17 ± 1.52 | |
| 18_iv | Integrated fits | | | | | | |
| | Sum 5600-7200 km/s | | | 2.93 ± 0.14 | | | |
| 7317_ | Integrated fits | | | 2.83 ± 0.64 | | | |
| | Sum 5600-7200 km/s | | | 3.71 ± 0.19 | | | |
| **Tot** | Integrated fits | 69.63 ± 3.06 | 21.63 ± 0.95 | 24.90 ± 1.69 | 3.09 ± 0.42 | 1.15 ± 0.09 | 0.14 ± 0.02 |
| | Sum 5600-7200 km/s | 101.82 ± 1.38 | 31.62 ± 0.43 | 48.80 ± 0.51 | 3.01 ± 0.17 | 1.54 ± 0.03 | 0.10 ± 0.01 |

**Figure 11.1:** Table containing the total $^{12}$CO(1 $\rightarrow$ 0), $^{12}$CO(2 $\rightarrow$ 1), $^{13}$CO(1 $\rightarrow$ 0) fluxes and H$_2$ masses per region. Displaying the difference in flux/mass present in clear lines vs diffuse emission. Included are the flux line ratios of $^{12}$CO(2 $\rightarrow$ 1)/$^{12}$CO(1 $\rightarrow$ 0) and $^{13}$CO(1 $\rightarrow$ 0)/$^{12}$CO(1 $\rightarrow$ 0).

| Region | Vlos average [km/s] | 12CO(1-0) T<sub>mb</sub> [mK] | 12CO(2-1) T<sub>mb</sub> [mK] | T<sub>mb</sub> ratio 12CO(2-1)/ 12CO(1-0) |
|---|---|---|---|---|
| **19_i** | 6645 | 9.27 ± 0.84 | 6.45 ± 2.55 | 0.70 ± 0.28 |
| **19_iii** | 6655 | 9.12 ± 1.18 | 6.62 ± 3.18 | 0.73 ± 0.36 |
| **b_i** | 6640 | 8.11 ± 1.28 | 4.06 ± 1.70 | 0.50 ± 0.22 |
| **b_ii** | 6420 | 6.76 ± 1.36 | 6.25 ± 2.35 | 0.93 ± 0.39 |
| **SQ-A** | 5845 | 3.94 ± 1.69 | 6.42 ± 2.33 | 1.63 ± 0.92 |
| **SF_i** | 5845 | 5.42 ± 1.45 | 6.43 ± 1.66 | 1.19 ± 0.44 |
| **SF_ii** | 5825 | 6.16 ± 1.90 | 7.70 ± 1.95 | 1.25 ± 0.50 |
| | 6575 | 4.30 ± 0.75 | 5.09 ± 1.59 | 1.18 ± 0.42 |
| **SF_iii** | 5805 | 2.76 ± 0.88 | 8.88 ± 1.67 | 3.22 ± 1.19 |
| | 6610 | 4.44 ± 1.50 | 5.25 ± 1.63 | 1.18 ± 0.54 |
| **SF_iv** | 6465 | 8.18 ± 1.87 | 5.49 ± 2.06 | 0.67 ± 0.29 |
| **18_i** | 5860 | 3.90 ± 1.46 | 11.29 ± 1.96 | 2.90 ± 1.20 |
| | 6440 | 4.36 ± 1.14 | 5.39 ± 1.93 | 1.24 ± 0.55 |

**Figure 11.2:** Table containing the line ratios of the main beam temperatures of $^{12}CO(2 \rightarrow 1)$ and $^{12}CO(1 \rightarrow 0)$, obtained from the Gaussian fits, where the line-of-sight velocities are similar. The velocities stated are the average of the two CO lines, separated by a maximum of 3 velocity channels, i.e., 120 km/s, but at a usual separation of $\sim 50$ km/s.
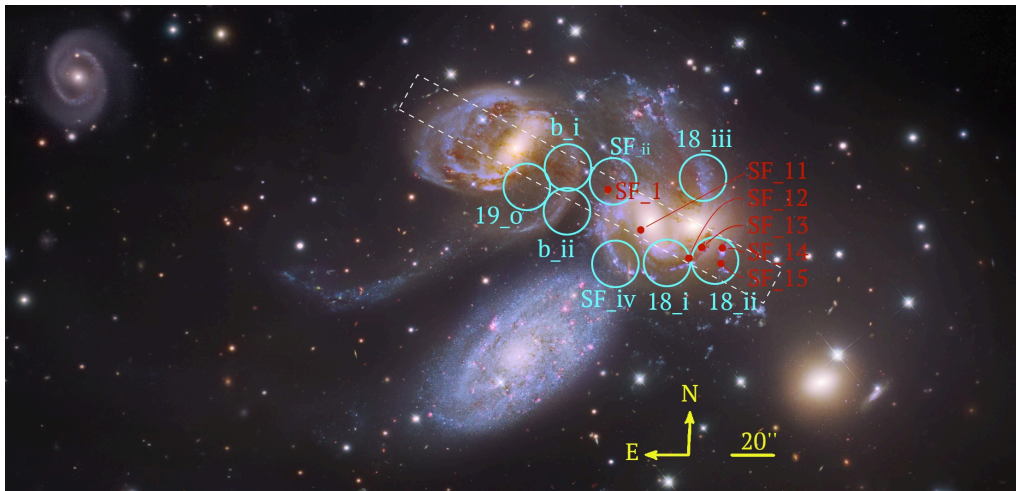
# Part III

# Concluding Discussion & Remarks

# 12

# The History, Future & Implications of Understanding Stephan's Quintet

Being one of the most well-known and well-studied compact galaxy groups, one could expect that Stephan's Quintet would have no new revelations to present. Fortunately, this compact group shows, over and over again, how fascinating and complex it is, by continuously revealing new intriguing details.

In this chapter I discuss the complexity of SQ, the impact of group environment on galaxy evolution and what an understanding of the processes occurring in this group can reveal about the evolution of groups and galaxies throughout cosmic time. This discussion relies on the information deduced from the optical spectroscopy and radio data presented in Chapter 6 and 10, as well as on the details presented in previously published papers summarised in Chapter 3. A number of regions from *Part I* and *Part II* of this thesis are discussed in this chapter, they are collected and marked in Fig.12.1.



**Figure 12.1:** The regions that are mentioned in this chapter are marked in this figure. The regions from the optical spectroscopy analysed in *Part I*, Chapter 6, are coloured red, while the regions from the radio observations in *Part II*, Chapter 10 are cyan. The white dotted rectangle is the area mapped with the LBT in this thesis (an additional slit position covers NGC7317). The background is a Subaru telescope and Hubble Space Telescope WFC3 composite colour image (as processed by Robert Gendler and Judy Schmidt). For the complete lists of regions in optical and radio see Fig.6.1 and 10.1.

## 12.1 The Interaction History of Stephan's Quintet

Stephan's Quintet has a rich and intriguing history of previous and current interactions, as we know from the data and analysis presented in this thesis as well as in previously published studies detailed in Chapter 3. This chapter is a summary as well as a continuation of the information provided in Chapter 3, this is the story of the most likely past of Stephan's Quintet as supported by the present data. The focus on the chapter is on the aspects and activity highlighted by the optical spectroscopy and radio observations detailed in this thesis. The noteworthy structures and features in SQ are shown in Fig.12.2, as a reminder for the reader.
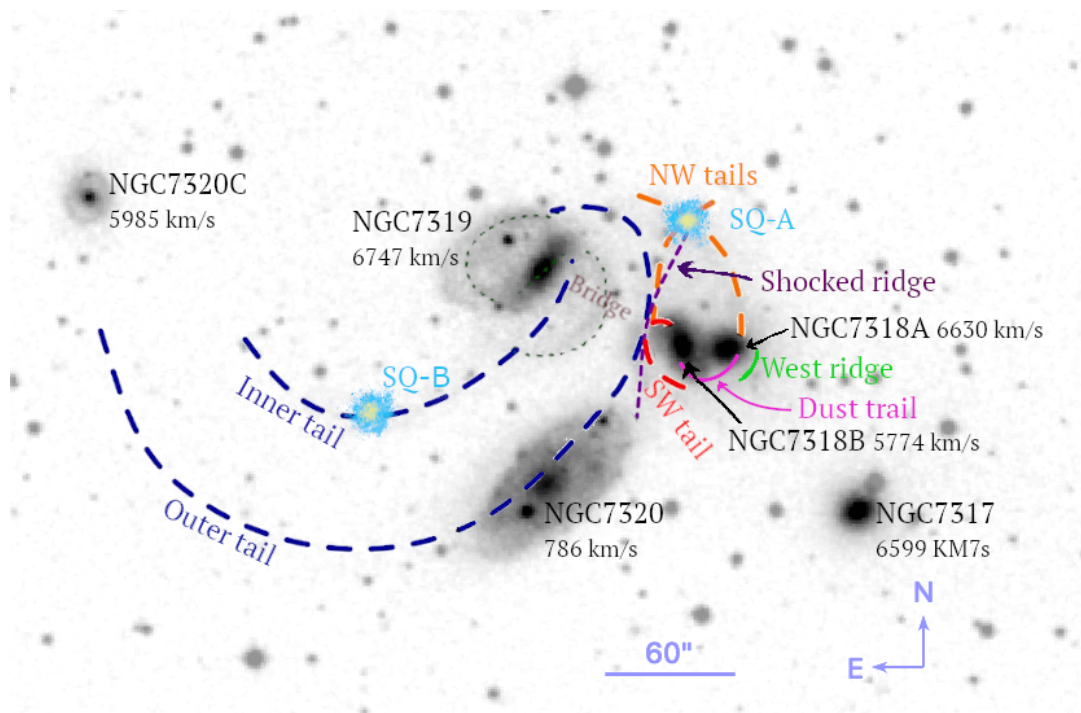


**Figure 12.2:** A reminder of the structures and galaxy velocities in Stephan's Quintet. The figure displays an adjusted DSS2 R-band image of SQ, overlaid with markings stating the naming convention of the different important tidal and interaction structures in the group, including line-of-sight velocities of the galaxies provided by the NASA/IPAC Extragalactic Database (NED).

### 12.1.1 First: Creating an IGM Deposit

Fig.6.1 illustrates how the atomic gas present in SQ favours NGC7319 and the star-forming ridge. But it is also clear that there is diffuse extended atomic gas present throughout the mapped area, in the bridge, along the south and south-east of the NGC7318 pair as well as in the west ridge. Interestingly there is a lack of atomic gas present between NGC7318A and B. The larger field of view of Duarte Puertas et al. (2019), also shows H$\alpha$ emission in the whole of the star-forming ridge, along the south and south-east of the NGC7318 pair and the west ridge, as well as in SQ-A and to a small extent along the inner tidal tail.

The molecular gas content shows a similar distribution, favouring NGC7319 and the star-forming ridge (Gao & Xu (2000); Guillard et al. (2012); Appleton et al. (2013, 2017), this work Chapter 10). There is also a significant amount of gas in SQ-B (Lisenfeld et al., 2002). Unpublished CARMA CO(1 → 0) data also show a detection in the bridge, while BIMA CO(1 → 0) data show a gas deposit to the north of the NGC7319 nucleus (Gao & Xu, 2000). The data presented in this work confirms the detection of CO in the bridge as well as to the north of the NGC7319 nucleus (Fig.10.15 and 10.9). Fig.12.3 shows the extension of the CO emission in these three studies. The molecular gas content along the bar in NGC7319 (Fig.10.5-10.8) is in this work found to be brighter than the gas deposit to the north, which raises the question as to why the bar was not detected in the BIMA observations. Furthermore, the optical data presented in Chapter 6 confirms the detection of the bridge in optical, as Duarte Puertas et al. (2019).
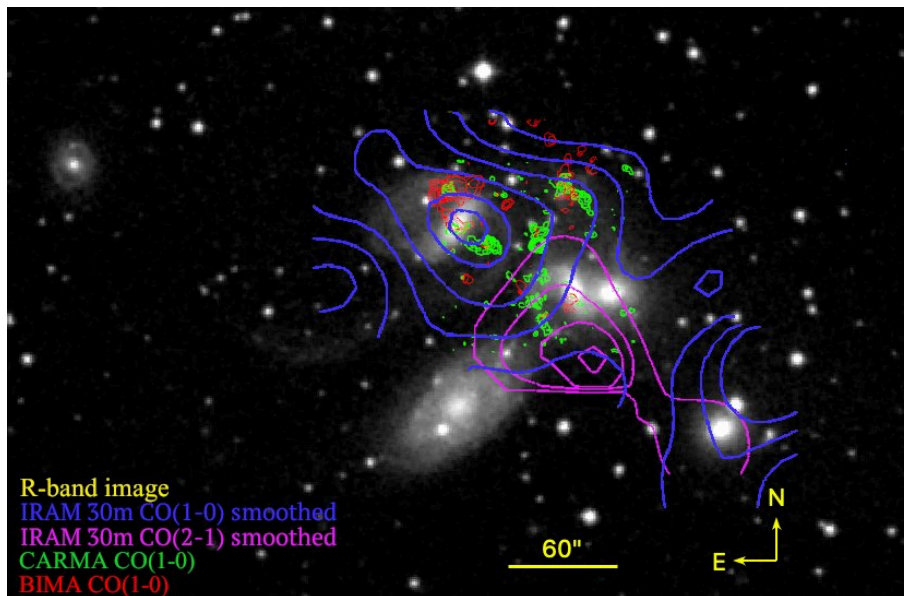


**Figure 12.3:** The blue and magenta contours outline the smoothed and summed $^{12}$CO(1 → 0) and $^{12}$CO(2 → 1) data as presented in Chapter 10 (Fig.10.2 and 10.3), while the green contours show the CARMA $^{12}$CO(1 → 0) and the red contours trace the BIMA $^{12}$CO(1 → 0) integrated intensity (as presented in Gao & Xu (2000)), overlaid on a R-band image of Stephan's Quintet.

Neutral hydrogen is predominantly detected in the inner and outer tail, the NW tails, SQ-A and to the south-west of NGC7318B (Williams et al., 2002). Showing a mean line-of-sight velocity in the inner and outer tidal tails of 6610 km/s (Williams et al., 2002). Actually, nearly all of the HI emission is outside of the galaxies (Allen & Sullivan, 1980; Shostak et al., 1984; Williams et al., 1999, 2002; Renaud et al., 2010). Furthermore, X-ray emission, tracing high energy processes and hot IGM, show that the main detection is in NGC7319 and the star-forming ridge, highlighting the presence of diffuse gas in the IGM heated via previous interactions (Sulentic et al., 1995; Pietsch et al., 1997; Trinchieri et al., 2003, 2005; O'Sullivan et al., 2009).

So, most of the gas in Stephan's Quintet is not contained within the galaxies. The question is how such large amounts of gas came to be in the intergalactic medium. Considering the harassed state of NGC7319 it is natural to draw the conclusion that this galaxy has been a vital participant in interactions with other, less massive, galaxies. These less massive galaxies have been highly affected by the interactions and have not had sufficient gravitational potential to retain their gas content. The simulations by Hwang et al. (2012) state that the interaction between NGC7320C and NGC7319 has created the inner and outer tidal tail simultaneously. Observations agree that this interaction was the cause for at least the outer tidal tail (Moles et al., 1997; Lisenfeld et al., 2004), where NGC7320C passed from the north-west to the south-east, just to the west of the NGC7319 nucleus. This interaction may also explain the gas in the IGM at a line-of-sight velocity similar to NGC7320C ($\sim$ 5985 km/s).

Whether or not NGC7319 has interacted with NGC7318A and/or NGC7317 previous to its interaction with NGC7320C is still unclear. The data presented in this work, both the radio data as well as the optical data, show up to 4 clear velocity components in the IGM, particularly in the CO gas in the bridge, Fig.10.15, in region b_ii, Fig.10.16, in region 19_o, Fig.10.6, and in the star-forming ridge, Fig.10.18-10.21. If we take a closer look at region SF_ii for example, there are clear velocity components at $5879.6 \pm 10.3$ km/s, $6553.7 \pm 24.1$ km/s and $6784.6 \pm 17.2$ km/s. Where the last velocity component can be directly related to NGC7319, the second component to NGC7317 or NGC7318A and the first component to NGC7318B or NGC7320C. Looking at the velocity components in the optical data, see the table in Fig.7.1, up to 4 velocity components can be found in the star-forming ridge a well. For example in region SF_1, which displays velocity components at $6115.7 \pm 13.4$ km/s, $6518.0 \pm 21.0$ km/s, $6751.7 \pm 16.2$ km/s and $6925.0 \pm 21.8$ km/s. Making it more likely that the first velocity component is related to NGC7320C, while the second can be related to NGC7317 or NGC7318A and the third to NGC7319. The fourth component originates from the [OII]$\lambda$3727 emission in the ridge, and while the origin of this high line-of-sight velocity component is yet to be determined, it is most likely a product of NGC7319 gas.

This means that NGC7319 has interacted with either NGC7317 (Sulentic et al., 2001; Rodríguez-Baras et al., 2014; Duc et al., 2018) or NGC7318A (Renaud et al., 2010), or both, before its interaction with NGC7320C. NGC7317 and NGC7318A are both gas poor, although NGC7317 more so. NGC7318A has also been suggested to have created the inner tidal tail (Renaud et al., 2010), although further simulations

disagree (Hwang et al., 2012). Duc et al. (2018) detect an extended diffuse halo of old stars extending towards NGC7317, indicating that it previously has interacted with the other galaxies in the group. Continued simulations and metallicity studies are required to shed further light on the early interactions in Stephan's Quintet.

There is a further fascinating discussion regarding the ages and origins of the inner and outer tidal tails. The inner tail may originate from NGC7319 gas and the outer tail from NGC7320C gas, created during two separate passages through the core of the group (Sulentic et al., 2001). For a furhter discussion of the stellar population ages of the different features, see Sulentic et al. (2001); Gallagher et al. (2001); Fedotov et al. (2011).

## 12.1.2 Second: Creating the SW tail & NW tails

It has been suggested that NGC7318A and B have already interacted once, that NGC7318B is currently $\sim 100$ kpc in front of NGC7318A (Xu et al., 2003, 2005). This collision then would explain the long outer arms of NGC7318B, the SW tail, the HI gas presence outside of the optical disk, and the immense UV disk of NGC7318B. Furthermore, assuming that the first encounter between NGC7318A and B has already occurred may explain the shape of the NW tails. However, NGC7318B retains an intact spiral disk, either due to a lack of large-scale interaction or due to a short time-scale since the beginning of the galaxy's interaction with the rest of the SQ group, so that any large tidal effects on the morphology have yet to form.

Distinguishing the SW tail from the SF ridge in the optical data presented in Chapter 6 is difficult, as the data mainly include the area in which these two features overlap. In the radio data, Chapter 10, region SF_iv contain the SW tail, while region 18_i encompass the dust trail and region 18_iii follow the western NW tail. In the optical region SF_11 is located at the edge of the dust trail closest to NGC7318B, and regions SF_12-15 further trace the connection between the SW tail and the western NW tail via the NGC7318A side of the dust trail and the west ridge.

Considering the SW tail, the radio region SF_iv, shows a distinct contribution from NGC7318B at $\sim 5830$ km/s, with a second velocity component at a line-of-sight velocity of $\sim 6450$ km/s. The dust trail connecting the SW tail and the western NW tail, optical region SF_12-13 and radio region 18_i, show velocity components at [$\sim 5740$ km/s, $\sim 6140$ km/s, $\sim 7030$ km/s] and [$\sim 5860$ km/s, $\sim 6050$ km/s, $\sim 6440$ km/s, $\sim 6680$ km/s] respectively. While the NGC7318B edge of the dust trail, region SF_11, shows two distinct velocity components, $5888.0 \pm 17.1$ km/s and $6952.0 \pm 26.9$ km/s, i.e., no clear contribution from NGC7318A.

The continuation of the western NW tail, i.e., regions SF_14-15 show velocity components at $\sim 5800$ km/s, $\sim 6240$ km/s and $\sim 6950$ km/s, while the radio region 18_ii shows diffuse emission favouring the two lower velocity components, as seen in the table in Fig.10.33. Regions SF_12-13 retain a physical position that indicate their inclusion in the NGC7318 pair interaction, however whether the west ridge, optical regions SF_14-15 and radio region 18_ii, is a continuation of the tails or a shock requires further investigation. The BPT diagrams in Fig.6.59-6.61 show LINER-like emission line ratios in the west ridge, indicating that a shock at least

is involved. Furthermore, radio region 18_iii follows the western NW tail, showing emission at $5876.6 \pm 18.3$ km/s and $6639.0 \pm 51.0$ km/s in $^{12}CO(1 \rightarrow 0)$ and at $5789.1 \pm 22.1$ km/s in $^{12}CO(2 \rightarrow 1)$.

In both the optical spectroscopy and radio data presented in this work there is a detection of a low line-of-sight velocity component similar to the line-of-sight velocity of NGC7318B present at the location of NGC7318A, indicating that there is a gas deposit from NGC7318B or NGC7320C in front of NGC7318A. In addition, the SW tail, the dust trail and the continuation of the western NW tail can all be related to NGC7318B. The data presented in here therefore favours the scenario in which the NGC7318 pair has interacted once, where NGC7318B is currently in front of NGC7318A and have formed large arms/tails connecting the structures.

## 12.1.3   Third: The Galaxy-Wide Shocked Star-Forming Ridge

Radio continuum emission trace AGNs and shocks, and the galaxy wide shock in SQ is particularly bright in radio (Allen & Hartsuiker, 1972; van der Hulst & Rots, 1981; Williams et al., 2002; Xanthopoulos et al., 2004; Xu et al., 2003; Nikiel-Wroczyński et al., 2013). The BPT line ratio diagnostic diagrams presented in Fig.6.59-6.60 show that the bridge and SF ridge is highly ionised by star formation processes, where the SF ridge reaches higher ionisation and displays LINER-like emission like ratios, induced by the shock (even Seyfert-like line ratios can be induced with a photoionised precursor if the shock is travelling fast enough (Allen et al., 2008; Rodríguez-Baras et al., 2014)). Furthermore, the radio data presented in Chapter 10, show warm, dense and optically thick CO gas in the SF ridge, existing at a higher temperature than in other regions of SQ. In addition, multiple velocity components are detected in the shocked star-forming ridge (Chapter 6, Chapter 10, Guillard et al. (2012); Iglesias-Páramo et al. (2012); Konstantopoulos et al. (2014); Rodríguez-Baras et al. (2014); Duarte Puertas et al. (2019)), implying a complex interplay between pre- and post-shocked gas present in the group and the intruder galaxy, NGC7318B.

X-ray emission details the high-energy processes and the extended hot gas present in the group. It is expected that a shock is created when the cold gas of the IGM collides with the cold gas of an intruder galaxy. Stephan's Quintet retain widespread cold HI (Shostak et al., 1984; Williams et al., 2002; Xu et al., 2003) and the intruder galaxy, NGC7318B, moves at the high relative velocity of $\sim 900$ km/s (Xu et al., 2003). The coincidence of X-ray and radio emission in SQ, see Fig.12.4, confirms the hypothesis that the star-forming ridge is created by the shock front (as argued by Xu et al. (1999)).

It is also interesting to note that the HI deficit (Verdes-Montenegro et al., 2001) can be compensated for by the amount of X-ray gas present, such that the lost HI is the heated gas now emitting in X-ray. It is possible that all the X-ray emission in the ridge originates from shock-heated HI (Sulentic et al., 2001). Furthermore, Sulentic et al. (2001) suggests that the weakness of the MIR emission in the star-forming ridge is due to the dust being diffused and/or destroyed by sputtering in the shocked region. It is possible that MIR emission is suppressed in the shock region, which means that SFR estimations of the post-shock gas will be underestimated.

The starburst region SQ-A is also associated with the collision between NGC7318B

and the IGM. SQ-A was first discovered in infrared (Xu et al., 1999) and is the first observation of an ongoing starburst triggered by such high speed collisions (Xu et al., 2003; Appleton et al., 2017). The line-of-sight velocities in SQ-A provided by the radio data presented in Chapter 10 of $5879.2 \pm 16.5$ km/s and $6574.2 \pm 19.5$ km/s, deviate by $\sim 120$ km/s from the values found by Lisenfeld et al. (2002) of $\sim 6030$ km/s and $\sim 6700$ km/s. The higher velocity component obtained here contain 3 times more molecular hydrogen than the low velocity component, contrary to the results by Lisenfeld et al. (2002), who find that their lower velocity component retain the highest mass. These discrepancies may arise from the difference in area analysed, as Lisenfeld et al. (2002) include the NW tails in their notion of SQ-A as well.



R-band image
VLA radio continuum (4.86 GHz)
CHANDRA X-ray (0.5–2.0 keV band)
60"
N
E
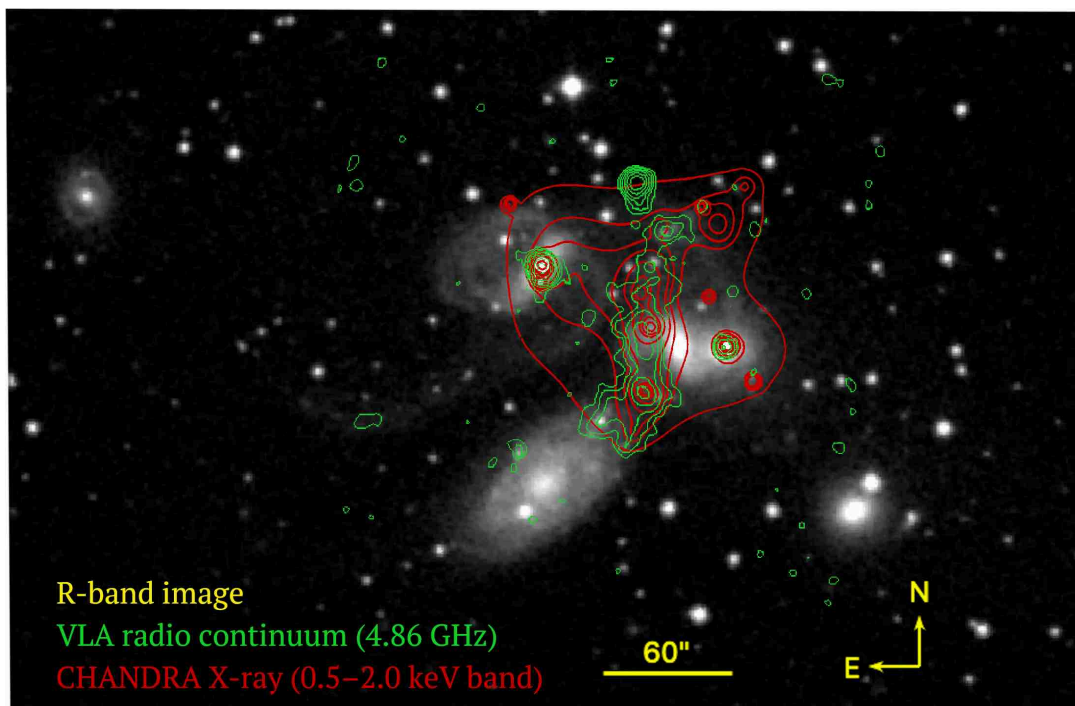
**Figure 12.4:** R-band image of Stephan's Quintet overlaid with Chandra X-ray contours in red (Trinchieri et al. (2003)) and 4.86 GHz (6.17 cm) VLA radio continuum contours in green (Xu et al. (2003)). The coincidence of the X-ray and radio emission proves that the star-forming ridge is created by the shock.

## 12.2  Stephan's Quintet Particulars

Stephan's Quintet displays a high amount of activity and interacting structures, and a number of particular connections warrant further attention and discussion. In the previous chapter I discussed the IGM deposit and how it came into existence, the creation of the outer and inner tidal tails, as well as the NW tails and the SW tail. I discussed the formation and cause of the shocked star-forming ridge. This chapter further expands on the effect of the outflow in NGC7319, as well as the origin and importance of the bridge and the activity in the west ridge.

### 12.2.1  The Effects of the Outflow in NGC7319

Aoki et al. (1996) state that the outflow in NGC7319 is one of the largest outflowing phenomenon ever observed in a Seyfert galaxy. They argue that the galaxy maintains strong anisotropic nuclear ionising radiation potentially produced by an obscuring torus. It is further suggested by Appleton et al. (2020) that the outflow is heating gas far into the IGM, an IGM filled with a complex tangled web of unstable molecular filaments embedded in radio continuum emission, strong magnetic fields and cosmic ray acceleration.

As seen in Chapter 6.1 all atomic species show a clear preference for extension along the outflow, forming a nuclear wind. There is also a decrease in UV emission in the area of the outflow, Fig.3.9, indicating that the outflow may be blowing away gas or increasing turbulence to hinder star formation.

Photoionisation recombination emission from dense star-forming regions detected in H$\alpha$, and forbidden [NII]$\lambda6585$ emission from low-density shocked gas, show an interesting interplay in NGC7319. Along the outflow the ratio of the amplitudes of H$\alpha$ and [NII]$\lambda6585$ changes, and H$\alpha$/[NII]$\lambda6585 < 1$, contrary to other regions of the galaxy. Fig.12.5 displays the ratio of the H$\alpha$ and [NII]$\lambda6585$ fluxes across NGC7319. On the other hand, the temperature sensitive ratio [OIII]$\lambda5008$/H$\beta$, in Fig.6.25b, shows the extension of the area shocked by the nuclear wind. Together these ratios highlight the large amount of shocked gas in and along the outflow. In addition, the extension of the "bluer" part around the centre in Fig.12.5, to the upper right and to the left, coincide with the angle which the two $^{12}$CO$(1 \rightarrow 0)$ deposits to either side of the nucleus form with reference to the galaxy's centre, see Fig.12.3. These CO deposits are expected to be caused by a bipolar outflow or gas deposited in front of NGC7319 during the previous interactions.

### 12.2.2  The Importance of the Bridge

The bridge is a fairly recently detected structure, after being observed in $^{12}$CO$(1 \rightarrow 0)$ by Gao & Xu (2000), it has also been detected in optical wavelengths, as confirmed by the data presented in Chapter 6. The gas in the bridge shows a prevalence towards NGC7319 content and velocities, but also indicate behaviours similar to the SF ridge. As we move closer to the SF ridge, the line emission becomes stronger, see Fig.6.29-6.32, and a low velocity component at a line-of-sight velocity of the intruder, NGC7318B, emerges, see the table in Fig.7.1. The molecular gas content as traced by
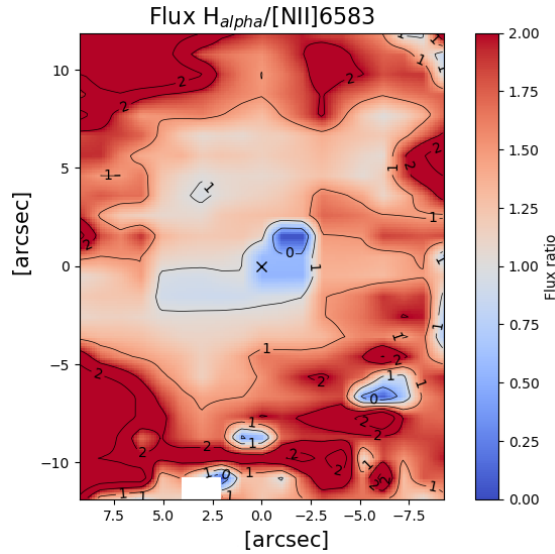
**Figure 12.5:** The flux ratio of Hα[NII]λ6585 in NGC7319, showing where the emission from the low-density shocked gas exceeds that of the photoionisation recombination, i.e., where Hα/[NII]λ6585 < 1.

the CO displayed by region b_i in the table in Fig.10.22, reveals a weak low velocity component consistent with the line-of-sight velocity of the intruder in the $^{12}$CO(2 → 1) line. Indicating a higher temperature in the low velocity component, expected to be caused by the shock created by the emergence of the intruder. Furthermore, the higher velocity components in the bridge are found to consist of low temperature optically thick gas, in agreement with the lower atomic gas emission in this area (compared to the SF ridge).

While the bridge connects to the intruder, NGC7318B, it is still unclear exactly why and how (Duarte Puertas et al., 2019). It is possible that this is a tidal effect by the passage of NGC7318B through the group (assuming that NGC7318B is currently located in front of the group). I suspect that understanding the bridge will unlock many of the secrets of the current interaction and the state of the IGM.

### 12.2.3 About the West Ridge

In optical emission the west ridge is bright, with emission in [OII]λ3727, [OIII]λ5008, [NII]λ6550,6585, [SII]λ6718,6732, Hα, Hβ and even Hγ in regions SF_13-15. In radio, however, the west ridge is near dark. Region 18_ii contain the west ridge and although a small amount of diffuse CO gas may be present, no emission is clear enough to allow a proper fit of a line, as seen in the spectra displayed in Fig.10.28. This shows that the west ridge contains large amounts of ionized gas and no significant amount of molecular gas.

The BPT diagnostic diagrams, in Fig.6.59-6.61, place the west ridge in the part of the plot indicating LINER-like emission-line ratios, showing high ionisation caused by shocks. In addition, the line-of-sight velocities of the emission in the west ridge favour that of the intruder, NGC7318B. But there is also a velocity component at ∼ 6200 km/s and one at ∼ 6990 km/s, where the velocity dispersions of the lower

two velocity components coincide with that of NGC7318B (see the table in Fig.7.1) while the high line-of-sight velocity component exhibits a higher velocity dispersion, closer to that of NGC7319 and NGC7318A. Indicating that this perhaps is a shock-front formed in the recesses of NGC7318A gas or NGC7319 and NGC7320C gas, in the interaction with NGC7318B.

Furthermore, the west ridge coincides with HI (Williams et al., 2002) and X-ray emission (Trinchieri et al., 2003, 2005). Fig.12.6 shows how the HI and X-ray emission relate to the emission of the $H\alpha-[NII]\lambda6585$ complex presented in this work. Showing that the west ridge contains ionised gas, hot IGM and a significant amount of neutral hydrogen.
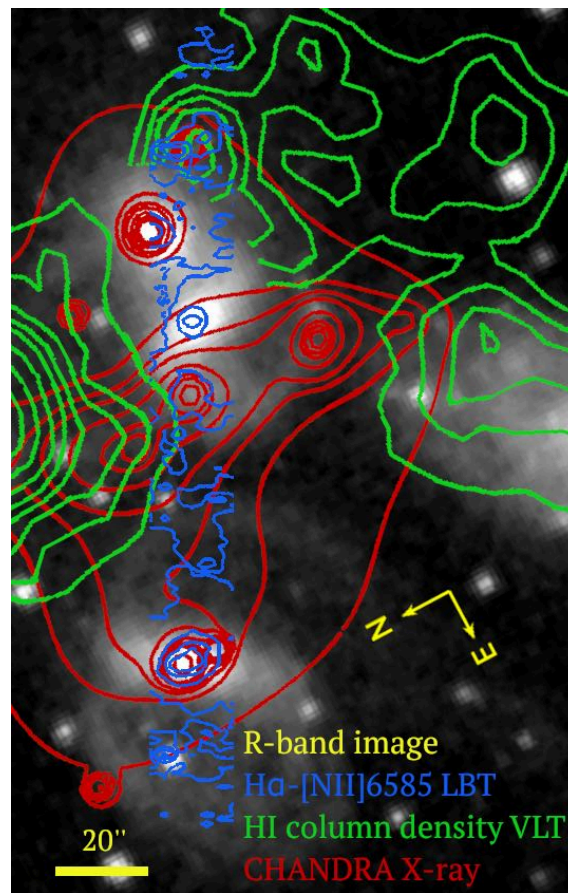


**Figure 12.6:** The blue contours outline the $H\alpha-[NII]\lambda6585$ emission as presented in Chapter 6, the green contours show the HI column density (Williams et al., 2002) and the red contours trace the Chandra X-ray emission (Trinchieri et al., 2003), overlaid on a R-band image of Stephan's Quintet.

## 12.3 Impact on Galaxy Groups, Black Hole Activity & Mergers

The brightness and low redshift of Stephan's Quintet enables high resolution studies of a compact galaxy group together with the galaxies and processes therein. Galaxies that reside within compact galaxy groups exhibit characteristics different from those of more isolated galaxies. This chapter begins with discussing the implications Stephan's Quintet has on the framework of compact galaxy groups, including the differences/similarities of elliptical, spiral and active group galaxies versus isolated galaxies. The chapter continues with a discussion of the differences/similarities of galaxy mergers inside and outside of compact group environments as seen via SQ.

### 12.3.1 Compact Galaxy Groups & the Galaxies Therein

The basis of how a sample of compact groups are created naturally will affect the results and discussion thereof. Therefore it is important to be aware of how a sample has been selected. The best known catalogue of compact groups, the Hickson Compact Groups (HCGs), which Stephan's Quintet is part of, are chosen with a maximum magnitude difference between four or more galaxies, a surface brightness limitation and a ring encircling the group devoid of galaxies (Tzanavaris et al., 2010). The HCGs have been found to be dynamically dominated by dark matter, to contain large amounts of diffuse gas, and, while they trace the large-scale structure, they tend to prefer low-density environments. Compared to a random distribution of galaxies, a HCG tend to consist of a similar type of galaxies.

NGC7319 is the only galaxy of the core group of SQ that can be classified as a spiral, whereas NGC7318A and NGC7317 are ellipticals, E2 and E4 respectively. NGC7320C, while having passed through the group in the past, remains a spiral galaxy, (R)SAB(s). Assuming that both NGC7320C and NGC7317 interacted with the inner parts of the group in the past, the conclusion can be drawn that NGC7320C retained its morphology due to the manner of its passing through the core group. NGC7317, at a more concordant redshift could have interacted with both NGC7319 and NGC7318A during its passage, while NGC7320C only interacted briefly with NGC7319 and was therefore simply stripped and not significantly disturbed.

Furthermore, Hickson (1997) states that elliptical galaxies in compact groups have lower velocity dispersion than ellipticals in other environments. The data presented in this work shows no clear agreement with this statement, with stellar velocity dispersions for NGC7317 and NGC7318B of $262.7 \pm 6.9$ km/s and $263.6 \pm 10.7$ km/s respectively. "Normal" elliptical galaxies commonly retain a velocity dispersion of $\sigma \approx 200$ km/s (Forbes & Ponman, 1999). In addition, the studies of Stephan's Quintet indicate that secular evolution is important for the evolution of galaxy morphology in compact groups, and that spiral galaxies likely transform into ellipticals (Sulentic et al., 2001). While there is no proof that NGC7317 and NGC7318A originally were spirals, it is clear that NGC7319, NGC7320C and NGC7318B are currently in a state of morphological transition.

Compared to other compact galaxy groups, Stephan's Quintet shows distinct differences. SQ has prominent and extended tidal features and a galaxy currently

entering the group and colliding with the old tidal gas content (Hwang et al., 2012). Whether these aspects of SQ are unique or if they only appear so since they are a result of the short time-scale during which these structures exist, is yet to be determined. Perhaps all compact groups exhibit such variety of galaxy interaction indicators, stellar and gaseous tidal features and galaxy-wide shock structures, at some point during their evolution.

One of the most prominent features in SQ, the shocked star-forming ridge, is quite a spectacular structure. Xu et al. (1999) argued strongly that the large-scale shock and the IGM starburst were closely connected and triggered by the same event, as was further shown and discussed in Chapter 12.1.3. How common such large-scale and powerful shocks are in compact group environments is still unknown, although a not-yet published major Spitzer survey of HCGs is being carried out by Cluver et al. according to Hwang et al. (2012). Hopefully this study can shed light on the matter. The creation of this kind of galaxy-wide star-forming shock front requires large structures at high relative velocities. To create a shock front containing as many velocity components as that in SQ (as detailed in Chapter 6 and 10) sets intense and many requirements on the structures involved. A shocked ridge as large as that in SQ may be created in the interaction between at minimum two galaxies, if the two galaxies are larger than those in SQ, but to create the sheer number of velocity components found in the ridge in SQ require multiple kinematical structures. In SQ a minimum three kinematical structures, but more likely 4, i.e., NGC7319, NGC7317, NGC7320C and most importantly at a high relative velocity: NGC7318B, are required to recreate the shocked ridge, although several tidal structures do require the existence of NGC7318A as well.

Verdes-Montenegro et al. (2001) find indications that compact groups evolve from HI rich to HI poor, where the young HI-rich groups mainly contain spiral and ir-regular galaxies, while the older HI-poor groups mainly ellipticals. Gas-rich groups can be separated from gas-poor via a gap in MIR colour space as presented by Johnson et al. (2007). Tzanavaris et al. (2010) build on this and speculates that, considering the X-ray emission present in SQ, loose groups contract to form more compact structures. At such an early state in a group's evolution the HI is still contained within the galaxy disks, but as the galaxies in the newly formed compact group interacts, an increasing part of the HI gas is stripped from the galaxies and deposited into the IGM, forming such structures as the tidal tails and bridge seen in SQ. The interactions heat and ionise the atomic gas in the IGM, as confirmed by the bright emission of the SF ridge presented in Chapter 6.2, until the IGM radiates hot X-ray emission. At this state the group probably consists mainly of gas-poor elliptical galaxies, which merge into the end state of a compact group. This evolu-tion scenario, from a loose group to a compact group and eventually a fossil group, requires extensive gas removal from the group's galaxies to enable enhanced star formation and rapid gas depletion followed by quiescence. The current state of SQ fits well into this evolution scenario, having gas poor galaxies, all its HI outside of the galaxies and current intense star formation in the shocked ridge, including warm optically thick molecular gas (as detailed in Chapter 10).

Hickson (1997) suggested several options of what compact groups really are, and what is clear from studying the complex interactions in Stephan's Quintet is that

this compact group is not simply a chance alignment of galaxies in a loose group. The ages of the stellar populations and creation of the tidal tails further indicate that compact groups are stable configurations, sustained for many Myrs. It is expected that both NGC7320C and NGC7318B with their large relative velocities insert energy into the group and ensure that the group does not merge. If compact groups form as dense configurations within larger loose groups this could explain the emergence of NGC7320C and NGC7318B as new group members, falling into the loose-group over-density that is SQ. What is clear from the work presented in Chapter 6 and 10, as well as previous studies carried out on SQ and other HCGs, is that compact groups are characterized by high galaxy number density and low galaxy velocity dispersion. And these factors accelerate galaxy evolution by enhancing star formation processes and push galaxies to quiescence and increased entropy/disorder, i.e., ellipticity.

## 12.3.2 Stephan's Quintet & Active Galaxies

Hickson (1997) suggests that only the most massive galaxy in a compact group forms an AGN, and in the case of SQ only NGC7319 has been confirmed to contain an AGN. Several scientists, such as Ellison (2019), claim a clear connection between mergers and AGN, and others, such as Netzer (2013), claim that major mergers cannot be common in causing AGN activity since such an event would result in a too large disruption of the disk. Coziol et al. (1998) claim that AGNs in groups are, like more isolated galaxies, associated with the most luminous, early-type galaxies, and HCG AGNs prefer denser group cores. Perhaps this is why we see no AGN activity in the NGC7318A and B merger, while the heavily harassed NGC7319 shows AGN activity. Or it is due to the manner in which NGC7318B interacts with both NGC7318A and IGM, increasing the energy of the gas involved and not enabling funneling of gas into the centre. Furthermore, it is also possible that any nuclear activity of NGC7318B has yet to begin, or that the nucleus is hidden - although if that was the case we would expect X-ray emission from the nucleus, which is not detected. In conclusion, secular evolution and galaxy harassment/minor mergers are expected to be the drivers of the AGN activity in NGC7319.

The morphology of NGC7319 shows a spiral with a broken ring structure and clear indications of previous harassment. At these times the gas in NGC7319 is decoupled from the stellar disk, meaning that the star formation required to propagate and define a Population I spiral pattern cannot be sustained (Sulentic et al., 2001) and that the nucleus is unlikely to be fed via secular processes. Furthermore, the ratio of the infrared luminosity, $L_{IR}$ and the molecular hydrogen gas mass, $M(H_2)$ is lower than common in spiral galaxies. The molecular gas content in NGC7319 is $52.86 \pm 1.11 \cdot 10^8 M_\odot$ (Chapter 11), while the MIR luminosity is $1.60 \pm 0.811 \cdot 10^9 L_\odot$ (Natale et al., 2010), which relates to a general sample of spiral galaxies as displayed in Fig.12.7. Commonly galaxies maintain a ratio $L_{IR}/M(H_2)$ of $2-200 L_\odot M_\odot^{-1}$, where larger values often are associated with interacting and merging galaxies (Young & Scoville, 1991). The low value of the $L_{IR}/M(H_2)$-ratio in NGC7319 highlights the lack of ongoing star formation and the excess of molecular gas content, potentially caused by the decoupling of the stellar and gaseous disk, as shown in Fig.6.21, where

a lot of the molecular gas is concentrated off centre (Gao & Xu (2000) etc.). This raises questions regarding the feeding mechanisms and the life-time/duty cycle of this AGN.
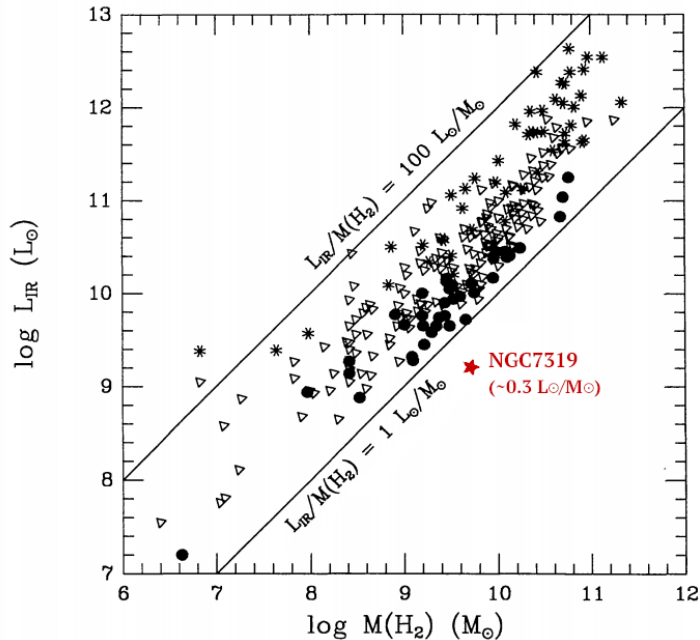


**Figure 12.7:** Comparison of total $H_2$ mass and IR luminosities in more than 200 galaxies from several studies as collected and displayed by Young & Scoville (1991). NGC7319 is positioned in this plot in red.

In addition, many Seyfert 2 nuclei show enhancement of star formation near the nucleus (Sulentic et al., 2001), but NGC7319 shows little evidence for a nuclear starburst. As seen in the data presented in Chapter 6.1, neither star formation enhancement nor star formation congregations are forthcoming. The data presented in the table in Fig.11.1 show a slight increase in the molecular hydrogen mass in the central region of the galaxy, which may indicate that there is ongoing star formation occurring. However, this data is from a $11''$ circular area containing the nucleus and may originate from the off-nuclear gas deposits or from the dust lane seen crossing the galaxy.

The northern arm displays low temperature optically thick gas, potentially conducive to star formation and AGN feeding, if a mechanism present can transfer the gas inwards. Most likely the AGN was ignited in the encounter with NGC7320C, when a small quantity of gas was funneled into the centre of NGC7319, creating a Seyfert nucleus with an outflow of shocked atomic gas (Sulentic et al., 2001). Little star formation occurred/occurs and the environment is heated by the outflow, showing emission in CO and optical wavelengths.

Whether this AGN formation process is common for active galaxies in compact groups is yet to be determined. Shih & Stockton (2015), for example, present observations of a compact galaxy group at $z = 2.48$, where the AGN activity originates from one of the merger galaxies. While NGC7319 does not produce large powerful radio structures (Baek et al., 2019), the AGN in the work by Shih & Stockton (2015)

does, which may be possible due to the gas rich systems involved in that merger and the high redshift, which indicate a younger group.

### 12.3.3 The NGC7318 Pair & Merging Galaxies

There are some obvious differences between mergers inside and outside of group environment, particularly the amount of IGM present. The large amount of IGM in groups sets immense possibilities in tracing the merger process but it also heavily affects the process and adds a whole new layer of complexity to the understanding of the merging system and the separation of the galaxy-galaxy interaction and galaxy-IGM interaction. Although large shocks are also common in galaxy mergers outside of compact group environment, the shock there is contained within the galaxies and ionise the ISM. Furthermore, the group environment lends itself to an increase in the galaxy merger rate, due to the low velocity dispersion between the group members, as the dynamical friction effects of a merger acts on timescales $\tau_{merge} \sim \sigma^3$, where $\sigma$ is the velocity dispersion of the group's galaxies. Velocity dispersions of $> 300$ km/s means merging timescales of more than $\sim 10^7$ years. It is likely that NGC7318A and B will not merge, but only extensively interact, due to the large relative velocities. I expect NGC7318B will deposit its ISM into the IGM and then continue on its merry way, as NGC7320C did.

A system of two colliding galaxies, the Antennae galaxies, have also suffered strong interactions and creation of large tidal structures, see Fig.12.8a. However, contrary to the NGC7318 pair, the Antennae galaxies are dominated by star-forming regions in which most of the diffuse X-ray emission emanates (Fabbiano et al., 2003; Metz et al., 2004; Tsuge et al., 2020). Furthermore, most of the gas in the Antennae galaxies still reside within the galaxies. In SQ we see small star-forming congregations in the stripped tidal gas, whereas the shocked emission is localised to the interaction between NGC7318B and the IGM (see Chapter 3, 6 and 10). However, a similarity of these two systems, the Antennae galaxies and SQ, is that the diffuse gas in both systems exhibits multiple velocity components. This is most likely an effect of the complex gas distribution and/or non-equilibrium aspects (Trinchieri et al., 2005). While SQ indicates the presence of both of these aspects, Fabbiano et al. (2003) show that the Antennae galaxies have a preference for the presence of multiple regions at different temperatures and absorption depths.

The Cartwheel galaxy, on the other hand, is a ring galaxy located in a 4 galaxy compact group at z= 0.03 (Crivellari et al., 2009), shown in Fig.12.8c. It is expected that an interaction between one of the other group members and the Cartwheel galaxy incited the creation of the prominent elliptical rings that is the origin of the name, "the Cartwheel galaxy". The two elliptical rings in the Cartwheel galaxy are connected by optically emitting filaments called spokes, which were created in the previous interaction by non-axisymmetric gravitational perturbations (Higdon et al., 2015). If we assume that NGC7318B is in front of NGC7318A, i.e., having already passed through the group, the NW tails in SQ may be analogous to the spokes found in the Cartwheel galaxy.

In conclusion, the NGC7318 pair will most likely not merge, and they are not particularly similar to more isolated pairs of interacting galaxies, as the composition

and gas distribution are significantly different (most of the gas in SQ is outside of the galaxies, whereas the gas in individually interacting galaxies is disturbed but mainly contained within the galaxies). However, I recommend studying and understanding the effects in many different interacting systems to acquire an intuition for the process and thereby enable a further discussion of the processes governing the dynamics in Stephan's Quintet.



**(a)**  **(b)**  **(c)**
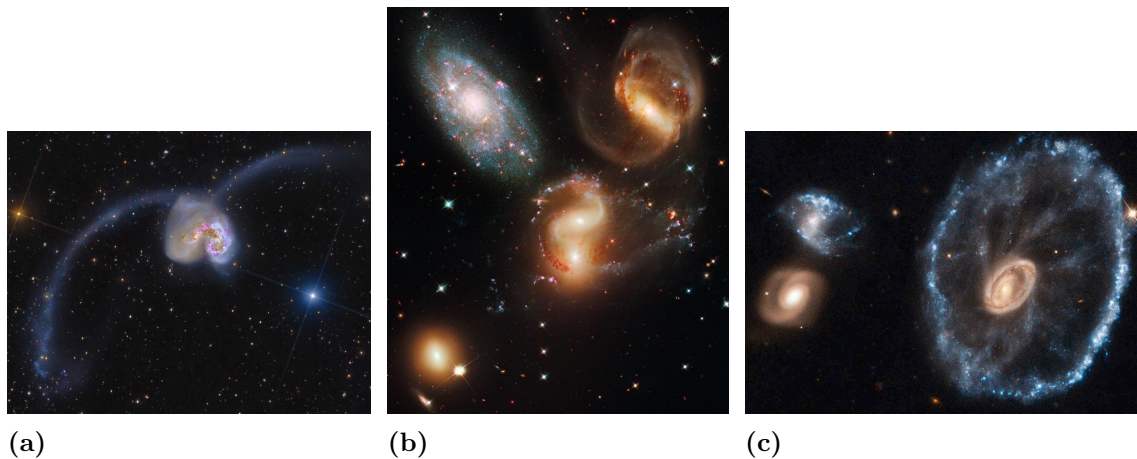
**Figure 12.8:** Three different interacting systems.
(a) The Antennae galaxies, a binary merger with large tidal structures. Credit: Subaru, NAOJ, NASA/ESA/Hubble, R.W. Olsen;
(b) Stephan's Quintet. Credit: NASA, ESA, & Hubble SM4 ERO Team;
(c) The Cartwheel galaxy, a ring galaxy subjected to previous interactions residing in a compact group of 4 galaxies. Credit: ESA/Hubble & NASA.

## 12.4 Implications on Galaxy Evolution & the History of the Universe

In the early Universe, galaxies were expected to be closely spaced and regularly interacting. Although low density environments predominantly contain spiral galaxies and high density environments elliptical galaxies, the Cartwheel galaxy shows that a spiral pattern can reform after a major interaction (Crivellari et al., 2009) and an elliptical galaxy is not always the result of galaxy-galaxy harassment albeit the most likely. An environment such as that in Stephan's Quintet, with most of the gas in the IGM outside of the galaxies, is not expected to be conducive to reforming spiral patterns. It is expected that NGC7319 and NGC7320C, which are currently in morphological transition, will slowly transform into lenticular or elliptical galaxies (Sulentic et al., 2001). This is assuming that the stellar disks have also been sufficiently destroyed by the interactions, already a Population I spiral pattern cannot be sustained in NGC7319 since the gas disk is decoupled from the stellar disk.

SQ sheds light on how spiral galaxies secularly evolve into elliptical galaxies, sped up using gas stripping via galaxy-galaxy harassment, which improve our understanding of the galaxy evolution process and the classical Hubble scheme. In addition, SQ adds its own weight to the "nature vs nurture" scenario. Stephan's Quintet favours, as Kauffmann et al. (2004), a scenario in which both "nature", the environment in which the galaxy is formed, and "nurture", the processes to which the galaxy is subjected, are important. While there are scientists who favour "nature" as the most important aspect of a galaxy's evolution, Stephan's Quintet clearly shows the immense impact of "nurture". To fully unveil how galaxies are formed and evolve, SQ is clear on the fact that both aspects have to be taken into account.

Drawing on the conclusions by Verdes-Montenegro et al. (2001); Tzanavaris et al. (2010), compact galaxy groups are assumed to evolve from gas-rich groups mainly containing spiral and irregular galaxies to gas-poor groups containing predominantly ellipticals. In this picture Stephan's Quintet is working towards depleting its gas content via the large-scale star-forming ridge, and the galaxies have already been stripped of gas, apart from the intruder, NGC7318B, which is in the process of being stripped. NGC7318B is adding to the group's gas content, increasing the energy of the group and IGM, and stalling the process of gas depletion, which may be a common process in compact groups enabling their long lifetimes.

In Stephan's Quintet we see a time when the Universe was awash with gas and galaxies closely spaced. The understanding of the interaction process of NGC7318B shows us the impact of the presence of diffuse IGM. The large-scale shocked ridge details the method of gas depletion through shock induced star formation. The activity and disrupted disk of NGC7319 illustrates how AGN feeding can progress and how a feedback process can impact the surrounding gas and further evolution. The many tidal structures provides a detailed history of exemplary galaxy interactions. Understanding these processes sheds light on a time in the history of the Universe when gas was abundant and interactions were common.

## 12.5    A Short Note on Further Research Required

Although a lot of research has been done on Stephan's Quintet, a lot of questions remain shrouded in mystery. Further observations and simulations, especially at high resolution and sensitivity, are required to shed light upon the many mysteries concerning the interaction history of the group and the peculiar aspects of compact galaxy groups and the galaxies therein.

High resolution radio observations are needed to further study the clumpiness of the CO emitting gas, while, FIR photometry would allow estimating the total dust mas independent of the choice of CO to $H_2$ conversion factor. Higher sensitivity/deeper spectroscopic observations of SQ are required to enable study of the fainter regions. Understanding the faint regions is a vital piece in the puzzle of understanding the history and activity in Stephan's Quintet. The NGC7318B interaction with NGC7318A and the multi-component IGM would especially benefit from deeper observations, as with deeper observations we could trace the filaments and start unravelling the connections of NGC7318B and the different gas deposits in the area. Further and more complex simulations of the manner in which NGC7318B interacts is required to enable a full understanding of the process. Furthermore, NGC7319 reveals a fascinating interplay of AGN feeding and feedback in a galaxy with a decoupled gas and stellar disk. The processes occurring here could be particularly illuminating for furthering our understanding of AGN feeding and feedback processes, but this requires deeper observations of the fainter outer parts of the disk and arms, as well as simulations that fit those observations.

As such a large amount of questions exist and more arise every day, I will not attempt to list them all here. But I would like to turn your attention to the complexity of the group's history and activity. Although I, as all Stephan's Quintet researchers, have my own interpretation preferences of what is going on, as detailed in the previous chapters, it is not confirmed whether NGC7317 has interacted with NGC7319/NGC7318A in the past or not, if NGC7319 and NGC7318A have interacted or not, if NGC7318A and B have already passed each other or not, what is going on in the interaction region between NGC7318A and B, what the origin of the different velocity components are, how the outflow of NGC7319 affects the IGM, what the origin of the inner tidal tail is, etc. As you can see, this is a truly fascinating system with near unending questions and answers.

If we look outside of Stephan's Quintet and broaden our view slightly by turning to compact groups themselves, there is another heap of unanswered questions. Deep high resolution studies of a wide variety of compact galaxy groups at different redshifts are required to shed light on these complex structures and further our understanding of the creation, impact and importance of compact galaxy groups.

# Acknowledgements

II

# References

Allam, S., Assendorp, R., Longo, G., Braun, M., & Richter, G. 1996, A&A Supplement, 117, 39

Allen, M. G., Groves, B. A., Dopita, M. A., Sutherland, R. S., & Kewley, L. J. 2008, ApJS, 178, 20

Allen, R. J. & Hartsuiker, J. W. 1972, Nature, 239, 324

Allen, R. J. & Sullivan, W. T., I. 1980, A&A, 84, 181

Amram, P., Mendes de Oliveira, C., Plana, H., Balkowski, C., & Bolte, M. 2002, Astrophysics and Space Science, 281, 397

Antonucci, R. 1993, Annual Review of Astronomy and Astrophysics, 31, 473

Aoki, K., Ohtani, H., Yoshida, M., & Kosugi, G. 1996, AJ, 111, 140

Appleton, P., Emonts, B., Fadda, D., et al. 2020, in American Astronomical Society Meeting Abstracts, American Astronomical Society Meeting Abstracts, 455.04

Appleton, P. N., Guillard, P., Boulanger, F., et al. 2013, ApJ, 777, 66

Appleton, P. N., Guillard, P., Togi, A., et al. 2017, ApJ, 836, 76

Appleton, P. N., Xu, K. C., Reach, W., et al. 2006, ApJL, 639, L51

Baek, J., Chung, A., Schawinski, K., et al. 2019, MNRAS, 488, 4317

Baldwin, J. A., Phillips, M. M., & Terlevich, R. 1981, PASP, 93, 5

Barnes, J. 1993, A Beginner's Guied to Using IRAF (Central Computer Services, National Optical Astronomy Observatories, Tucson, Arizona 85726)

Barnes, J. E. & Hernquist, L. 1992, Annual Review of Astronomy and Astrophysics, 30, 705

Barnes, J. E. & Hernquist, L. 1996, ApJ, 471, 115

Beckmann, V. & Shrader, C. 2012, in Proceedings of "An INTEGRAL view of the high-energy sky (the first 10 years)" - 9th INTEGRAL Workshop and celebration of the 10th anniversary of the launch (INTEGRAL 2012). 15-19 October 2012. Bibliotheque Nationale de France, 69

## References

Bertola, F., Bettoni, D., Danziger, J., et al. 1991, ApJ, 373, 369

Boschetti, C. S., Rafanelli, P., Ciroi, S., et al. 2003, Memorie della Societa Astronomica Italiana Supplementi, 3, 226

Braine, J., Duc, P. A., Lisenfeld, U., et al. 2001, A&A, 378, 51

Burbidge, E. M. & Burbidge, G. R. 1961, ApJ, 134, 244

Cappellari, M. 2017, MNRAS, 466, 798

Cappellari, M. & Emsellem, E. 2004, PASP, 116, 138

Cluver, M. E., Appleton, P. N., Boulanger, F., et al. 2010, ApJ, 710, 248

Combes, F., García-Burillo, S., Audibert, A., et al. 2019, A&A, 623, A79

Coziol, R., Ribeiro, A. L. B., de Carvalho, R. R., & Capelato, H. V. 1998, ApJ, 493, 563

Crivellari, E., Wolter, A., & Trinchieri, G. 2009, A&A, 501, 445

de Mello, D. F., Urrutia-Viscarra, F., Mendes de Oliveira, C., et al. 2012, MNRAS, 426, 2441

De Rosa, A., Bianchi, S., Bogdanović, T., et al. 2017, Astronomische Nachrichten, 338, 262

de Vaucouleurs, G. 1959, Handbuch der Physik, 53, 275

Dekel, A. & Birnboim, Y. 2006, MNRAS, 368, 2

Dekel, A., Sari, R., & Ceverino, D. 2009, ApJ, 703, 785

Di Mille, F., Ciroi, S., Rafanelli, P., et al. 2008, Astronomical Society of the Pacific Conference Series, Vol. 396, 3D Spectroscopy of the Nuclear Environment of a Selected Sample of Nearby Active Galactic Nuclei: NGC 7319, ed. J. G. Funes & E. M. Corsini, 61

Diaferio, A., Geller, M. J., & Ramella, M. 1994, AJ, 107, 868

Díaz-Giménez, E. & Zandivarez, A. 2015, A&A, 578, A61

Dressler, A. 1980, ApJ, 236, 351

Duarte Puertas, S., Iglesias-Páramo, J., Vilchez, J. M., et al. 2019, A&A, 629, A102

Duc, P.-A. 2012, Astrophysics and Space Science Proceedings, 28, 305

Duc, P.-A., Cuillandre, J.-C., & Renaud, F. 2018, MNRAS, 475, L40

Dultzin-Hacyan, D., Krongold, Y., Fuentes-Guridi, I., & Marziani, P. 1999, ApJL, 513, L111

IV

Eckart, A., Downes, D., Genzel, R., et al. 1990, ApJ, 348, 434

Einasto, J., Einasto, M., Hütsi, G., et al. 2003, A&A, 410, 425

Ellison, S. 2019, in Linking Galaxies from the Epoch of Initial Star Formation to Today, 37

Ellison, S. L., Catinella, B., & Cortese, L. 2018, MNRAS, 478, 3447

Event Horizon Telescope Collaboration, Akiyama, K., Alberdi, A., et al. 2019, ApJL, 875, L1

Fabbiano, G., Krauss, M., Zezas, A., Rots, A., & Neff, S. 2003, ApJ, 598, 272

Falcón-Barroso, J., Sánchez-Blázquez, P., Vazdekis, A., et al. 2011, A&A, 532, A95

Fan, L., Han, Y., Fang, G., et al. 2016, ApJL, 822, L32

Fazeli, N., Busch, G., Valencia-S., M., et al. 2019, A&A, 622, A128

Fedotov, K., Gallagher, S. C., Konstantopoulos, I. S., et al. 2011, AJ, 142, 42

Forbes, D. A. & Ponman, T. J. 1999, MNRAS, 309, 623

Gallagher, S. C., Charlton, J. C., Hunsberger, S. D., Zaritsky, D., & Whitmore, B. C. 2001, AJ, 122, 163

Gao, Y. & Xu, C. 2000, ApJL, 542, L83

Glikman, E., Simmons, B., Mailly, M., et al. 2015, ApJ, 806, 218

Guillard, P., Boulanger, F., Cluver, M. E., et al. 2010, A&A, 518, A59

Guillard, P., Boulanger, F., Pineau Des Forêts, G., & Appleton, P. N. 2009, A&A, 502, 515

Guillard, P., Boulanger, F., Pineau des Forêts, G., et al. 2012, ApJ, 749, 158

Ha, J.-H., Ryu, D., & Kang, H. 2018, ApJ, 857, 26

Hewlett, T., Villforth, C., Wild, V., et al. 2017, MNRAS, 470, 755

Hickson, P. 1997, Annual Review of Astronomy and Astrophysics, 35, 357

Higdon, J. L., Higdon, S. J. U., Martín Ruiz, S., & Rand, R. J. 2015, ApJL, 814, L1

Ho, L. C., Filippenko, A. V., & Sargent, W. L. W. 1997, ApJ, 487, 591

Hönig, S. F. 2016, Astrophysics and Space Science Library, Vol. 439, Tori, Discs, and Winds: The First Ten Years of AGN Interferometry, ed. H. M. J. Boffin, G. Hussain, J.-P. Berger, & L. Schmidtobreick, 95

Hopkins, P. F., Hernquist, L., Cox, T. J., et al. 2006, ApJS, 163, 1

# References

Hopkins, P. F., Hernquist, L., Cox, T. J., & Kereš, D. 2008, ApJS, 175, 356

Hwang, J.-S., Struck, C., Renaud, F., & Appleton, P. N. 2012, MNRAS, 419, 1780

Iglesias-Páramo, J., López-Martín, L., Vílchez, J. M., Petropoulou, V., & Sulentic, J. W. 2012, A&A, 539, A127

Iglesias-Páramo, J. & Vílchez, J. M. 2001, ApJ, 550, 204

Jiang, N., Wang, H., Mo, H., et al. 2016, ApJ, 832, 111

Johnson, K. E., Hibbard, J. E., Gallagher, S. C., et al. 2007, AJ, 134, 1522

Jones, L. R., Ponman, T. J., Horton, A., et al. 2003, MNRAS, 343, 627

Kauffmann, G., Heckman, T. M., Tremonti, C., et al. 2003, MNRAS, 346, 1055

Kauffmann, G., White, S. D. M., Heckman, T. M., et al. 2004, MNRAS, 353, 713

Kewley, L. J., Dopita, M. A., Sutherland, R. S., Heisler, C. A., & Trevena, J. 2001, ApJ, 556, 121

Khachikian, E. Y. & Weedman, D. W. 1974, ApJ, 192, 581

Knapen, J. H., Shlosman, I., & Peletier, R. F. 2000, ApJ, 529, 93

Konstantopoulos, I. S., Appleton, P. N., Guillard, P., et al. 2014, ApJ, 784, 1

Kormendy, J. 2013, Secular Evolution in Disk Galaxies, ed. J. Falcón-Barroso & J. H. Knapen, 1

Koulouridis, E., Plionis, M., Chavushyan, V., et al. 2006, ApJ, 639, 37

Laurikainen, E., Salo, H., & Buta, R. 2004, ApJ, 607, 103

Leon, S., Combes, F., & Menon, T. K. 1998, A&A, 330, 37

Lilly, S. J., Le Fevre, O., Hammer, F., & Crampton, D. 1996, ApJL, 460, L1

Lisenfeld, U., Braine, J., Duc, P. A., et al. 2016, A&A, 590, A92

Lisenfeld, U., Braine, J., Duc, P. A., et al. 2004, A&A, 426, 471

Lisenfeld, U., Braine, J., Duc, P. A., et al. 2002, A&A, 394, 823

Madau, P., Ferguson, H. C., Dickinson, M. E., et al. 1996, MNRAS, 283, 1388

Mamon, G. A. 1986, ApJ, 307, 426

Mendes de Oliveira, C. & Hickson, P. 1994, ApJ, 427, 684

Mendes de Oliveira, C., Plana, H., Amram, P., Balkowski, C., & Bolte, M. 2001, AJ, 121, 2524

Metz, J. M., Cooper, R. L., Guerrero, M. A., et al. 2004, ApJ, 605, 725

Mihos, J. C. 2004, in Clusters of Galaxies: Probes of Cosmological Structure and Galaxy Evolution, ed. J. S. Mulchaey, A. Dressler, & A. Oemler, 277

Misquitta, P., Bowles, M., Eckart, A., et al. 2020, A&A, 639, A30

Moles, M., Marquez, I., & Sulentic, J. W. 1998, A&A, 334, 473

Moles, M., Sulentic, J. W., & Márquez, I. 1997, ApJL, 485, L69

Monreal-Ibero, A., Arribas, S., Colina, L., et al. 2010, A&A, 517, A28

Mulchaey, J. S. & Regan, M. W. 1997, ApJL, 482, L135

Natale, G., Tuffs, R. J., Xu, C. K., et al. 2010, ApJ, 725, 955

Netzer, H. 2013, The Physics and Evolution of Active Galactic Nuclei

Nikiel-Wroczyński, B., Soida, M., Urbanik, M., Beck, R., & Bomans, D. J. 2013, MNRAS, 435, 149

Nishimura, A., Tokuda, K., Kimura, K., et al. 2015, ApJS, 216, 18

Nishiura, S., Shimada, M., Ohyama, Y., Murayama, T., & Taniguchi, Y. 2000, AJ, 120, 1691

Osterbrock, D. E. & Ferland, G. J. 2006, Astrophysics of gaseous nebulae and active galactic nuclei

O'Sullivan, E., Giacintucci, S., Vrtilek, J. M., Raychaudhury, S., & David, L. P. 2009, ApJ, 701, 1560

Pearson, W. J., Wang, L., Alpaslan, M., et al. 2019, A&A, 631, A51

Petitpas, G. R. & Taylor, C. L. 2005, ApJ, 633, 138

Pietsch, W., Trinchieri, G., Arp, H., & Sulentic, J. W. 1997, A&A, 322, 89

Planck Collaboration, Aghanim, N., Akrami, Y., et al. 2018, arXiv e-prints, arXiv:1807.06209

Plauchu-Frayn, I., Del Olmo, A., Coziol, R., & Torres-Papaqui, J. P. 2012, A&A, 546, A48

Pogge, R. W., Atwood, B., Brewer, D. F., et al. 2010, Society of Photo-Optical Instrumentation Engineers (SPIE) Conference Series, Vol. 7735, The multi-object double spectrographs for the Large Binocular Telescope, 77350A

Renaud, F., Appleton, P. N., & Xu, C. K. 2010, ApJ, 724, 80

Rich, J. A., Kewley, L. J., & Dopita, M. A. 2011, ApJ, 734, 87

Rich, J. A., Kewley, L. J., & Dopita, M. A. 2015, ApJS, 221, 28

## References

Rodríguez-Baras, M., Rosales-Ortega, F. F., Díaz, A. I., Sánchez, S. F., & Pasquali, A. 2014, MNRAS, 442, 495

Romanowsky, A. J., Douglas, N. G., Kuijken, K., et al. 2004, in IAU Symposium, Vol. 220, Dark Matter in Galaxies, ed. S. Ryder, D. Pisano, M. Walker, & K. Freeman, 165

Rothberg, B., Kuhn, O., Edwards, M. L., et al. 2016, in Society of Photo-Optical Instrumentation Engineers (SPIE) Conference Series, Vol. 9906, , 990622

Ryu, D., Kang, H., Hallman, E., & Jones, T. W. 2003, ApJ, 593, 599

Sánchez-Blázquez, P., Peletier, R. F., Jiménez-Vicente, J., et al. 2006, MNRAS, 371, 703

Schmidt, M. 1963, Nature, 197, 1040

Schneider, P. 2015, Extragalactic Astronomy and Cosmology: An Introduction

Seyfert, C. K. 1943, ApJ, 97, 28

Shih, H.-Y. & Stockton, A. 2015, ApJ, 815, 50

Shostak, G. S., Sullivan, W. T., I., & Allen, R. J. 1984, A&A, 139, 15

Silk, J. & Norman, C. 2009, ApJ, 700, 262

Smith, B. J. & Struck, C. 2001, AJ, 121, 710

Sobral, D., Smail, I., Best, P. N., et al. 2013, MNRAS, 428, 1128

Solomon, P. M. & Vanden Bout, P. A. 2005, Annual Review of Astronomy and Astrophysics, 43, 677

Somerville, R. S., Primack, J. R., & Faber, S. M. 2001, MNRAS, 320, 504

Sparke, L. S. & Gallagher, John S., I. 2007, Galaxies in the Universe: An Introduction

Springel, V., White, S. D. M., Jenkins, A., et al. 2005, Nature, 435, 629

Steinborn, L. K., Hirschmann, M., Dolag, K., et al. 2018, MNRAS, 481, 341

Stephan, M. 1877, MNRAS, 37, 334

Stott, J. P., Sobral, D., Smail, I., et al. 2013, MNRAS, 430, 1158

Sulentic, J. W., Pietsch, W., & Arp, H. 1995, A&A, 298, 420

Sulentic, J. W., Rosado, M., Dultzin-Hacyan, D., et al. 2001, AJ, 122, 2993

Toomre, A. & Toomre, J. 1972, ApJ, 178, 623

Trancho, G., Konstantopoulos, I. S., Bastian, N., et al. 2012, ApJ, 748, 102

Tremaine, S. 1989, in Dynamics of Astrophysical Discs, ed. J. A. Sellwood, 231–238

Trinchieri, G., Sulentic, J., Breitschwerdt, D., & Pietsch, W. 2003, A&A, 401, 173

Trinchieri, G., Sulentic, J., Pietsch, W., & Breitschwerdt, D. 2005, A&A, 444, 697

Tsuge, K., Fukui, Y., Tachihara, K., et al. 2020, Publications of the Astronomical Society of Japan[[arXiv]1909.05240]

Tzanavaris, P., Hornschemeier, A. E., Gallagher, S. C., et al. 2010, ApJ, 716, 556

Urrutia, T., Lacy, M., & Becker, R. H. 2008, ApJ, 674, 80

van der Hulst, J. M. & Rots, A. H. 1981, AJ, 86, 1775

Vantyghem, A. N., McNamara, B. R., Edge, A. C., et al. 2017, ApJ, 848, 101

Vazdekis, A., Sánchez-Blázquez, P., Falcón-Barroso, J., et al. 2010, MNRAS, 404, 1639

Veilleux, S. & Osterbrock, D. E. 1987, ApJS, 63, 295

Verdes-Montenegro, L., Yun, M. S., Perea, J., del Olmo, A., & Ho, P. T. P. 1998, ApJ, 497, 89

Verdes-Montenegro, L., Yun, M. S., Williams, B. A., et al. 2001, A&A, 377, 812

Villforth, C., Hamilton, T., Pawlik, M. M., et al. 2017, MNRAS, 466, 812

Violino, G., Ellison, S. L., Sargent, M., et al. 2018, MNRAS, 476, 2591

Wagner, R. M., Edwards, M. L., Kuhn, O., Thompson, D., & Veillet, C. 2014, Society of Photo-Optical Instrumentation Engineers (SPIE) Conference Series, Vol. 9147, An overview and the current status of instrumentation at the Large Binocular Telescope Observatory, 914705

Wiens, C. D., Wenger, T. V., Tzanavaris, P., et al. 2019, ApJ, 873, 124

Williams, B. A., Yun, M., & Verdes-Montenegro, L. 1999, in American Astronomical Society Meeting Abstracts, Vol. 194, American Astronomical Society Meeting Abstracts #194, 19.05

Williams, B. A., Yun, M. S., & Verdes-Montenegro, L. 2002, AJ, 123, 2417

Wilson, T. L., Rohlfs, K., & Hüttemeister, S. 2009, Tools of Radio Astronomy

Xanthopoulos, E., Muxlow, T. W. B., Thomasson, P., & Garrington, S. T. 2004, MNRAS, 353, 1117

Xu, C., Sulentic, J. W., & Tuffs, R. 1999, ApJ, 512, 178

Xu, C. K., Iglesias-Páramo, J., Burgarella, D., et al. 2005, ApJL, 619, L95

Xu, C. K., Lu, N., Condon, J. J., Dopita, M., & Tuffs, R. J. 2003, ApJ, 595, 665

## References

Young, J. S. & Scoville, N. Z. 1991, Annual Review of Astronomy and Astrophysics, 29, 581

Yun, M. S., Verdes-Montenegro, L., del Olmo, A., & Perea, J. 1997, ApJL, 475, L21

Zackrisson, E. & Riehm, T. 2010, Advances in Astronomy, 2010, 735284

Zschaechner, L. K., Bolatto, A. D., Walter, F., et al. 2018, ApJ, 867, 111

X